



The
University
Of
Sheffield.

**Evaluation of extracellular vesicle biogenesis in oral
squamous cell carcinoma**

Wenyi Jiang

A thesis submitted in partial fulfilment of the requirements for the degree of

Doctor of Philosophy

The University of Sheffield

Faculty of Medicine, Dentistry and Health

School of Clinical Dentistry

February 2023

Acknowledgements

First and foremost, I would like to show my best appreciation to my primary supervisor Dr Stuart Hunt, who provided me with constant support, encouragement, and guidance all the time during my PhD study, not only academically but also in life. I thank him for carrying me through every stage with his enthusiasm and immense knowledge. Without his valuable support, I could not finish my PhD study.

Second, I would like to show my sincere gratitude to my secondary supervisor Dr Barbara Ciani and tertiary supervisor Dr Helen Colley for their selfless guidance on my project.

Third, I would like to thank Mrs Brenka McCabe, Dr Matt Worsley, Mr Jason Heath from the School of Clinical Dentistry; Mr Christopher J Hill from the Department of Molecular Biology and Biotechnology; Mrs Sarah L Elliott and Ms Susan Clark from the Department of Oncology and Metabolism for their kind technical support.

Fourth, I would like to thank my group members Dr Xinming Liu, Ms Cathy Park, and Mr Helal Alanazi for sharing their precious advice on experimental design. Additionally grateful to all my colleagues, in particular Miss Lin Zhang. Thanks for giving me a lot of help not only in research but also in life.

Fifth, special gratitude to my uncle, Dr Yadong Jiang for funding me during my study since undergraduate until now. Thanks for having confidence in me and caring for me all the time. I would not have had a chance to start and finish this PhD study or even come to study in Sheffield without his support.

Last but not least, thanks must go to my parents. Thanks for always supporting my decision, believing in me, encouraging me, and listening to me.

Publications and presentations

Publication:

Jiang W, Ciani B, Colley H, and Hunt S. Oral cancer extracellular vesicle biogenesis and release of epidermal growth factor receptor is regulated by hepatocyte growth factor-regulated tyrosine kinase substrate. *In preparation*.

Presentations:

UKEV forum 2022-presented oral presentation “Oral cancer EV biogenesis and release of epidermal growth factor receptor is regulated by hepatocyte growth factor-regulated tyrosine kinase substrate” Dec 2022, Edinburgh.

School of Clinical Dentistry Departmental Seminar-presented oral presentation “The role of ESCRT in oral cancer EV biogenesis” Mar 2022, Sheffield.

UKEV forum 2021-presented flash talk “The role of hepatocyte growth factor-regulated tyrosine kinase substrate (HGS) in oral cancer tumourigenesis” Dec 2021, online.

School of Clinical Dentistry Postgraduate Research Day-presented oral presentation “Evaluation of extracellular vesicle biogenesis in oral squamous cell carcinoma” Jul 2020, Sheffield.

UKEV forum 2019-presented poster “Evaluation of extracellular vesicle biogenesis in oral squamous cell carcinoma” Dec 2019, London.

Abbreviations

2D	2-dimensional
3D	3-dimensional
AAA ATPase	ATPases Associated with diverse cellular Activities
ADP	Adenosine diphosphate
AKT	Protein kinase B
Alix	ALG-2-interacting protein X
ANXA1	Annexin A1
APS	Ammonium persulfate solution
ARF	ADP-ribosylation factor
ARRDC1	Arrestin domain-containing protein 1
ATP	Adenosine triphosphate
ATPase	P-type adenosine triphosphatase
BCA	Bicinchoninic acid
Bro1	BCK1-like resistance to osmotic shock protein-1
BSA	Bovine serum albumin
CAFs	Cancer-associated fibroblasts
Cas9	CRISPR-associated protein 9
cDNA	Complementary DNA
CHMP	Charged multivesicular body protein
CML	Chronic myelogenous leukaemia
CRISPR	Clustered regularly interspaced palindromic repeats
crRNA	Crispr RNA
CTD	C-terminal domain
DAPI	6-diamidino-2-phenylindole
Did2	Diaphanous inhibitory domain 2
DMEM	Dulbecco's modified eagle's medium
DMSO	Dimethyl sulfoxide
dNTP	Deoxynucleoside triphosphate
DSB	Double-strand breaks
dsRNA	Double-stranded RNA
ECM	Extracellular matrix
EDTA	Ethylenediamine tetraacetic acid
EEA1	Early endosome antigen 1
EGF	Epidermal growth factor
EGFR	Epidermal growth factor receptor
EMT	Epithelial to mesenchymal transition
EMT	Epithelial to mesenchymal transition
ERK	Extracellular signal-regulated kinase
ESCRT	Endosomal sorting complex required for transport
EVs	Extracellular vesicles
FBS	Fetal bovine serum
FYVE	Fab1p, YOTB, Vac1p, and EEA1

GAPDH	Glyceraldehyde 3-phosphate dehydrogenase
GAT	GGA and Tom1
GLUE	GRAM-Like Ubiquitin-binding in EAP45
gRNA	Guide RNA
GTP	Guanosine triphosphate
GTPase	Nucleotide GTP binding protein
HD-PTP	His domain protein tyrosine phosphatase
HDR	Homologous directed repair
HGS	Hepatocyte growth factor-regulated tyrosine kinase substrate
HIF- α	Hypoxia-inducible factor 1-alpha
HIV-1	Human immunodeficiency virus-1
HNSCC	Head and neck squamous cell carcinoma
HPRT	Hypoxanthine-guanine phosphoribosyl transferase
HPV	Human papilloma virus
HRP	Horseradish peroxidase
Hse1	Has symptoms of class E Vps mutant 1
hTERT	Human telomerase reverse transcriptase
IL	Interleukin
ILVs	Intraluminal vesicles
Ist1	Increased sodium tolerance 1
JACoP	Just another colocalization plugin
JAK/STAT	Janus kinase-signal transducer and activator of transcription
JNK	C-Jun N-terminal kinase
KGM	Keratinocyte growth medium
LAIR-1	Leukocyte-associated immunoglobulin-like receptor 1
LAMP1	Lysosomal-associated membrane protein 1
Linc	Long non coding
LIP5	Cleavage interaction protein 5
mAb	Mouse chimeric monoclonal antibody
MALAT1	Metastasis associated lung adenocarcinoma transcript 1
MAPK	Mitogen-activated protein kinase
MEK	Mitogen-activated protein kinase
MIM	MIT-interacting motif
miRNA	Micro RNA
MIT	Microtubule interacting and transport
MLC	Myosin light chain (MLC)
mRNA	Messenger RNA
MVB	Multivesicular bodies
NaCl	Sodium chloride
NF- κ B	Nuclear factor kappa B
NHEJ	Non-homologous end joining
NOKs	Normal oral keratinocytes
nSMase	Neutral sphingomyelinase
NTA	Nanoparticle tracking analysis

NZF	Np14-type zinc finger
OME	Oral mucosal equivalents
OSCC	Oral squamous cell carcinoma
PAM	Protospacer adjacent motif
PBS	Phosphate buffered saline
PBST	Phosphate buffered saline tween-20
PCR	Polymerase chain reaction
PD-L1	Programmed death ligand-1
PFA	Paraformaldehyde
pH	Power of Hydrogen
PI	Phosphatidylinositol
PI	Propidium iodide
PI3K	Phosphoinositide-3-kinase
PRR	Proline-rich region domains
PtdIns (3) P	Lipid phosphatidylinositol 3-phosphate
PTP	Protein tyrosine phosphatase
qPCR	Quantitative polymerase chain reaction
RAB	Ras-associated binding
Rac1	Rac family small GTPase 1
Rho	Ras-homologous
RISC	RNA induced silencing complex
RNA	Ribonucleic acid
RNAi	RNA-interference
RNase	Ribonucleases
RNP	Ribonucleoprotein
ROCK	Rho-associated protein kinase
<i>S.p. Cas9</i>	<i>Streptococcus pyogenes and Staphylococcus aureus Cas9</i>
SDS	Tris base Sodium dodecyl sulphate
SDS-PAGE	Sodium dodecyl sulfate-polyacrylamide gel electrophoresis
SEM	Standard error of mean
sgRNA	Single strand gRNA
SH3	Src homology 3
siRNA	Small interfering RNA
Snf	Sucrose non-fermenting
STAM	Signal transducing adaptor molecule
T7EI	T7 endonuclease
TALENs	Transcription activator-like effector nucleases
TAM	Tumour associated macrophages
TBS	Tris-buffered saline
TBST	Tris-buffered saline tween-20
TEM	Transmission electron microscopy
TEMED	Tetramethyl ethylenediamine
TFR	Transferrin receptor
TGF- β	Transforming growth factor beta

TME	Tumour microenvironment
tracrRNA	Trans-activating crRNA
TSG101	Tumour susceptibility
UBAP1	Ubiquitin associated protein 1
UEV	Ubiquitin E2 variant
UF-dFBS	Ultra-filtered EV-depleted FBS
UIM	Ubiquitin interaction motif
UKEV	UK Society for Extracellular Vesicles
V-domain	V-central proline-rich domain
VE	Vascular endothelial
VEGF	Vascular endothelial growth factor
Vfa1	Vps four-associated 1
VHS	Vps-27, HGS and STAM
Vps	Vacuolar protein sorting associated protein
VSE	Vps4 stimulatory element
VSL	Vta1 SBP1 LIP5
Vta1	Vacuolar protein sorting-associated protein Vta1 homolog
WT	Wild-type
ZFNs	Zinc-finger nucleases

Contents

Acknowledgements	I
Publications and presentations	II
Abbreviations	III
Contents.....	VII
List of Tables	XI
List of Figures	XII
Abstract	XIV
Chapter 1: Introduction	1
1.1 Head and Neck Squamous Cell Cancer	1
1.1.1 Oral squamous cell carcinoma.....	1
1.1.2 Diagnosis, prognosis, and therapy of OSCC	2
1.1.3 Tumour microenvironment in HNSCC.....	3
1.1.4 Extracellular vesicles in the tumour microenvironment	4
1.1.5 Extracellular vesicles in OSCC.....	7
1.2 Extracellular vesicles	8
1.2.1 Exosomes.....	9
1.2.2 Microvesicles.....	13
1.2.3 Apoptotic bodies.....	14
1.3 ESCRT machinery.....	16
1.3.1 ESCRT-0	18
1.3.2 ESCRT-I.....	19
1.3.3 ESCRT-II.....	21
1.3.4 ESCRT-III	22
1.3.5 Vps4-Vta1	24
1.3.6 Physiological functions of ESCRT machinery in human cancer	30
1.4 Scope of the current study.....	32
1.5 Hypothesis, aims and objectives	33
1.5.1 Hypothesis	33
1.5.2 Aims and objectives.....	33
Chapter 2: Materials and methods.....	35

2.1 Supplies of materials and chemical reagents.....	35
2.2 Cell culture.....	35
2.2.1 Primary cells	35
2.2.2 Cell lines	35
2.2.3 Cell culture medium.....	36
2.2.4 Cell culture and passage	37
2.2.5 Cell counting and seeding.....	38
2.2.6 Storage of mammalian cells.....	38
2.3 Extracellular vesicles analysis.....	39
2.3.1 Preparation of EV-depleted FBS.....	39
2.3.2 Preparation of conditioned medium.....	39
2.3.3 Differential centrifugation	40
2.3.4 Nanoparticle tracking analysis.....	41
2.4 DNA methods.....	42
2.4.1 Genomic DNA isolation.....	42
2.4.2 Polymerase chain reaction (PCR).....	43
2.4.3 Agarose gel electrophoresis	45
2.5 CRISPR-Cas9 genome editing.....	46
2.5.1 Preparation of RNA oligos.....	47
2.5.2 Formation of ribonucleoprotein RNP complex.....	47
2.5.3 Reverse transfection of RNP complexes.....	47
2.5.4 T7EI mutation detection	47
2.5.5 Single clone isolation and cell line establishment	50
2.6 RNA methods.....	51
2.6.1 RNA extraction	51
2.6.2 RNA quantification.....	52
2.6.3 Reverse transcription	52
2.6.4 Quantitative polymerase chain reaction (qPCR).....	54
2.7 Protein methods.....	57
2.7.1 Protein harvesting	57
2.7.2 Protein quantification.....	57
2.7.3 Sodium dodecyl sulfate-polyacrylamide gel electrophoresis (SDS-PAGE) and	

protein transfer.....	58
2.7.4 Protein transfer, western blotting, and densitometry	60
2.7.5 Membrane stripping and storage.....	61
2.7.6 Transmission electron microscopy.....	62
2.7.7 Immunofluorescence.....	63
2.7.8 Pulse-chase experiments	65
2.7.9 Data analysis	65
2.8 Transient transfection.....	65
2.9 Cells growth assay and viability	68
2.9.1 Growth assay.....	68
2.9.2 Viability	69
2.9.3 Apoptosis detection by flow Cytometry	69
2.10 Statistical analysis.....	70
Chapter 3: Characterisation of ESCRT machinery subunits in OSCC cells.....	71
3.1 Introduction.....	71
3.2 Results.....	73
3.2.1 HGS transcript expression and protein abundance	73
3.2.2 TSG101 transcript expression and protein abundance.....	75
3.2.3 Vps22 transcript expression and protein abundance.....	77
3.1.1 Post-transcriptional regulation of HGS.....	79
3.1.2 Investigation of the interaction between HGS and early endosomes in OSCC .	84
3.2 Discussion	89
3.2.1 ESCRT subunits expressed in primary oral keratinocytes, immortalised oral keratinocyte and OSCC cell lines	89
3.2.2 Post-transcriptional regulation.....	92
3.2.3 The interaction between ESCRT subunit HGS and early endosomes in OSCC	93
Chapter 4: HGS gene silencing strategies in OSCC.....	95
4.1 Introduction.....	95
4.2 Results.....	97
4.2.1 HGS silencing by siRNA transfection	97
4.2.2 HGS silencing by CRISPR-Cas9 genome editing	102
4.3 Discussion	106

4.3.1 Transient HGS silencing using siRNA transfection.....	106
4.3.2 Generation of a HGS deficient OSCC cell line.....	107
Chapter 5: Functional consequences of HGS knockout in OSCC cells	111
5.1 Introduction.....	111
5.2 Results.....	113
5.2.1 Cellular phenotypical changes after HGS knockout.....	113
5.2.2 The effect of HGS depletion on endosomal compartments	116
5.2.3 The effect of HGS depletion on extracellular vesicle release and cargo.....	121
5.2.4 Determining the role of HGS in EGF/EGFR cellular trafficking	129
5.3 Discussion	131
5.3.1 The phenotypical and morphological changes of HGS knockout OSCC	131
5.3.2 Characterisation of EV pellets derived from HGS deficient cells	133
5.3.3 Characterisation of EGF/EGFR cellular trafficking upon HGS knockout in OSCC.....	135
Chapter 6: Final discussion	137
6.1 HGS is a master regulator modulating MVB biogenesis and EGFR trafficking	137
6.2 ESCRT mediated EV release may support OSCC tumourigenesis.....	140
6.3 Could OSCC-derived EVs play a role in cetuximab therapeutic response?	142
6.4 Limitations of the study	143
6.5 Future work.....	145
6.6 Concluding remarks	146
Supplementary materials	147
References	148

List of Tables

Table 1.1: List of ESCRT proteins.....	28
Table 2.1: Details of cells	36
Table 2.2: The composition of 500 ml growth medium with Fetal Bovine Serum	37
Table 2.3: Setting of ZetaView instrument.....	42
Table 2.4: Master mix for PCR.....	44
Table 2.5: Setting of PCR cycles	45
Table 2.6: Assembled PCR reactions for CRISPR-Cas9 mutation detection	49
Table 2.7: Composition of PCR reactions to form heteroduplexes for T7EI digestion.....	50
Table 2.8: Gradient PCR cycle to form heteroduplexes for T7EI digestion.....	50
Table 2.9: Composition of RT-PCR master mix	53
Table 2.10: Setting of RT-PCR conditions	54
Table 2.11: TaqMan probes used in this study.....	55
Table 2.12: Composition of Real-time PCR master mix	56
Table 2.13: Setting of Real-time PCR two-step cycling conditions	56
Table 2.14: Composition of protein lysis buffer.....	57
Table 2.15: The components and quantity to make 12% SDS-PAGE gels.....	59
Table 2.16: Buffers and reagents used in SDS-PAGE and western blotting.....	60
Table 2.17: Lists of antibodies used in western blotting	62
Table 2.18: Antibodies used in immunofluorescence	64
Table 2.19: Set up the dilution of transient transfection reagents with Opti-MEM.....	67
Table 2.20: Composition of Annexin V incubation reagent	70

List of Figures

Figure 1.1: Schematic illustration of tumour microenvironment.	4
Figure 1.2: Schematic illustration of extracellular vesicles subtypes.....	9
Figure 1.3: ESCRT dependent endosome biogenesis pathway.....	17
Figure 1.4: The modelled structures of ESCRT-subunits.	30
Figure 2.1 Diagram illustrating differential centrifugation.	41
Figure 2.2 Workflow summarising CRISPR-Cas9 genome editing.	46
Figure 3.1: HGS transcript expression and protein abundance.	74
Figure 3.2: TSG101 transcript expression and protein abundance.....	76
Figure 3.3: Vps22 transcript expression and protein abundance.....	78
Figure 3.4: Expression of putative post-transcriptional regulators of HGS.	81
Figure 3.5: MiR-142-3p inhibition or overexpression in H357 for 24 hours.	83
Figure 3.6: MiR-142-3p inhibition or overexpression in H357 for 48 hours.	84
Figure 3.7: Representative immunofluorescence microscopy images of HGS and EEA1.....	86
Figure 3.8: Representative confocal microscopy images of immunofluorescence staining of HGS and EEA1.	88
Figure 4.1: Optimisation of 24 hour HGS siRNA silencing.....	99
Figure 4.2: Optimisation of 48 hour HGS siRNA silencing.....	101
Figure 4.3: Validation of HGS silencing by CRISPR-Cas9 genome editing in H357.....	105
Figure 4.4: HGS is stably silenced in H357 Δ HGS.....	106
Figure 5.1: Growth rate, doubling time and viability in HGS knockout OSCC cells.	114
Figure 5.2: Apoptosis assay using flow cytometry.....	116
Figure 5.3: Immunofluorescence microscopy images of endosomal markers in WT and Δ HGS cells.....	118
Figure 5.4: Quantification of co-localisation of HGS with endosome markers and fluorescence intensity.	119
Figure 5.5: TEM characterisation of MVBs.....	120
Figure 5.6: Assessment of particles number in conditioned medium from WT and Δ HGS cells.	121

Figure 5.7: Characterisation of extracellular particle size distribution in conditioned medium and differential centrifugation pellets derived from WT and Δ HGS cells.	123
Figure 5.8: Characterisation of particle concentration in conditioned medium and pellets derived from WT and Δ HGS cells by NTA.....	124
Figure 5.9: Assessment of EVs derived from WT cells and Δ HGS cells by Western blot....	126
Figure 5.10: Western blot and densitometry of cellular abundance of the EV cargo and EV markers in WT and Δ HGS cells.	128
Figure 5.11: Cellular trafficking of EGF/EGFR upon HGS knockout.	130
Figure 6.1: Schematic summary of how HGS depletion affects the endosomal pathway.	140
Figure 6.2: Hypothetical mechanisms of EV-mediated cetuximab therapy resistance in OSCC cells.....	143
Figure S1: Assessment of particles number in conditioned medium from mock, negative silencer and HGS silencer transfected OSCC cells.	147

Abstract

Oral cancer cells produce increased numbers of extracellular vesicles (EVs) compared to normal controls. However, the underlying mechanism was previously unknown. The endosomal sorting complex required for transport (ESCRT) subunits are implicated in cellular processing of ubiquitinated proteins such as epidermal growth factor receptor (EGFR) and EV biogenesis. We hypothesised that ESCRT members are overexpressed in oral cancer cells, leading to increased production of EVs.

In order to test this hypothesis, gene expression and protein abundance of representative ESCRT-0, -I, -II subunits in an immortal normal oral keratinocyte cell line and oral cancer cell lines were compared to primary oral keratinocytes by qPCR and western blotting, respectively. Co-localisation of HGS (ESCRT-0) with early and late endosomal markers (EEA1 and RAB7) was determined by immunofluorescence. CRISPR-Cas9 genome editing was used to knockout HGS in the H357 oral cancer cell line. Endosomal structures were imaged by transmission electron microscopy (TEM). EVs were enriched by ultracentrifugation and analysed by nanoparticle tracking analysis (NTA) and western blotting. Processing of EGFR was tracked by EGF pulse-chase experiments.

HGS protein abundance was >4-fold higher in oral cancer cell lines compared to normal controls. Immunofluorescence revealed that HGS co-localised with early endosomal structures (EEA1). Enlarged endosomes were visualised in the HGS knockout cell line by TEM and a 3-fold reduction in particle release was observed by NTA. EGFR processing was stalled in the HGS mutant leading to cellular accumulation and a significant decrease in EV-associated EGFR.

Chapter 1: Introduction

1.1 Head and Neck Squamous Cell Cancer

Head and neck squamous cell carcinoma (HNSCC) is the sixth most common cancer worldwide and accounts for more than 90% of head and neck cancers and 5% of all cancer cases in the UK (Alsaifi *et al.*, 2019, Sanderson and Ironside, 2002, Thomas and Jefferson, 2013). It consists of a series of cancers that occur in upper aerodigestive tract mucosa including the larynx, nasal cavity, hypo-pharynx, pharynx and oral cavity (Ragin *et al.*, 2007, Hammerman *et al.*, 2015). Symptoms can include difficulty swallowing (dysphagia), ear pain, and hoarseness (Sanderson and Ironside, 2002). According to a recent report, there were 800,000 new cases diagnosed as HNSCC in 2018 worldwide (Canning *et al.*, 2019). Within these patients, around 70% are male and 30% are female. The 5-year survival rate is low at 40%-50% (Sanderson and Ironside, 2002). 80% of HNSCC patients are tobacco and alcohol consumers (Canning *et al.*, 2019). The pre-carcinogen chemical elements of cigarettes are nitrosamines, benzopyrenes and aromatic amines, which can combine with oxygen to induce mutations. One additional potential carcinogen is the human papilloma virus (HPV). A previous study showed that females with HPV-16-positive cervical cancer had a higher risk of developing HNSCC (Ajila *et al.*, 2015). As the commonest subtype of HNSCC, oral squamous cell carcinoma accounts for 40% of all cases (Ragin *et al.*, 2007).

1.1.1 Oral squamous cell carcinoma

Oral squamous cell carcinoma (OSCC) is a malignant neoplasm occurring in the oral cavity, pharyngeal region and salivary glands (Markopoulos, 2012). Tumours of the oral cavity can be further subdivided based on their anatomical location including tongue, lip, and gum

(Bundgaard *et al.*, 1994). The main risk factors for OSCC are lifestyle choices such as smoking tobacco, alcohol consumption, chewing betel nuts, paan dip and snuff, and using oral rinse products that contain ethyl alcohol (Werner and Seymour, 2009). In addition, some reports show that lack of nutrition is also a risk factor for OSCC (Bravi *et al.*, 2013). High consumption of fruits and vegetables decreases the risk of OSCC by 40%-50% (Tandon *et al.*, 2017).

1.1.2 Diagnosis, prognosis, and therapy of OSCC

The mortality and morbidity of OSCC are usually high because of late detection. The 5-year survival rate of OSCC is higher in the early stages when cancer remains *in situ*. Stage I OSCC has an 12% higher survival rate than stage II (Chan *et al.*, 2002). Through using microscopy, clinicians are able to observe abnormal or cancerous oral lesions. Other ways to diagnose OSCC include using immunohistochemistry to various different molecular weight keratin species (Sciubba, 2001). Moreover, polymerase chain reaction (PCR) is also a useful way to check the existence of deoxyribonucleic acid (DNA) mutations in samples (Kugimoto *et al.*, 2012). Surgery is the most efficient way to treat early-stage OSCC. Patients treated by surgery showed a higher survival rate compared with patients who did not (Ribeiro *et al.*, 2014, Shah and Gil, 2009). Radiotherapy is another treatment modality in cases with a small-volume tumour, especially at stages I and II. Chemotherapy is commonly used to treat advanced-stage OSCC, metastatic disease or recurrence at the primary site. Adjuvant therapy which combines surgery and radiotherapy can achieve a better result than using chemotherapy only (Liu *et al.*, 2017). In order to increase the patient survival rate and quality of life, researchers continue to search for new diagnostic/prognostic biomarkers and treatments.

1.1.3 Tumour microenvironment in HNSCC

In recent years, the tumour microenvironment (TME) has proven to be important in cancer progression. Tumourigenesis is a multifactor, multi-stage dynamic process (Wu and Dai, 2017). This process includes stages of initiation, progression, and metastasis. The tumour cells are encircled by extracellular matrix (ECM) and stromal cells. Similar to other cancers, HNSCC is derived from normal keratinocytes at the primary site. The TME includes cancer-associated fibroblasts (CAFs), neutrophils, macrophages, regulatory T cells, natural killer cells, mast cells and pericytes (Curry *et al.*, 2014). These subpopulations communicate with each other, switching between anti-tumour and pro-tumour phenotypes, to promote activities such as; secreting chemokines, cytokines, and growth factors; and remodelling of the basement membrane and ECM (Figure 1.1). For example, as the predominant type of stromal cells, the main function of CAFs is creating and maintaining a TME to support cancer cell proliferation and progression. The commonest markers used to detect CAFs are α -smooth muscle actin and fibroblast activation protein which were found to be up-regulated in HNSCC and related to poor prognosis (Park *et al.*, 1999, Wonganu and Berger, 2016). The interaction between tumour cells and TME is a determining factor of tumour progression. As mentioned above, the release of soluble factors (chemokines etc.) is important in intercellular communication. One additional method of intercellular communication within the TME is via extracellular vesicles.

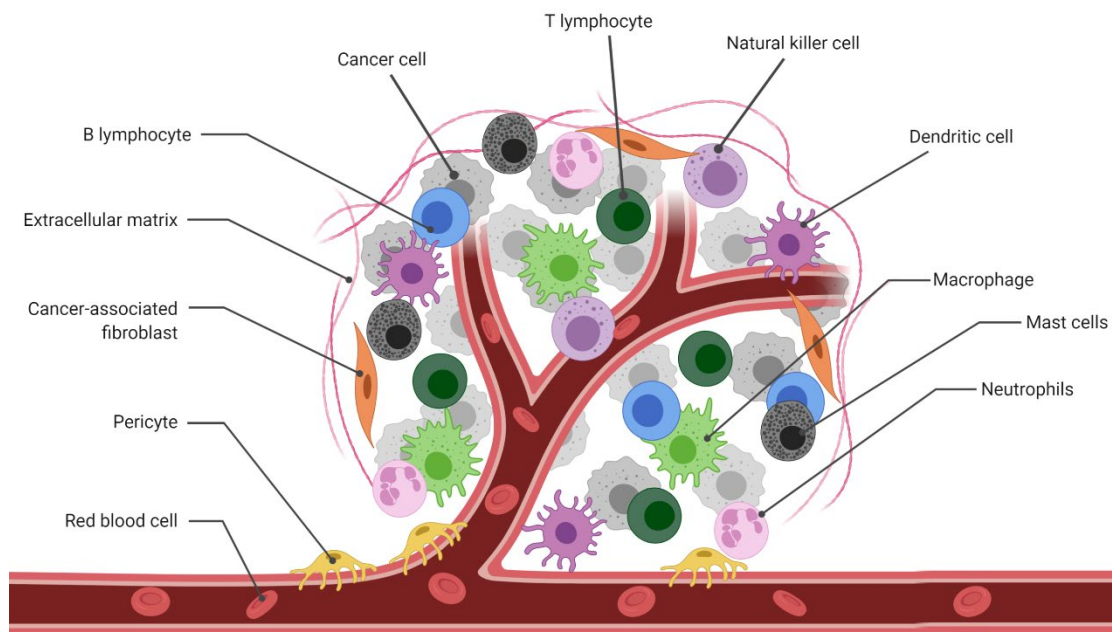


Figure 1.1: Schematic illustration of tumour microenvironment. Tumour microenvironment consists of cancer cells (grey), T lymphocytes (dark green), natural killer cells (light purple), dendritic cells (dark purple), Macrophages (light green), mast cells (black), neutrophils (pink), red blood cells (red), pericytes (yellow), cancer-associated fibroblast (orange), B lymphocytes (blue) and surrounding extracellular matrix. Figure was created with BioRender.

1.1.4 Extracellular vesicles in the tumour microenvironment

Extracellular vesicles (EVs) are lipid bilayer-enclosed particles that carry different molecules including lipid, protein, coding and non-coding RNAs and DNA (Mulcahy *et al.*, 2014). Horizontal transmission of molecules from donor cells to recipient cells is important in TME communication, which affects many processes such as tumour proliferation, angiogenesis, and immune responses.

Cancer cell-derived EVs play an important role in tumour proliferation. The growth of tumours is regulated through activating receptors of signalling pathways such as protein kinase B (AKT) and mitogen-activated protein kinase (MAPK). EVs released by oesophageal cancer

cells up-regulated oncogene adenosine triphosphate (ATP) binding cassette subfamily G member 2, which enhanced cancer proliferation. In addition, this activity is positively correlated with the expression of long non coding (Linc) ribonucleic acid (RNA)-very low density lipoprotein receptor in EVs (Chen *et al.*, 2019). Leukocyte-associated immunoglobulin-like receptor 1 (LAIR-1) is over-expressed in renal cell carcinoma. EVs enriched with LAIR-1 up-regulated the phosphorylation status of AKT, which increased renal cell carcinoma progression (Jingushi *et al.*, 2019).

Metastasis is a complex and multi-step process that usually involves: epithelial to mesenchymal transition (EMT); cancer cells invade the basement membrane, allowing vascular and lymphatic migration, and finally implantation and division of cancer cells at a secondary site (Gopal *et al.*, 2017, Hingorani, 2015). EMT is significant in tumour metastasis. During EMT, epithelial cells lose polarised organisation and cell adhesion molecules. Thus, EMT promotes the invasive and metastatic ability of tumours (Diepenbruck and Christofori, 2016). Cancer-derived EVs contain transforming growth factor beta (TGF- β), β -catenin, Hypoxia-inducible factor 1-alpha (HIF- α) and Caveolin-1 which are able to induce EMT and strengthen the migratory ability of cells and invasion (Syn *et al.*, 2016). Exosomes from nasopharyngeal carcinoma were shown to overexpress HIF-1 α , which interacts with the Snail pathway to up-regulate Twist and finally result in EMT induction (Hood, 2016). The integrins present in cancer-derived EVs are believed to mediate organotrophic metastatic spread. For example, α 6 β 4 and α 6 β 1 positive EVs may promote lung metastasis whereas, α v β 5 positive EVs are related to liver metastasis (Hoshino *et al.*, 2015). The RNA cargo of prostate cancer-derived EVs have been shown to promote metastatic spread to bone by prostate cancer cells (Probert *et*

al., 2019).

In addition to promoting proliferation and metastasis, cancer-derived EVs are also important in the production of new blood vessels by angiogenesis. The growth of a tumour relies on oxygen and nutrients provided by blood vessels. Cancer-derived vesicles contain many vascular endothelial (VE) growth factors which induce proliferation, migration, maturation and remoulding of these tumour endothelial vessels such as vascular endothelial growth factor (VEGF), fibroblast growth factor, TGF- β , platelet-derived growth factor, and interleukin (IL)-8 (Katoh, 2013). Wnt family member 5A overexpression in melanoma induced cancer-derived EVs that contain angiogenic growth factors VEGF, IL-6, and matrix metalloproteinase 2 (Ekström *et al.*, 2014). In addition, epidermal growth factor (EGF)-positive EVs that are taken up by endothelial cells caused up-regulation of VEGF and VEGF receptor 2, which promoted angiogenesis (Al-Nedawi *et al.*, 2009). Other research found that microRNA (miRNA) in EVs could promote angiogenesis. MiR-9 in EVs down-regulated SOCS5 which resulted in janus kinase/signal transducer and activator of transcription (JAK/STAT) signalling pathway activation (Zhuang *et al.*, 2012). Microvesicle-enclosed miR-150 targets tumour associated macrophages (TAM) causing up-regulation of VEGF levels, which created an angiogenic microenvironment in the tumour (Liu *et al.*, 2013).

EVs are also involved in regulating immune responses. The TME contains innate immune cells and adaptive immune cells. The former includes macrophages, neutrophils, mast cells, myeloid dendritic cells, and NKs. The latter includes T and B lymphocytes. Within the TME, TAMs and T cells are most frequently found (Grivennikov *et al.*, 2010). Cancer-derived EVs play the role of communicator between cancer cells and immune cells. These vesicles are able

to activate and balance immune mediators to indicate inflammatory responses and anti-tumour immunity which further causes anti-tumour activity (Mehrra *et al.*, 2007, Andre *et al.*, 2002). For example, EVs from lung cancer cells migrate to myeloid cells through pulmonary vessels, causing activation of dendritic cells and anti-tumour immune responses (Headley *et al.*, 2016, Moroishi *et al.*, 2016). On the other hand, EVs can also suppress immune responses which help tumour cells undergo immune escape (Xie *et al.*, 2019). There is a study showed, EVs from breast cancer cells create an immunity-suppressed microenvironment to support cancer cells escaping from the immune system through activating nuclear factor kappa B (NF- κ B) in TAMs. The activation of NF- κ B results in the secretion of pro-inflammatory cytokines such as IL-6, tumour necrosis factor- α , colony-stimulating factor and C-C motif chemokine ligand 2. These cytokines suppress anti-tumour immune responses in the TME (Chow *et al.*, 2014).

1.1.5 Extracellular vesicles in OSCC

The anatomical relationship between saliva and the oral cavity has led researchers to believe that salivary EVs represent a potential source of biomarkers for clinical use in relation to oral disease. Indeed, the tetraspanin protein profiles of EVs isolated from healthy volunteers and oral cancer patients are significantly different (Zlotogorski-Hurvitz *et al.*, 2016). CD63 was more abundant in salivary EVs from oral cancer patients, but CD81 and CD9 were less abundant. Comparison of salivary EV miRNA cargo found that miRNA-31, miRNA-125a and miRNA-200a were higher in OSCC patients compared to healthy controls, which means these miRNAs could be potential biomarkers in clinical diagnosis and detection of oral cancer (Liu *et al.*, 2010, Park *et al.*, 2009). Furthermore, miRNAs in EVs are able to regulate many cellular activities, such as altering OSCC chemotherapy resistance (Yu *et al.*, 2010). EVs may also be

used as novel treatments for OSCC. EVs can carry cargo such as drugs or therapeutic molecules (siRNAs and miRNAs) which are able to target cancer cells and promote anti-tumour activities (Ren, 2019). For example, gamma-delta ($\gamma\delta$) T cell-derived EVs that carry miR-138 were shown to regulate anti-tumour immunity by targeting CD8⁺ T Cells in OSCC (Li *et al.*, 2019).

1.2 Extracellular vesicles

EVs are small particles that are enclosed by a lipid bilayer (Colombo *et al.*, 2014). These vesicles are released by different types of cells and exist in body fluids including breast milk, lymphatic fluid, saliva, blood, urine, and seminal fluid (Caby *et al.*, 2005, Pisitkun *et al.*, 2004). Cancer cells are able to communicate with neighbouring or distant cells by secreting these vesicles. EVs can horizontally transfer cell-specific cargos including proteins, lipids, and genetic material (Baglio *et al.*, 2015). There are three recognised mechanisms that form EVs, which are exocytosis, budding and blebbing. Based on their different biogenesis, EVs can be grouped into three different subtypes, which are exosomes, microvesicles and apoptotic bodies/EVs (Liu *et al.*, 2017) (Figure 1.2).

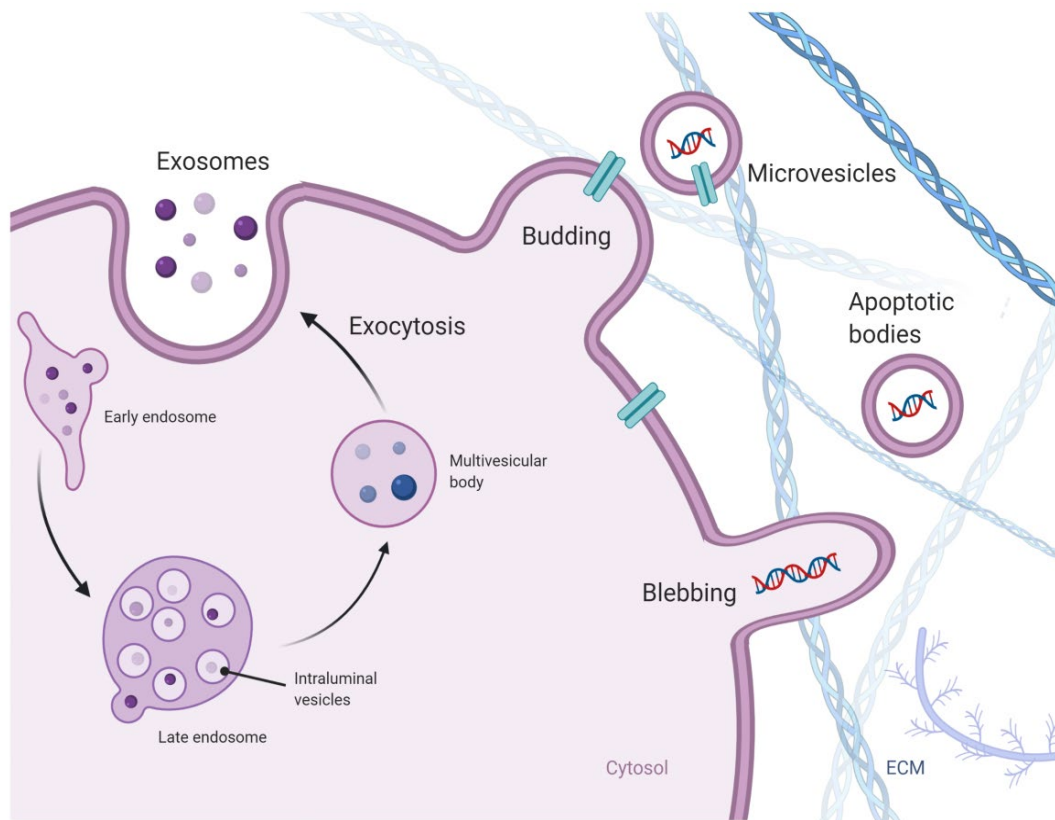


Figure 1.2: Schematic illustration of extracellular vesicles subtypes. Extracellular vesicles are grouped into three subtypes. They are exosomes, microvesicles, and apoptotic bodies/EVs. Based on different biogenesis pathways, these three categories of nanoparticles are produced through exocytosis, budding and blebbing. Figure was created with BioRender.

1.2.1 Exosomes

Exosomes are the most commonly studied subtype of EVs. They measure 30-100 nm in diameter and float at a density of 1.13g/ml in a sucrose gradient (Al-Nedawi *et al.*, 2008). Exosomes carry transmembrane proteins including CD63, CD9, CD81, CD82, transferrin receptor (TFR), lipid rafts and cell receptors. Exosomes can also carry other cargos such as small RNAs and cytosolic proteins including tumour susceptibility (TSG101), clathrin, ALG-2-interacting protein X (Alix), antigen-major histocompatibility complex I and II (Al-Nedawi *et al.*, 2008). Exosomes are involved in many cellular processes like antigen presentation, signal transduction and immune response. In addition, their cargo (e.g. miRNA, messenger RNA (mRNA), and DNA) function in regulating cellular stimulation, transformation and

differentiation (Rajagopal and Harikumar, 2018). Exosomes have been implicated as prognostic biomarkers for many diseases including cardiovascular, renal, neurodegenerative, lipid metabolic diseases and cancers (Zhang *et al.*, 2019). Exosomes are endocytic in origin. Multivesicular bodies (MVB) are formed by the inward budding of early endosomal membranes to produce intraluminal vesicles (ILVs) (Alshafi *et al.*, 2019). If the MVB fuse with the plasma membrane, these ILVs are released as exosomes into the extracellular space (Grant and Donaldson, 2009). Alternatively, if MVBs fuse with lysosomes (membrane-bound organelles that contain digestive enzymes) ILVs will be degraded (Dobrowolski and De Robertis, 2011). There are thought to be two modes of exosomes biogenesis, which are the endosomal sorting complex required for transport (ESCRT) dependent and independent pathways (Rajagopal and Harikumar, 2018).

During the maturation process from early endosomes to MVBs, the ESCRT machinery is important in regulating endosomal membrane invagination to generate ILVs in the lumen of the endosomes (Huotari and Helenius, 2011). Meanwhile, it is also essential in the endolysosomal degradation pathway. The ESCRT machinery consists of four cytoplasmic complexes, wherein ESCRT-0, ESCRT-I, ESCRT-II and ESCRT-III function on membrane remodelling and vesicle budding. The final functional complex, vacuolar protein sorting associated protein (Vps)-4, works together with vacuolar protein sorting-associated protein Vta1 homolog (Vta1) to allow the inward membrane scission and ESCRT recycling (Henne *et al.*, 2013). Previous studies found knockdown of ESCRT-0 subunits hepatocyte growth factor-regulated tyrosine kinase substrate (HGS), signal transducing adaptor molecule (STAM)-1 and ESCRT-I subunit TSG101 were able to reduce the total exosome secretion in breast cancer cell lines (Colombo *et al.*,

2013). Meanwhile, disruption of Vps4 and Vtal cooperation has the potential to result in defective MVB formation which results in failure to shed ILVs and release of exosomes to the extracellular space (Kojima *et al.*, 2014, Schmidt and Teis, 2012). Furthermore, the ESCRT subunits also show their importance in selecting exosomal-related cargos. Previous studies highlighted that the ESCRT-0 proteins are essential in the ubiquitination and recruiting epidermal growth factor receptor (EGFR) to endosomes, and the knockdown of HGS can potentially affect ubiquitinated cargo sorting (Katz *et al.*, 2002, Malerød *et al.*, 2007). Depletion of Vps22 in breast cancer cells caused EGFR accumulation, demonstrating that ESCRT-II is required for lysosomal degradation of EGFR (Malerød *et al.*, 2007). All in all, ESCRT machinery is important in EV formation and release. Lack of ESCRT proteins may affect EV secretion or cargo selection. The ESCRT machinery will be described in further detail in section 1.3.

Some studies indicated that exosome biogenesis can happen without ESCRT participation. It has been shown that although key subunits of four ESCRT subunits (ESCRT-0, ESCRT-I, ESCRT-II and ESCRT-III) were silenced, ILVs can still be formed which suggests the existence of ESCRT-independent pathways (Stuffers *et al.*, 2009). However, it is thought that ESCRT-dependent and ESCRT-independent pathways may work in concert instead of entirely separated (Maas *et al.*, 2017). Trajkovic *et al.* (2008) knocked down the ESCRT members HGS, TSG101 or Alix and found exosomes that contain proteolipid protein still can form normally. Further studies found neutral sphingomyelinase (nSMase) hydrolyses sphingomyelin to produce ceramide. Ceramide (a special cone-shaped lipid) was reduced when nSMase was inhibited (Trajkovic *et al.*, 2008, Raposo and Stoorvogel, 2013). Ceramide reduction is able to affect

MVB inward budding and potentially regulates exosomal biogenesis (Raposo and Stoorvogel, 2013). Moreover, cholesterol is an important component of MVB and is abundant in the membrane of exosomes (Hornick *et al.*, 1985, Llorente *et al.*, 2013). In oligodendrocytes, the accumulation of cholesterol in late MVB can promote the secretion of exosomes that contain flotillin-2, Alix, CD63 and cholesterol. This process depends on flotillin-2 (Strauss *et al.*, 2010). There is evidence that transmembrane protein tetraspanins play a role in exosome biogenesis. In melanoma, CD63 is able to select melanin protein into ILVs. This process does not rely on ceramide or ESCRT pathways (van Niel *et al.*, 2011). Knockout of CD63 in kidney cells resulted in reduced EV biogenesis (Hurwitz *et al.*, 2016). Other tetraspanins, TSPAN8 and CD81, are able to select some ligands into exosomes (Nazarenko *et al.*, 2010, Perez-Hernandez *et al.*, 2013). In addition, overexpression of CD9 or CD82 has been reported to promote exosome formation (Chairoungdua *et al.*, 2010). Knockout of CD9 in mice dendritic cells resulted in reduced exosomal flotillin-1 which was involved in vesicular trafficking (Chairoungdua *et al.*, 2010). The molecular chaperone HSP70 recruits TFR to transfer cytoplasmic pentapeptide KFERQ into ILVs and then exosomes (Géminard *et al.*, 2004, Sahu *et al.*, 2011). Taken together, this information suggests a complex relationship between exosome formation and ESCRT-independent pathways.

Another part of the cellular machinery that regulates endocytic trafficking and vesicle budding are the Ras-associated binding (RAB) proteins (Stenmark, 2009). Knockdown of RAB2b, RAB5a, RAB9a, RAB27a and RAB27b resulted in reduced exosome release (Ostrowski *et al.*, 2010). As the key markers of early and late endosomes, RAB5 to RAB7 conversion was proven to be the mechanism of driving cargo progress from early endosome

traffic to downstream of MVBs (Rink *et al.*, 2005).

1.2.2 Microvesicles

Microvesicles are also lipid-enclosed vesicles, but their morphology and biogenesis differ from exosomes. The size range of microvesicles is 100-1000 nm and their density is around 1.19 g/ml in a sucrose gradient (Jackson *et al.*, 2017). They can carry membrane-derived receptors, and different proteins including cytokines, chemokines, lipids, carbohydrates, and genetic materials including miRNA and mRNA. According to 146 studies, exosomes and microvesicles combined are able to carry 13,333 various proteins, 764 miRNAs and 2375 different kinds of mRNAs (Zha *et al.*, 2017). A previous study shows that when cells are exposed to conditions of injury, pro-inflammation, hypoxia, stimulation, and oxidative stress, more microvesicles were produced (Guo *et al.*, 2019). For example, the activation of relevant oncogenes has the potential to increase the number of microvesicles released by prostate cancer cells (Di Vizio *et al.*, 2009).

Microvesicles are released into the extracellular space through budding directly from the cell membrane (Ståhl *et al.*, 2019). This budding is accompanied by change of various localised membrane proteins including adenosine diphosphate (ADP)-ribosylation factor (ARF)-1, ADP-ribosylation factor 6 (ARF6), Ras-related protein (RAB22a), and Ras-homologous (Rho)-A. ARF1 activates the contractile machinery via regulating the myosin light chain (MLC). A lack of ARF1 was found to inhibit invadopodia maturation which affects microvesicles shedding (Schlienger *et al.*, 2014). ARF6 coordinates with ARF1 and recruits proteins selectively into microvesicles (Muralidharan-Chari *et al.*, 2009). TSG101 interacts with the arrestin domain-containing protein 1 (ARRDC1), which induces TSG101 relocation from the endosomal

membrane to the plasma membrane (Nabhan *et al.*, 2012). It is interesting that ESCRT machinery is not only involved in exosome production but also significant in the biogenesis of microvesicles. The release of the ARRDC1-mediated microvesicles requires P-type adenosine triphosphatase (ATPase) activity of ESCRT sub-complex Vps4 and TSG101 (Nabhan *et al.*, 2012). RAB22a mainly shows influence on selecting and recruiting proteins into microvesicles under hypoxic conditions. Overexpression of RAB22a leads to increased microvesicles shedding in breast cancers, which results in invasion and metastasis (Wang *et al.*, 2014). Rho nucleotide guanosine triphosphate (GTP) binding protein (GTPase) family has the potential to control switching on and off activities of microvesicles shedding. RhoA links to ARF6 and can activate MLC kinase-mediated MLC phosphorylation through the Rho-associated protein kinase (ROCK) signalling pathway (Sedgwick *et al.*, 2015, Schlienger *et al.*, 2014). Based on this phospho-MLC and actin interaction, the intracellular tension and contractility are increased, which then allows for vesicle pinching and stimulates microvesicles production (Tricarico *et al.*, 2017). In addition, another member of the Rho family is Rac family small GTPase 1 (Rac1). The switching of microvesicle production is regulated by an antagonistic relationship between RhoA and Rac1 (Sanz-Moreno *et al.*, 2008, Tricarico *et al.*, 2017). Although the release of microvesicles needs the participation of ESCRT proteins, the shedding of microvesicles is mainly regulated and activated by changing calcium concentration (Ståhl *et al.*, 2019).

1.2.3 Apoptotic bodies

Apoptotic bodies/EVs are released when cells are undergoing apoptosis (Saraste and Pulkki, 2000). Their size is very heterogeneous, with diameters ranging from 50-5000 nm (Saraste and Pulkki, 2000). When cells are undergoing apoptosis, they can produce fragments

or blebs to form sub-cellular membrane-bound vesicles. The formation of apoptotic bodies is important because they play a role in the clearance of apoptotic cells. Apoptotic bodies recruit macrophages and phagocyte to engulf cell fragments (Poon *et al.*, 2014b). Similar to exosomes and microvesicles, apoptotic bodies are able to communicate with neighbouring or distant cells through carrying proteins, lipids and nucleic acids (Schlienger *et al.*, 2014).

The biogenesis of apoptotic bodies is controlled by cell disassembly. This process can be divided into three steps, which start with blebs formed from the cell membrane. This is followed by cell membrane protrusions and finally, fragmentation forms individual apoptotic bodies (Jiang *et al.*, 2017). Usually, these steps are regulated by different molecular factors. Membrane blebbing is driven by cytoskeleton collapse and increased hydrostatic pressure, which is regulated by activating caspases to initiate apoptosis (Zhang *et al.*, 2018, Li *et al.*, 2020, Poon *et al.*, 2014a). ROCK1 GTPase-mediated target caspase-3 leads to myosin light chain phosphorylation to induce actomyosin contraction (Zhang *et al.*, 2018, Zirngibl *et al.*, 2015). LIN-11, Isl-1, and MEC-3-kinase 1 promote actin polymerisation to undergo membrane deformation (Zirngibl *et al.*, 2015, Arber *et al.*, 1998). Blebbing was described as fundamental for membrane protrusion. However, one study indicated that epidermoid carcinoma cells can form the microtubule spike (a rigid membrane protrusion) without blebbing (Moss *et al.*, 2006). After membrane blebbing and protrusions, single apoptotic bodies are generated through fragmentation. The underlying mechanism that regulates this process is still unclear, but the shear force or intercellular physical force to dissemble blebs is possibly involved (Atkin-Smith and Poon, 2017).

1.3 ESCRT machinery

ESCRT machinery was identified in yeast and eukaryotic cells in the beginning of the 21st century (Hurley, 2008). It is important in the biogenesis of EVs (in particular exosomes) and selection of their cargo. ESCRT machinery can be grouped into 5 complexes which are composed of 30 proteins (Al-Nedawi *et al.*, 2008, Gonciarz *et al.*, 2008, Hurley, 2008). These 5 complexes are ESCRT-0, ESCRT-I, ESCRT-II, ESCRT-III and Vps4-Vta1. It was found that ESCRT machinery is the essential to sort ubiquitinated cargos in the endocytic pathway. Generally, membrane bound proteins are taken into cells by endocytosis and a ubiquitin tag may be added to produce monoubiquitinated or polyubiquitinated proteins. These ubiquitinated proteins are recognised and selected by ESCRT machinery and recruited into early endosomes where they are sequestered into ILVs of newly formed MVBs (Shields and Piper, 2011) (Figure 1.3), which may be destined to fuse with lysosomes for degradation or released at the cell surface as exosomes (Gurung *et al.*, 2021). In addition to their role in endocytic sorting, some ESCRT subunits also participate in other cellular functions, such as cell division, retrovirus budding, autophagy, cytokinesis, and power of Hydrogen (pH) value measurement in fungi (Hurley, 2008, Filimonenko *et al.*, 2007, Lee *et al.*, 2007, Carlton and Martin-Serrano, 2007).

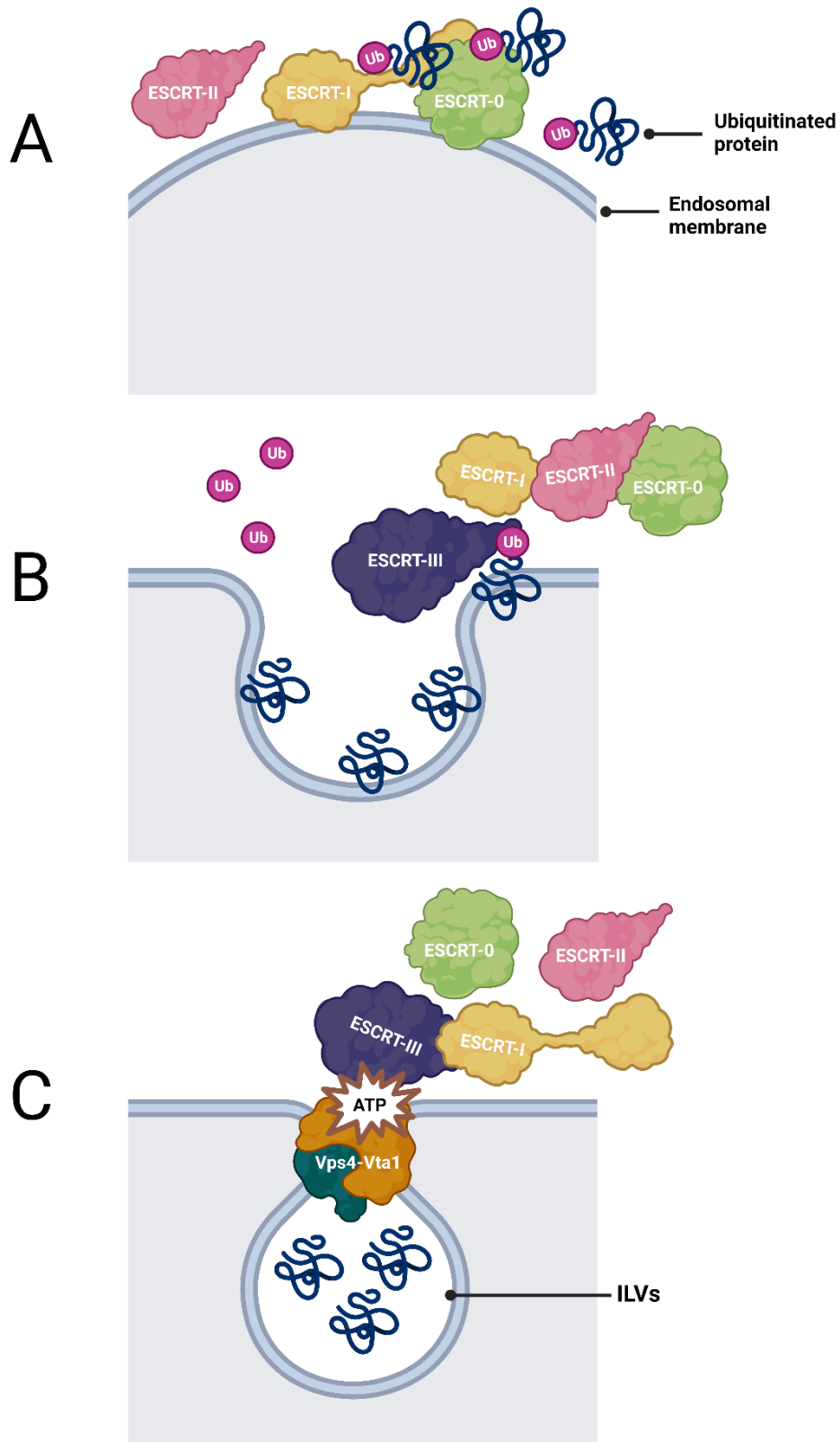


Figure 1.3: ESCRT dependent endosome biogenesis pathway. (A) ESCRT-0 recognises monoubiquitinated proteins and recruits ESCRT-I and ESCRT-II. (B) ESCRT-I and ESCRT-II induce the formation of the initial bud during the budding process. ESCRT-III acts with ESCRT-II to scissor a bud and de-ubiquitinate modified proteins. (C) Vps4 depolymerises ESCRT-III for recycling through ATPase activity. Figure was created with BioRender.

1.3.1 ESCRT-0

Different ESCRT complexes show various functions in endosome maturation/formation. The first step of the endosomal pathway is the sorting of ubiquitin-tagged proteins. ESCRT-0 recognises monoubiquitinated proteins and recruits subsequent ESCRT complexes to carry cargo to early endosomes (Figure 1.3 A). The yeast Vps27 and Hsc70 homologues of class E Vps mutant 1 (Hse1), which are homologous to HGS and STAM in humans, are part of the ESCRT-0 complex (Mayers *et al.*, 2011) (Table 1.1). ESCRT-0 is an ~8 nm long heterodimer which is composed of two short intertwined helical proteins that are bound through coiled-coil GAT (GGAs and Tom) domain interactions (Asao *et al.*, 1997, Ren *et al.*, 2009) (Figure 1.4 A). Loss of either of the domains impairs MVB biogenesis (Razi and Futter, 2006, Bache *et al.*, 2003). Between the two proteins, there are two N-terminal ubiquitin-binding Vps-27, HGS and STAM (VHS) domains, three ubiquitin interaction motif (UIM) and five ubiquitin-binding sites which function on mediating recognition and selection of ubiquitinated cargos (Bilodeau *et al.*, 2002, Ren and Hurley, 2010). Wherein, Hse1/STAM possess a SRC Homology 3 (SH3) domain that is able to recruit de-ubiquitinating enzymes including ubiquitin-specific processing protease Y and associated molecule with the SH3 domain of STAM that produces a marked effect in de-ubiquitinating activity and, in addition, affect ubiquitinated cargos fate (Mizuno *et al.*, 2005, McCullough *et al.*, 2004, Row *et al.*, 2006). On the other hand, Vps27/HGS possess a specific Fab1p, YOTB, Vac1p, and early endosome antigen 1 (EEA1) (FYVE) zinc finger domain which combines with lipid phosphatidylinositol 3-phosphate (PtdIns (3) P) on the membrane with affinity (Stahelin *et al.*, 2002). PtdIns (3) P enriched in late endosomes and ILVs facilitates ESCRT-0 targeting to the endosomal membrane (Raiborg *et al.*, 2001). Meanwhile, the double

UIM shows a higher affinity to bind with ubiquitinated cargos than the UIM of STAM (Mayers *et al.*, 2011). Hydrodynamic analysis revealed that HGS and STAM form heterodimers and heterotetramers which display multiple functions in proper sorting of cargos to the endosomal membrane (Mayers *et al.*, 2011). Although the ESCRT machinery was discovered several years ago, extensive study of the endolysosomal pathway led to the identification of new ESCRT subunits. His domain protein tyrosine phosphatase (HD-PTP) (homologous to yeast BCK1-like resistance to osmotic shock protein-1 (Bro1)) is a novel ESCRT-0 component, but its function remains to be fully elucidated. It contains five domains: Bro1, V-central proline-rich domain (V-domain), Protein Tyrosine Phosphatase (PTP) and two proline-rich region domains (PRR) (Lee *et al.*, 2016). The V-domain was reported to be able to bind ubiquitin and interact with ubiquitin associated protein 1 (UBAP1), another novel ESCRT-I component which was identified recently (Pashkova *et al.*, 2021, Gahloth *et al.*, 2016).

1.3.2 ESCRT-I

Once the ubiquitinated cargos are sorted by the ESCRT-0 complex, the ESCRT-I subunit is recruited followed by transferring cargos from ESCRT-0 to ESCRT-I (Figure 1.3 A). ESCRT-I was the first complex of ESCRT machinery to be described in yeast. It was described as a heteromeric complex with the equal stoichiometry of Vps23, Vps28, Vps37, and Multivesicular body sorting factor 12 (Mvb12) (homologous to TSG101, hVps28, hVps37, and hMvb12 in mammals). Vps23 has three isoforms and hMvb12 has two isoforms (Bache *et al.*, 2004, Morita *et al.*, 2007a) (Table 1.1). However, the significance of these multiple isoforms is still unclear. The core subunits of ESCRT-I assemble into an 18 nm-long structure which consists of a 13 nm intertwined antiparallel coiled-coil stalk with a globular head group (Teo *et al.*, 2006,

Kostelansky *et al.*, 2007) (Figure 1.4 B). A ubiquitin E2 variant (UEV) domain possessed by Vps23/TSG101 on their N-terminal is responsible for engaging ubiquitinated cargos or binding to Pro–Thr/Ser–Ala–Pro-like motifs of the ESCRT-0 subunit Vps27/HGS (Katzmann *et al.*, 2003, Kostelansky *et al.*, 2007). This interaction between HGS and TSG101 was mimicked by the human immunodeficiency virus-1 (HIV-1) Gag protein through usurping TSG101 to facilitate viral budding (Pornillos *et al.*, 2003). The conserved C-terminal domain (CTD) of Vps28 is responsible for combining with ESCRT-II to facilitate the budding of the MVB limiting membrane to the lumen (Gill *et al.*, 2007, Kostelansky *et al.*, 2006, Wollert and Hurley, 2010). Furthermore, the Vps28 CTD domain is highly conserved and acts as an adaptor interacting with ESCRT-II Vps22 and ESCRT-III Vps20 (Pineda-Molina *et al.*, 2006). Thereby, ESCRT-I is also significant for ESCRT-III recruitment. The N-terminus of Vps37 contains a basic helix which facilitates ESCRT-I membrane binding and stability (Kolmus *et al.*, 2021, Kostelansky *et al.*, 2007). The yeast Mvb12 showed low sequence homology with the hMvb12 isoforms thus, their identification depended on proteomics and functional characterisation (de Souza and Aravind, 2010). The N-terminus region of hMvb12 forms the Mvb12-associated β -prism (MABP) which has a vesicular membrane-associated function (de Souza and Aravind, 2010, Audhya *et al.*, 2007). A novel accessory protein UBAP1 contains two ubiquitin-binding motifs (UIM and ubiquitin binding domain) that play a role in endosomal function (Agromayor *et al.*, 2012, Haglund and Dikic, 2012). It was demonstrated that UBAP1 binds to ubiquitinated proteins and is essential for degradation of the antiviral cell surface protein tetherin (Agromayor *et al.*, 2012).

1.3.3 ESCRT-II

ESCRT-II is responsible for the initiation of the nucleation of ESCRT-III (Babst *et al.*, 2002b). At this stage, membrane deformation is initiated, where the ubiquitinated cargo is clustered at the origin of inward vesiculation (Figure 1.3 B). ESCRT-II is a heterotetrametric structure that contains Vps22 (EAP30), Vps36 (EAP45) and Vps25 (EAP25) subunits with 1:1:2 stoichiometry (Hierro *et al.*, 2004) (Table 1.1) (Figure 1.4 C). This complex is ‘Y’ shaped, 15 nm long, and consists of Vps22 and Vps36 that have two tandem winged-helix (WH) motifs and each arm of the subunits bind a Vps25 (Im and Hurley, 2008, Irion and St Johnston, 2007, Hierro *et al.*, 2004). Loss of either copy of Vps25 impairs ESCRT-II functions (Hierro *et al.*, 2004, Teis *et al.*, 2010). On the C-terminal of Vps25, there is a locus for recruiting and activating Vps20, which is a subunit of ESCRT-III (Hurley, 2008, Im *et al.*, 2009). Thereby bridging the upstream ubiquitin-tagged ESCRT complex to the downstream ESCRT-III, which is involved in membrane scission (Hurley, 2008). ESCRT-II Vps36/EAP45 have a kind of variant pleckstrin homology domain called GRAM-Like Ubiquitin-binding in EAP45 (GLUE) domain on their N-terminus but they share different mechanisms (Teo *et al.*, 2006, Slagsvold *et al.*, 2005). In Vps36, there are two Np14-type zinc finger (NZF) insertions of which one binds to ESCRT-I Vps28-CTD and another one binds to ubiquitin (Alam *et al.*, 2004). However, in human EAP45, the GLUE domain lacks NZF insertions, but can still bind to ubiquitin directly with an unknown mechanism (Slagsvold *et al.*, 2005, Hirano *et al.*, 2006). The GLUE domain shows a similar function with the FYVE domain in ESCRT-0 which interacts with PtdIns (3) P with high affinity (Slagsvold *et al.*, 2005). Thus, ESCRT-II provides endosomal localisation specificity by collaborating with ESCRT-0. Through interacting with MVB-related

functional proteins RAB-interacting lysosomal protein, RAB7, and dynein, ESCRT-II is able to facilitate MVBs targeting microtubules (Wang and Hong, 2006). ESCRT-II plays a more significant role than ESCRT-I in MVB biogenesis as the previous evidence showed ESCRT-II overexpression rescued ESCRT-mediated sorting defect which was caused by ESCRT-I depletion, but not vice versa (Babst *et al.*, 2002b).

1.3.4 ESCRT-III

ESCRT-III functions by cutting buds and transferring vesicles into endosomes (Babst *et al.*, 2002a) (Figure 1.3 B). Unlike the earlier complexes, ESCRT-III does not contain a known ubiquitin-binding domain and exists in the cytosol as inactive subunit monomers or on the endosomal membrane as activated homo-oligomers or hetero-oligomers complexes (Babst *et al.*, 2002a). In yeast, there are eight subunits, of which four core subunits Vps2, Vps20, sucrose non-fermenting (Snf)-7, and Vps24 are required to produce marked effects (Babst *et al.*, 2002a) (Table 1.1). They are assembled in order where Vps20, Snf7, and Vps24 function on membrane scission. Furthermore, Vps2 function on interacting with the Vps4 recycling machinery (Wollert *et al.*, 2009, Adell *et al.*, 2017). Specifically, when ESCRT-II subunit Vps25 binds to ESCRT-III subunit Vps20, the ESCRT-III complex is initiated (Teo *et al.*, 2006). Then the homo-oligomerised Snf7 is recruited by Vps20. Snf7 is capped by Vps24 under normal conditions, but Vps24-dependent attenuation is limited upon excess Snf7 (Teis *et al.*, 2008, Saksena *et al.*, 2009). Snf7 is the most abundant ESCRT-III subunit which is a key driving force in deforming helical membrane tubular structures of the neck of the HIV-1 buds and ILVs (Teis *et al.*, 2008, Lata *et al.*, 2008b, Moser von Filseck *et al.*, 2020, Saksena *et al.*, 2009). Through recruiting ESCRT-III adaptor protein Bro1 and Alix, Snf7 filaments are stabilised. The further

recruitment of deubiquitinating enzyme degradation of alpha-4 facilitates cargo de-ubiquitination (Luhtala and Odorizzi, 2004, Odorizzi *et al.*, 2003). The other ESCRT-III subunits including Diaphanous inhibitory domain 2 (Did2), Increased sodium tolerance 1 (Ist1), Vps60 and Vps four-associated 1 (Vfa1) showed less significance for function. Among them, Did2 and Vps60 facilitate recruiting and activating the Vps4-Vta1 complex meanwhile Ist1 inhibits Vps4 activity (Dimaano *et al.*, 2008). In yeast, there is preferential pairing of Vps20 with Snf7, Vps24 with Vps2, and Did2 with Ist1, but the stoichiometry of the ESCRT-III complex is still unclear (Rue *et al.*, 2008, Xiao *et al.*, 2009). ESCRT-III subunits in eukaryotic cells are also known as charged multivesicular body proteins (CHMP) (Katsiarimpa *et al.*, 2013). Like yeast, there are four core ESCRT-III subunits, CHMP2, CHMP3, CHMP4, and CHMP6 and their isoforms (Babst *et al.*, 2002a). There are two isoforms belonging to CHMP2 (CHMP2 A/B) and three isoforms of CHMP4 (CHMP4 A/B/C). The functions of these different isoforms are still disputed. Some studies suggested that these isoforms showed redundant functions whereas emerging studies showed different predominant functions (Effantin *et al.*, 2013). For example, CHMP4 B is considered more involved in viral budding, but CHMP4 C mainly function in cellular cytokinesis (Capalbo *et al.*, 2016, Carlton *et al.*, 2008). Other ESCRT-III subunits include CHMP1, CHMP5, Ist1 and their isoforms. Wherein, the microtubule severing ATPases Associated with diverse cellular Activities (AAA ATPase) spastin can be recruited by CHMP1 B which functions alongside Ist1 to remodel the membrane and disassemble the microtubule (Connell *et al.*, 2020, Vietri *et al.*, 2015, Hurley, 2015). CHMP5 associates with Vta1 via MIT-MIM interaction. Vta1 is a cofactor of Vps4 that function to enhance ATPase activity (Azmi *et al.*, 2006, Shim *et al.*, 2008, Xiao *et al.*, 2008). In relation

to assembly of ESCRT-III, most is known about the structure and function of the CHMP3 subunit. CHMP3 is ~7 nm long with five electrically polarized helical hairpin structures, where helices $\alpha 1$ and $\alpha 2$ combine to form the base of the complex (Muzioł *et al.*, 2006) (Figure 1.4 D). Helices $\alpha 3$ and $\alpha 4$ fold anti-parallel and stack with the first two helices. The $\alpha 5$ helix folds back and is located next to the $\alpha 3$ and $\alpha 4$ (Bajorek *et al.*, 2009). $\alpha 1-4$ forms a four-helix bundle which localises in the cytoplasm instead of endosomes (Lata *et al.*, 2008a). The $\alpha 5$ helix plays an important role to determine the state of the ESCRT-III complex. When $\alpha 5$ binds to the C-terminus of the four-helix bundle, the ESCRT-III complex is under the autoinhibited, inactive, monomeric, and cytosolic state (Lata *et al.*, 2008a, Shim *et al.*, 2007, Zamborlini *et al.*, 2006). Conversely, the state of ESCRT-III is converted to active and polymerises on the endosomal membrane when $\alpha 5$ is released to cause conformational change (Zamborlini *et al.*, 2006, Bajorek *et al.*, 2009). This polymerisation is the main driving force to form and cut buds (Bajorek *et al.*, 2009, Hierro *et al.*, 2004). In order to turn back to the inactive state, the ESCRT-III complex is removed from the endosomal membrane by interacting with Vps4. This function of ESCRT-III is governed by its MIT-interacting motif (MIM) on the C-terminus which binds to microtubule interacting and transport (MIT) domains present on Vps4 (Table 1.1). The ESCRT-III complex is able to recruit proteins that contain the MIT domain (Hurley and Yang, 2008).

1.3.5 Vps4-Vta1

Once the ESCRT-III complex is assembled, it requires energy to disaggregate from the membrane (Figure 1.3 C). Vps4 is the only enzyme within the ESCRT machinery able to provide this energy (Babst *et al.*, 1997). In eukaryotes, there are two Vps4 subtypes, Vps4 A

and Vps4 B, which are 80% identical to each other and 60% identical to the yeast homologue (Scheuring *et al.*, 2001, Scheuring *et al.*, 1999). Vps4 belongs to the family of class I ATPase Associated with various cellular Activities (AAA ATPases) which depolymerise ESCRT-III subunits at the cost of ATP hydrolysis and provide the thermodynamic driving force for the ESCRT cycle (Frickey and Lupas, 2004, Erzberger and Berger, 2006). Thus, Vps4 depletion impairs ESCRT machinery recycling and causes the accumulation of hyper oligomeric ESCRT-III subunits on the endosomal membrane (Bishop and Woodman, 2000, Fujita *et al.*, 2003, Shestakova *et al.*, 2013). In addition, AAA ATPase functions in many cellular activities such as membrane trafficking and fusion, DNA replication, and reorganisation of the cytoskeleton (Striebel *et al.*, 2009, Barends *et al.*, 2010). Vps4 contains an ATPase cassette, which is composed of a small helical AAA sub-domain and a large AAA mixed α/β sub-domain. Between these two domains, there is a conserved Walker A/B motif which is able to bind ATP or GTP (Hanson and Whiteheart, 2005, Babst *et al.*, 1998) (Figure 1.4 E). Within the small AAA sub-domain, a unique three anti-parallel β -domain is inserted, which functions on binding to Vta1 cofactor, Vta1 SBP1 LIP5 (VSL) (Scott *et al.*, 2005) (Table 1.1). Beyond the β -domain, another sub-domain linked to small AAA is a C-terminal helix which is adjacent to the large AAA sub-domain. The C-terminal helix is significant in stabilising the large ATPase which further facilitates the stability of Vps4 (Xiao *et al.*, 2007, Vajjhala *et al.*, 2008, Scott *et al.*, 2005). Beyond the ATPase domain, the MIT domain is linked to the N-terminal of the complex via a flexible linker which is responsible for recruiting the ESCRT-III complex (Scott *et al.*, 2005). The flexible linker is thought to have the ability to inhibit Vps4 ATPase activity but the MIM and MIT domain binding relieves this autoinhibition (Merrill and Hanson, 2010,

Shestakova *et al.*, 2013). Vps4 exists as monomers or dimers without nucleotides or ADP binding *in vitro*, but polymerised into a catalysed oligomer, dodecamer or infrequently as the form of tetramer, when assembled to Vta1 to be a super complex (Scott *et al.*, 2005, Landsberg *et al.*, 2009, Hartmann *et al.*, 2008). The dodecamer is formed by two distinct conformational hexameric rings which function to disassemble the ESCRT-III complex whilst passing filaments through the constricted oligomer pore located under the lower ring (Han *et al.*, 2017, Monroe *et al.*, 2014). Previous research indicated that mutated residues in the oligomer pore impair HIV-1 budding (Gonciarz *et al.*, 2008).

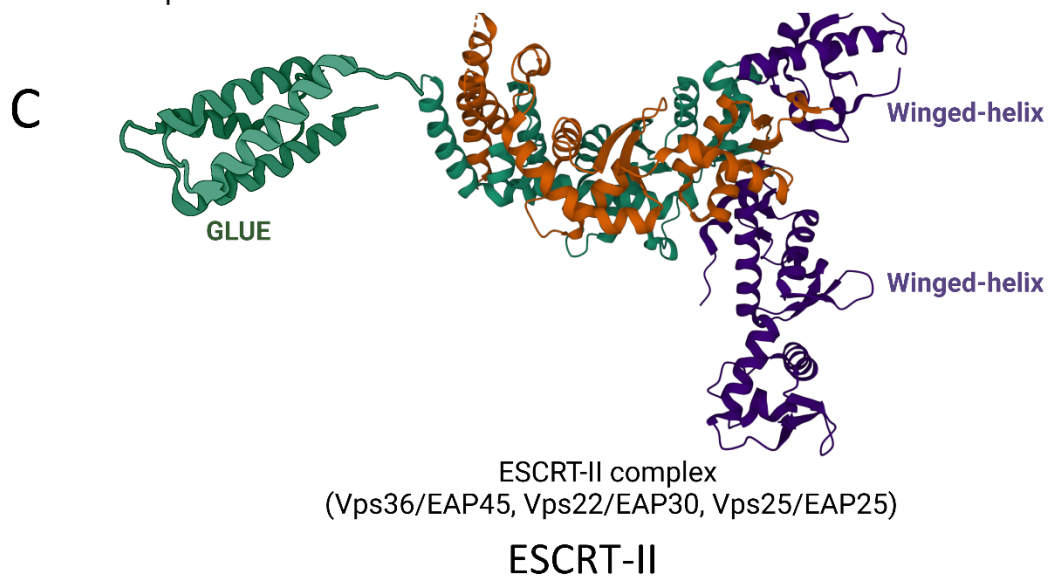
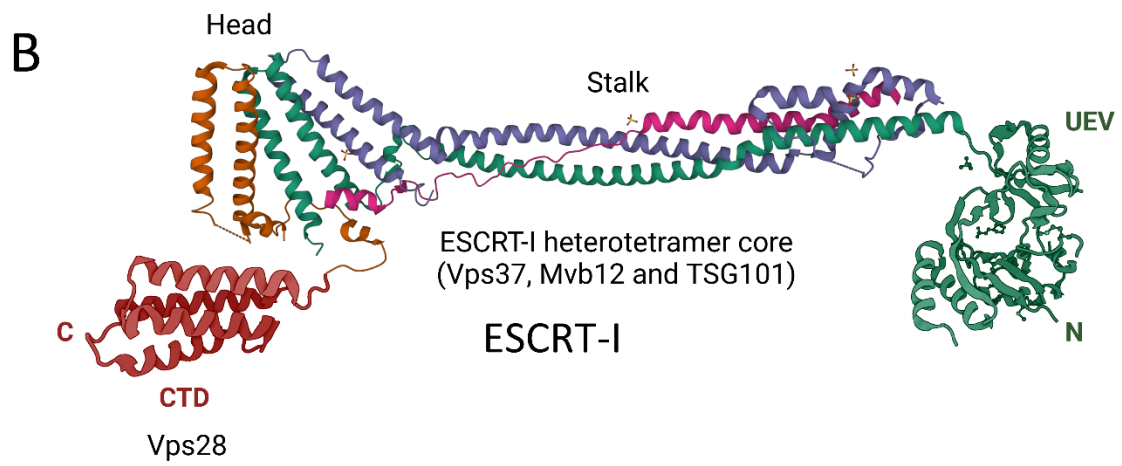
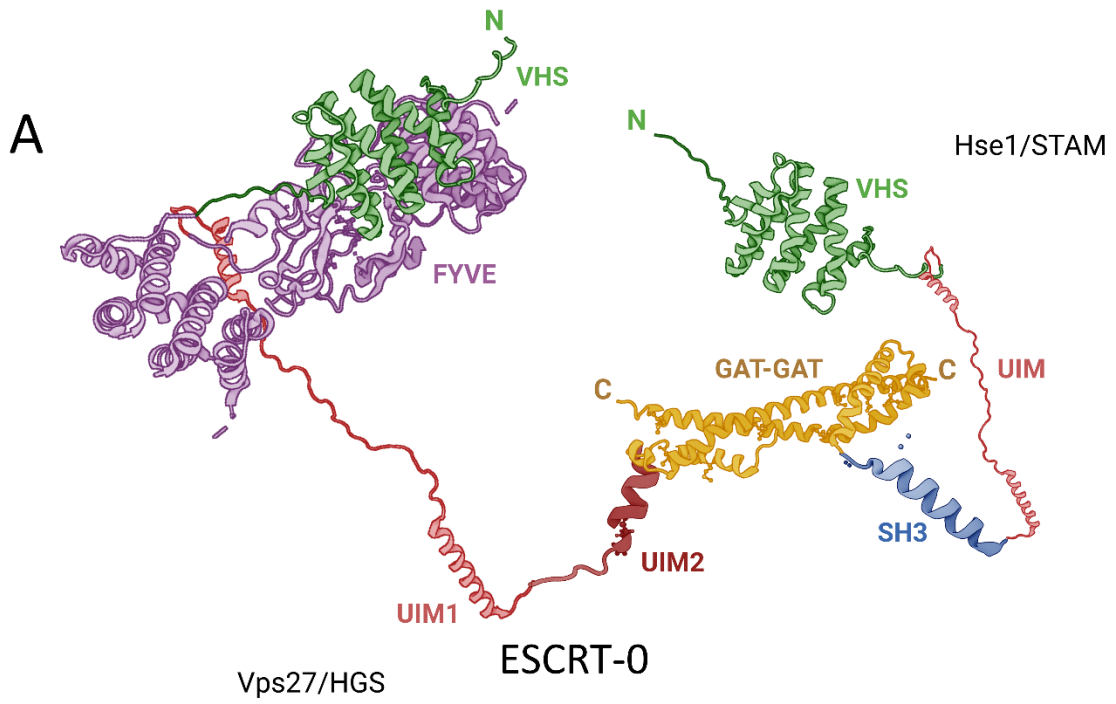
Vps4 can be self-assembled but with low efficiency. As described above, the Vps4 is assisted by its cofactor Vta1 (homologues in the human: cleavage interaction protein 5 (LIP5)) to form a heteromeric super complex (Hartmann *et al.*, 2008, Azmi *et al.*, 2006) (Table 1.1) (Figure 1.4 F). Vta1 is a dimer, with two domains which are linked by a flexible linker. It contains two MIT domains at its N-terminus that can bind to different ESCRT-III subunits (Skalicky *et al.*, 2012, Xiao *et al.*, 2008). MIT1 only binds to proteins containing the MIM1 domain. MIT2 domain is able to interact with MIM5 distinctly. Through MIT-MIM5 interaction, Vta1 is strongly associated with the late-acting ESCRT-III protein Vps60 (Yang *et al.*, 2012, Skalicky *et al.*, 2012). At the C-terminus of Vta1 is the VSL domain which allows Vta1 dimerization followed by binding β -domain of Vps4 directly (Scott *et al.*, 2005, Lottridge *et al.*, 2006). Here, the dimerization of Vta1 is important, as the dimer contact residues are required for Vps4 function (Xiao *et al.*, 2008). Some studies identified a continuous domain near the VSL which was named Vps4 stimulatory element (VSE), that further functions on greatly stimulating Vps4 ATPase activity in yeast (Bashkirov *et al.*, 2008, Norgan *et al.*, 2013). But the

existence of a VSE-like region in the Vps4 homologues LIP5 is still unclear. In yeast, Vta1 functions in Vps4-dependent pathways and accelerates its ATPase activity with oligomerisation that further promotes ESCRT-III disassembly (Azmi *et al.*, 2008, Lottridge *et al.*, 2006). Through interacting with MIT domains, Vta1 facilitates the recruitment of Vps4 to the endosomal membrane (Shestakova *et al.*, 2010). Electron tomography showed that depletion of Vta1 impaired MVB formation but does not cause a serious defect in cargo sorting which can be caused by Vps4 mutation (Lottridge *et al.*, 2006, Nickerson *et al.*, 2010). On the other hand, LIP5 can be detected in the epithelial cells of almost all mammals. It has an integral role in the recycling and lysosomal degradation of cargos such as aquaporin 2 and EGFR (Boone *et al.*, 2010).

Overall, ESCRT-0, -I, -II mainly function by recognising and recruiting ubiquitinated cargos. ESCRT-III functions by cutting buds and transferring vesicles into endosomes. Once the ESCRT-III complex is assembled, Vps4-Vta1 provides energy to disaggregate buds from the membrane.

Table 1.1: List of ESCRT proteins

Yeast proteins	Human proteins	Domains/Motifs
ESCRT-0		
Vps27	HGS	UIM, VHS, GAT, FYVE, Proline-rich motif
Hse1	STAM1/2	UIM, VHS, GAT, SH3
Bro1	HD-PTP	Bro1, V-domain, PTP, PRR
ESCRT-I		
Vps23	TSG101	UEV, Coiled-coil
Vps28	hVps28	CTD
Vps37	hVps37 A/B/C	Coiled-coil
Mvb12	hMvb12 A/B, UBAP1	Coiled-coil
ESCRT-II		
Vps22	EAP30 (SNF8)	
Vps36	EAP45	NFZ in yeast, GLUE in human
Vps25	EAP25	Winged-helix
ESCRT-III		
Core proteins		
Vps20	CHMP6	MIM2
Snf7	CHMP4 A/B/C	MIM2
Vps24	CHMP3	MIM1
Vps2	CHMP2 A/B	MIM1
ESCRT-III		
Related proteins		
Did2	CHMP1 A/B	MIM1
Ist1	Ist1	MIM1/MIM2
Vps60	CHMP5	MIM5
Vfa1		MIM2
Vps4-Vta1		
Vps4	Vps4 A/B	MIT, β -domain, AAA
Vta1	LIP5	MIT, VSL



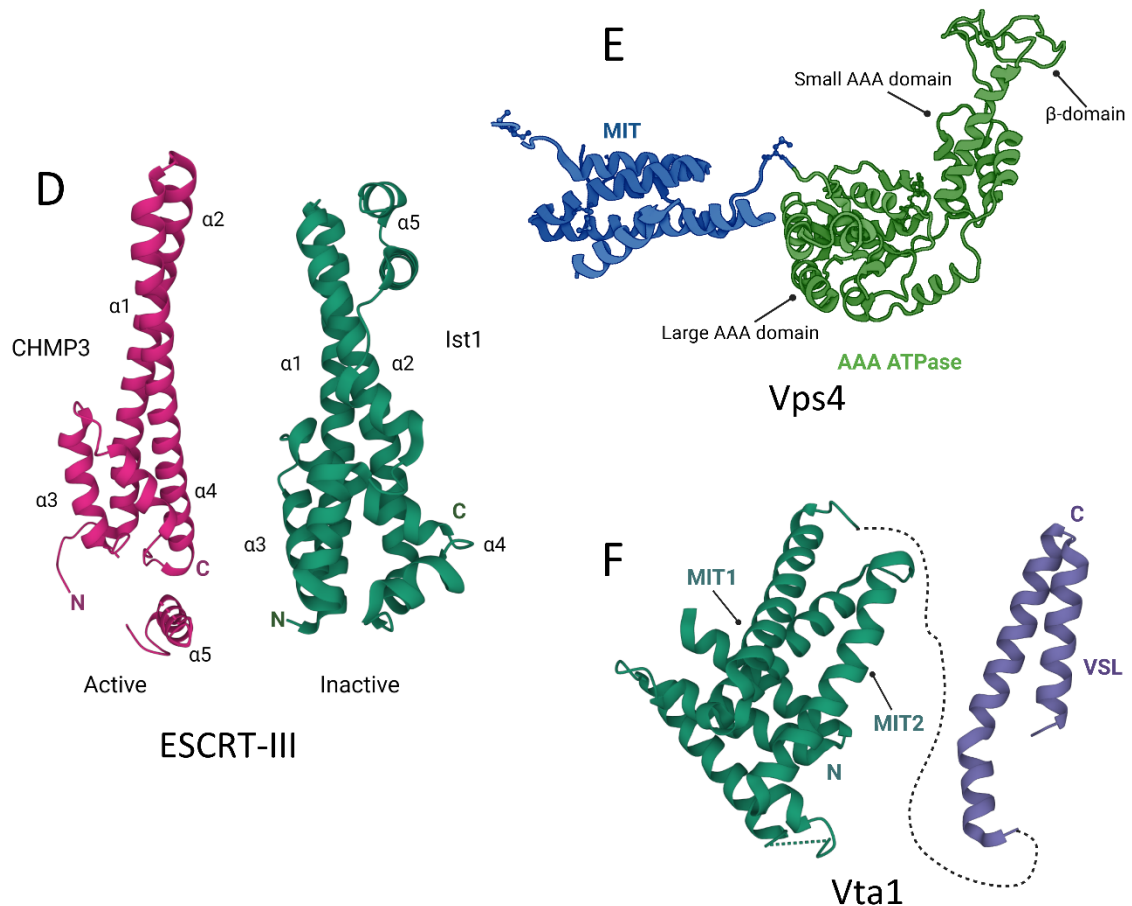


Figure 1.4: The modelled structures of ESCRT-subunits. (A) The ESCRT-0 subunit consists of the Vps27/Hse1 complex (GAT domain, PDB code: 2PJW), the HGS (FYVE domain, PDB code: 1DVP), the Vps27 (UIM1/2 domain PDB code: 1O06), the STAM2 (SH3 domain, PDB code: 1UJ0), the Vps27 (Tandem UIM domains, PDB code: 1Q0V), and the STAM2 (VHS domain, PDB code: 1X5B). (B) The ESCRT-I subunit consists of the ESCRT-I heterotetramer complex (PDB code: 2P22), the ESCRT-I heterotetramer headpiece (6VME), the Vps28 (CTD domain, PDB code: 2G3K), and the TSG101 (UEV domain, PDB code: 2F0R). (C) The ESCRT-II subunit consists of the integrated ESCRT-II complex (PDB code: 3CUQ) and the EAP45 (GLUE domain, PDB code: 2HTH). (D) The structure of monomer ESCRT-III subunit, left is the CHMP3 with $\alpha 5$ releasing, which suggests active conformation (PDB code: 2GD5), right is the Ist1 with $\alpha 5$ binding, which suggests inactive conformation (PDB code: 3GGY). (E) The structure of monomer Vps4 subunit consists of the MIT domain (PDB code: 2V6X) and the AAA ATPase domain (PDB code: 2QPA). (F) The structure of monomer Vta1 consists of the MIT domains (PDB code: 2RKK) and VSL domain (PDB code: 2RKL). Figure was created with PDB Protein Data Bank and BioRender.

1.3.6 Physiological functions of ESCRT machinery in human cancer

Different ESCRT proteins play critical roles in human tumourigenesis and progression.

For example, overexpression of HGS and TSG101 was observed in human breast tumour and

papillary thyroid carcinomas specimens, respectively (Toyoshima *et al.*, 2007, Liu *et al.*, 2002). On the other hand, Vps37 A and CHMP1 A were found down-regulated in hepatocellular carcinoma and pancreatic tumour cells, respectively (Xu *et al.*, 2003, Li *et al.*, 2008). Furthermore, chromosome region 3p21.3 containing the ESCRT protein HD-PTP was reported to be usually lost in human cancers such as nasopharyngeal carcinoma and lung cancer (Manteghi *et al.*, 2016, Yau *et al.*, 2006, Yamakawa *et al.*, 1993). Similarly, another ESCRT protein, UBAP1, was reported to be less expressed in nasopharyngeal carcinoma (Xiao *et al.*, 2006).

The ESCRT machinery-mediated functions of endolysosomal degradation control the degradation of many cell surface receptors, which are related to the physiological and pathological processes of many types of cancers. Epithelial cells may lose polarity, resulting in EMT to promote cancer migration and metastasis, when integrin, adhesion molecules and tight junctional protein are inappropriately degraded via the MVB pathway (Lobert *et al.*, 2010, Dukes *et al.*, 2011, Gotzmann *et al.*, 2004). Moreover, ESCRT machinery controls the trafficking of cellular signalling receptors, such as EGFR. Loss of ESCRT subunits HGS or TSG101 leads to EGFR accumulation on the endosomal membrane to prolong EGFR phosphorylation and downstream signals of kinases to promote a cancerous state (Brankatschk *et al.*, 2012). In mammalian cells, most ESCRT complexes localise to the midbody, which means they play a role in disassembling the intercellular bridge, and then separating cells by cytokinesis (Samson *et al.*, 2008). TSG101 depletion and Vps4 ATPase inhibition impair the cytokinesis activity of the breast cancer cells (Morita *et al.*, 2007b). Incomplete cell division has the potential to induce multinucleation, which is a morphological phenotype in

tumourigenic cells (Weihua *et al.*, 2011, Ariizumi *et al.*, 2009).

1.4 Scope of the current study

The ESCRT machinery serves to complete a unique set of endolysosomal events that are essential for EV biogenesis and EV-related cargo trafficking, which are important in tumourigenesis. There is a dearth of understanding about how ESCRT proteins regulate MVB biogenesis, EV release and cancer-related receptor trafficking and lysosomal degradation in oral cancer. Therefore, the current study aims to address this lack of knowledge. In chapter 3, the expression of representative ESCRT-0, -I and -II subunits were determined in OSCC cells relative to normal controls. In chapter 4, Clustered regularly interspaced palindromic repeats (CRISPR)-Cas9 genome editing was used to create a functional HGS knockout in OSCC. In Chapter 5, we focus on how HGS depletion alters the biogenesis of EVs and the trafficking of the cell surface receptor EGFR. Altogether, this study aims to understand the role of ESCRT machinery in OSCC EV biogenesis and the extracellular release of EGFR.

1.5 Hypothesis, aims and objectives

1.5.1 Hypothesis

ESCRT proteins are overexpressed in oral cancer cells, leading to increased production of EVs and altered export of cargo such as EGFR.

1.5.2 Aims and objectives

To test this hypothesis, the following aims will be addressed:

1. Characterise the relative abundance of ESCRT components in normal and oral cancer cells. Gene expression and protein abundance of representative ESCRT members HGS (ESCRT-0), TSG101 (ESCRT-I) and Vps22 (ESCRT-II) will be measured by quantitative polymerase chain reaction (qPCR) and western blotting in OSCC cell lines and compared to normal oral keratinocytes. Afterwards, compare gene expression with protein abundance to determine if post-transcriptional gene regulation may play a role in ESCRT expression. If differences are found between gene expression and protein abundance, *in silico* analysis will be performed to identify putative post-transcriptional gene regulators, which will be validated by qPCR.
2. Determine the role of ESCRT-0 subunit HGS in OSCC EV production. SiRNA (small interfering RNA) transfection and CRISPR-Cas9 genome editing will be used to knockdown and knockout HGS in the H357 oral cancer cell line, respectively. EVs will be enriched by ultracentrifugation and analysed by nanoparticle tracking analysis (NTA) and western blotting.
3. Examine any phenotypical changes in OSCC cells upon HGS depletion. Cell doubling time and apoptosis will be determined by growth assay and flow cytometry, respectively.

Furthermore, investigate how HGS depletion alters MVB biogenesis and trafficking of cell surface receptors such as EGFR. Endosomal structures will be analysed by immunofluorescence microscopy and transmission electron microscopy (TEM). Processing of EGFR will be tracked by EGF pulse-chase experiments and export in EVs determined by western blotting.

Chapter 2: Materials and methods

2.1 Supplies of materials and chemical reagents

All chemicals and reagents were purchased from Sigma-Aldrich (Merck) Company Ltd., Dorset, United Kingdom and Thermo Fisher Scientific Inc. Horsham and Loughborough, United Kingdom unless otherwise stated.

2.2 Cell culture

2.2.1 Primary cells

Primary normal oral keratinocytes (NOKs) were a gift from Dr Helen Colley and were derived from three healthy volunteers through oral mucosal biopsies with ethical approval (003463) as described by Colley *et al.* (2011) (Table 2.1). NOKs were used at passage number 6 in this study.

2.2.2 Cell lines

One immortalized normal oral keratinocyte cell line, FNB6 (a gift from Prof Keith Hunter, RRID: CVCL_F734), and three oral squamous cell carcinoma cell lines, H357 (ESACC Catalogue No.: 06092004, RRID: CVCL_2462), SCC9 (ESACC Catalogue No.: 89062003, RRID: CVCL_1685), and SCC4 (ESACC Catalogue No.: 89062002, RRID: 1684), were used in this study (Table 2.1).

Table 2.1: Details of cells

Name of cells	Patients' details	Anatomical location	Original reference
NOK805	28-year-old female	buccal mucosa	-
NOK829	22-year-old female	buccal mucosa	-
NOK830	28-year-old male	buccal mucosa	-
FNB6	-	buccal mucosa	McGregor et al., 2002
H357	74-year-old male	Tongue	Fahey et al., 1996
SCC9	25-year-old male	Tongue	Rheinwald and Beckett, 1981
SCC4	55-year-old male	Tongue	Rheinwald and Beckett, 1981

2.2.3 Cell culture medium

To compare the differences between NOKs, FNB6, and OSCC cell lines, all cells were routinely cultured in keratinocyte growth medium (KGM) (Table 2.2). When performing transfection and genome editing experiments, H357 were cultured in 1:1 ratio of Dulbecco's Modified Eagle's Medium: Nutrient Mixture F-12 Ham (DMEM: F-12) (Table 2.2), which is the original growth medium recommended for H357 (Rheinwald and Beckett, 1981, Fahey *et al.*, 1996).

Table 2.2: The composition of 500 ml growth medium with Fetal Bovine Serum

Component	Volume		Final concentration	
	KGM	DMEM: F-12	KGM	DMEM: F-12
Low glucose Dulbecco's Modified Eagle Medium (DMEM)	335 ml	225 ml	-	-
Ham's Nutrient Mixture F-12	115 ml	225 ml	-	-
Fetal Bovine Serum	50 ml	50 ml	10% (v/v)	10% (v/v)
Penicillin-Streptomycin	5 ml	-	100 units penicillin and 100 µg/ml streptomycin	-
Amphotericin B	5 ml	-	2.5 µg/ml	-
L-Glutamine,	5 ml	5 ml	2 mM	2 mM
Adenine	5 ml	-	1.8x10 ⁻⁴ M	-
Hydrocortisone	2 ml		0.5 µg/ml	0.5 µg/ml
Insulin	250 µl		5 µg/ml	-
EGF	500 µl		10 ng/ml	-

2.2.4 Cell culture and passage

Cells were cultured in 75 cm² flasks and passaged in Class II Biosafety Cabinets when they reached ~80% confluence. Cells were washed twice with phosphate buffered saline (PBS) and enzymatically stripped from flasks by addition of 3 ml 0.25% trypsin-ethylenediamine tetraacetic acid (EDTA) solution. Trypsin was neutralised by addition of 7 ml medium; cells

were reseeded into new flasks at 1:3-1:5 ratios based on their confluence and maintained at 37°C in a humidified 5% CO₂ atmosphere.

2.2.5 Cell counting and seeding

Cells were trypsinised as above (section 2.2.4) and 10 µl of cell suspension was added onto a hemocytometer. The cell number was counted in each 4×4 corner square, averaged and multiplied by 10,000 to calculate the concentration of cells in the suspension. Cells were then seeded at an appropriate density. Depending on different experiments, 10,000-30,000 cells per well were seeded in 24-well plates onto 13 mm glass coverslips for immunofluorescence experiments, 100,000 cells per well were seeded in 6-well plates for transient transfection, 150,000 cells per well were seeded in 6-well plates for measuring number of particles derived by cells, 200,000 cells per well were seeded in 6-well plates for DNA, RNA, or protein extraction. Cells were allowed to adhere for 18-24 hours before downstream processing.

2.2.6 Storage of mammalian cells

Cells were trypsinised and counted as above (section 2.2.5.). After cell counting, they were centrifuged at $192 \times g$ (Sigma 3-18K centrifuge with swing-out rotor, 11180, Round bucket, 13190 and adapter for 3 falcon tubes 50 ml, 17346) for 5 minutes at room temperature. Cell pellets were resuspended in cell cryopreservation medium (10% (v/v) dimethyl sulfoxide (DMSO) and 90% (v/v) fetal bovine serum (FBS)) to reach a concentration of 1 million cells per millilitre. 1 to 2 ml cell suspension was added per cryogenic storage vial and placed in a Mr. Frosty™ freezing container and then incubated at -80°C to achieve cooling rate of -1°C per minute. After 24 hours, the cryogenic storage vials were transferred into liquid nitrogen for long-term storage.

2.3 Extracellular vesicles analysis

2.3.1 Preparation of EV-depleted FBS

EV-depleted FBS was produced as described by Kornilov *et al.* (2018). Endogenous bovine EVs present in FBS were depleted by ultra-filtration using an Amicon Ultra-15 centrifugal filter unit with 100,000 Dalton molecular weight cut off. FBS was loaded into the upper chamber of centrifugation unit and centrifuged at $3,000 \times g$, 4°C . The flow through containing ultra-filtered EV-depleted FBS (UF-dFBS) was collected from the lower chamber of centrifugation unit. UF-dFBS was then sterilised using $0.2 \mu\text{m}$ syringe filter.

2.3.2 Preparation of conditioned medium

Cells were trypsinised and counted as above (section 2.2.5). To measure concentration of particles released by cells, 150,000 cells were seeded per well of a 6-well plate in 1.5 ml normal growth medium and allow to adhere overnight. The growth medium was discarded and the monolayer was washed with PBS two times. 2 ml fresh growth medium with 10% (v/v) UF-dFBS was added into each well. After incubating overnight, the medium was centrifuged at $300 \times g$ for 10 minutes to pellet floating cells. Conditioned medium was kept on ice and transferred for NTA (section 2.3.4).

For assessing size distribution of particles in conditioned medium and pellets generated by ultracentrifugation, 2 million cells were seeded per T75 culture flask with 10 ml regular growth medium (DMEM: F-12) and allowed to adhere for 24 hours. The growth medium was discarded and the monolayer was washed with PBS two times. 6 ml fresh growth medium with 10% (v/v) UF-dFBS was added into each flask. After 24 hours incubation, the medium was centrifuged at $300 \times g$ for 10 minutes to pellet floating cells. Conditioned medium was obtained for

differential centrifugation (Figure 2.2.3).

2.3.3 Differential centrifugation

Conditioned medium (section 2.3.2) was processed by differential centrifugation as described by Théry *et al.* (2006) to isolate EVs (Figure 2.1). The medium was generated from section 2.3.2 was centrifuged at $2000 \times g$ for 10 minutes to generate pellet, which was washed with 1 ml PBS before re-centrifugation at the same speed for another 10 minutes. The supernatant was centrifuged at $10,000 \times g$ (Beckman Coulter Avanti J26 centrifuge with JA 12 conical rotor) for 30 minutes, then washed and re-centrifuged at same speed for another 30 minutes. The supernatant was centrifuged at $100,000 \times g$ for 60 minutes (Beckman Coulter Optima TLX ultracentrifuge with a TLA-100.4 fixed-angle rotor), and then washed with PBS and re-centrifuged at same speed for 60 minutes. All centrifugation steps were performed at 4°C . Pellets generated from different centrifugation speed were resuspended in 50 μl PBS or lysis buffer for NTA (section 2.3.4) and western blotting (section 2.7.4). Samples were stored at -20°C .

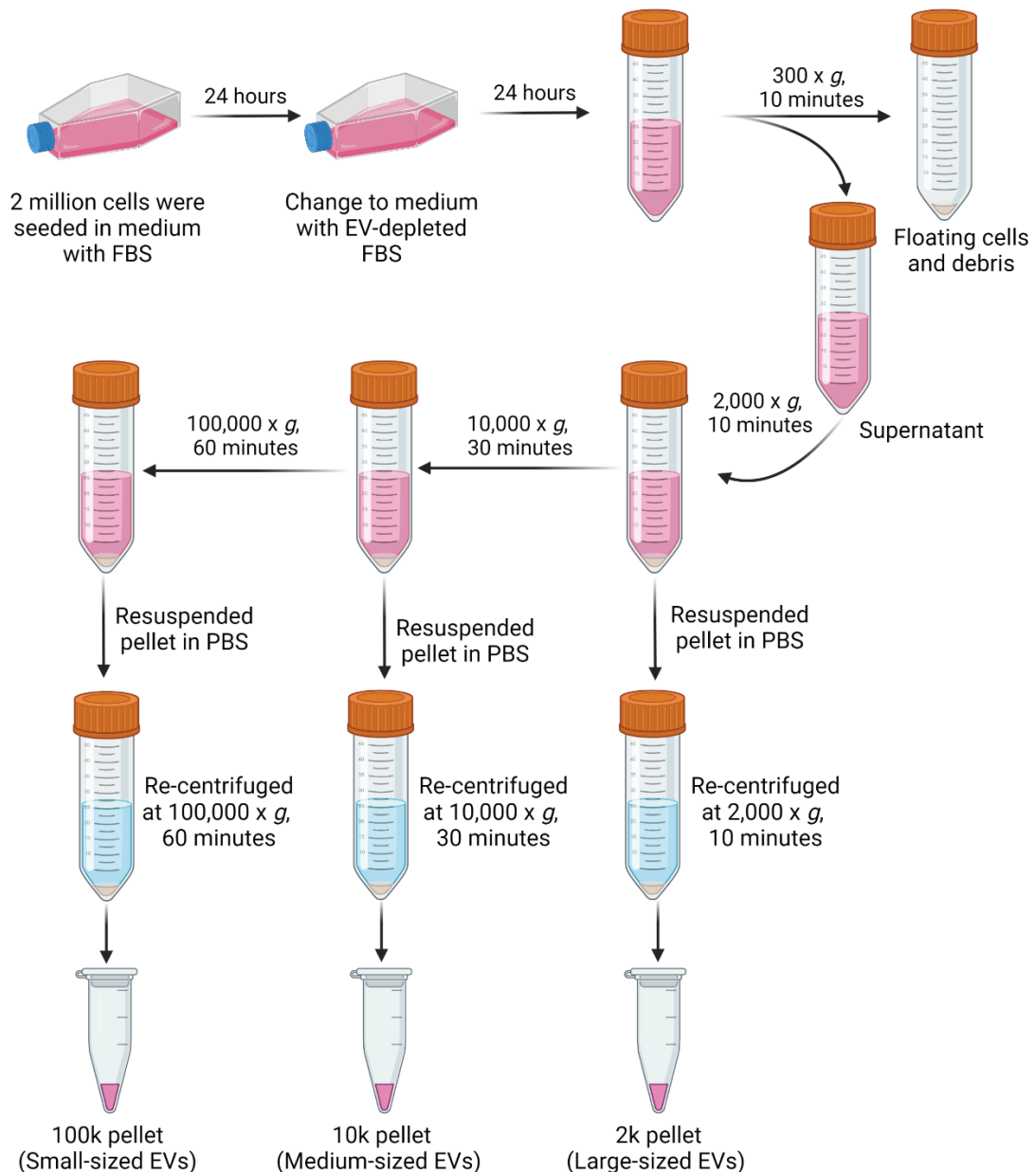


Figure 2.1 Diagram illustrating differential centrifugation. 2 million cells were seeded per T75 flask with normal medium. After 24 hours, they were changed into EV-free medium. 24-hour conditioned medium was centrifuged at increasing speeds: $300 \times g$ for 10 minutes, $2,000 \times g$ for 10 minutes, $10,000 \times g$ for 30 minutes, and $100,000 \times g$ for 1 hour. Pellets were washed in PBS and re-centrifuged at the same speed and duration. Figure was created with BioRender.

2.3.4 Nanoparticle tracking analysis

NTA of pre-cleared conditioned medium (section 2.3.2) and isolated EVs pellets (section 2.3.3) were performed using a ZetaView PMX-120 instrument (Particle Metrix GmbH,

German). Nanoparticles were analysed according to standard settings of both small (~100 nm) and large (>200) particles measurement (Table 2.3). The instrument was calibrated using 100 nm polystyrene beads in Milli-Q water. The Milli-Q water was used to wash the instrument for 3 times with 5 ml each time before samples loading. Samples were diluted in Milli-Q water and injected into the ZetaView instrument with a 5 ml syringe. Image acquisition and analysis was performed using the instrument software (version 8.05.11 SP1) to give concentration and size profile of nanoparticles.

Table 2.3: Setting of ZetaView instrument

Parameters	Settings for small particles (~100 nm)	Settings for large particles (>200 nm)
Sensitivity	85	65
Shutter	70	90
Minimum Brightness	25 pixels	15 pixels
Maximum Brightness	255 pixels	255 pixels
Minimum Area	20 pixels	25 pixels
Maximum Area	500 pixels	3000 pixels
Trace length	15	15
Framerate	30 frames per second	3.75 frames per second
Position	11	11
#Cycles	3	1

2.4 DNA methods

2.4.1 Genomic DNA isolation

Genomic DNA was isolated from mammalian cells by using the QIAamp DNA Mini kit (QIAGEN, 51304). Cells were seeded in 6-well plates as described (section 2.2.5). When cells

reached ~80% confluence, they were trypsinised in 0.5 ml trypsin and resuspended in 1 ml complete medium. Cells in suspension were centrifuged for 5 minutes at $300 \times g$ in a 1.5 ml micro centrifuge tube and washed twice in PBS. Supernatant was discarded and cell pellet was resuspended in PBS to reach a final volume of 200 μ l. After that, 20 μ l QIAGEN proteinase K were added into the microfuge tube. 200 μ l Buffer AL were added to the sample. Then vortexed microfuge tube for 15 seconds to allow sufficient mixing for purpose of efficient lysis then incubated at 56°C for 10 minutes. 200 μ l 99.99% ethanol were added to the sample and mixed again by pulse-vortexing for 15 seconds. The lysate was applied to the QIAamp Mini spin column with a 2 ml collection tube, then centrifuged at $6,000 \times g$ for 1 minute. The column was washed with 500 μ l Buffer AW1 by centrifugation at $6,000 \times g$ for 1 minute and 500 μ l Buffer AW2 by centrifugation at $20,000 \times g$ for 3 minutes. In order to eliminate the chance of possible Buffer AW2 carryover, the QIAamp Mini spin column was placed with a new 2 ml collection tube and centrifuged at $20,000 \times g$ for 1 minute. Genomic DNA was eluted in 200 μ l Buffer AE into a new collection tube by centrifugation at $6,000 \times g$ for 1 minute. The concentration of collected genomic DNA was quantified by NanoDrop™ 1000 UV-VIS spectrophotometer (Thermo Fisher Scientific, USA). According to manufacturer's instructions, 1 μ l of purified genomic DNA was loaded between the two optic pedestals. Nuclease-free water was used as a blank. Collected genomic DNA was stored at -20°C.

2.4.2 Polymerase chain reaction (PCR)

DNA was amplified by PCR using standard conditions. Standard PCR reactions were carried out in 0.2 ml PCR tubes, each reaction containing 2.5 μ l 2 \times PCR BIO VeriFi™ Mix Red (PCR Biosystems, PB10.44-01), 1 μ l forward primer stock (10 μ M), 1 μ l reverse primer stock

(10 μ M), 100 ng genomic DNA which was generated in section 2.4.1, and nuclease-free water, up to 25 μ l final volume (Table 2.4). The forward primer HGS-F (5' CATTACCATCACGCCCG 3') and reverse primer HGS-R (5' TGTTGGCCACCTCATCATGA 3') were purchased from Sigma-Aldrich, UK. PCR tubes were placed in Applied Biosystems™ 2720 Thermal cycler (Applied Biosystems, UK), which was programmed with the PCR cycle conditions (Table 2.5). PCR products were stored at -20°C.

Table 2.4: Master mix for PCR

Reagent	25 μl reaction	Final Concentration
2× PCRBIO VeriFi™ Mix	12.5 μ l	1×
Forward primer (10μM)	1.0 μ l	400 nM
Reverse primer (10μM)	1.0 μ l	400 nM
Template DNA	100ng genomic DNA	100 ng
PCR grade dH₂O	Up to 25 μ l final volume	-

Table 2.5: Setting of PCR cycles

Cycles	Temperature	Time	Notes
1	95°C	1 minute	Initial denaturation
30	95°C	15 seconds	Denaturation
	60-63°C	15 seconds	Anneal
	72°C	30 seconds	Extension
1	4°C	∞	Hold

2.4.3 Agarose gel electrophoresis

Agarose gel electrophoresis was performed to analyse amplified PCR products. Electrophoresis was carried out using 2% (w/v) agarose gels, consisting of 1 g agarose powder and 50 ml 1× Tris-acetate-EDTA buffer (0.04 M Tris, 0.04 M acetate and 0.001 M EDTA, pH 8.3). The agarose was dissolved by heating in a microwave until boiling and then cooled to ~55°C. Ethidium bromide was added to a final concentration of 200 µg/ml. The liquid gel was poured in the mini-Sub Cell GT Horizontal tank, 7 × 7 cm tray, with 8-well mini-gel caster (Bio-Rad, USA). After solidification, 5 µl PCR products or 3 µl PCR BIO Ladder IV (100bp-1500bp) (PCR Biosystems, PB40.14-01) were loaded per well. Genomic DNA was separated by electrophoresis using a Bio-Rad Power Pac 300 (Bio-Rad, USA) at a voltage of 100 V for 45 minutes. The gel was imaged on a transilluminator (Syngene, India) under the ultraviolet (UV) light. The images were acquired by GeneSys image acquisition software (Syngene, India).

2.5 CRISPR-Cas9 genome editing

Genome editing was achieved using the Alt-R CRISPR-Cas9 kit (Integrated DNA Technologies, 1072554) according to manufacturer's instructions (the work flow is summarised in Figure 2.2).

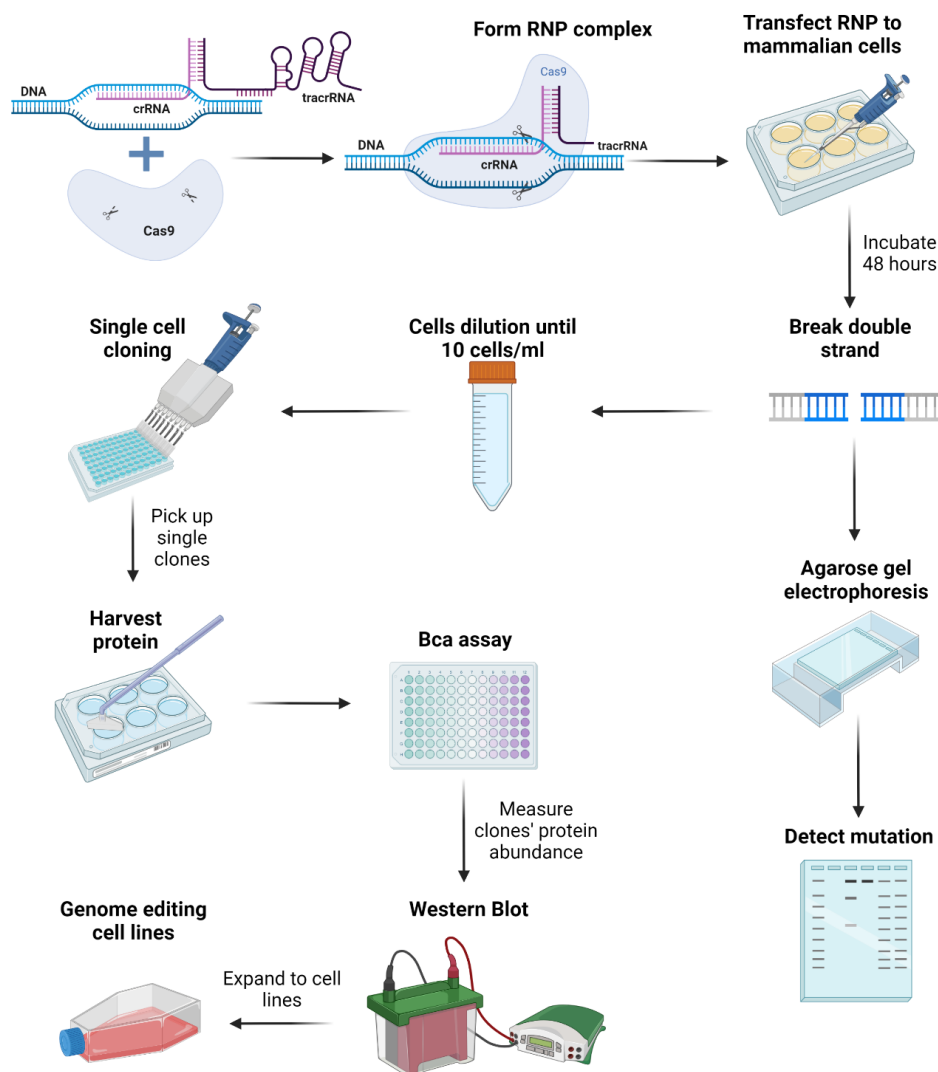


Figure 2.2 Workflow summarising CRISPR-Cas9 genome editing. Trans-activating crRNA (tracrRNA) and CRISPR RNA (crRNA) were firstly combined together then incubated with the Cas9 enzyme to form RNP complex. The Ribonucleoprotein (RNP) complex was transfected into mammalian cells using Lipofectamine CRISPRMAX transfection reagent. After 48 hours, half of the cells were used to recognise deletions of ≥ 2 bases by T7 endonuclease (T7EI) mismatch assay. The remaining cells were diluted and seeded in 96-well plates at concentration of 1 cell/well. Clones were expanded and proteins were harvested for western blotting to confirm loss of the targeted protein. Once confirmed, deficient cells were expanded to produce cell lines. Figure was created with BioRender.

2.5.1 Preparation of RNA oligos

Alt-R CRISPR-Cas9 crRNA for HGS and Alt-R CRISPR-Cas9 tracrRNA were re-suspended in 20 μl and 50 μl nuclease-free duplex buffer, respectively, to produce 100 μM stock solutions and stored at -20°C . 1 μM working concentration of duplex was made by mixing of 1 μl crRNA (100 μM), 1 μl tracrRNA (100 μM) and 98 μl nuclease-free buffer to reach the final volume of 100 μl . The mixture was heated at 95°C for 5 minutes then cooled to room temperature. The duplex mixture was stored at -20°C and used within 6 months.

2.5.2 Formation of ribonucleoprotein RNP complex

Alt-R *S.p.* enzyme was diluted to 1 μM stock by mixing of 1 μl of original enzyme and 61 μl Opti-MEM. In a 24-well plate, 6 μl RNA duplex (1 μM), 6 μl diluted CRISPR-associated protein 9 (Cas9) enzyme (1 μM), 2.4 μl Cas9 PLUS reagent and 85.6 μl Opti-MEM were mixed to reach 100 μl overall per reaction and incubated at room temperature for 5 minutes to assemble the RNA complexes. Assembled RNP complexes were stored at 4°C for up to 4 weeks.

2.5.3 Reverse transfection of RNP complexes

In the same 24-well plate, 100 μl assembled RNP complex was combined with 4.8 μl Lipofectamine CRISPRMAX transfection reagent and 95.2 μl Opti-MEM to reach 200 μl overall volume, then incubated at room temperature for 20 minutes. Wild-type H357 cells were trypsinised as above (section 2.2.4) and diluted to 400,000 cells/ml in DMEM: F-12 medium without antibiotics. 400 μl of cell suspension (160,000 cells) was added per well containing transfection complexes. The 24-well plate was incubated at 37°C , 5% CO_2 for 48 hours.

2.5.4 T7EI mutation detection

After 48 hours transfection, cells were washed with PBS twice and trypsinised with 0.5 ml

trypsin. Trypsinised cells were resuspended in 1.5 ml complete growth medium and then split into two halves. One half was used for T7EI mutation detection, and another half was used for single cell colony expansion (section 2.5.5).

2.5.4.1 Amplify genomic DNA and detect mutations

For T7EI mutation detection, genomic DNA was extracted using QIAamp DNA mini kit (section 2.4.1). To detect mutation, reactions were assembled (Table 2.6) and PCR was performed using the recommended conditions for the PCR master mix (Table 2.5) with an annealing temperature of 63°C.

To form heteroduplexes for T7EI digestion, samples, or hypoxanthine-guanine phosphoribosyl transferase (HPRT) control reactions were assembled with 10 µl of target of PCR product or 10 µl HPRT control (Table 2.7). Homoduplex and heteroduplex reactions were assembled as controls (Table 2.7). Reactions were subject to gradient PCR cycle (Table 2.8). Afterwards, 2 µl of T7EI (1 U/µl) was added and incubated at 37°C for 1 hour.

Table 2.6: Assembled PCR reactions for CRISPR-Cas9 mutation detection

Component	Reaction for samples	Reaction for HPRT control samples	Alt-R Control A reaction	Alt-R Control B reaction
Genomic DNA	~40 ng	~40 ng	-	-
10 μ M Forward primer (HGS)	1 μ l	-	-	-
10 μ M Reverse primer (HGS)	1 μ l	-	-	-
Alt-R HPRT PCR Primer Mix	-	1 μ l of 10 μ M stock	-	-
Alt-R Control A (Template/primer mix)	-	-	1 μ l	-
Alt-R Control B (Template/primer mix)	-	-	-	1 μ l
2 \times VeriFi Red PCR Mix	12.5 μ l	12.5 μ l	12.5 μ l	12.5 μ l
Nuclease-Free water	Up to 25 μ l	Up to 25 μ l	Up to 25 μ l	Up to 25 μ l
Total per reaction	25 μl	25 μl	25 μl	25 μl

Table 2.7: Composition of PCR reactions to form heteroduplexes for T7EI digestion

Component	Sample/HPRT control reaction	Homoduplex control reaction	Heteroduplex control reaction
PCR products	10 µl of experimental target/HPRT control	10 µl Control A	5 µl Control A 5 µl Control B
10× T7EI Reaction Buffer	2 µl	2 µl	2 µl
Nuclease-Free Water	6 µl	6 µl	6 µl
Total per reaction	18 µl	18 µl	18 µl

Table 2.8: Gradient PCR cycle to form heteroduplexes for T7EI digestion

Step	Temperature (°C)	Time
Denature	95	10 min
Ramp 1	95-85	Ramp rate -2°C/sec
Ramp 2	85-25	Ramp rate -0.3°C/sec

2.5.4.2 T7EI mismatch detection

T7EI mismatch detection was visualised by agarose gel electrophoresis (section 2.4.3). Digested PCR reactions were separated on a 2% (w/v) agarose gel to identify gene editing events.

2.5.5 Single clone isolation and cell line establishment

Cells were plated to produce single cell colonies. As described above (section 2.5.4.1), half of cells generated from CRISPR-Cas9 transfection were counted by a hemocytometer and serially diluted to reach 10 cells per ml. 100 µl cell suspension was added per well in a 96-well

plate to reach the density of 1 cell per well. Wells with 1 cell were identified and as cells divided, they were transferred gradually into 48, 24, 12, 6-well plates. Colonies were finally cultured in T75 flasks. HGS protein abundance in the H357 wild-type cells and expanded cloned cells were assessed by western blotting (section 2.7). Successfully edited cells were stored in liquid nitrogen (section 2.2.6) or used for further experiments.

2.6 RNA methods

In order to avoid contamination with ribonucleases (RNase), all experiments involving RNA were performed using filtered RNase free pipette tips, RNase free tubes and nuclease-free water.

2.6.1 RNA extraction

RNA was extracted from monolayers (section 2.2) using the Monarch[®] Total RNA Mini Prep Kit (New England Biolabs, T2010S). After washing cells three times in PBS, 350 μ l of lysis buffer was added to each well. Monolayers were scraped and collected in lysis buffer. All samples were filtered through genomic DNA removal columns. After centrifuging for 30 seconds at $16,000 \times g$, the flow through (containing RNA) was retained. The same volume of 100% ethanol was added to the flow through and mixed gently. RNA in the mixture was bound to an RNA purification column by centrifugation at $16,000 \times g$ for 30 seconds. The column was washed with 500 μ l wash buffer and on-column DNase I treatment for enzymatic removal of residual genomic DNA was performed. 5 μ l DNase I was added to 75 μ l DNase I reaction buffer, pipetted on to the top of each column and incubated at room temperature for 15 minutes. Afterwards, 500 μ l RNA priming buffer was added per column and centrifuged at $16,000 \times g$ for 30 seconds. The columns were then washed two further times by adding wash buffer and

centrifuged at same speed for 30 seconds and 2 minutes, respectively. Total RNA was eluted in RNase free tubes in 100 µl nuclease-free water. RNA samples were aliquot and stored at -80 °C.

2.6.2 RNA quantification

NanoDrop™ 1000 UV-VIS spectrophotometer (Thermo Fisher Scientific, USA) was used to quantify RNA concentration and purity. According to instructions from the company, 1 µl of purified RNA was loaded between the two optic pedestals. Nuclease-free water was used as a blank.

2.6.3 Reverse transcription

2.6.3.1 Total RNA

RNA was converted to complementary DNA (cDNA) by reverse transcription using the High-Capacity cDNA Reverse Transcription Kit (Applied Biosystems, 4368814). After NanoDrop quantification (section 2.6.2), 100 ng of total RNA, in a volume of 10 µl, was added to 10 µl reaction master mix (Table 2.9) and placed in an Applied Biosystems™ 2720 Thermal cycler (Applied Biosystems, UK). Reaction cycles was conducted according to the manufacturer's instructions (Table 2.10) and where necessary were stored at -20°C.

2.6.3.2 Small RNA

Small RNAs were converted to cDNA by reverse transcription using TaqMan® MicroRNA Reverse Transcription Kit (Applied Biosystems, 4366596). Reactions were assembled according to the manufacturer's instructions (Table 2.9). Each reaction contained 7 µl master mix, 3µl miRNA specific reverse transcription primer and 5 µl total RNA (100 ng). Reactions were performed in an Applied Biosystems™ 2720 Thermal cycler according to the manufacturer's instructions (Table 2.10). CDNA was stored at -20°C if required.

Table 2.9: Composition of RT-PCR master mix

Component	High-Capacity cDNA reverse transcription	TaqMan® MicroRNA Reverse Transcription
10× RT Buffer	2 µl	1.5 µl
25× dNTP Mix (100 mM)	0.8 µl	0.15 µl
10× RT Random Primers	2 µl	-
5× MicroRNA RT primers	-	3 µl
MultiScribe™ Reverse Transcriptase	1 µl	1 µl
RNase Inhibitor	-	0.19 µl
Nuclease-free H₂O	4.2 µl	4.16 µl
Template RNA	10 µl	5 µl
Total per reaction	20 µl	15 µl

Table 2.10: Setting of RT-PCR conditions

		High-Capacity cDNA reverse transcription		TaqMan® MicroRNA Reverse Transcription	
Steps	Temperature	Time	Temperature	Time	
Reverse transcription	25°C	10 minutes	16°C	30 minutes	
	37°C	120 minutes	42°C	30 minutes	
Stop reaction	85°C	5 minutes	85°C	5 minutes	
Hold	4°C	Hold	4°C	Hold	

2.6.4 Quantitative polymerase chain reaction (qPCR)

2.6.4.1 Multiplex qPCR for transcript expression

Transcript expression was analysed using TaqMan primer/probes (Table 2.11). Each multiplex reaction was assembled (Table 2.12) and utilised Glyceraldehyde 3-phosphate dehydrogenase (GAPDH) as endogenous control. Samples were assayed duplicate in a Rotor-Gene Q 2 plex real-time PCR cycler (QIAGEN, German). A two-step programme was performed (Table 2.13), with data from green and yellow fluorescence channels collected. The cycle threshold was set to 0.04 and Ct values obtained to perform data analysis.

2.6.4.2 Small RNA qPCR

QPCR reactions were performed by using primers specific for miR-142-3p and the endogenous control RNU48 (Table 2.12). Each target was assayed independently (i.e., not multiplexed) (Table 2.12). Samples were assayed in duplicate on a Rotor-Gene Q 2 plex real-

time PCR cycler (QIAGEN, German) to minimise pipetting errors. A two-step programme was performed (Table 2.13), with data collected from the green fluorescence channel. The cycle threshold was set to 0.04 and Ct values obtained to perform data analysis.

Table 2.11: TaqMan probes used in this study

Target (reporter)	Assay ID	Probe sequence
HGS (FAM)	Hs00610371_m1	5' CCTCGCGGCTCTAGGGCCGG 3'
Vps22 (FAM)	Hs00273125_m1	5' GGGACGTGGAGACCCGGGG 3'
TSG101 (FAM)	Hs00173072_m1	5' GAAGCGGAAGTGGTGTAGTG 3'
GAPDH (VIC)	Hs99999905_m1	5' GGCACCGCAGGCCCCGGGAT 3'
MALAT1 (FAM)	Hs00273907_s1	5'CGCAGCCTGCAGCCCGAGAC 3'
Mir-142-3p (FAM)	000464	5' UGUAGUGUUUCCUACUUUAU 3'
RNU48 (FAM)	001006	5' GATGACCCAGGTA ACTCTG 3'

Table 2.12: Composition of Real-time PCR master mix

Component	Multiplex qPCR	Small RNA qPCR
2× qPCRBio Probe Blue Mix Lo-ROX	5 µl	5 µl
RNase free water	3.5 µl	4 µl
TaqMan test probe	0.5 µl	0.5 µl
cDNA templates	0.5 µl	0.5 µl
GAPDH probe	0.5 µl	-
Total per reaction	10 µl	10 µl

Table 2.13: Setting of Real-time PCR two-step cycling conditions

Steps	Temperature	Time
PCR initial activation step	95°C	10 minutes
Combined	Denaturing	95°C 10 seconds
	Annealing	60°C 45 seconds

2.6.4.3 Data analysis

After generating Ct values (section 2.6.4), ΔCt was calculated by subtracting the endogenous control from the Ct value of target gene. Quantification of $2^{-\Delta Ct}$ was calculated in order to determine the expression fold change (Rizzacasa *et al.*, 2019).

2.7 Protein methods

2.7.1 Protein harvesting

Cells were seeded in 6-well plates as described above (section 2.2.5). Monolayers were washed twice with PBS and scraped in 50 μ l protein lysis buffer (Table 2.14). Lysates were transferred into fresh microfuge tubes, incubated for 30 minutes on ice and 10 minutes at room temperature in order to degrade nucleic acids. After centrifugation at $13,000 \times g$ for 5 minutes, the supernatant was transferred into a fresh microfuge tube and stored at -20°C or used straight away for downstream analysis.

Table 2.14: Composition of protein lysis buffer

Component	Volume	Final concentration
Pierce™ Universal Nuclease for cell lysis	0.5 μ l	250 U/ μ l
7 \times cOmplete™, Mini, EDTA-free Protease Inhibitor Cocktail	143 μ l	With one cocktail tablet dissolved in 1.5 ml distilled water
10 \times RIPA buffer	100 μ l	0.5 M Tris-HCL, 1.5 M Sodium Chloride (NaCl), 2.5% deoxycholic acid, 10% NP-40, 10 mM EDTA
Distilled water	756.5 μ l	
Total	1 ml	

2.7.2 Protein quantification

The Pierce bicinchoninic acid (BCA) Protein Assay Kit (Thermo Fisher Scientific, 23227) was used following manufacturer's instructions. Standards of bovine serum albumin (BSA)

were diluted with protein lysis buffer to give a range of concentrations (0, 0.025, 0.125, 0.25, 0.5, 0.75, 1, 1.5, 2 mg ml⁻¹). Samples were diluted 1 in 5 or 1 in 10 with protein lysis buffer to ensure their absorbance fell within the standard concentration range. 10 µl of sample or standard was assayed in duplicate in a 96-well plate by addition of 200 µl assay reagent (consisting of solution A and solution B mixed at a ratio of 50:1). The plate was sealed and incubated at 37°C for 30 minutes. Colorimetric change was measured (absorbance 562 nm) by TECAN Infinite M200 microplate reader. Through plotting a standard curve of absorbance against BSA concentration, a polynomial equation was generated to calculate the protein concentration in samples.

2.7.3 Sodium dodecyl sulfate-polyacrylamide gel electrophoresis (SDS-PAGE) and protein transfer

Proteins were separated by 12% SDS-PAGE. Components used to make gels are listed in Table 2.15. All buffers used in separating SDS-PAGE and protein transfer were made in-house (Table 2.16). Resolving gel mixture was poured between two glass plates and overlaid with a thin layer of isopropanol. After resolving gel solidification, the isopropanol was washed away with distilled water. Stacking gel mixture was added above the resolving gel and a 15-well comb was inserted. After stacking gel solidification, the comb was removed, and the wells washed with copious amounts of distilled water. The prepared gel was transferred into a tank which filled with 1× SDS-PAGE running buffer. Samples were prepared as 10 µg for cell lysate in general cellular protein analysis and 2 µg for cell lysate in EVs protein analysis. Samples were diluted with dH₂O in total volume of 10 µl or 20 µl depends on different loading buffer concentrations. 20 µl diluted samples combined with 5 µl of 5× loading buffer (National

Diagnosics, EC-887). 10 μ l diluted samples combined with 10 μ l 2 \times loading buffer (National Diagnosics, EC-886). Samples were heated at 95°C for 5 minutes and loaded alongside 5 μ l Precision Plus Protein Dual Colour Standards (Bio-Rad, 1610394). Proteins were separated by electrophoresis at 100-120 V and when samples passed the gel interface the setting was changed to 120-150 V for 60 minutes.

Table 2.15: The components and quantity to make 12% SDS-PAGE gels		
	Reagent	Volume
Stacking gel	40% Acrylamide	0.975 ml
	Upper tris buffer	2.1 ml
	dH ₂ O	4.725 ml
	10% (v/v) Ammonium persulfate solution (APS)	100 μ l
	Tetramethyl ethylenediamine (TEMED)	10 μ l
Resolving gel	40% Acrylamide	3 ml
	Lower tris buffer	2.5 ml
	dH ₂ O	4.3 ml
	10% (v/v) Ammonium persulfate solution (APS)	200 μ l
	TEMED	5 μ l

Table 2.16: Buffers and reagents used in SDS-PAGE and western blotting		
Buffer	Concentration	pH
Upper Tris buffer	1500 mM Tris base, 14 mM Sodium dodecyl sulphate (SDS)	8.8
Lower Tris buffer	545 mM Tris base, 14 mM SDS	6.8
1× SDS-PAGE running buffer	25 mM Tris base, 192 mM glycine, 3 mM SDS	8.3
1× TBS buffer	20 mM Tris base, 150 mM NaCl	7.6
1× TBS Tween-20 buffer (TBST)	As above with 0.1% (v/v) Tween-20	7.6
Blocking buffer	As above with 5% (w/v) skimmed milk powder	-

2.7.4 Protein transfer, western blotting, and densitometry

After electrophoresis (section 2.7.3), the stacking gel was discarded. The resolving gel, with separated proteins, was assembled into a transfer sandwich by placing the gel on the top of a piece of Amersham Protran 0.45 μm nitrocellulose membrane (Merck, German) and sandwiched in the middle of 6 filter papers. Care was taken to remove any air bubbles using a roller. The proteins were transferred using a Trans-Blot Turbo Transfer system (Bio-Rad, USA) at 1 A, 25 V, 30 minutes. Nitrocellulose membranes were blocked with tris-buffered saline (TBS) supplemented with 0.1% (v/v) TBST containing 5% (w/v) skimmed milk powder for one hour. Membranes were incubated at 4°C overnight with primary antibodies (Table 2.17). Membranes were washed with 1× TBST three times for 15 minutes each and then incubated with an

appropriate secondary antibody (Table 2.17) diluted in blocking buffer, at room temperature for 1 hour. Membranes were washed as above before bound antibody complexes were detected using Pierce™ ECL Substrate (Bio-Rad, 1705061) or WESTAR SUPERNOVA (Cyanagen, XLS3) dependent on protein abundance. After incubation in substrate for 5 minutes, the membrane was imaged on a C-DiGit Blot Scanner (Li-Cor, USA) or exposure to CL-XPosure X-ray films (Thermo Fisher Scientific, UK) in a dark room. Films were developed and fixed using an automatic Xograph Compact X4 processor (Xograph Imaging Systems, UK). Densitometry of western blot was performed by Li-Cor Image Studio Lite-5.2.5-av5 software (Li-Cor, USA).

2.7.5 Membrane stripping and storage

If membranes need to be used again, antibodies on the membrane were stripped off from the membrane using Restore™ western blot stripping buffer (Thermo Fisher Scientific, 21059). The membrane was incubated in 10 to 20 ml buffer on a shaker for 10 to 15 minutes at room temperature. The membrane was washed with 1× TBST for 3 times for 10 minutes. The membrane was then re-blocked and probed as above (section 2.7.4). To store a membrane, it was submerged in 1× TBST and sealed in a plastic bag, to keep membrane surface wet. The membrane was stored at 4°C for up to 2 weeks.

Table 2.17: Lists of antibodies used in western blotting

Antibody	Catalogue No.	Primary/ Secondary	Host species	Antibody type	Dilution	Molecular weight
Anti-HGS	ab155539 (Abcam)	Primary	Rabbit	Polyclonal	1 in 1000	110 kDa
Anti-EAP30	sc390747 (Santa Cruz Biotechnology)	Primary	Mouse	Monoclonal	1 in 200	30 kDa
Anti-TSG101	ab125011 (Abcam)	Primary	Mouse	Monoclonal	1 in 1000	44 kDa
Anti-EGFR	ab52894 (Abcam)	Primary	Rabbit	Monoclonal	1 in 5000	175 kDa
Anti-CD63	ab134045 (Abcam)	Primary	Rabbit	Monoclonal	1 in 1000	26 kDa
Anti-β actin	A1978 (Sigma-Aldrich)	Primary	Mouse	Monoclonal	1 in 10000	42 kDa
Anti-GAPDH	G9545 (Sigma-Aldrich)	Primary	Rabbit	Polyclonal	1 in 10000	36 kDa
Mouse Horseradish peroxidase (HRP)	A25112 (Abbkine)	Secondary	Goat	Polyclonal	1 in 3000	50 kDa
Rabbit HRP	A25022 (Abbkine)	Secondary	Mouse	Monoclonal	1 in 3000	50 kDa

2.7.6 Transmission electron microscopy

Cells were trypsinised and counted as above (section 2.2.5.). 500,000 of WT or Δ HGS cells were seeded per T25 culture flask with 5 ml regular growth medium (DMEM: F-12) and

allowed to adhere for 24 hours. The growth medium was discarded, and the monolayer was washed with PBS two times. 1 ml trypsin was added into each well to trypsinise the cells after washing with PBS 3 times. Cells were resuspended in 1.5 ml medium and centrifugation at $192 \times g$ for 5 minutes. The supernatant was discarded, and cells were resuspended in 1.5 ml medium and re-centrifugation at $192 \times g$ for 5 minutes. The pellets were processed and imaged by Mr Chris Hill at the Electron Microscopy Service, The University of Sheffield.

2.7.7 Immunofluorescence

Glass coverslips were placed in a 24-well plate and sterilised with 2 ml 70% IMS, before washing with a copious volume of sterile PBS. 10,000 cells were seeded onto sterilised coverslips as above (section 2.2.5) and allowed to adhere for 24 hours, before washing three times with PBS. Monolayers were fixed in 4% (w/v) paraformaldehyde (PFA). 500 μ l PFA in PBS (pH 7.4) was added per 24 well and incubated at room temperature for 10 minutes. The cells were then washed with ice-cold PBS three times for 10 minutes each. Cells were permeabilised by incubation for 10 minutes in PBS containing 0.1% (v/v) Triton X-100. Cells were washed with PBS three times for 5 minutes each and were blocked with 500 μ l PBS tween-20 (PBST) supplemented with 10% (v/v) normal goat serum, 0.3 M glycine and 1% (w/v) bovine serum albumin (BSA) for one hour at room temperature. Cells were washed three times for 10 minutes each in PBS. Primary antibodies were diluted in PBST supplemented with 1% (w/v) BSA (Table 2.17). 500 μ l of primary antibody solution were added into each well and incubated on the rocker overnight at 4°C. Unbound primary antibody was washed away by three washes in PBS for 10 minutes each. Cells were incubated with secondary antibodies that were diluted in PBST supplemented with 1% (w/v) BSA for one hour at room temperature in

the dark (Table 2.17). The PBS wash steps above were repeated and, 500 μ l 4', 6-diamidino-2-phenylindole (DAPI) (Thermo Fisher Scientific, 1890543A) diluted in PBS (300 nM) was added to each well to stain cell nuclei. After washing with PBS for three times in the dark, coverslips were mounted on a microscope slide using soft Molecular Probes™ ProLong™ Gold Antifade Mountant (Invitrogen, 1651296). The edge of coverslips was sealed with nail polish and stored in the dark at 4°C ready for imaging. Cells were imaged using Zeiss Axioplan 2 imaging microscope for 2-dimensional (2D) version imaged and imaged by Zeiss LSM 880 AiryScan confocal microscope and Leica DMI8 inverted microscope with z-stack setup for 3-dimensional (3D) version images.

Table 2.18: Antibodies used in immunofluorescence

Antibody	Catalogue No.	Primary/ Secondary	Host species	Antibody type	Dilution
Anti-HGS	ab155539 (Abcam)	Primary	Rabbit	Polyclonal	1 in 200
Anti-EEA1	ab70521 (Abcam)	Primary	Mouse	Monoclonal	1 in 1000
Anti-RAB7	ab50533 (Abcam)	Primary	Mouse	Monoclonal	1 in 4000
Rabbit IgG-UNLB	0111-01 (Southern Biotech)	Primary	Rabbit	Isotype control	1 in 5000
Mouse IgG1 kappa	14-4714-85 (Thermo Fisher Scientific)	Primary	Mouse	Isotype control	1 in 500
Anti-rabbit IgG Alexa Fluor 488	A32731 (Thermo Fisher Scientific)	Secondary	Goat	Polyclonal	1 in 1000
Anti-mouse IgG Alexa Fluor 594	A32744 (Thermo Fisher Scientific)	Secondary	Donkey	Polyclonal	1 in 1000

2.7.8 Pulse-chase experiments

Glass coverslips were placed in a 24-well plate and sterilised with 2 ml 70% IMS, before washing with a copious volume of sterile PBS. 10,000 WT or Δ HGS cells were seeded onto sterilised coverslips as above (section 2.2.5) with serum free medium (DMEM: F-12) for consistent time starvation. Cells were allowed to adhere for 24 hours, before washing three times with PBS. At the next day, pre-incubated 50 ng/ml Alexa Fluor™ 488 EGF complex (Thermo Fisher Scientific, E13345) with serum free medium for 60 minutes at 4°C. Cells were pulse-stimulated during 10 minutes with 50 ng/ml of Alexa Fluor™ 488 EGF complex (Thermo Fisher Scientific, E13345). Then cells were chased by culturing in warm serum free DMEM: F-12 at indicated time (0, 10, 20, 60, 120 minutes) after washing with serum free medium for 2 times. Chase stopped by washing the cells with ice-cold PBS for three times. Then, cells were fixed by 4% PFA for 10 minutes and immuno stained and mounted as described in section 2.7.7. Cells were imaged using Leica DMI8 inverted microscope.

2.7.9 Data analysis

Immunofluorescence-stained images were quantitatively analysed by software FIJI (Image J, version 1.52 r). The acquisitioned images were firstly split into different channels. The integrated density of single channel was calculated by the sum of the grey values of all the pixels in the selected objectives divided by the number of pixel values. Colocalization between red and green channels was determined by Pearson's correlation coefficient through using plugin JACoP (Just Another Colocalization Plugin).

2.8 Transient transfection

Preliminary scale transient transfection experiment was conducted with H357 cancer cells.

All transient transfection reagents were bought from Thermo Scientific, UK unless otherwise stated. 5 nmol HGS siRNA powder (Ambion, AM16708) was dissolved in 250 μ l nuclease-free water which was included in the kit to give a 20 μ M stock concentration. The Invitrogen™ Silencer™ Negative Control No. 2 siRNA (Ambion, AM4613), Pre-miR™ miRNA Precursor hsa-miR-142-3p (Ambion, AM17100), mirVana® miRNA inhibitor (Ambion, MH10398) was already dissolved in a volume of 100 μ l at concentration of 50 μ M. 150 μ l nuclease-free water was added to adjust the concentration of 20 μ M for next step. 0.1 million cells per 6-well plate that had been seeded the day before and incubated 18-24 hours for adherent as described above (section 2.2.5). After overnight incubation, cells reached 30% to 50% confluence and were ready for transient transfection. On the next day, set up the dilution of transfection reagents with Opti-MEM (Gibco, 31985070) to give the final concentration of 0 to 50 nM (Table 2.19). Two sets of sterile eppendorf tubes were placed to one transfection reagent for 24-hours and 48-hours transfection respectively. According to manufactory's instructions, 4 μ l oligofectamine transfection reagents (Invitrogen, 12252011) were added to 11 μ l Opti-MEM, and then incubated at room temperature for 5 to 10 minutes. Diluted transfection reagents were combined with 15 μ l diluted oligofectamine transfection reagent, and then incubate at room temperature for 15 to 20 minutes. During waiting time, the cells which were seeded the day before were washed twice with 1ml Opti-MEM each time followed with 800 μ l Opti-MEM added to each well. 200 μ l of incubated transfection reagents and oligofectamine reagents mixture were added to each well. Cells were then placed in an incubator at 37°C, 5% CO₂ atmosphere for 4 hours. 500 μ l normal growth medium with 30% FBS were then added to each well and cells were cultured 24 and 48 hours respectively for post-transfection RNA prep (section 2.6.1) or protein

lysis (section 2.7.1). Collected mRNA and protein were then analysed through using qPCR (section 2.6.3) and western blotting (section 2.7.3) to determine the best diluted transient transfection reagents concentration in full-scale experiments.

When the best concentration of transient transfection reagents was determined, the same procedures were repeated as previously described of seeding cells in 6 well plates, combining determined concentration of transfection reagents with diluted oligofectamine, and place at same condition. After 24 hours, cells were washed with PBS. 6 ml EV-free medium (section 2.9.1.1) was added and then incubate overnight. Finally, RNAs, proteins and EVs can be collected from 2 dishes scrambled, 2 dishes negative and 2 dishes with transients transfected cells and medium at the next day. After 24 hours, cells were washed with PBS. Medium was changed into 1 ml DMEM: F-12 (section 2.2.3) with 10% EV-depleted FBS (section 2.3.1.1) then incubated for another 24 hours. Proteins and EVs were collected from same well cells that exposed in diluted oligofectamine with MOCK, scrambled with negative silencer and transient transfected cells and medium at 48 hours post-transfection activity.

Final concentration (nM)	Volume of 20 μM stock (μl)	Volume of Opti-MEM (μl)
0	-	185
10	0.5	184.5
20	1.0	184
30	1.5	183.5
40	2.0	183
50	2.5	182.5

2.9 Cells growth assay and viability

2.9.1 Growth assay

To assess cell proliferation over time as described by Marayati *et al.* (2022). 50000 cells per well of H357 WT or HGS ΔHGS were plated in 6-well plates with normal growth medium. They were incubated at 37 °C in a humidified 5% CO₂ atmosphere for 24, 48, 72, or 96 hours. 0.5 ml trypsin was added into each well to trypsinise the cells after washing with PBS 3 times. Cells were resuspended in 1.5 ml medium and counted with a hemocytometer. Doubling time was calculated as follows:

Growth rate:

$$r = \frac{\ln\left(\frac{N(t)}{N_0}\right)}{t}$$

$$\text{Doubling time} = \frac{\ln(2)}{r}$$

Or:

$$\text{Douling time} = t \times \frac{\log(2)}{\log(N(t)) - \log(N_0)}$$

Where:

- $N(t)$ = the number of cells at time t
- N_0 = the number of cells at time 0
- r = growth rate
- t = time (in hours)

2.9.2 Viability

Viable and dead cell numbers were determined using trypan blue staining (0.4%, Sigma), and counted with a hemocytometer. Under a light microscope, dead cells showed blue staining and live cells showed no staining. Viability was calculated as follows:

$$Viability (\%) = \frac{live\ cells}{live\ cells + dead\ cells} \times 100\%$$

2.9.3 Apoptosis detection by flow Cytometry

Apoptotic rate of WT and Δ HGS were measured using TACS™ Annexin V-FITC Apoptosis Detection Kit (R&D Systems, 4830-01-K). 300,000 WT or Δ HGS were seeded in 6-well plates with normal growth medium (DMEM: F-12) then incubated at 37 °C in a humidified 5% CO₂ atmosphere for 48 hours. After washing with PBS 3 times, 0.5 ml trypsin was added into each well to trypsinise the cells. Cells were accounted and resuspended in 1.5 ml medium and placed on centrifugation at 300 × g for 10 minutes at room temperature. Cells were washed by resuspending them in 500 µl of cold PBS and then pelleting by re-centrifugation at 300 × g for another 10 minutes. The pellets were resuspended in Annexin V incubation reagent (Table 2.20) with concentration of 100 µl per sample of 100,000 cells following with incubation in the dark and on the ice for 15 minutes. 400 µl of 1× Binding Buffer per sample for washing cells after incubation were made by diluting with 10× Binding Buffer in 1:10 ratio in distilled water. The fluorescence intensity of cells was processed by flow cytometry multi-laser and detector analyser LSR II Flow Cytometer (BD Bioscience, UK) at the medical school, the University of Sheffield with help of Ms Susan Clark within 1 hour for maximal signal. Light is gathered by two lenses, the forward (FSC-A) and side (SSC-A) scatter channels. Excitation wavelengths of 660 nm (Annexin V) and 530 nm (Propidium iodide) were set. Flow cytometry was analysed

using the FlowJo software (version V10). Cells were gated by FSC-area/SSC-area in order to get single cell population of viable, necrosis and apoptosis.

Table 2.20: Composition of Annexin V incubation reagent

Component	Volume
10× Binding Buffer	10 µl
Propidium iodide (PI)	10 µl
TACS Annexin V-FITC	1 µl
Distilled water	79 µl
Total	100 µl

2.10 Statistical analysis

The data of pulse-chase experiments are representative of four independent experiments. All other data are representative of three independent experiments. All calculation and results were performed using GraphPad Prism 9 (GraphPad software Inc., USA). Values are shown as mean ± standard error of mean (SEM). The Student's t test was used to compare the means between two independent groups. ANOVA was used to compare the means between three or more groups, whereas one-way ANOVA with Dunnett's multiple comparisons test was used when it has one categorical independent variable and two-way ANOVA with Šídák's multiple comparisons test was used when it has two categorical independent variables. Statistical significance was considered as P value less than 0.05 (*P<0.05, **P<0.01, ***P<0.001 and ****P<0.0001).

Chapter 3: Characterisation of ESCRT machinery subunits in OSCC cells

3.1 Introduction

Oral cancer is the sixth most common cancer worldwide, and more than 90% of those are OSCC (Feller and Lemmer, 2012). Similar to other cancers, OSCC evolved from precancerous oral epithelial cells like keratinocytes at different transformation stages. These precancerous keratinocytes may become cancerous after genetic mutation acquisition (Feller *et al.*, 2013). The sustained cancer cells growth, invasion and metastasis depends on intercellular communication within the TME, which includes secretion of soluble factors by cancer cells or stromal cells. EVs carry molecules such as oncopeptides, lipids and RNAs from donor to recipient cells to trigger phenotypic changes within the TME (Xu *et al.*, 2018). Many studies showed EVs are important in tumour progression as cancer cells release more EVs than non-malignant cells (Xu *et al.*, 2018, Vasconcelos *et al.*, 2019). Indeed, the saliva of oral cancer patients has been shown to contain up to four-fold more EVs than healthy controls (Sharma *et al.*, 2011). In addition, plasma EVs are also significantly higher in the OSCC patients compared to healthy counterparts (Zlotogorski-Hurvitz *et al.*, 2019, Momen-Heravi and Bala, 2018). Furthermore, EV cargos (including proteins and miRNAs) were found to promote OSCC tumourigenesis by recruiting CAF and contributing to angiogenesis and lymph angiogenesis by stimulating endothelial cells (Sjoqvist *et al.*, 2019, de Andrade *et al.*, 2018). Despite their varied role in OSCC progression little is known about EV biogenesis in this type of cancer.

Cell membrane invagination forms early endosomes. Afterwards, early endosomal membrane invagination forms MVB. Most of MVB are degraded by lysosome binding, and the

others are fused with cell membrane, releasing ILVs to the outside of the cell membrane as exosomes (Colombo *et al.*, 2014). Various mechanisms involved in this process of EVs biogenesis. As previously described, the ESCRT machinery is closely associated with EV biogenesis, which is the main pathway of ILVs biogenesis and secretion (Ventimiglia and Alonso, 2016). ESCRT complex formation is an ubiquitination dependent process, which composed by about 30 proteins and mainly grouped into 5 complexes (Deatherage and Cookson, 2012). They are ESCRT-0, ESCRT-I, ESCRT-II, ESCRT-III and Vps4-Vta1. Ubiquitin first tag proteins. Afterwards, monoubiquitinated cargos are recognised and recruited by the key subunit HGS of ESCRT-0. Then, ESCRT-0 recruits ESCRT-I by interacting with the ESCRT-subunit TSG101. ESCRT-I along with Vps22 in ESCRT-II initiates endosomal inward budding around ubiquitinated proteins clusters. The subunits from ESCRT-III then binds to ESCRT-II that trigger cleavage to form ILVs, followed with recruiting Vps4 to disassemble membranes through ATPase catalysis (Yang and Hurley, 2010). To date, many studies have indicated the critical role of ESCRT in ILV biogenesis. Loss of ESCRT-0 and ESCRT-I subunits HGS and TSG101 causes a reduction in exosome release in many types of cells such as breast cancer cells and dendritic cells (Hessvik and Llorente, 2018, Hoshino *et al.*, 2013, Colombo *et al.*, 2013). Thus, it is essential to examine the role of these subunits in HNSCC EV biogenesis.

Previous work in the Hunt lab indicated that a number of ESCRT members were overexpressed at the mRNA and/or protein level in OSCC cell lines (unpublished data). Therefore, our first objective was to validate these previous findings. A panel of cells were assembled for *in vitro* expression and protein analysis studies. Primary NOKs were selected as healthy control cells to be used as a reference for comparison to the immortalised normal oral

keratinocyte cell line, FNB6, and a panel of three OSCC cell lines (H357, SCC9 and SCC4). NOKs can only be passaged several times before replicative senescence. Therefore, FNB6 was included as a representative normal epithelial cell line. The OSCC cell lines are all commercially available and were all derived from OSCC of the tongue. All cells were cultured in the same medium to remove any variation caused by medium composition. The transcript abundance of HGS (ESCRT-0), TSG101 (ESCRT-I) and Vps22 (ESCRT-II) was quantified by qPCR, and protein abundance of these ESCRT subunits was determined by western blotting. The subcellular location of HGS was explored by immunofluorescence microscopy to visualise any association with endosomal compartments.

3.2 Results

3.2.1 HGS transcript expression and protein abundance

QPCR revealed that HGS transcript expression was 1.6-fold higher in SCC9 than NOKs ($P < 0.01$). However, there was no significant difference between NOKs and the other cells tested (Figure 3.1 A). HGS protein abundance did not mirror the transcript expression (Figure 3.1 B). FNB6 and two cancer cell lines (H357 and SCC9) had an increased HGS protein abundance compared to NOKs (Figure 3.1 C); FNB6 was 3.4-fold higher ($P < 0.01$); H357 was 4-fold higher ($P < 0.01$); SCC9 was 3.7-fold higher ($P < 0.01$). There was no significant difference between SCC4 and NOKs.

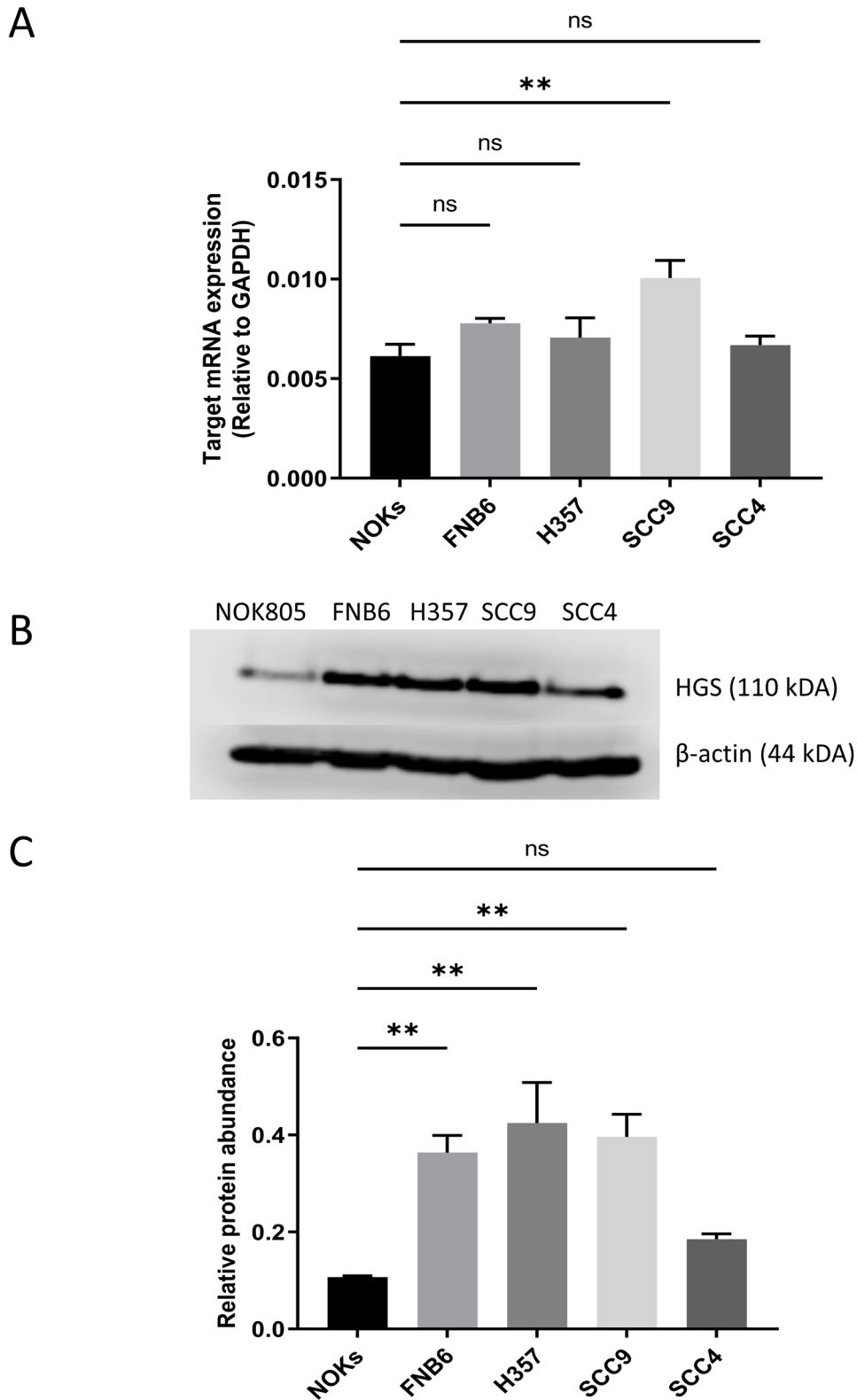


Figure 3.1: HGS transcript expression and protein abundance. (A) Transcript expression of HGS relative to GAPDH was determined by Taqman based qPCR. (B) Representative western blot of HGS and loading control β -actin. (C) Densitometry analysis of HGS protein abundance relative to β -actin abundance. All data were calculated as mean of three biological replicates \pm SEM. **= $p < 0.01$, ns= not significant by Dunnett test.

3.2.2 TSG101 transcript expression and protein abundance

QPCR revealed that the expression of TSG101 was 1.2-fold higher in FNB6 ($P < 0.05$); and 1.8-fold lower in SCC9 ($P < 0.0001$) compared to NOKs. There was no significant difference between NOKs and the other cells tested (Figure 3.2 A). TSG101 protein abundance showed a different pattern to that of the transcript expression (Figure 3.2 B). The protein abundance in FNB6 and H357 were 1.3-fold ($P < 0.05$) and 1.6-fold ($P < 0.001$) higher than NOKs, respectively (Figure 3.2 C). There was no significant difference between the remaining cell lines (SCC9 and SCC4) and NOKs.

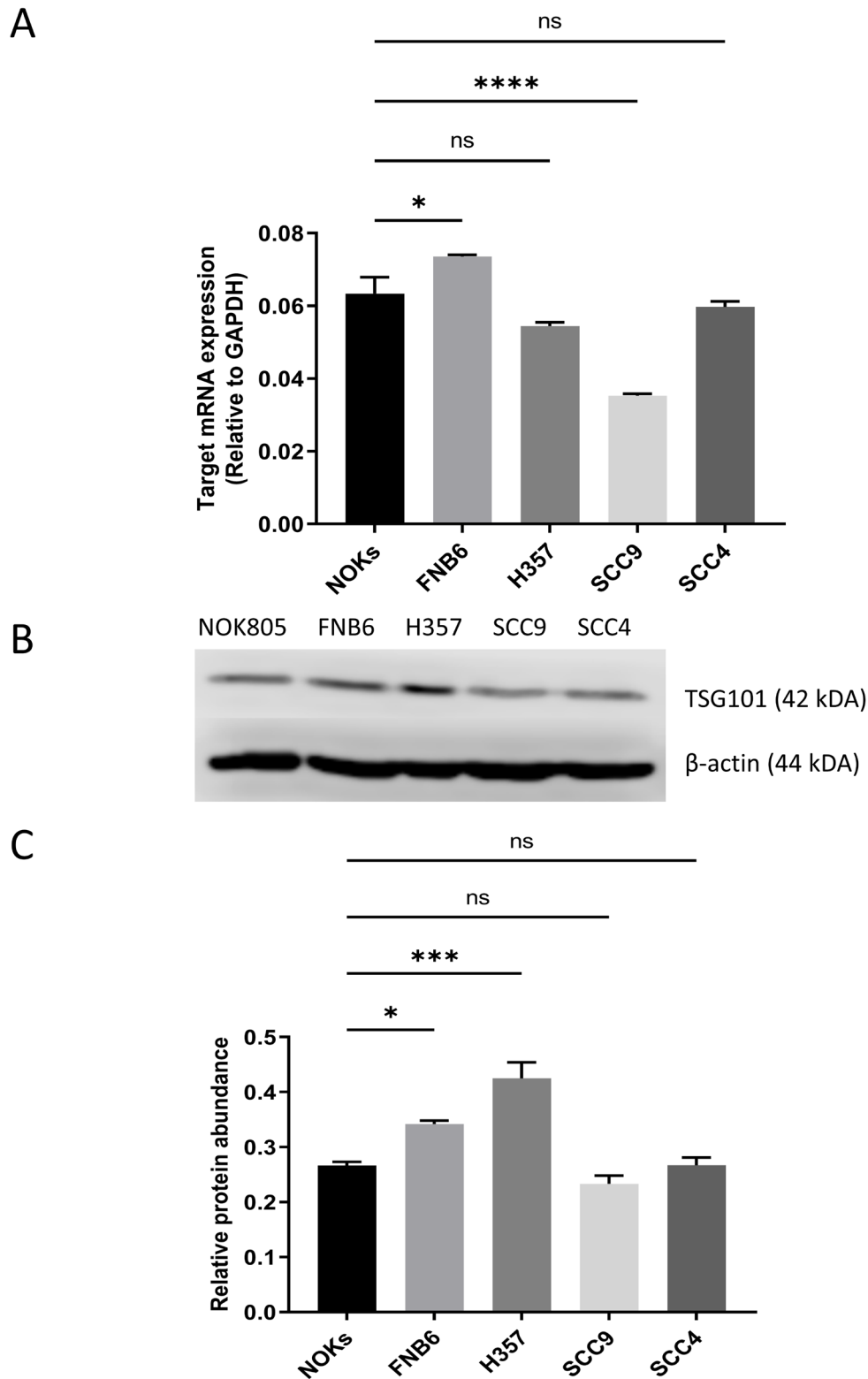


Figure 3.2: TSG101 transcript expression and protein abundance. (A) Transcript expression of TSG101 relative to GAPDH was determined by Taqman based qPCR. (B) Representative western blot of TSG101 and β -actin. (C) Densitometry analysis of TSG101 protein abundance relative to β -actin abundance. All data were calculated as mean of three biological replicates \pm SEM. * = $p < 0.05$, *** = $p < 0.001$, **** = $p < 0.0001$, ns = not significant by Dunnett test.

3.2.3 Vps22 transcript expression and protein abundance

QPCR showed the expression of Vps22 was 1.8-fold higher in FNB6 ($P < 0.05$), 2.4-fold higher in SCC9 ($P < 0.001$) and 1.7-fold higher in SCC4 ($P < 0.05$) compared to NOKs (Figure 3.3 A). There was no significant difference between NOKs and H357 (Figure 3.3 A). Protein abundance of Vps22 was determined by western blot (Figure 3.3 B). Vps22 protein abundance was 3-fold higher ($P < 0.001$) in FNB6, 3.3-fold higher in H357 ($P < 0.001$) and 2.5-fold higher in SCC9 ($P < 0.01$) compared to NOKs (Figure 3.3 C). There is no significant difference between NOKs and SCC4.

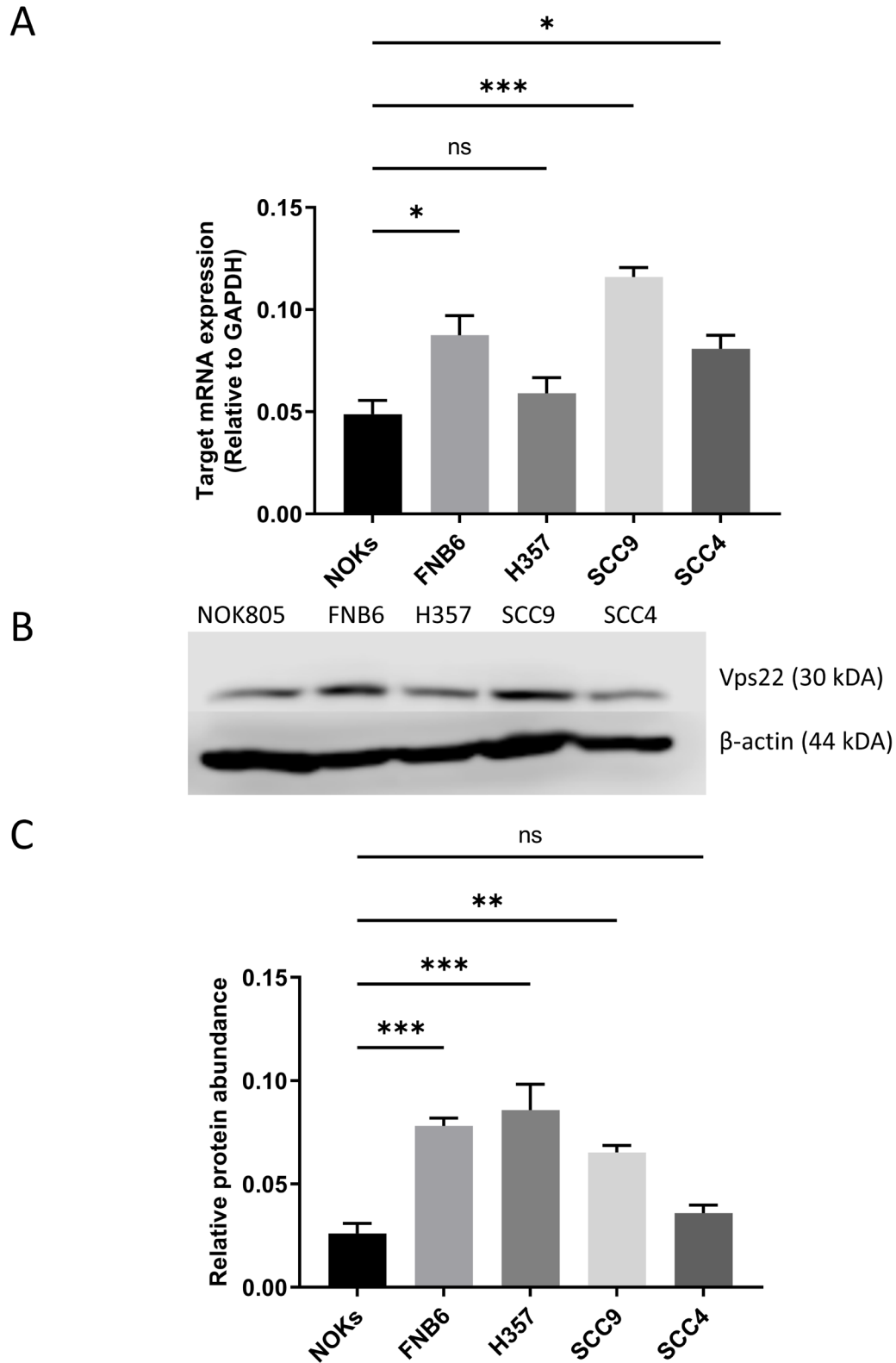


Figure 3.3: Vps22 transcript expression and protein abundance. (A) Transcript expression of Vps22 relative to GAPDH was determined by Taqman based qPCR. (B) Representative western blot of Vps22 and β -actin. (C) Densitometry analysis of Vps22 protein abundance relative to β -actin abundance. All data were calculated as mean of three biological replicates \pm SEM. * = $p < 0.05$, ** = $p < 0.01$, *** = $p < 0.001$, ns = not significant by Dunnett test.

3.1.1 Post-transcriptional regulation of HGS

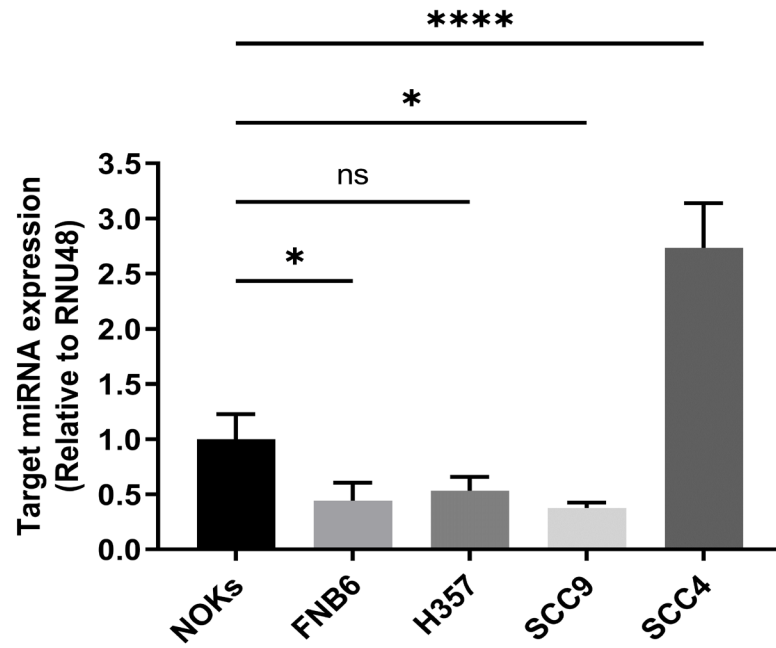
The most compelling data above was the increased HGS protein abundance in three of the four cell lines (FNB6, H357 and SCC9) compared to NOKs (Figure 3.1 B/C). However, the increased protein abundance could not be explained by increased gene expression (except for in SCC9), suggesting that HGS expression is controlled in a post-transcriptional manner. MicroRNAs (miRNA) play a role in post-transcriptional gene regulation. They are small non-coding RNAs comprised of 19-25 nucleotides. Through binding to the target mRNA, usually via the 3'-untranslated region (3'UTR) (although there is evidence that they can bind to other mRNA regions), miRNAs repress translation of the target mRNA or can cause transcript degradation (Xie *et al.*, 2021, Martin *et al.*, 2014). MiRNA have previously been shown to promote a cancerous phenotype in OSCC cells (Hunt *et al.*, 2011). We hypothesised that miRNA targeting HGS might be down-regulated in the cell lines tested, resulting in de-repression of HGS (i.e. higher protein abundance). *In silico* analysis, using a predictive miRNA target algorithm called Target Scan (Agarwal *et al.*, 2015), identified one microRNA, miR-142-3p, as a putative post-transcriptional regular of HGS. Thus, mature miR-142-3p expression was determined by qPCR. In addition, a synthetic miR-142-3p precursor and anti-miR-142-3p were transiently transfected into cells to elucidate any role in the regulation of HGS expression.

3.1.1.1 MiR-142-3p is a putative post-transcriptional regular of HGS

Mature miR-142-3p was quantified relative to endogenous control RNU48. It showed a trend that the three cell lines with highest HGS protein abundance (FNB6, H357 and SCC9) had the lowest miR-142-3p expression compared to NOKs, however, there was no statistically significant difference between NOKs and H357 (Figure 3.4 A). A further mechanism involved

in post-transcriptional gene regulation is miRNA sequestration by long non-coding RNAs. The long non-coding RNA metastasis associated lung adenocarcinoma transcript 1 (MALAT1) has been shown to bind to miR-142-3p (Liu *et al.*, 2017, Raiborg and Stenmark, 2009). We hypothesised that dysregulation of MALAT1, which can sequester miR-142-3p, would affect HGS protein abundance. Thus, qPCR was used to measure transcript expression of MALAT1. MALAT1 expression was lower in all cells compared to NOKs: FNB6 was 1.9-fold lower ($P < 0.0001$), H357 was 4.6-fold lower ($P < 0.0001$), SCC9 was 2.1-fold lower ($P < 0.0001$), and SCC4 was 2.4-fold lower ($P < 0.0001$) (Figure 3.4 B).

A



B

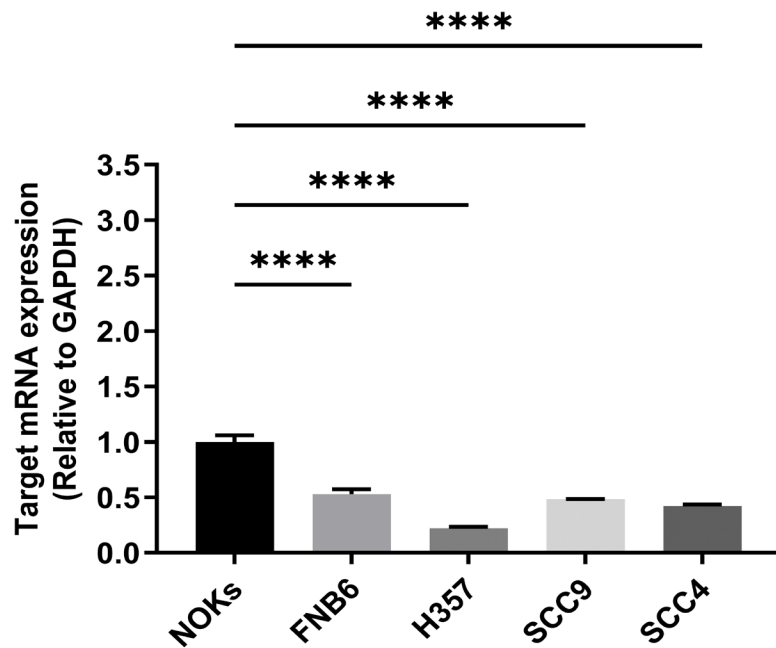


Figure 3.4: Expression of putative post-transcriptional regulators of HGS. (A) Mature miR-142-3p relative to RNU48 was determined by qPCR. (B) MALAT1 expression relative to GAPDH was determined by qPCR. Data is reported relative to NOKs. All data were calculated as mean of three biological replicates \pm SEM. * = $p < 0.05$, **** = $p < 0.0001$, ns = not significant by Dunnett test.

3.1.1.2 Inhibition and overexpression of mature miR-142-3p

Two of the cell lines (FNB6 and SCC9) expressed significantly less miR-142-3p than NOKs, which could partly explain their increased HGS protein abundance (i.e. by depression). We hypothesised that inhibition or up-regulation of miR-142-3p expression would cause an increase or decrease in HGS protein abundance, respectively. H357 cells were transiently transfected with a synthetic miR-142-3p inhibitor or miR-142-3p precursor. A range of inhibitor and precursor concentrations were used (0-50 nM) to determine any dose-response effects. HGS protein abundance was determined 24 and 48 hours post-transfection by western blotting.

There appeared to be a dose-dependent increase in HGS protein abundance when cells were transfected with increasing concentrations of miR-142-3p inhibitor, 24 hours post-transfection (Figure 3.5 A), but there was no statistical significance according to densitometry analysis (Figure 3.5 B). There was no change in HGS protein abundance 24 hours after transfection with miR-142-3p precursor (Figure 3.5 A/C). To ensure that enough time was given to observe changes in protein abundance, the same analysis was conducted 48 hours post-transfection. No significant differences in HGS protein abundance were observed for cells transfected with the miR-142-3p inhibitor or precursor, 48 hours post-transfection (Figure 3.6).

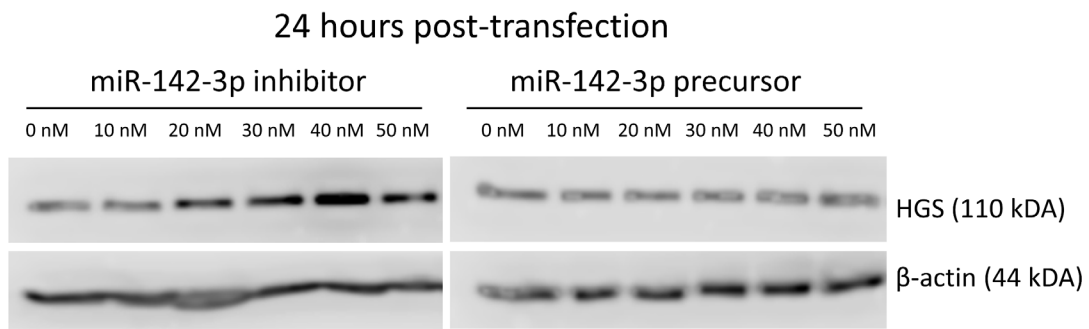
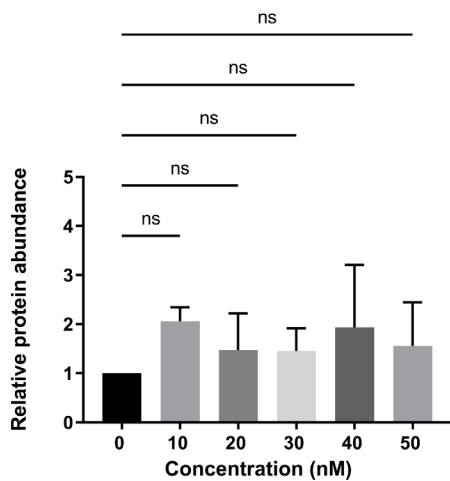
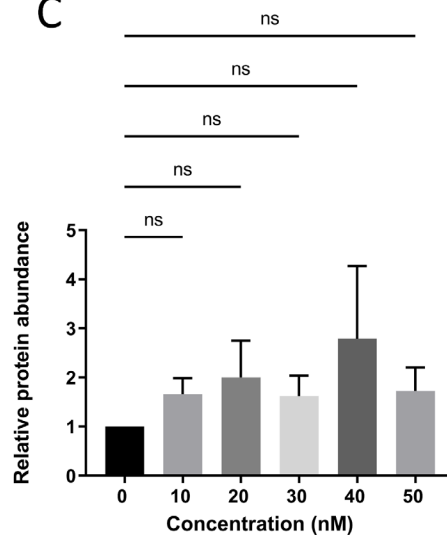
A**B****C**

Figure 3.5: MiR-142-3p inhibition or overexpression in H357 for 24 hours. (A) Representative western blot of HGS and loading control β -actin abundance in H357 cells that were transfected with miR-142-3p inhibitor or precursor (0-50 nM). Densitometry analysis of HGS protein abundance relative to β -actin abundance in H357 cells that were transfected with (B) miR-142-3p inhibitor (C) or miR-142-3p precursor. All data were calculated as mean of three biological replicates \pm SEM. ns= not significant by Dunnett test.

A

48 hours post-transfection

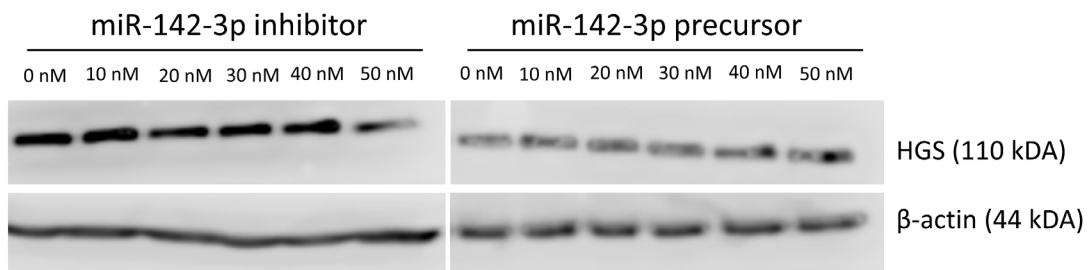
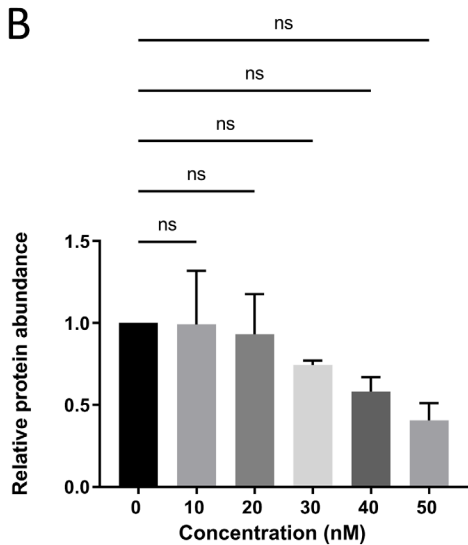
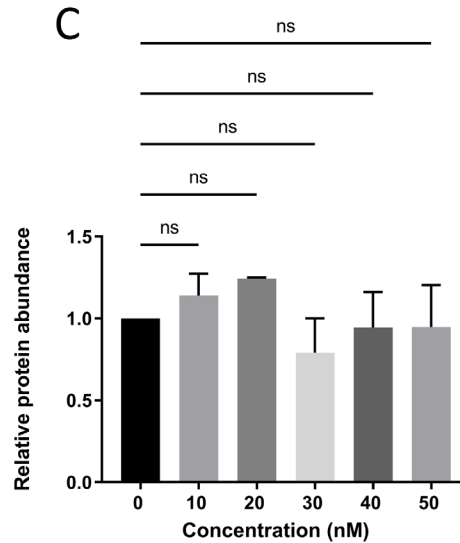
**B****C**

Figure 3.6: MiR-142-3p inhibition or overexpression in H357 for 48 hours. (A) Representative western blot of HGS and loading control β -actin abundance in H357 cells that were transfected with miR-142-3p inhibitor or precursor (0-50 nM). Densitometry analysis of HGS protein abundance relative to β -actin abundance in H357 cells that were transfected with (B) miR-142-3p inhibitor (C) or miR-142-3p precursor. All data were calculated as mean of three biological replicates \pm SEM. ns= not significant by Dunnett test.

3.1.2 Investigation of the interaction between HGS and early endosomes in OSCC

HGS has a functional FYVE domain that recognises PtdIns (3) P, a phospholipid enriched in the membrane of early endosomes. The FYVE domain is present in a number of proteins (including EEA1) and mediates their recruitment to endocytic membranes (Burd and Emr, 1998, Gaullier *et al.*, 1998, Patki *et al.*, 1998, Stenmark *et al.*, 1996), where they are involved in protein trafficking (Toker and Cantley, 1997). More recently, HGS has also been shown to co-

localise with RAB5 positive early endosomes (Yu *et al.*, 2021).

Our data showed that the cell lines used in the current study (except for SCC4) have a higher HGS protein abundance compared to NOKs. As described above, it is already known that HGS regulates endosomal sorting and should therefore be localised at early endosomal structures (McLean *et al.*, 2022). EEA1 localises exclusively to early endosomes and has an important role in endosomal trafficking (Nagano *et al.*, 2019). We therefore used immunofluorescence microscopy to reveal the cellular location of HGS in relation to the early endosomal marker, EEA1. Three OSCC cell lines (H357, SCC9, and SCC4) and an immortalized normal oral keratinocyte cell line (FNB6) were seeded onto glass coverslips for standard immunofluorescence microscopy and confocal microscopy to visualise the subcellular location of HGS and EEA1, and to investigate any co-localisation.

Samples were imaged by using an Axioplan 2 imaging microscope (Zeiss). The resulting fluorescence revealed punctate staining throughout the cytoplasm, with some spatial overlap of HGS (green fluorescence) and EEA1 (red fluorescence). The spatial overlap of HGS and EEA1 fluorescent signal can be seen in the merged images as yellow or orange fluorescence (Figure 3.7).

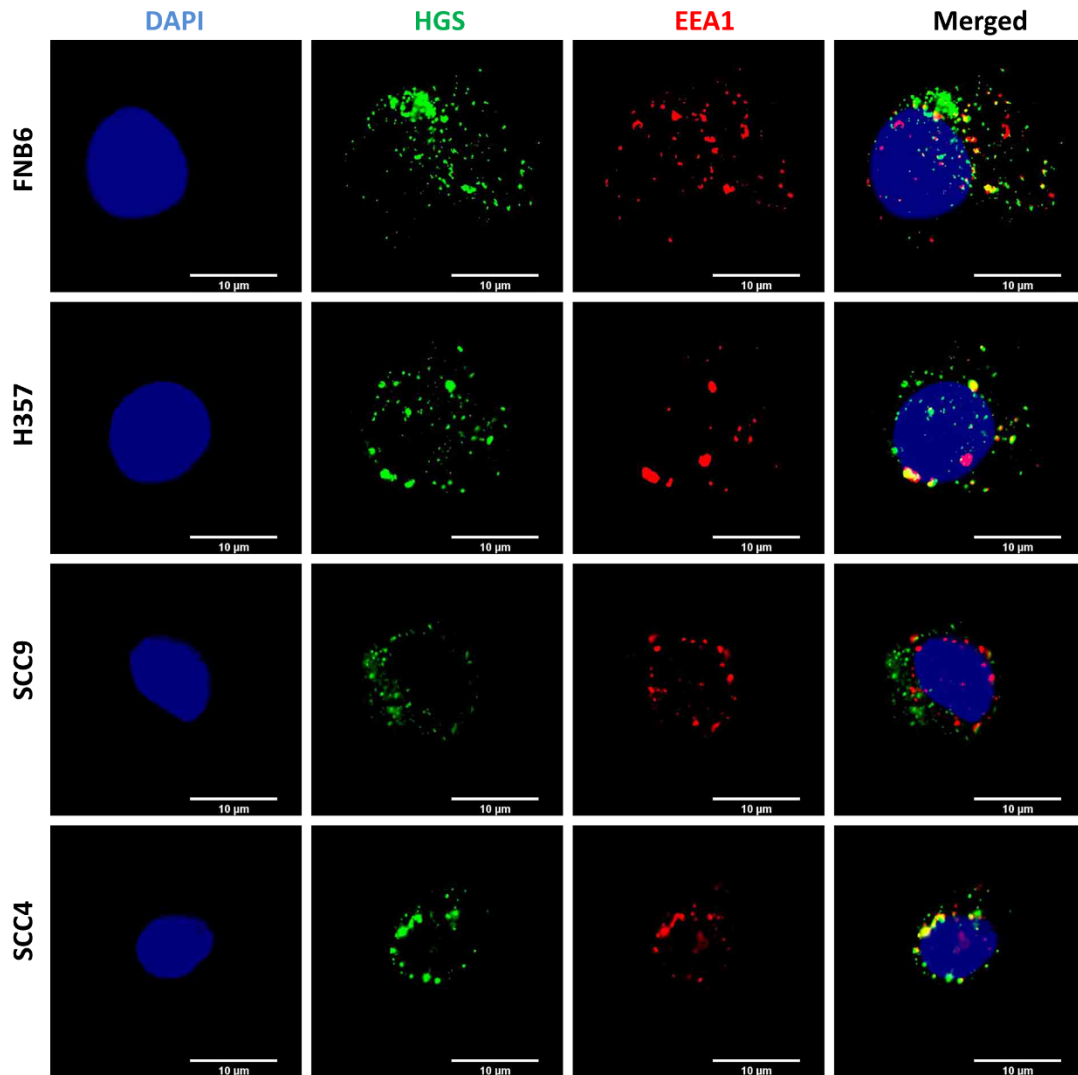


Figure 3.7: Representative immunofluorescence microscopy images of HGS and EEA1. Localisation of HGS and EEA1 were determined in all cell lines. Cells were permeabilised by PBS containing 0.1% (v/v) Triton X-100 prior to fixation. They were incubated with anti-HGS and anti-EEA1 antibodies, then incubated with Alexa 488 and Alexa 568-conjugated secondary antibodies. Cell nuclei were stained with DAPI. Images were taken using a Zeiss Axioplan 2 imaging microscope. Images are representative of three independent repeats. Scale bar: 10 µm.

To further quantify the apparent spatial overlap observed, cells were prepared as above, but analysed using a confocal laser scanning microscope. 3D images were obtained by combining z-stacked images. Fluorochromes were acquired separately to evaluate the expression and location of HGS and EEA1. Yellow or orange staining reveals the potential co-localisation of two antigens (Figure 3.8 A). Based on different channel's intensity level, each

pixel in the split image was plotted in the 2D histogram (Figure 3.8 B). The green channel (HGS) is shown on the x-axis, and the read channel (EEA1) is shown on the y-axis and the linear regression represents the rate of the two fluorochromes area association. The scatter plot for the four cell lines consists of dots, which were concentrated together, indicating the potential co-localisation of HGS and EEA1. Based on linear regression, Pearson's R value was calculated to quantitatively analyse the degree of co-localisation for each cell line (Dunn *et al.*, 2011, Adler and Parmryd, 2010). The Pearson's R value ranges from -1 and 1. A value of 1 would mean the perfect positive correlation. Every pixel that contains both Alexa Fluor 488 and Alexa Fluor 584 and *vice versa*, while the value of 0 is no correlation and the value of -1 is perfect negative correlation. Based on different images, the Pearson's R values were above 0.5 in all cell lines, which indicated strong co-localisation of HGS and EEA1 (Figure 3.8 C).

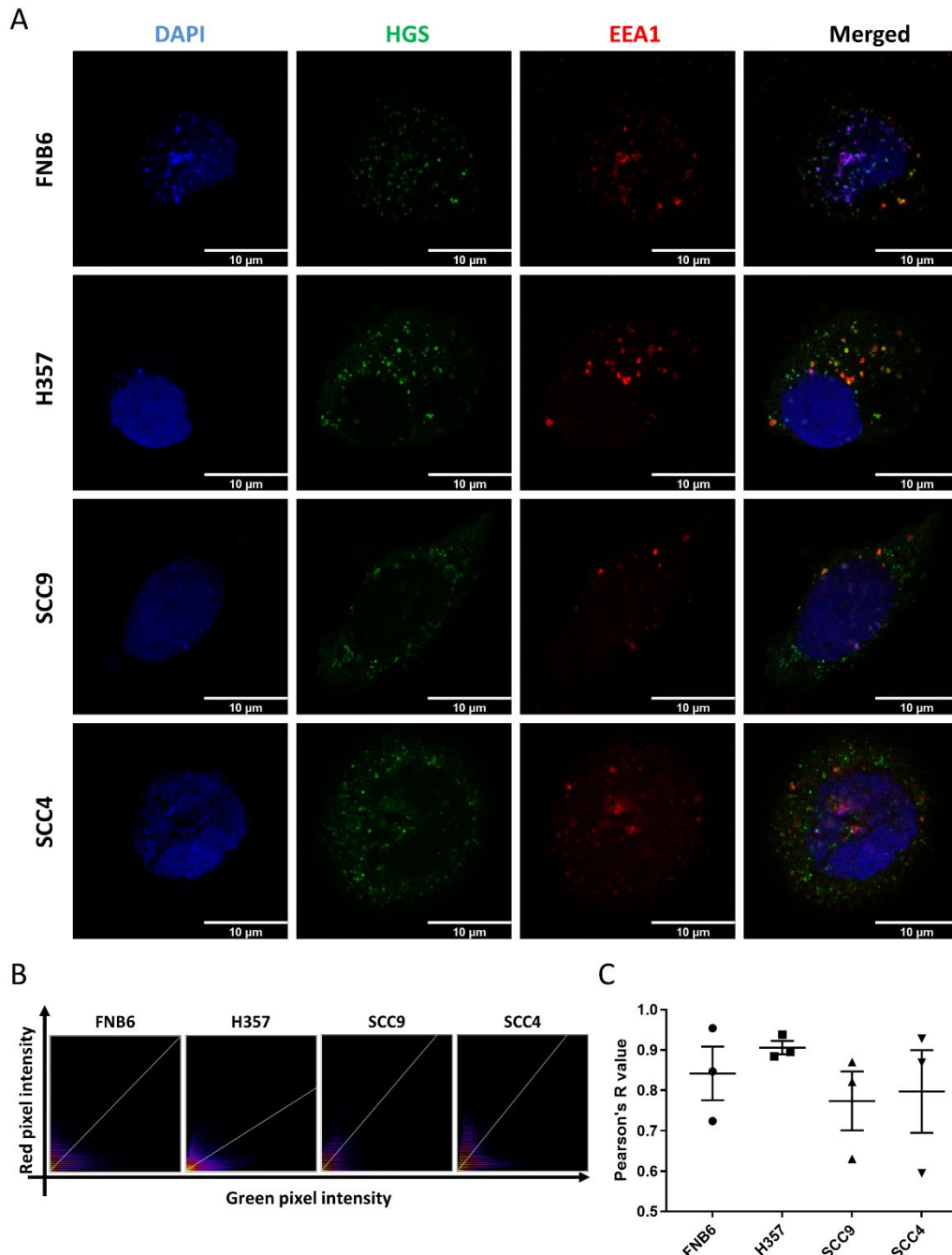


Figure 3.8: Representative confocal microscopy images of immunofluorescence staining of HGS and EEA1. (A) Localisation of HGS and EEA1 were determined in all cell lines. Cells were permeabilised by PBS containing 0.1% (v/v) Triton X-100 prior to fixation. They were incubated with anti-HGS and anti-EEA1 antibodies, then incubated with Alexa 488 and Alexa 568-conjugated secondary antibodies. 3D images were acquired by z-stack. Yellow/orange pixels indicate potential co-localisation between HGS and EEA1. Cell nuclei were stained with DAPI. Images were taken by Zeiss LSM 880 AiryScan confocal microscope. (B) Individual pixels in each channel were plotted in the scatter plot. HGS (green) is shown on the x-axis, and EEA1 (red) is shown on the y-axis. (C) Co-localisation between HGS and EEA1 in all cell lines were quantified using Pearson's R value. All data represent three different biological replicates \pm SEM. Scale bar: 10 μ m.

3.2 Discussion

3.2.1 ESCRT subunits expressed in primary oral keratinocytes, immortalised oral keratinocyte and OSCC cell lines

The saliva of oral cancer patients contains up to 4-fold more EVs than healthy controls (Sharma *et al.*, 2011). Which is consistent with other studies showing that EV production is increased in cancer (Bebelmann *et al.*, 2018). Three early ESCRT complexes ESCRT-0, ESCRT-I, and ESCRT-II are able to cooperate to sort cargos into the early endosomes and MVB (Schmidt and Teis, 2012). We therefore hypothesised that the ESCRT machinery, which is intrinsically linked to EV biogenesis, is dysregulated in OSCC leading to increased EV production. In this *in vitro* study, we have determined the expression and protein abundance of selected ESCRT subunits (HGS, TSG101 and Vps22) in OSCC.

Previous studies found the ESCRT-0 protein HGS was up-regulated in many different types of tumour such as colon, stomach, liver, melanoma, and cervix (Toyoshima *et al.*, 2007). HGS has been implicated in intracellular trafficking and signal transduction in addition to selecting ubiquitinated proteins into MVBs (Zhang *et al.*, 2019, Raiborg *et al.*, 2001). Comparison of HGS abundance in an immortalised human normal oral keratinocyte cell line (FNB6), 3 OSCC cell lines (H357, SCC9, SCC4) and normal oral keratinocytes (NOKs) revealed differences in transcript and protein levels in the cell panel. Transcript expression data revealed that HGS was overexpressed in the SCC9 cell line, but not in the other cell lines tested. HGS has previously been shown to be overexpressed in pituitary adenomas and breast tumours (Rayala *et al.*, 2006, da Rocha *et al.*, 2006). Our next aim was to determine the protein abundance of HGS by western blot, which showed that all cell lines, except for SCC4, had

higher protein abundance compared with NOKs. This finding was consistent with previous studies showing that many different cancer cell lines, such as cervical and liver cancer, have higher HGS protein abundance (Mattissek and Teis, 2014). Overexpression and increased HGS protein abundance in colorectal cancer has been linked with a poor prognosis (Sun *et al.*, 2016). Our data also indicated that HGS protein abundance is independent of gene expression in OSCC, *in vitro*.

TSG101 was selected as the model ESCRT-I subunit. It is involved in early and late endosome formation in addition to ubiquitinated protein recognition and cargo trafficking (Tu *et al.*, 2011). Effective recruitment of ESCRT-I from cytoplasm to endosomes needs protein-to-protein interaction with the ESCRT-0 complex (Schmidt and Teis, 2012). We measured TSG101 transcript level and protein abundance, which revealed no clear pattern in expression levels. Transcript expression was significantly lower in the SCC9 cell line compared with NOKs, but there was no difference in the other cell lines examined. Western blotting showed that FNB6 and H357 produced more TSG101 protein than the other cells in the panel. Previous studies indicated contradictory roles of TSG101 in cancers. In breast cancer, papillary thyroid, and colorectal carcinomas, TSG101 was up-regulated (Oh *et al.*, 2007, Liu *et al.*, 2002, Ma *et al.*, 2008). In addition, the overexpression of TSG101 was also associated with poor prognosis in ovarian cancer (Young *et al.*, 2007a). Depletion of TSG101 had a negative impact on tumorigenesis including suppressed tumour growth and proliferation (Tu *et al.*, 2011). However, in some samples of lung cancer, TSG101 was down-regulated (Jiang *et al.*, 2013). Increased TSG101 protein abundance has been shown in thyroid, ovarian, and colon cancer cells or tissues (Liu *et al.*, 2002, Young *et al.*, 2007b, Ma *et al.*, 2008).

Vps22, a member of ESCRT-II, was overexpressed in FNB6, SCC9 and SCC4 compared to NOKs. At the protein level FNB6, H357 and SCC9 had higher abundance than NOKs. This was consistent with previous work from our laboratory which showed that Vps22 was overexpressed in OSCC cell lines (unpublished). Vps22 has been linked to the sorting of cargo for lysosomal degradation. Knockdown of Vps22 led to impaired degradation of EGFR and its ligand EGF (Malerød *et al.*, 2007, Bache *et al.*, 2006). Thus, taken together, we suspect that increased Vps22 protein in OSCC cell lines may limit EGFR signalling by causing its rapid degradation, but why this would be beneficial to tumour cells remains to be elucidated. On the other hand, loss of function of Vps22 can lead to neoplastic transformation like up-regulation of several signalling pathways including Notch, JAK/STAT and c-Jun N-terminal kinase (JNK) (Woodfield *et al.*, 2013).

The FNB6 cell line has proven useful as alternative to NOK to generate tissue-engineered oral mucosal equivalents (OME). FNB6 OME showed a similar global gene expression profile to NOK-based OME after stimulation with pro-inflammatory molecules (Jennings *et al.*, 2016). Throughout the current study, the data obtained from the FNB6 cell line was more similar to the OSCC cell lines than the primary NOKs. FNB6 cells share a similar pattern of ESCRT subunit transcript and protein expression with OSCC cell lines. In particular, FNB6 displayed a higher HGS protein abundance compared to NOKs. The FNB6 cell line was generated by human telomerase reverse transcriptase (hTERT) immortalisation of normal buccal mucosa (McGregor *et al.*, 2002). However, the process of immortalisation appears to have skewed the cellular phenotype (at least in the cellular machinery that we were characterising) towards that of the immortal cancer cell lines. According to our result, the protein abundance of HGS is

higher in the FNB6 than predicted. Hence, FNB6 may not be a suitable normal control for this type of study going forward.

3.2.2 Post-transcriptional regulation

As discussed above (Section 3.3.1), our data showed that HGS protein abundance is independent of gene expression in OSCC, *in vitro*. Thus, we hypothesised that HGS might be regulated post-transcriptionally. *In silico* analysis identified one microRNA, miR-142-3p, as a putative post-transcriptional regulator of HGS. Previous research found that this miRNA was overexpressed in *ex vivo* OSCC tissue samples (Manikandan *et al.*, 2016). Conversely, our hypothesis was that miR-142-3p would be down-regulated in OSCC cell lines, allowing de-repression of HGS. QPCR data showed a trend that the three cell lines with highest HGS protein abundance (FNB6, H357 and SCC9) had the lowest miR-142-3p expression. A further complexity in the post-transcriptional regulation of HGS is the long-noncoding RNA MALAT1 that can sequester miR-142-3p (Liu *et al.*, 2017) and has been reported to be up-regulated in OSCC (Chang and Hu, 2018). We hypothesised that MALAT1 was overexpressed in the cell lines, which would bind to miR-142-3p and then de-repress HGS. However, MALAT1 expression was significantly lower in all cell lines (including FNB6) compared to NOKs. The previous study that stated that MALAT1 was overexpressed in OSCC was also conducted *in vitro*. They used a normal human oral cell line, Hs680 as the baseline for expression data (Chang and Hu, 2018). However, this cell line does not appear to be widely used and is no longer available commercially.

We hypothesised that inhibition or up-regulation of miR-142-3p in OSCC cell lines would increase or decrease HGS protein abundance of HGS, respectively. The transfection

experiments were performed using H357 cells as a representative OSCC cell line, but no significant difference in HGS protein abundance was observed post-transfection. H357 cells have high cellular HGS protein abundance and low miR-142-3p expression, so was a good candidate for miR-142-3p overexpression studies. Data from these experiments was inconclusive and additional controls would be needed if further experiments were carried out. For example, determining the abundance of known miR-142-3p targets, such as Integrin Subunit Alpha V and Wiskott-Aldrich syndrome-like genes would be useful to confirm that transfection of the cells was successful (Schwickert *et al.*, 2015).

3.2.3 The interaction between ESCRT subunit HGS and early endosomes in OSCC

After revealing that ESCRT-0 subunits HGS protein abundance was increased in the majority of cell lines examined, we next sought to determine the subcellular location of HGS by immunofluorescence microscopy and laser confocal microscopy, and compare it to the location of EEA1, which localises exclusively to early endosomes (Komada and Soriano, 1999). Early endosomes are organelles that function by receiving and sorting macromolecules and solutes into recycling and degradation compartments of late and lysosomal endosomes through endocytosis (Kaur and Lakkaraju, 2018). Endocytosis is a complicated cellular process that regulates homeostasis and communication in cells through internalising plasma membrane receptors on the cell surface and their ligands (Jovic *et al.*, 2010). As a key role in the endocytosis pathway, early endosomes are significant in cancer progression by regulating several signalling pathways (Fraser *et al.*, 2019, Johnson *et al.*, 2014). EEA1 is an early endosome marker which contains a FYVE domain and is involved in the fusion of endocytic membranes (Gaulhier *et al.*, 2000). The PtdIns (3) P-binding FYVE domain of HGS is able to

combine with the specific domain present on EEA1 (Stenmark and Aasland, 1999). The binding of these domains facilitates HGS targeting to endosomes. Previous studies indicated co-localisation of HGS and endosomes (Raiborg *et al.*, 2001). Our data is consistent with that of previous findings, indicating that HGS co-localises with early endosomes in the cell lines used in this study. According to quantitative analysis, the Pearson's R value indicated the degree of co-localisation were varied in different biological repeats which may be due to the diverse cell cycle stages upon fixation. But the Pearson's coefficient of these cell lines is above 0.5 and confirms the strong but not precise co-localisation between HGS and EEA1, indicating HGS and EEA1 localise to early endosomes, potentially to different regions. The lack of complete co-localisation between HGS and EEA1 suggests they may be involved in diverse biochemical pathways. EEA1 was found to regulate membrane fusion. Whereas, HGS regulates endosomal trafficking including receptor sorting and vesicle budding, and this could be reflected by precise co-localised with clathrin, a protein that mediates endocytosis and can also be recruited to early endosomes by HGS (Stoorvogel *et al.*, 1996, Sorkina *et al.*, 1999, Raposo *et al.*, 2001). Most FYVE domain proteins have been confirmed to localise to early endosomes, but the relative distribution of those proteins has not been investigated in early endosomes. It is possible that the precise localisation of these proteins is not only driven by FYVE to PtdIns (3) P interactions (Raiborg *et al.*, 2001). This chapter provides further evidence to prove the interaction between HGS and EEA1 through identifying their co-localisation. However, the mechanisms that define different membrane microdomains of early endosomes are still not known, which needs to be elucidated by further research.

Chapter 4: HGS gene silencing strategies in OSCC

4.1 Introduction

As described in the previous chapter, the ESCRT-0 subunit HGS was found to be overexpressed at the protein level in three of the four immortal cell lines tested, including the OSCC cell lines H357 and SCC9. Previous studies have shown that ESCRT-0 subunits are involved in many activities relating to EV biogenesis such as recruiting other ESCRT subunits, MVB formation and cargo transportation (Katz *et al.*, 2002, Zhang *et al.*, 2017b). Thus, we attempted to deplete HGS transiently and stably by siRNA transfection and CRISPR-Cas9 genome editing, respectively, for downstream functional studies. The two silencing strategies were attempted in parallel because knockout of HGS resulted in serious defects in some *in vivo* studies. For example, it was lethal to mice and *drosophila* (Komada and Soriano, 1999, Lloyd *et al.*, 2002a). Thus, we did not know if HGS knockout would be lethal to the cells. In which case, transient silencing of HGS would be required.

SiRNA is a form of RNA-interference (RNAi). Double-stranded RNA (dsRNA) complementary to the target mRNA sequence is produced (Meister and Tuschl, 2004). After dsRNA enters into cells, it is recognised by dicer, a two-subunit RNase III-family enzyme located in the cytoplasm (Bernstein *et al.*, 2001). Dicer is able to cleave dsRNA into siRNA fragments that are usually 21-23 nucleotide-long. In the current study, synthetic siRNA was used to achieve gene silencing due to the high yield and purity of the molecules. Synthetic siRNA can also be chemically modified to improve the stability of siRNA, reduce the potential off-target effects or prevent the activation of natural immune response (Fedorov *et al.*, 2006). Entry of the siRNA requires overcoming the plasma membrane hurdle. Thus, we used

oligofectamine Transfection Reagent to facilitate synthetic siRNA entry into the cells. Once in the cytoplasm, the siRNA molecules are able to recruit proteins to trigger the RNA induced silencing complex (RISC) cellular machinery. RISC then splits the double-strand siRNA into a sense and anti-sense strand by action of the endonuclease Argonaute 2 (Liu *et al.*, 2004). The anti-sense strand guides RISC to find complementary sequence of target mRNA then cleaves the endogenous mRNA strand (Martinez *et al.*, 2002). The cleaved mRNA is then rapidly degraded in the cells, thereby achieving post-transcriptional gene silencing. SiRNA transfection provides a quick and convenient way to achieve gene silencing, but it is short-term because the siRNA is diluted over time by cell division (Kim, 2010).

Long-term gene silencing can be achieved by CRISPR-Cas9 genome editing. CRISPR-Cas is a natural prokaryotic adaptive immune system from many bacteria and archaea (Bhaya *et al.*, 2011). This system recognises and integrates invading nucleic acids such as virions and plasmids into CRISPR (Terns and Terns, 2011). CRISPR-Cas system can be classified into six types (I-VI), of which the most commonly used is type II CRISPR-Cas system that only exists in bacteria and the main feature is the mono subunit Cas9 protein (Terns and Terns, 2011, Wiedenheft *et al.*, 2012). The CRISPR-Cas9 system has been harnessed to allow genome editing in eukaryotic cells by co-expressing the *Streptococcus pyogenes* and *Staphylococcus aureus* Cas9 (*S.p.* Cas9) nuclease along with a guide RNA (gRNA) (Hendriks *et al.*, 2020). *S.p.* Cas9 can be either targeted with a double-strand gRNA which is composed of a specifically designed mature crRNA and tracrRNA or a single strand gRNA (sgRNA), which is a synthetically fused pre-crRNA and tracrRNA (Hsu *et al.*, 2014). The later complex showed higher efficiency in practice, after transfecting these components into eukaryotic cells. The

gRNA can recognise the complementary sequence with a protospacer adjacent motif (PAM) (NGG or NAG) followed by specifically cutting the target DNA and causing DNA double-strand breaks (DSB). There are two pathways to repair DSB which are the non-homologous end joining (NHEJ) and the homologous directed repair (HDR) pathways (Burma *et al.*, 2006, Dudás and Chovanec, 2004). NHEJ connects the broken DNA ends directly and is prone to generate insertion or deletion mutations, leading to mRNA degradation or the production of non-functional proteins. However, this pathway is not precisely controlled (Song *et al.*, 2021). HDR pathway allows more precise repair by integrating, deleting, or editing DNA sequences at the target site according to a template donor DNA sequence (Liu *et al.*, 2018).

This chapter firstly explored the optimal concentration of siRNA required for transient HGS gene silencing by transfecting H357 cells with increasing concentrations of siRNA. Gene silencing at 24 and 48 hours post-transfection was determined at mRNA and protein level by qPCR and western blotting, respectively. In parallel, CRISPR-Cas9 genome editing was utilised to permanently silence HGS expression in H357 cells. Screening and selection of gene edited clones was achieved by T7EI mismatch assay and western blotting.

4.2 Results

4.2.1 HGS silencing by siRNA transfection

Transient siRNA transfection experiments were carried out in the OSCC cell line H357 due to its high HGS protein abundance (section 3.2.1). To determine the optimum concentration of siRNA to silence HGS expression, sub-confluent monolayers (30%-50%) were incubated with oligofectamine-siRNA complexes. The final concentration of siRNA ranged from 0-50 nM. Cells were also transfected with an equivalent amount of negative control siRNA (that is

not predicted to target any transcript) to check for off-target effects that result from introducing synthetic RNAs.

4.2.1.1 HGS silencing 24 hours post siRNA transfection

Transcript expression 24 hours post-transfection was assessed by qPCR, and reported relative to mock transfected control (i.e. no siRNA added), which showed an inverse relationship between increasing HGS siRNA concentration and transcript expression. HGS mRNA expression was down-regulated 4.1-fold with 10 nM siRNA ($p<0.001$); 4.6-fold with 20 nM siRNA ($p<0.001$); 5.6-fold with 30 nM siRNA ($p<0.001$); 7.1-fold with 40 nM siRNA ($p<0.001$); and 8.2-fold with 50 nM siRNA ($p<0.001$) (Figure 4.1 A). Compared to mock transfected control, transfection of H357 cells with 40 nM negative control siRNA resulted in 2-fold ($p<0.05$) increase in HGS transcript expression, while no significant difference was observed when cells were transfected with the other concentrations (Figure 4.1 B). Gene expression data was validated at protein level by western blotting (Figure 4.1 C). Compared with mock transfected control, the protein abundance of HGS was decreased 4.2-fold with 10 nM siRNA ($p<0.01$); 8.0-fold with 20 nM siRNA ($p<0.001$); 12.8-fold with 30 nM siRNA ($p<0.01$); 9.0-fold with 40 nM siRNA ($p<0.01$); and 46-fold with 50 nM siRNA ($p<0.01$) (Figure 4.1 D). There was no significant difference in HGS protein abundance comparing mock transfected cells and those transfected with increasing concentrations of negative control siRNA (Figure 4.1 E).

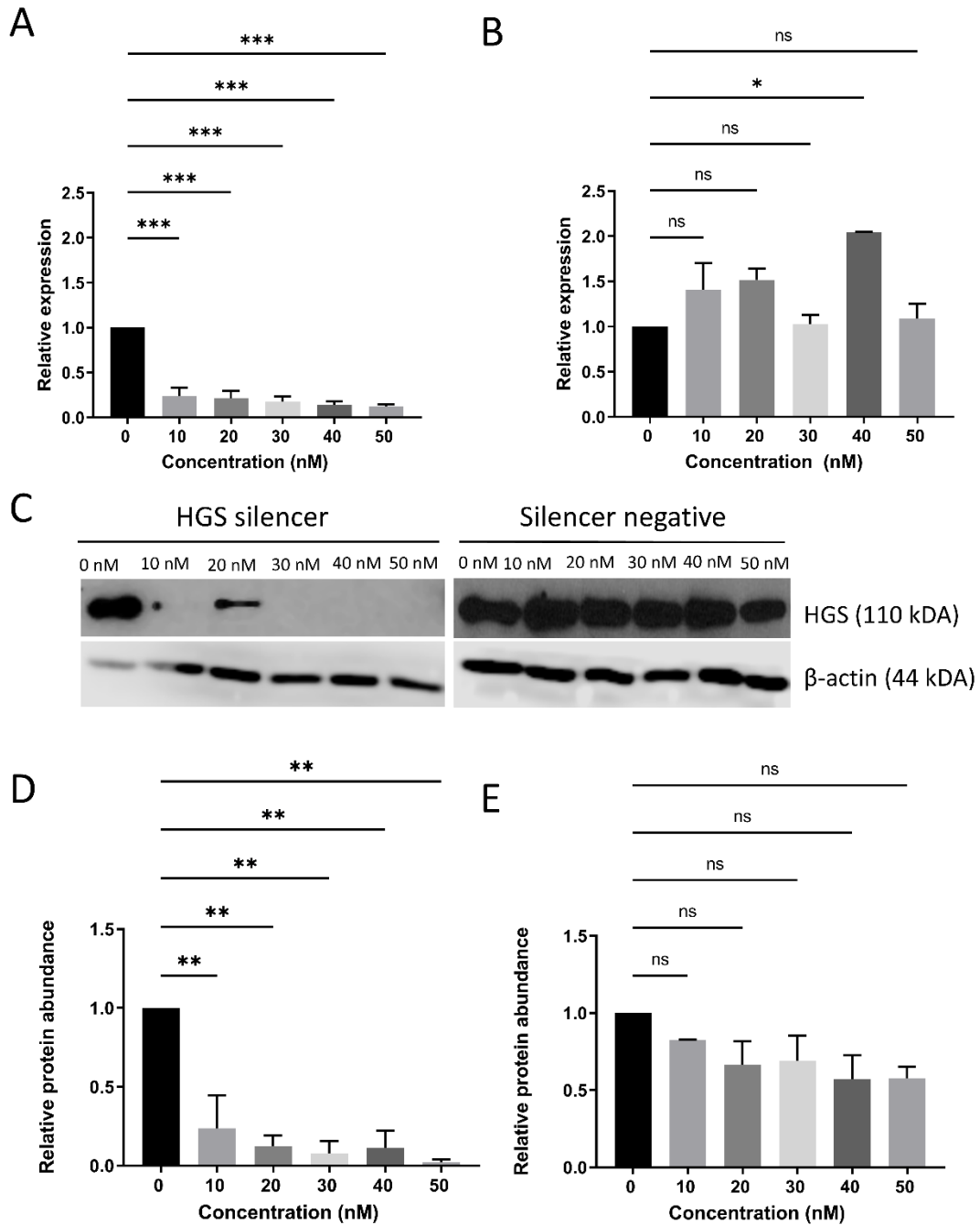


Figure 4.1: Optimisation of 24 hour HGS siRNA silencing. SiRNA transfection experiment was optimized by transfecting H357 cells with increasing concentrations (0-50 nM) of HGS silencer and negative silencer. (A) Transcript expression of HGS relative to GAPDH in HGS silencer transfected cells was determined by qPCR. (B) Transcript expression of HGS relative to GAPDH in silencer negative transfected cells was determined by qPCR. (C) Representative western blot of HGS and loading control β -actin abundance in cells transfected with HGS silencer and silencer negative siRNA. (D) Densitometry analysis of HGS protein abundance relative to β -actin abundance in cells were transfected with HGS silencer. (E) Densitometry analysis of HGS protein abundance relative to β -actin abundance in cells transfected with silencer negative. All data were calculated as mean of two biological replicates \pm SEM. * = $p < 0.05$, ** = $p < 0.01$, *** = $p < 0.001$, ns = not significant by Dunnett test.

4.2.1.2 HGS silencing 48 hours post siRNA transfection

Transcript expression 48 hours post-transfection was determined by qPCR and reported relative to mock transfected control. HGS mRNA expression was down-regulated 5.5-fold with 10 nM siRNA ($p < 0.0001$); 7.4-fold with 20 nM siRNA ($p < 0.0001$); 11.5-fold with 30 nM siRNA ($p < 0.0001$); 12.5-fold with 40 nM siRNA ($p < 0.0001$); and 13.5-fold with 50 nM siRNA ($p < 0.0001$) (Figure 4.2 A). While there was no significant difference between mock transfected cells and those transfected with increasing concentrations of negative control siRNA (Figure 4.2 B). The successful knockdown of HGS gene expression was then confirmed at protein level by western blotting (Figure 4.2 C). Compared with mock transfected cells, HGS protein abundance was decreased 3.4-fold with 10 nM siRNA ($p < 0.01$); 4.6-fold with 20 nM siRNA ($p < 0.001$); 7.8-fold with 30 nM siRNA ($p < 0.01$); 23.4-fold with 40 nM siRNA ($p < 0.01$); and 62.4-fold with 50 nM siRNA ($p < 0.01$) (Figure 4.2 D). There was no significant difference in HGS protein abundance between mock transfected cells and those transfected with increasing concentrations of negative control siRNA (Figure 4.2 E).

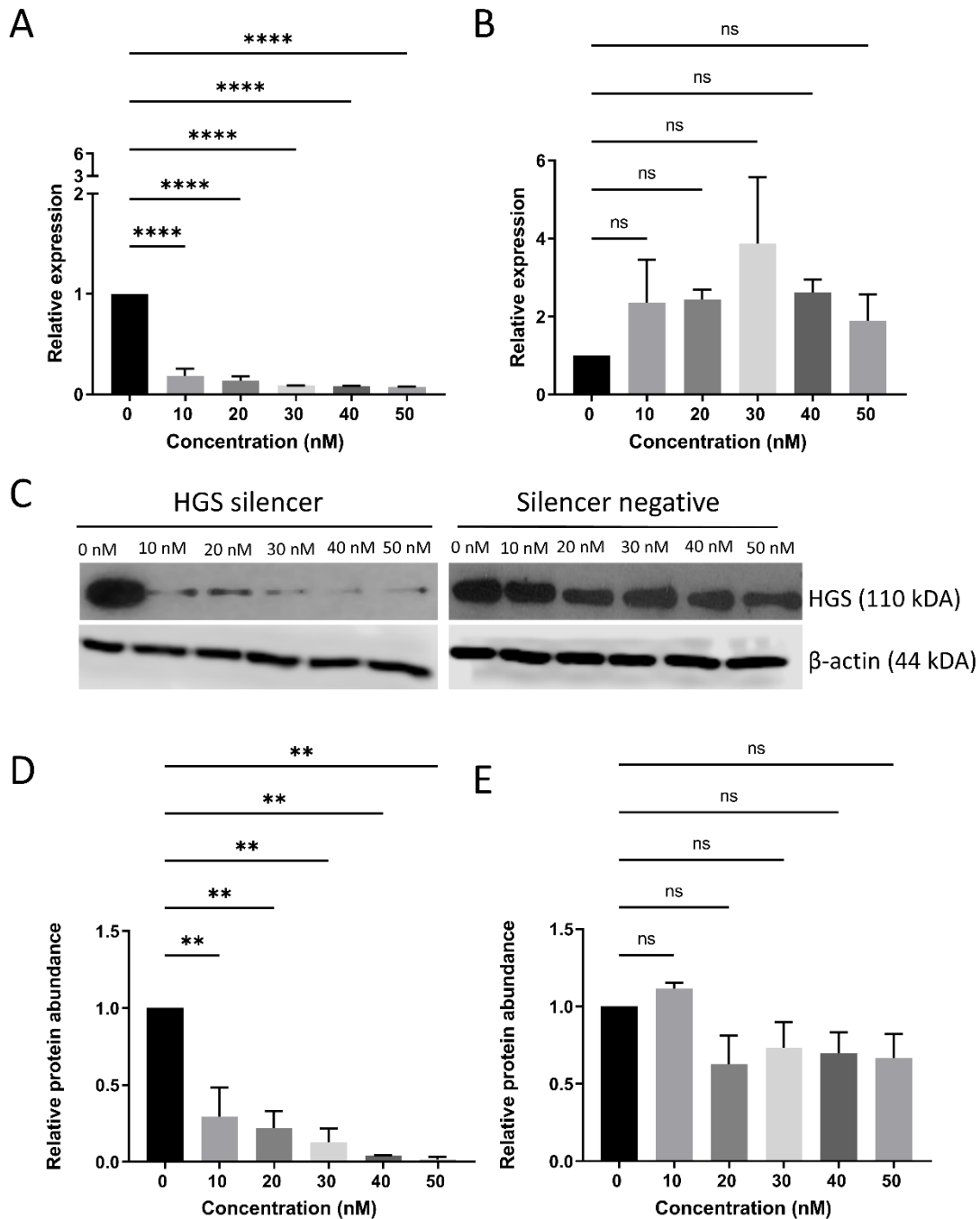


Figure 4.2: Optimisation of 48 hour HGS siRNA silencing. SiRNA transfection experiment was optimized by transfecting H357 cells with increasing concentrations (0-50 nM) of HGS silencer and negative silencer. (A) Transcript expression of HGS relative to GAPDH in HGS silencer transfected cells was determined by qPCR. (B) Transcript expression of HGS relative to GAPDH in silencer negative transfected cells was determined by qPCR. (C) Representative western blot of HGS and loading control β -actin abundance in cells were transfected with HGS silencer and silencer negative. (D) Densitometry analysis of HGS protein abundance relative to β -actin abundance in cells were transfected with HGS silencer. (E) Densitometry analysis of HGS protein abundance relative to β -actin abundance in cells were transfected with silencer negative. All data were calculated as mean of two biological replicates \pm SEM. * = $p < 0.05$, ** = $p < 0.01$, *** = $p < 0.001$, **** = $p < 0.0001$, ns = not significant by Dunnett test.

4.2.2 HGS silencing by CRISPR-Cas9 genome editing

According to the data shown above, the expression of HGS could be transiently silenced by siRNA transfection. However, siRNA transfection can only provide a short-term effect. In parallel, CRISPR-Cas9 genome editing was used to permanently silence HGS expression in the H357 cell line. Previous experiments in our lab showed that H357 was susceptible to transfection-mediated CRISPR-Cas9 genome editing and could tolerate plating at single cell density for clonal selection.

Genome editing was performed using the Alt-R CRISPR-Cas9 kit in conjunction with a standard tracrRNA and predesigned crRNA, which were combined to form a gRNA to target HGS (workflow summarised in Figure 2.2). The gRNA was incubated with purified Cas9 protein to form the RNP complex, before being delivered into cells using Lipofectamine CRISPRMAX reagent. Several experimental controls were included to ensure on-target editing and to allow troubleshooting should problems arise. Cells were transfected with Cas9 enzyme in the absence of HGS gRNA. In addition, a crRNA was provided in the kit to produce a gRNA to target HPRT, which served as a positive control (HPRT⁺). Omission of the HPRT gRNA served as an additional negative control (HPRT⁻). After 48 hours post-transfection, cells were trypsinised and split into two halves. Half were subject to T7 T7EI mutation detection and the other half (of those transfected with HGS gRNA) were plated to produce single cell colonies. PCR primers were designed to amplify 986 bp of the HGS genomic region containing the PAM site, which was the target for Cas9 enzyme cleavage. The PCR primers were designed so that the PAM site was off centre within the amplicon.

4.2.2.1 Determining the specificity of PCR primers

We designed 4 different primers, to determine the target-specificity of the primers that would be used in the T7EI assay, a test PCR reaction was firstly performed using genomic DNA extracted from H357 WT cells. The PCR reaction yielded a single amplicon of the expected size (986 bp) confirming the specificity of the primers (Figure 4.3 A).

4.2.2.2 Determining successful genome editing by T7EI DNA mismatch assay

To confirm that genome editing events had occurred, the target HGS and control HPRT genomic regions of transfected cells were amplified by PCR, prior to digestion with T7EI and analysis by agarose gel electrophoresis. The template DNA used in PCR reactions was polyclonal and so will contain mutated and unmutated DNA. Therefore, the double-stranded amplicons will be either be homoduplex (e.g. both strands unedited WT sequence) or heteroduplex (e.g. one strand edited and one strand unedited WT sequence). The T7EI enzyme recognises heteroduplex DNA and cleaves at the site of the DNA mismatch, yielding two smaller DNA products (Figure 4.3 B). This is exemplified in the T7EI controls, where homoduplex DNA has a single band at 692 bp, due to no T7EI cleavage (Figure 4.3 B, lane 5). Whereas in the heteroduplex control, a proportion of the full-length amplicon (692 bp) was cleaved into two smaller products (436 bp and 256 bp), indicating successful T7EI action (Figure 4.3 B, lane 6). In addition, T7EI cleavage was also observed in HPRT⁺ control cells with cleaved fragments at 256 bp and 827 bp, indicating successful genome editing (Figure 4.3 B, lane 3). In the absence of gRNA, only one amplicon of 1083 bp can be observed in the HPRT⁻ control (Figure 4.3 B, lane 4). There was successful genome editing of HGS, as seen by the full-length HGS amplicon (986 bp) being cleaved bands to produce two smaller products

of 695 bp and 291 bp (Figure 4.3 B, lane 1). The genome editing was specifically mediated by the gRNA as for the negative control (in the absence of gRNA) only the full-length amplicon of 986 bp was present, indicating that no genome editing of HGS had occurred (Figure 4.3 B, lane 2).

4.2.2.3 Selection and validation of HGS silenced clones

As described above, half of the transfected cells were subject to T7EI mismatch assay, and the other half were plated in 96-well plates at concentration of 1 cell/well to produce single cell colonies. Colonies were frequently monitored and moved from 96-well plates to 48-well plates, 24-well plates, 12-well plates, 6-well plates and finally to larger culture vessels as they became confluent before finally reaching 75 cm² flasks. Seventeen clones were generated for validation of HGS silencing by western blotting and six were taken forward for further passaging and screening after measuring protein abundance of HGS for several times. Three of the six clones showed successful HGS silencing (Figure 4.3 C) and one was chosen (HGS KO No.2, lane 2, Figure 4.3 C), which will be referred to as H357 Δ HGS, for further experiments (Figure 4.4 A). To confirm stable HGS silencing and exclude any multi cell colonies, H357 Δ HGS was passaged several times at different passage numbers. HGS protein abundance was measured again, which confirmed functional knockout with no detectable HGS protein compared to H357 WT ($p < 0.05$) (Figure 4.4 B/C).

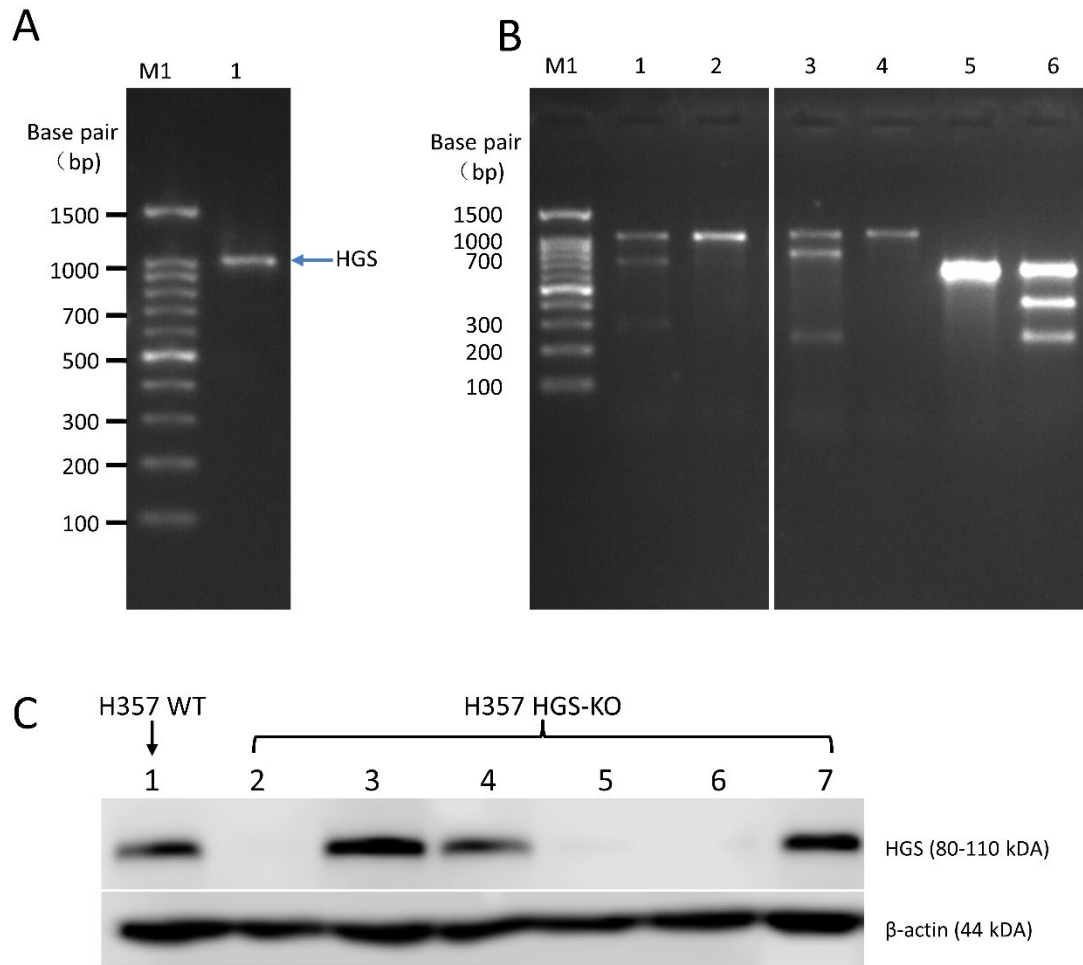


Figure 4.3: Validation of HGS silencing by CRISPR-Cas9 genome editing in H357. (A) Lane M1: DNA ladder range from 100-1500 bp. Lane 1: HGS PCR product from H357 WT genomic DNA, separated by 2% (w/v) agarose gel electrophoresis, showing a single 986 bp amplicon. (B) CRISPR-Cas9 genome editing was confirmed by T7EI mismatch assay. Digested products were separated by 2% agarose gel electrophoresis in Lane M1: DNA ladder range from 100-1500 bp. Lane 1: genomic DNA from transfected H357 cells with ribonucleoprotein (RNP) complexes which consist of HGS gRNA and Cas9 enzyme. Lane 2: Negative control with only Cas 9 enzyme. Lane 3: Control of HPRT positive (HPRT+) gRNA. Lane 4: Control of HPRT negative (HPRT-) gRNA. Lane 5: Homoduplex DNA control. Lane 6: Heteroduplex DNA control. (C) Validation of HGS knockout by western blotting with loading control β -actin, n=4.

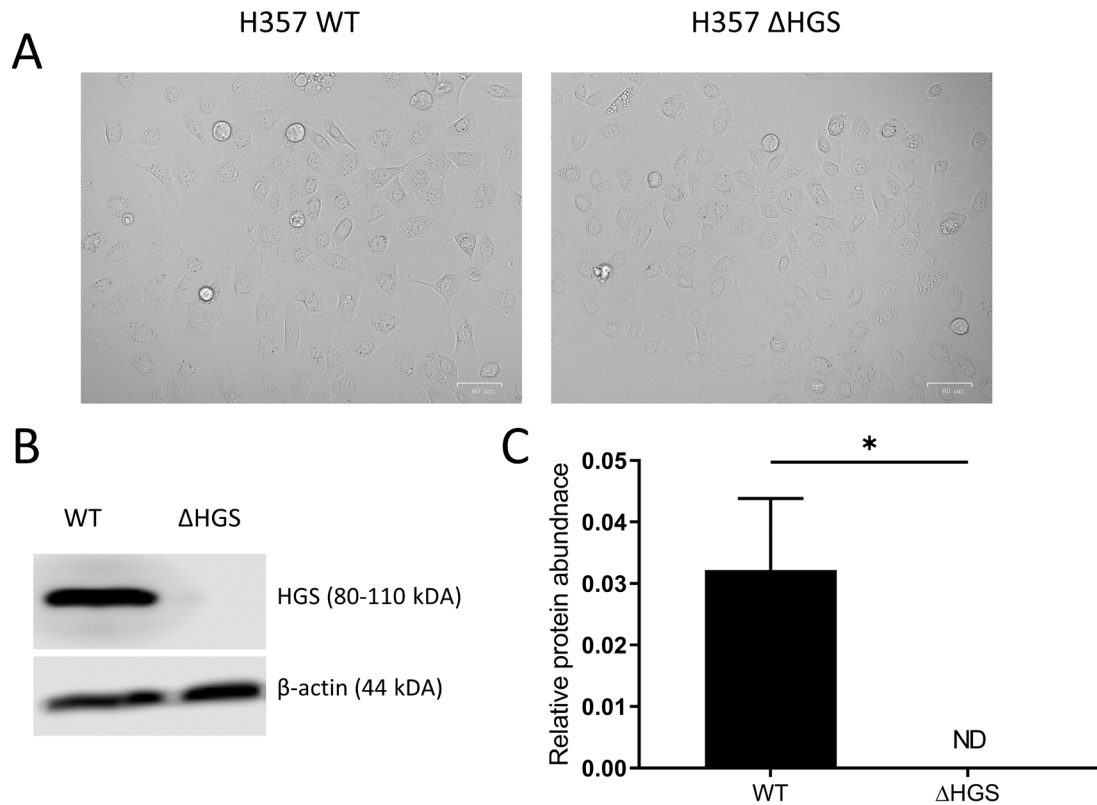


Figure 4.4: HGS is stably silenced in H357 ΔHGS. (A) Representative images of H357 WT and ΔHGS cell line when ~80% confluent. Scale bar: 60 μm. (B) Representative western blot of HGS and loading control β-actin abundance in H357 WT and ΔHGS cell line. (C) Densitometry analysis of HGS protein abundance relative to β-actin abundance. Data represents mean of three different biological replicates ± SEM. * = $p < 0.05$

4.3 Discussion

4.3.1 Transient HGS silencing using siRNA transfection

The aim of this chapter was to optimise methodology to silence HGS expression to allow further functional studies. SiRNA transfection experiments confirmed the successful knockdown of HGS expression, leading to a significant decrease in HGS protein abundance in H357 with as little as 10 nM siRNA, which is similar to an earlier study (Canal *et al.*, 2015). However, 50 nM HGS siRNA gave the largest knockdown in HGS transcript and protein at both timepoints and was chosen as the concentration to use in further experiments (Supplementary materials, Figure S1 A/B). Under some circumstances, siRNA transfection may

cause non-specific interference especially when the concentration of siRNA is high (Caffrey *et al.*, 2011). The use of a negative control siRNA can provide a baseline to compare with targeting siRNA treated samples to define the impacts of siRNA oligo delivery (Zagalak *et al.*, 2015). In the current study, transfecting cells with 50 nM negative control siRNA caused no significant difference in HGS expression compared to mock transfected control (Supplementary materials, Figure S1 A/B). SiRNA transfection provides a convenient and quick way to achieve functional knockdown in cells. However, it still has specific and nonspecific off-target effects (Vickers *et al.*, 2009). The former may be caused by the sequence of sense or anti-sense siRNA strands complementary to non-target mRNA. Previous studies reported that at least 7 nucleotides complementation can cause off-target inhibition, which is related to the sequence composition of the adjacent complementary region, the position of the sequence in the mRNA, and the copy number of the sequence in the mRNA (Sudbery *et al.*, 2010, Lin *et al.*, 2005). A common way to confirm that gene silencing is caused by true RNAi rather than off-targets effects is the use of two independent siRNA targeting the same gene (Echeverri *et al.*, 2006). Each siRNA may have unique off-target effects, but the same phenotype should be observed when for designed for the same target. Off-target effects can be reduced when cells are treated with the lowest functional dose of siRNA (Caffrey *et al.*, 2011). SiRNA represents a quick and easy way to knockdown HGS in OSCC cells, but the gene silencing effect is short term, as demonstrated by the detection of HGS protein 48 hours post-transfection. To achieve permanent HGS silencing, CRISPR-Cas9 genome editing was applied to create a HGS deficient OSCC cell line.

4.3.2 Generation of a HGS deficient OSCC cell line

The application of targeted nucleases has endowed researchers with the ability to

manipulate genome sequences to create isogenic cell lines *in vitro* and *in vivo* animal models for scientific research. CRISPR-Cas9 together with transcription activator-like effector nucleases (TALENs), and zinc-finger nucleases (ZFNs) are three foundational genome editing technologies (Gaj *et al.*, 2016). CRISPR-Cas9 genome editing system is a technology developed based on the immune mechanism of archaea against foreign nucleic acid invasion (Bhaya *et al.*, 2011). Compared with TALENSs and ZFNs, CRISPR-Cas9 genome editing has advantages such as its ease of use and less cytotoxicity. Constructing a CRISPR sgRNA allows easy targeting of a DNA sequence and cleavage by Cas9 protein (Wu *et al.*, 2014). Moreover, CRISPR-Cas9 enables simultaneous multi-site genome editing with low cost (Triozi *et al.*, 2021). In this study, we chose Alt-R CRISPR-Cas9 system from Integrated DNA Technologies to achieve HGS silencing. Compared with conventional Cas9 nuclease, this system used structure-guided protein engineering to improve the Cas9 targeting specificity and less off-target effects (Slaymaker *et al.*, 2016). In addition, *in vitro* assembled RNA duplex showed a more stable and quicker way to transfect RNP into cells than plasmid-based expression systems. At present, CRISPR-Cas9 genome editing technology has been applied in many aspects of tumour research, including functional research of tumour related genes, construction of animal tumour models, screening of tumour cell phenotypes after editing, and gene therapy of cancer (Austin *et al.*, 2004, Hsu *et al.*, 2014, Chen *et al.*, 2014, Zhang *et al.*, 2021). However some problems with this technology have also been exposed, and the most prominent one is the off-target effect (Liu and Fan, 2014). Since the fragments of gRNA in CRISPR-Cas9 system only needs 20 nucleotides to match with the target, it is highly likely that this gRNA will also bind with other sites outside of the intended target. Off-target effects interferes with the stability of

other genes in the cell, leading to unexpected phenotypes which challenge research and clinical application (Lin *et al.*, 2019). These effects were reduced through improving Cas9 specificity, controlling the concentration of Cas9-sgRNA compound, modifying Cas9 enzyme, and choosing the correct delivery carrier. Firstly, it was found the efficiency of genome editing is proportional to the GC content of gRNA seed region, which is a short sequence located upstream of PAM site (Ren *et al.*, 2014). In addition, the off-target effect was decreased when there were more than three base mismatches between seed region sequence and off-target site. Hence, designed gRNA sequence with 60% GCs is able to decrease the off-target effects (Ren *et al.*, 2014). Fu *et al.* (2014) and Singh *et al.* (2018) indicated that, using truncated gRNA was able to reduce off-target effect which was induced by paired nickases, but Kleinstiver *et al.* (2016) stated this approach is only partially effective and has potential to create new off-target sites. Furthermore, modified of crRNA chemically by 2'-fluoro (2'-F) and 2'-O-methyl 3'-phosphorothioate has potential to increase specificity of CRISPR-Cas9 system (Rahdar *et al.*, 2015, Hendel *et al.*, 2015). Secondly, it was found the sustained Cas9 expression in cells will increase the risk of off-target effects (Hsu *et al.*, 2013). Thirdly, transforming WT Cas9 by inactivating one restriction site of Cas9 to generate mutated Cas9^{D10A} and Cas9^{H840A} can reduce off-target effect with increased editing efficiency in cell lines (Shen *et al.*, 2014). Fourthly, it was reported that choosing appropriate delivery vectors including RNPs, cationic liposomes and gold nanoparticles are able to improve the Cas9 specificity (Brunetti *et al.*, 2018, Zuris *et al.*, 2015, Lee *et al.*, 2017). Wherein, the RNP delivery system avoid inserting foreign DNA sequences to target genome which was applied in this study.

Whilst the H357 cells used in this study tolerated and survived HGS depletion, the effects

of *in vivo* HGS knockout are inconsistent when comparing different knockout mouse models (Hall *et al.*, 2009). Transgenic flox mice with HGS knockout in brain endothelial cells (ECs) displayed distorted polarity of ECs and brain vessel collapse which finally leads to death at birth (Yu *et al.*, 2020). Moreover, mutated mice with HGS knockout in smooth muscle cells showed no abnormalities within 1-month after birth compared with the control mice. However, they exhibited oesophagus dilation and weight loss, which resulted in death within 5 months after birth (Chen *et al.*, 2015). On the other hand, mice with HGS knockout in cardiomyocyte did not show premature death compared to the control mice. They were able to reproduce but showed enhanced cardiac fibrosis and diastolic dysfunction which finally leads to cardiomyopathy (Li *et al.*, 2022). Constructing a mouse model by CRISPR-Cas9 mediated HGS knockout still needs further research (Platt *et al.*, 2014).

Overall, this study has demonstrated the successful creation of HGS deficient cell line *in vitro*, by siRNA transfection and CRISPR-Cas9 genome editing, which will allow exploration of its role in oral cancer tumourigenesis.

Chapter 5: Functional consequences of HGS knockout in OSCC cells

3.1 Introduction

According to multiple *in vivo* experiments, mutation of ESCRT-machinery leads to cell apoptosis. ESCRT deficient mice and *drosophila* showed serious developmental defects which resulted in early embryonic and pupal lethality, respectively (Lloyd *et al.*, 2002b, Rink *et al.*, 2005). Investigation of HGS deficient mice embryos revealed enlarged early endosomes in many mutant tissues, suggesting HGS has an important role to maintain normal cellular homeostasis (Rink *et al.*, 2005, Komada and Soriano, 1999). In dendritic cells, silencing HGS led to reduced exosome release and reduced abundance of downstream ESCRT proteins TSG101 and Vps4 B, which proved a key role of ESCRT-0 in exosome biogenesis (Tamai *et al.*, 2010). The role of ESCRT in tumourigenesis could be attributed to exosome production which improves intercellular communication (Théry, 2011).

Deficiency of ESCRT machinery alters epithelial cell polarity and results in EMT which facilitates tumour metastasis (Dukes *et al.*, 2011, Gotzmann *et al.*, 2004). This impact could also be due to modifying the abundance of transmembrane proteins including growth factor receptors, integrins and cell adhesion molecules (Tu *et al.*, 2010, Lobert *et al.*, 2010). As the clients of ESCRT machinery, these cargos are recruited by ESCRT and degraded via the endosomal-lysosomal pathway (Babst, 2005). EGFR has been frequently studied to investigate the influence of ESCRT malfunction on degradation of transmembrane proteins. EGFR is a receptor tyrosine kinase, which has a role in various types of cancers through conducting extracellular growth signals to regulate multiple cellular responses such as promoting

proliferation, differentiation, migration, and inhibiting apoptosis (Du and Lovly, 2018). In healthy cells, the expression of EGFR and its downstream signalling are tightly controlled. One of the key mechanisms to initiate EGFR signalling termination is the endocytosis, intraluminal sorting, and lysosomal degradation of EGFR (Tomas *et al.*, 2014, Vieira *et al.*, 1996). EGFR signalling is activated by 'ligand-induced dimerisation model' (Purba *et al.*, 2017). EGF ligands combined to receptors' binding domain, induce receptor dimerisation, subsequently with auto-phosphorylation to activate downstream signalling cascades. Activated EGFR complexes are internalised immediately by clathrin-dependent mechanism followed by targeting to early endosomes (Tomas *et al.*, 2014). Some EGFR complexes are transported back to the plasma membrane mediated by recycling endosomes (Tomas *et al.*, 2014). The remaining EGFR molecules are sorted to MVBs, which fuse with lysosomes, consequently leading to signal termination by EGFR degradation. ESCRT dysfunction has an impact on downstream signalling of EGFR, but which parts of the MVB pathway can block degradation is still unclear. Previous studies reported that ESCRT-I, -II and -III are all involved in mediating multivesicular endosome biogenesis and endosomal sorting of ubiquitinated proteins, but have differential roles at distinct stages of the endocytic pathway (Raiborg *et al.*, 2008). Overexpression of ESCRT-0 subunit HGS hyper-activates EGFR downstream signal transducer and activator of transcription 3 (STAT3), which is a hallmark of HNSCC (Rehmani and Issaeva, 2020, Scoles *et al.*, 2005). Knockdown of ESCRT-0 (HGS), ESCRT-I (TSG101), ESCRT-II (Vps22) and ESCRT-III (CHMP3) impaired EGFR degradation, however only ESCRT-0 and ESCRT-I depletion resulted in sustained activation of EGFR and downstream MAPK pathway due to enhanced recycling of endocytosed EGFR, which was not observed upon ESCRT-II and

ESCRT-III depletion (Coudert *et al.*, 2021, Raiborg *et al.*, 2008, Bache *et al.*, 2006).

In the current study, we used CRISPR-Cas9 genome editing to establish a functional knockout of HGS in an OSCC cell line, H357. This new cell line was used to evaluate the role of HGS in OSCC MVB biogenesis, EV release and EGFR trafficking. We firstly explored the cellular phenotypical and morphological changes of H357 cells after HGS knockout. Growth assay, trypan blue exclusion assay and flow cytometry were utilised to measure proliferation and cell viability. Immunofluorescence microscopy was used to evaluate endosomal markers (EEA1 and RAB7) in WT and Δ HGS cells. TEM was used to view the morphological changes of endosomal structures after HGS depletion. NTA and western blotting were used to evaluate the effect of HGS depletion on EV release and protein cargo, respectively. Finally, we used EGF pulse-chase experiments to determine the consequence of HGS depletion on EGFR processing.

3.2 Results

3.2.1 Cellular phenotypical changes after HGS knockout

The previous chapter showed the successful generation of the H357 Δ HGS cell line, which was utilised in the following experiments to determine the effect of HGS depletion on H357 cell phenotype.

3.2.1.1 Assessing growth rate, doubling time and viability of H357 cells after HGS knockout

We firstly assessed the cell growth rate, doubling time and cellular viability (Figure 5.1). H357 Δ HGS cells exhibited a 1.6-fold slower growth rate compared to WT cells at the 72-hour timepoint ($p < 0.01$) (Figure 5.1 A) and 1.7-fold slower growth rate compared to WT cells at the

96-hour timepoint ($p < 0.0001$) (Figure 5.1 A). The time taken for H357 Δ HGS to double in cell number was 26.6 hours compared to 21.9 hours for WT cells, which represents a 1.2-fold increase in doubling time ($P < 0.05$) (Figure 5.1 B). Cell viability was measured at the final timepoint by trypan blue exclusion assay. H357 Δ HGS cells exhibited a 10.1% decreased viability compared to WT cells ($P < 0.01$) (Figure 5.1 C).

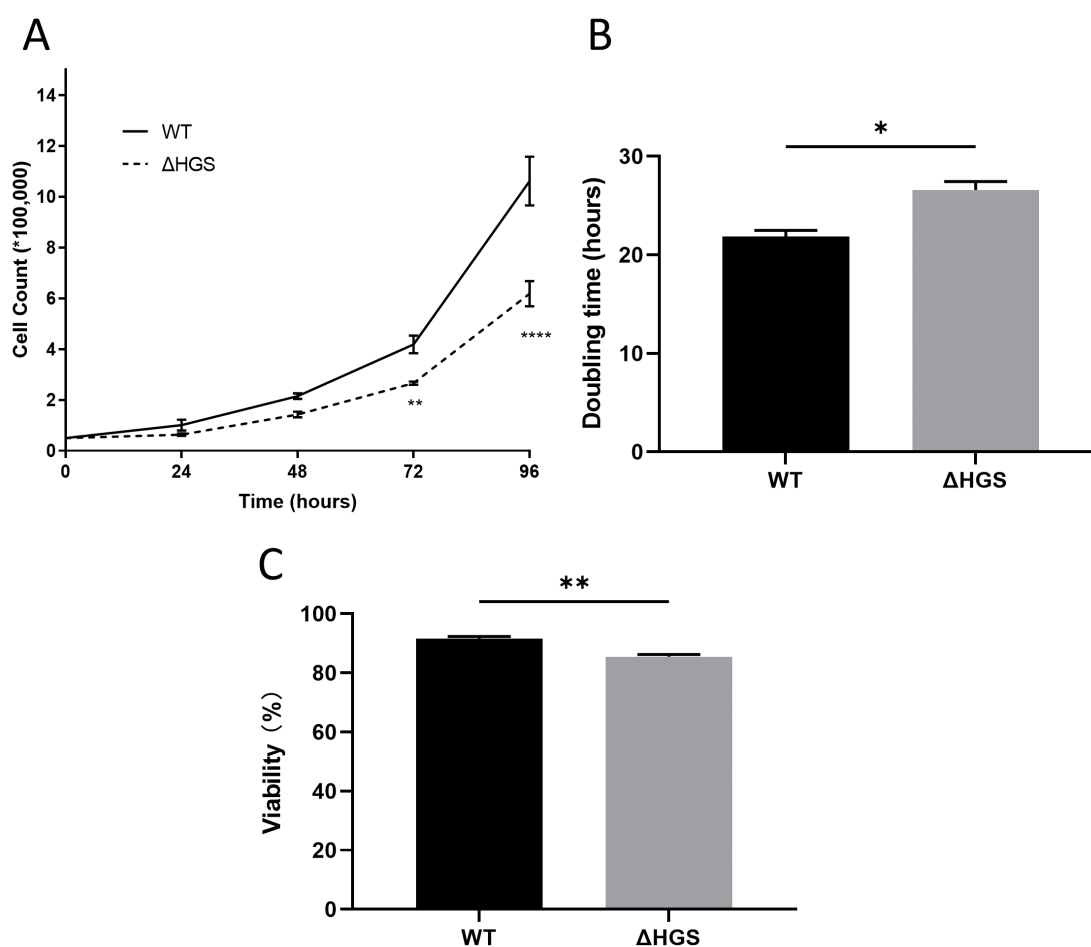


Figure 5.1: Growth rate, doubling time and viability in HGS knockout OSCC cells. 50,000 WT and Δ HGS were seeded in 6-well plates. (A) Individual wells were trypsinised and cells counted at each timepoint to generate a growth curve. (B) At the 96-hour timepoint cell numbers were used to calculate the doubling time and (C) viability by Trypan blue exclusion assay. All data were calculated as mean of three biological replicates \pm SEM. * = $p < 0.05$, ** = $p < 0.01$, **** = $p < 0.0001$ by Student's t-test.

3.2.1.2 Assessing the apoptosis level in WT and Δ HGS cells

The trypan blue exclusion assay indicated a reduction in H357 Δ HGS viability. Therefore,

we next sought to assess cell viability and apoptosis by a more sophisticated method. Flow cytometry with Annexin V-FITC and PI double staining was used to measure the percentage of live, apoptotic, and dead cells in WT (Figure 5.2 A) and Δ HGS (Figure 5.2 B) cells. Phosphatidyl serine (PS) exposure on the outer membrane is one of the hallmarks used to identify cellular apoptosis. In healthy cells, PS is restricted to the inner leaflet of the plasma membrane by the amino-phospholipid translocase (Rieger *et al.*, 2011). When apoptosis occurs, the asymmetry of phospholipid distribution on the cell membrane is destroyed through loss of the enzyme's activity, which results in PS being exposed outside the cell membrane. Annexin V is a Ca^{2+} dependent phospholipid binding protein that can bind to PS with high affinity. Annexin V can be conjugated with fluorescent tag FITC, which is often used with PI, a DNA-binding dye. In late apoptotic and dead cells, PI can penetrate their porous plasma membrane to stain the nuclear material red. The combination of using Annexin V-FITC and PI allowed us to distinguish the subpopulations of the live (Annexin V⁻/PI⁻), early apoptotic (Annexin V⁺/PI⁻), late stage apoptotic/dead (Annexin V⁺/PI⁺), and necrotic (Annexin V⁻/PI⁺) cells. The scatter plot represents the cell population distribution into three gated areas (live, apoptotic, and dead) (Figure 5.2 A/B). The average percentage of apoptotic cells in WT and Δ HGS were $5.83\% \pm 1.24\%$ and $7.55\% \pm 1.62\%$, respectively (Figure 5.2 C). There was no statistical difference in live, apoptotic, and dead cell populations between WT and Δ HGS cells (Figure 5.2 C).

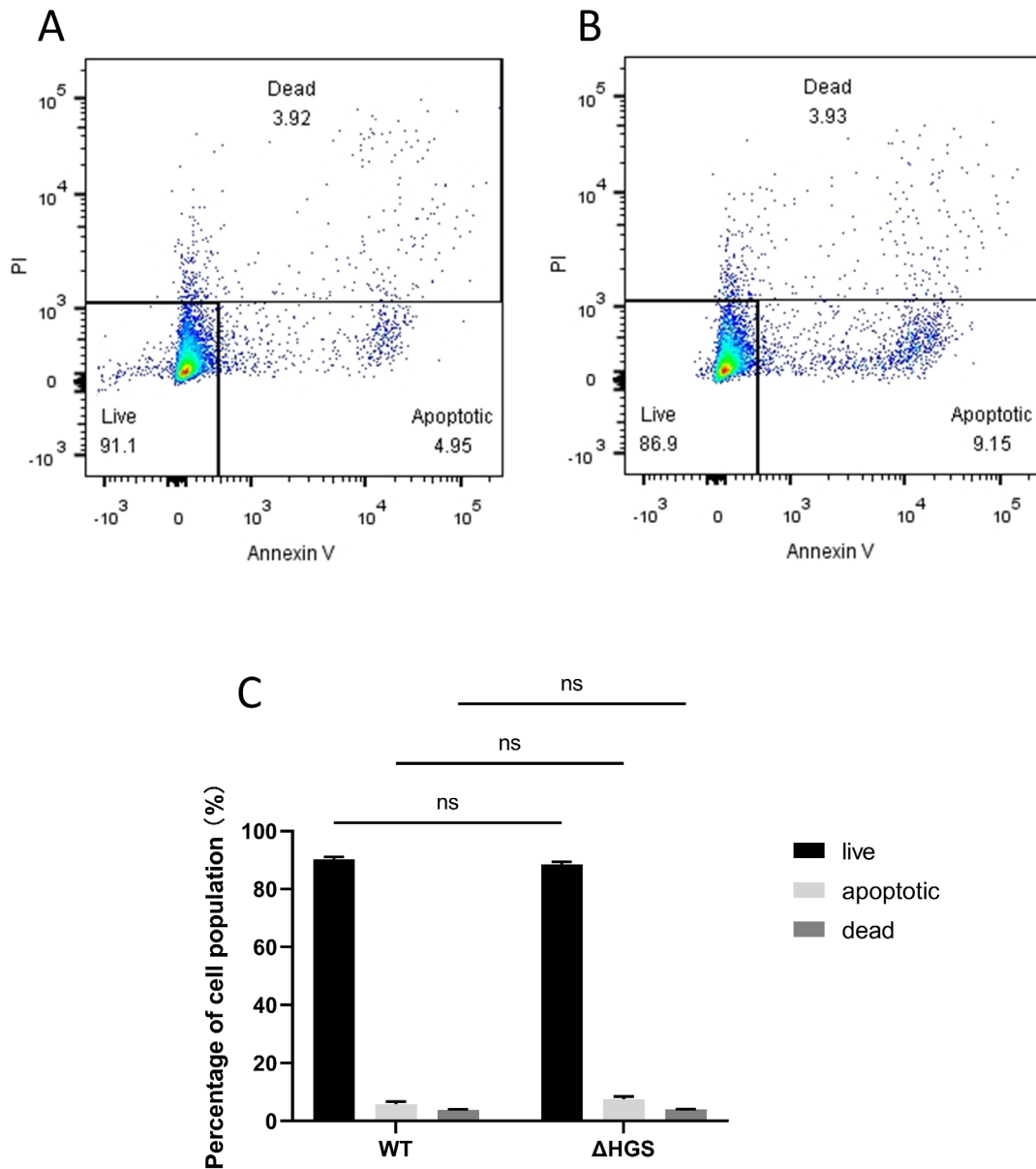


Figure 5.2: Apoptosis assay using flow cytometry. Apoptotic and dead cell populations were determined by flow cytometry after staining with Annexin V-FITC and PI. Wild-type H357 (WT) and HGS knockout (Δ HGS) cells were cultured in medium for 48 hours. Representative scatter plots PI (y-axis) vs. annexin V (x-axis) of (A) WT and (B) Δ HGS. (C) Percentage of viable, apoptotic, and dead cells. All data were calculated as mean of three biological replicates \pm SEM. ns= not significant by two-way ANOVA.

3.2.2 The effect of HGS depletion on endosomal compartments

Previous data showed that HGS co-localised with the early endosome marker EEA1 in H357 WT cells (Section 3.2.3), supporting a role for HGS in endosomal sorting in OSCC. The role of late endosomal marker Ras-related protein RAB-7 (RAB7) in earlier steps of endosomal

trafficking is still controversial. Some studies reported that RAB7 depletion led to the accumulation of internalized low-density lipoproteins in enlarged early endosomes that indicate RAB7 associates with early endosomes to mediate the sorting and transport of selective cargos to late endosomes (Girard *et al.*, 2014, Vonderheit and Helenius, 2005). By contrast, another study showed that under the same circumstance of RAB7 depletion, the EGFR transportation from early to late endosomes was not changed. Still, the process of exiting from late endosomes was impaired, which indicates RAB7 is necessary to transfer cargo from late endosomes to the lysosomes (Vanlandingham and Ceresa, 2009). We therefore used immunofluorescence microscopy to further explore the effect of HGS depletion on EEA1 and RAB7-positive compartments.

HGS was well-distributed in the cytoplasm, whereas EEA1 and RAB7 showed more focal punctate staining (Figure 5.3). There was no fluorescence observed when cells were stained with the relevant isotype controls and corresponding secondary antibodies, which confirms antibody specificity. The quantitative analysis showed co-localisation of HGS with EEA1, but little co-localisation of HGS with RAB7 in WT cells with a 5.1-fold difference ($p < 0.01$) (Figure 5.4 A). Mean gray value was calculated to reveal the fluorescence intensity of EEA1 and RAB7 in WT compared to Δ HGS cells. Δ HGS EEA1 mean gray value was 1.8-fold higher than WT cells ($p < 0.05$) (Figure 5.4 B). There was no significant difference of RAB7 mean gray value between WT and Δ HGS (Figure 5.4 C).

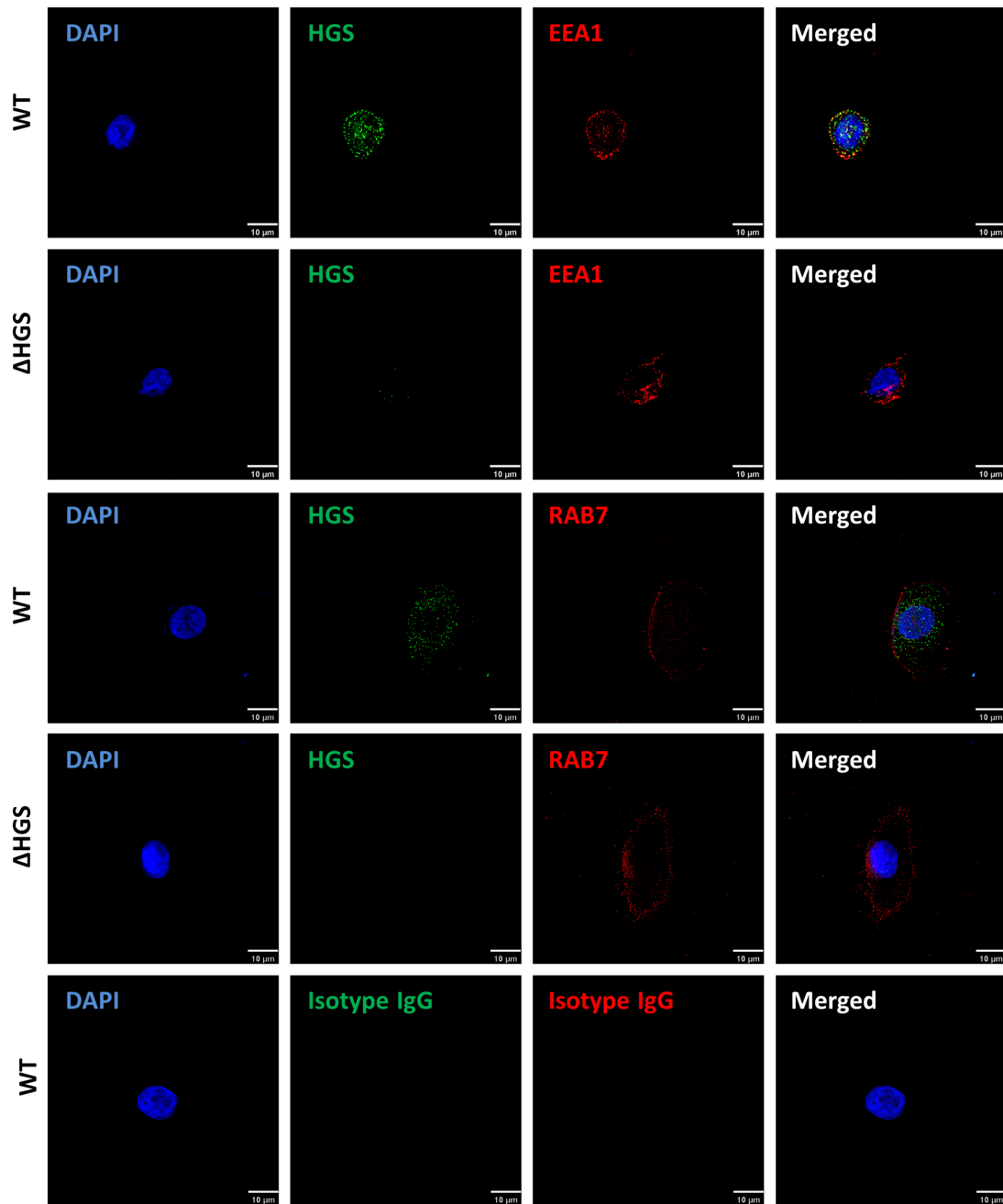


Figure 5.3: Immunofluorescence microscopy images of endosomal markers in WT and Δ HGS cells. Localisation of HGS, EEA1 and RAB7 were determined in WT and Δ HGS cell lines. Cells were fixed before blocking, followed by incubation with anti-HGS, anti-EEA1, anti-RAB7 and isotype IgG primary antibodies, and then Alexa 488 and Alexa 568-conjugated secondary antibodies. 3D images were acquired by z-stack. Yellow/orange pixels indicate potential co-localisation between HGS and EEA1; HGS and RAB7. Cell nuclei were stained with DAPI. Images were taken by Leica DMi8 inverted Microscope. All images are representative of three different biological replicates. Scale bar: 10 μ m.

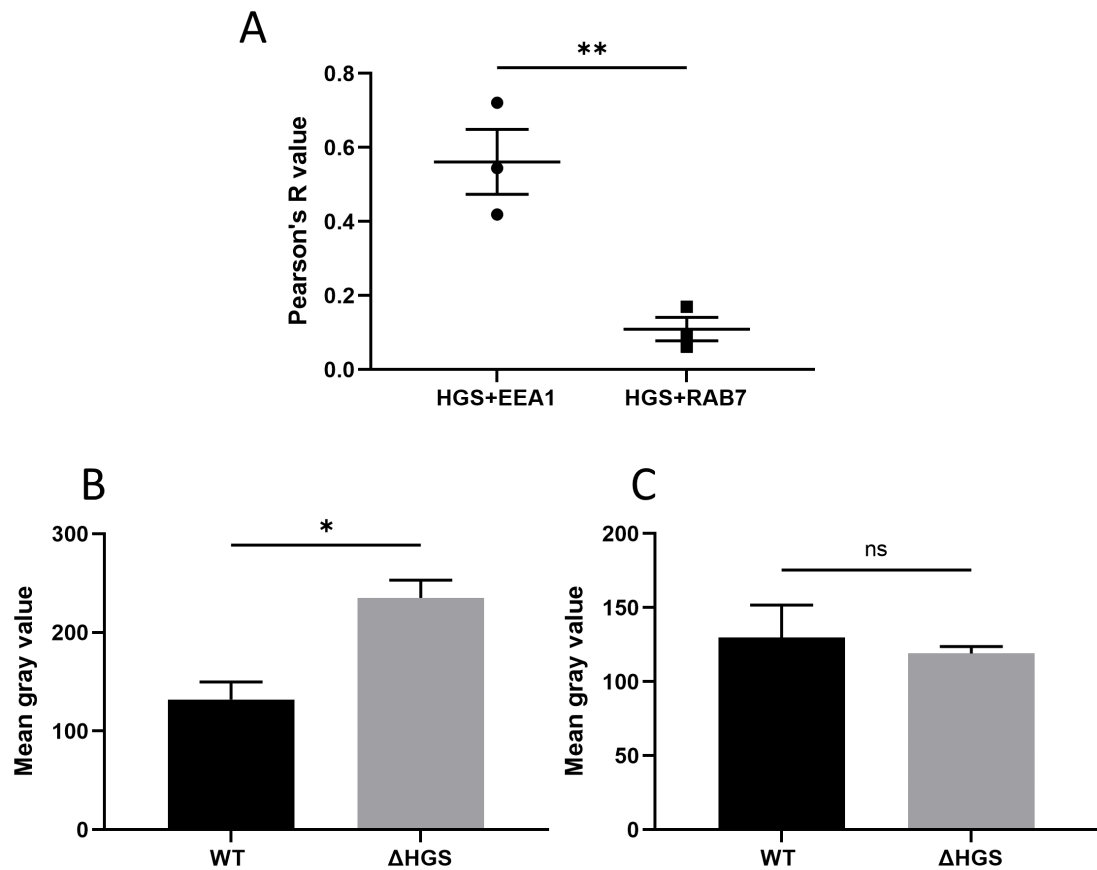


Figure 5.4: Quantification of co-localisation of HGS with endosome markers and fluorescence intensity. (A) Co-localisation between HGS and EEA1, HGS and RAB7 in WT cells were quantified using Pearson's R value. Fluorescence intensity of (B) EEA1 and (C) RAB7 in Δ HGS compared to WT cells. All data were calculated as mean of three biological replicates \pm SEM. * = $p < 0.05$, ** = $p < 0.01$, ns = not significant by Student's t-test.

The increase in EEA1 fluorescence intensity suggested that HGS depletion had affected early endosomal compartments. This finding was further explored by utilising TEM to image cell ultrastructure. WT and Δ HGS cell pellets were fixed and embedded to allow imaging of ultrathin sections. Structures with the expected MVB morphology (diameter 200-500 nm, electron-lucent matrix, limited by a double membrane, and ILVs of 40-150 nm) were visible in WT cells (Figure 5.5A). However, these structures were absent in Δ HGS cells. Endosome-like structures were greatly enlarged in HGS knockout cells with fewer ILVs observed compared to WT (Figure 5.5 A). Calculation of MVB area revealed an 8.4-fold enlargement of endosomes in Δ HGS compared to WT cells (Figure 5.5 B).

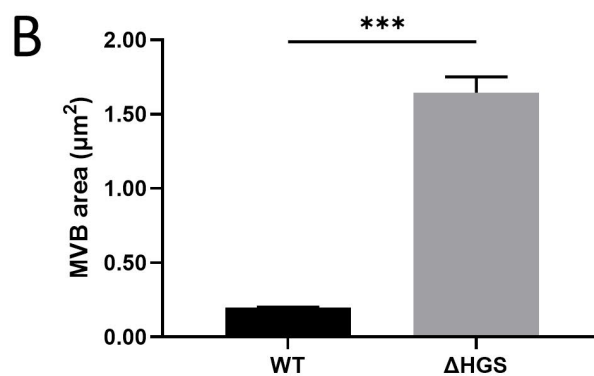
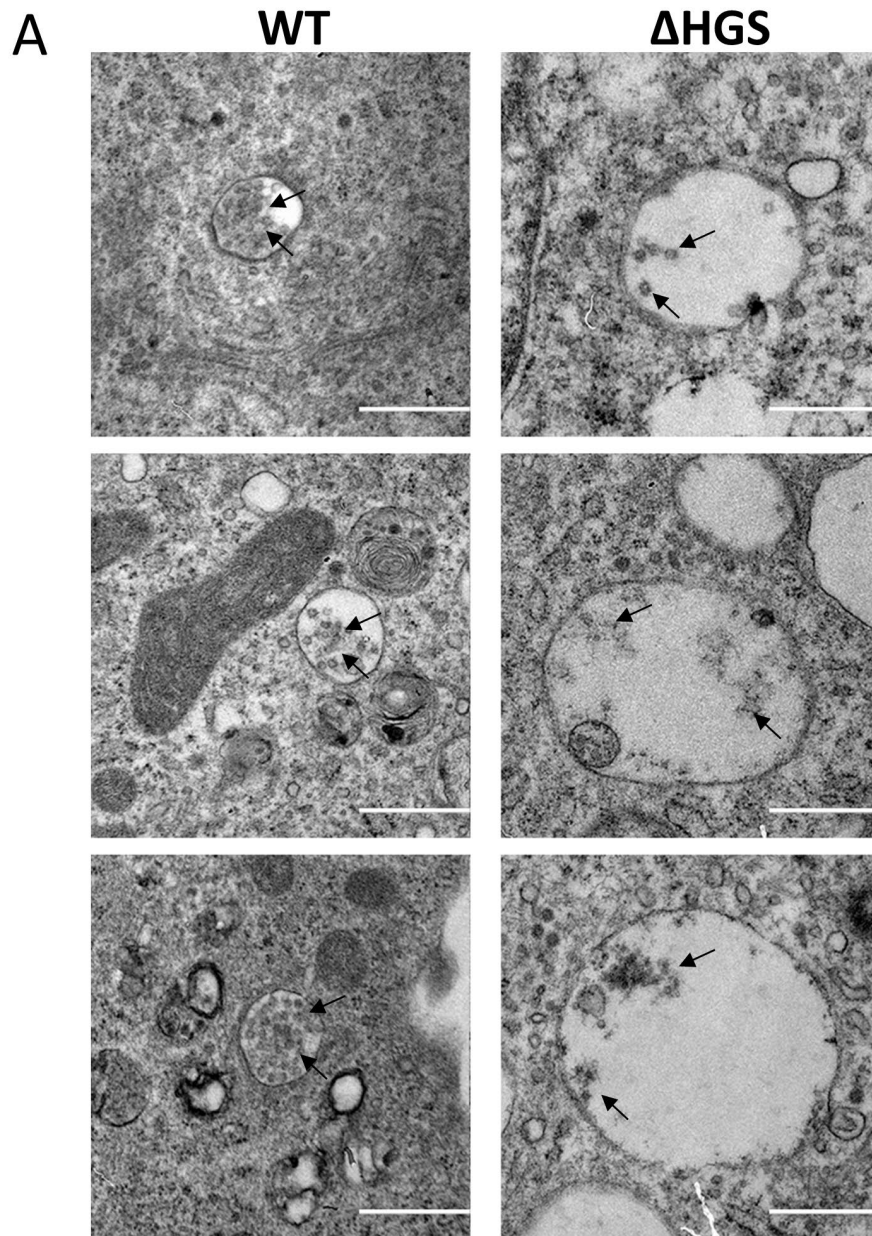


Figure 5.5: TEM characterisation of MVBs. (A) Representative images of MVBs in WT and Δ HGS cells. Arrows indicate ILVs. (B) Quantification of MVB area. All data were calculated as mean of three biological replicates \pm SEM. ***= $p < 0.001$ by Student's t-test. Scale bar: 0.5 μm .

3.2.3 The effect of HGS depletion on extracellular vesicle release and cargo

HGS depletion had a significant effect on the formation of MVBs and ILVs, which are the precursors of exosomes. Therefore, we next sought to verify the effect of HGS depletion on EV release and their molecular cargos. Firstly, small particles in cell line conditioned medium were quantified by NTA and normalised to cell number, which showed a 3-fold decrease in particle release for Δ HGS compared to WT ($p < 0.001$) (Figure 5.6).

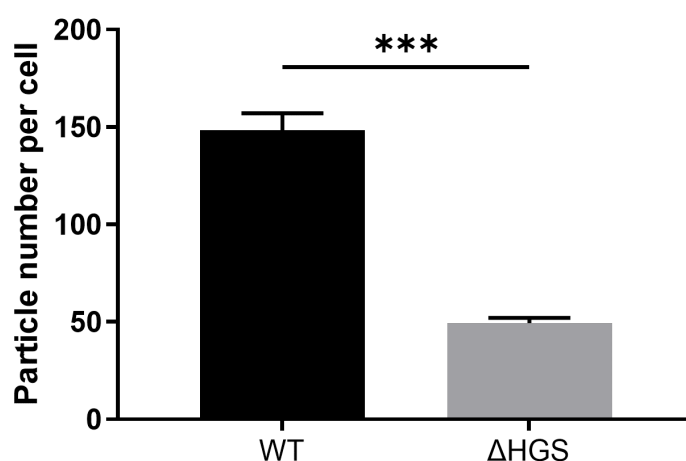


Figure 5.6: Assessment of particles number in conditioned medium from WT and Δ HGS cells. The concentration of small particles in the conditioned medium from WT and Δ HGS cell lines were measured by NTA, and normalized by the counted cell number. All data were calculated as mean of three biological replicates \pm SEM. ***= $p < 0.001$ by Student's t-test.

Extracellular particles were pelleted from conditioned medium by differential centrifugation. As described by Théry *et al.* (2018), increasing g -force was used to pellet increasingly smaller particles, which resulted in pellets generated at $2,000 \times g$ (2k), $10,000 \times g$ (10k) and $100,000 \times g$ (100k). Pellets were resuspended in PBS ready for characterisation of particle size and concentration by NTA, using distinct small (~ 100 nm diameter) and large particle (> 200 nm) settings. When using the small particle setting, conditioned medium from WT and Δ HGS had a peak of particle size of ~ 135 and ~ 165 nm respectively (Figure 5.7 A).

However, for large particles settings, multiple peaks of particle size were observed in both samples (Figure 5.7 A). NTA determined the size distribution of 2k (Figure 5.7 B), 10k (Figure 5.7 C) and 100k pellets (Figure 5.7 D). Due to there being too few large particles to analyse, there is only data for one biological repeat for Δ HGS 2k (Figure 5.7 B) and Δ HGS 100k samples (Figure 5.7 D). The results of size distribution showed the majority of the small particles in 2k pellets were around 135 nm for both WT and Δ HGS samples (Figure 5.7 B) which shared the same peak size diameter as 100k pellets (Figure 5.7 D). The peak size of 10k pellets were shifted to larger diameters with 165 nm for both samples (Figure 5.7 C). When analysing the same pellets with NTA settings to detect larger particles, there was a wide spread of particle sizes (ranging from 50 nm to 1000 nm) (Figure 5.7 B-D).

Analysis of small and large particle concentration in conditioned medium revealed no statistical significance between WT and Δ HGS samples (Figure 5.8 A). Particles concentrations in resuspended 2k (Figure 5.8 B), 10k (Figure 5.8 C) and 100k pellets (Figure 5.8 D) were generated. More small particles were detected in 10k and 100k pellets derived from WT compared to Δ HGS cell conditioned medium (Figure 5.8 C/D). Small particles enriched in WT 10k and 100k pellets were 2.3-fold ($p < 0.001$, Figure 5.8 C) and 7.3-fold higher than Δ HGS ($p < 0.05$, Figure 5.8 D), respectively.

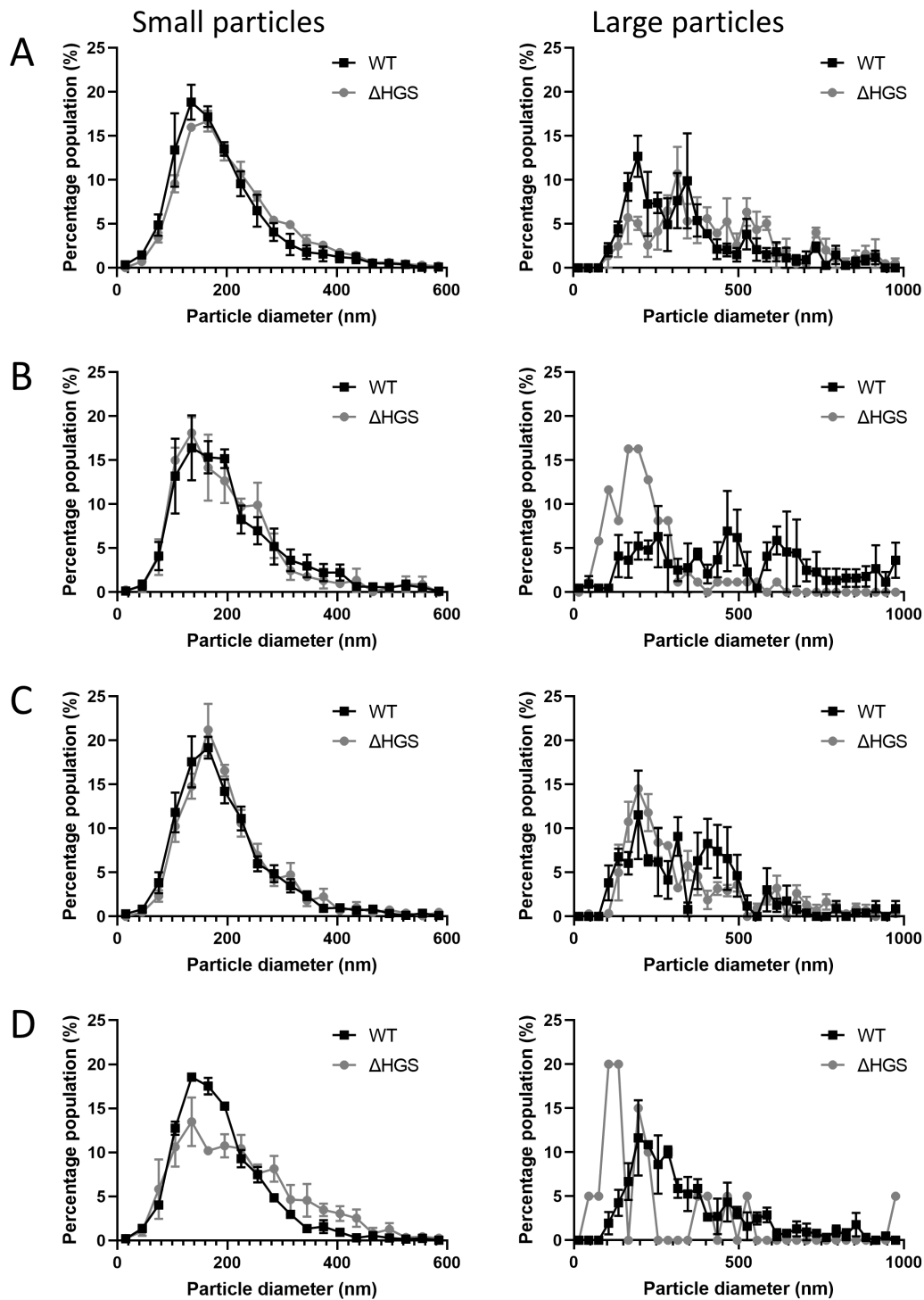


Figure 5.7: Characterisation of extracellular particle size distribution in conditioned medium and differential centrifugation pellets derived from WT and Δ HGS cells. The size distribution profile of small particles (\sim 100 nm) and large particles ($>$ 200 nm) in the (A) conditioned medium, (B) 2k, (C) 10k, and (D) 100k pellets from WT and Δ HGS cell lines by NTA. Data were calculated as mean of three biological replicates (except for large particles in Δ HGS 2k and Δ HGS 100k) \pm SEM.

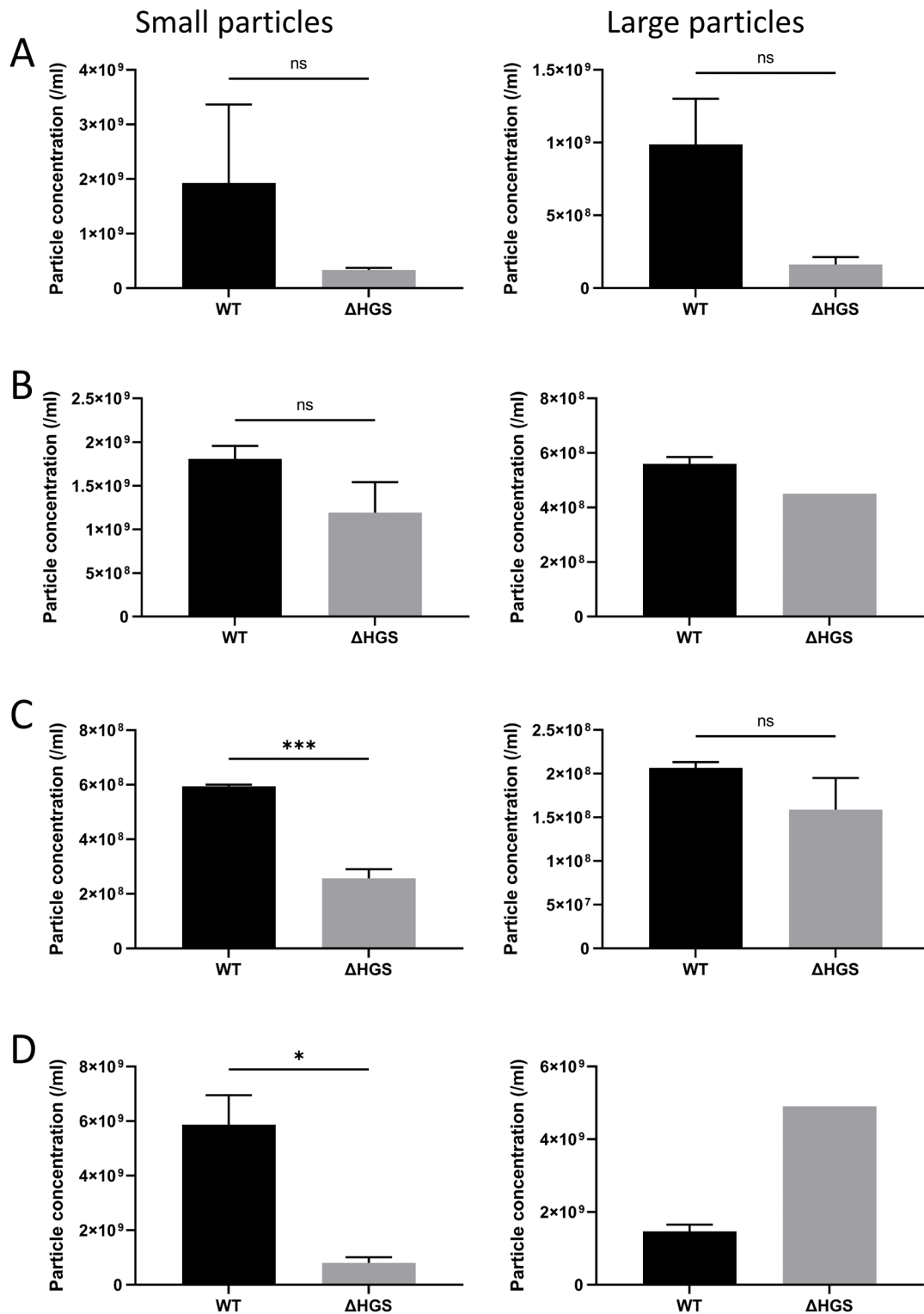


Figure 5.8: Characterisation of particle concentration in conditioned medium and pellets derived from WT and Δ HGS cells by NTA. NTA showed the number of particles per ml of small particles (\sim 100 nm) and large particles ($>$ 200 nm) in the (A) conditioned medium, (B) 2k, (C) 10k, and (D) 100k pellets from WT and Δ HGS cell lines by using corresponded settings on ZetaView instrument. Data were calculated as mean of three biological replicates (except for large particles in Δ HGS 2k and Δ HGS 100k) \pm SEM. * = p <0.05, ***= p <0.001, ns= not significant by Student's t-test.

To confirm the presence of EVs in differential centrifugation pellets they were processed for western blotting to assess the abundance of EV cargo (EGFR) and common EV markers (CD63 and TSG101) (Figure 5.9). EGFR was enriched in 100k pellets derived from WT cells and was 4.4-fold higher ($P < 0.05$) compared to Δ HGS samples by densitometry analysis (Figure 5.9 A/B). Low abundance of EGFR can be seen in 2k and 10k pellets of WT cells and no band was detected in Δ HGS (Figure 5.9 A). However, there was no significant difference between them by densitometry analysis (Figure 5.9 B). TSG101 showed a similar pattern to EGFR. HGS depletion caused a 4.2-fold reduction ($P < 0.0001$) of TSG101 in 100k pellets (Figure 5.9 C). Clear TSG101 bands above background were not detectable in 2k and 10k pellets from either cell line (Figure 5.9 A). Because of glycosylation, multiple CD63 bands were detected from 25-75 kDa, which was heavily enriched in 100k pellets (Figure 5.9 A). Densitometry analysis revealed there were no statistical differences in CD63 abundance between 2k, 10k, and 100k pellets from WT and Δ HGS cells (Figure 5.9 D).

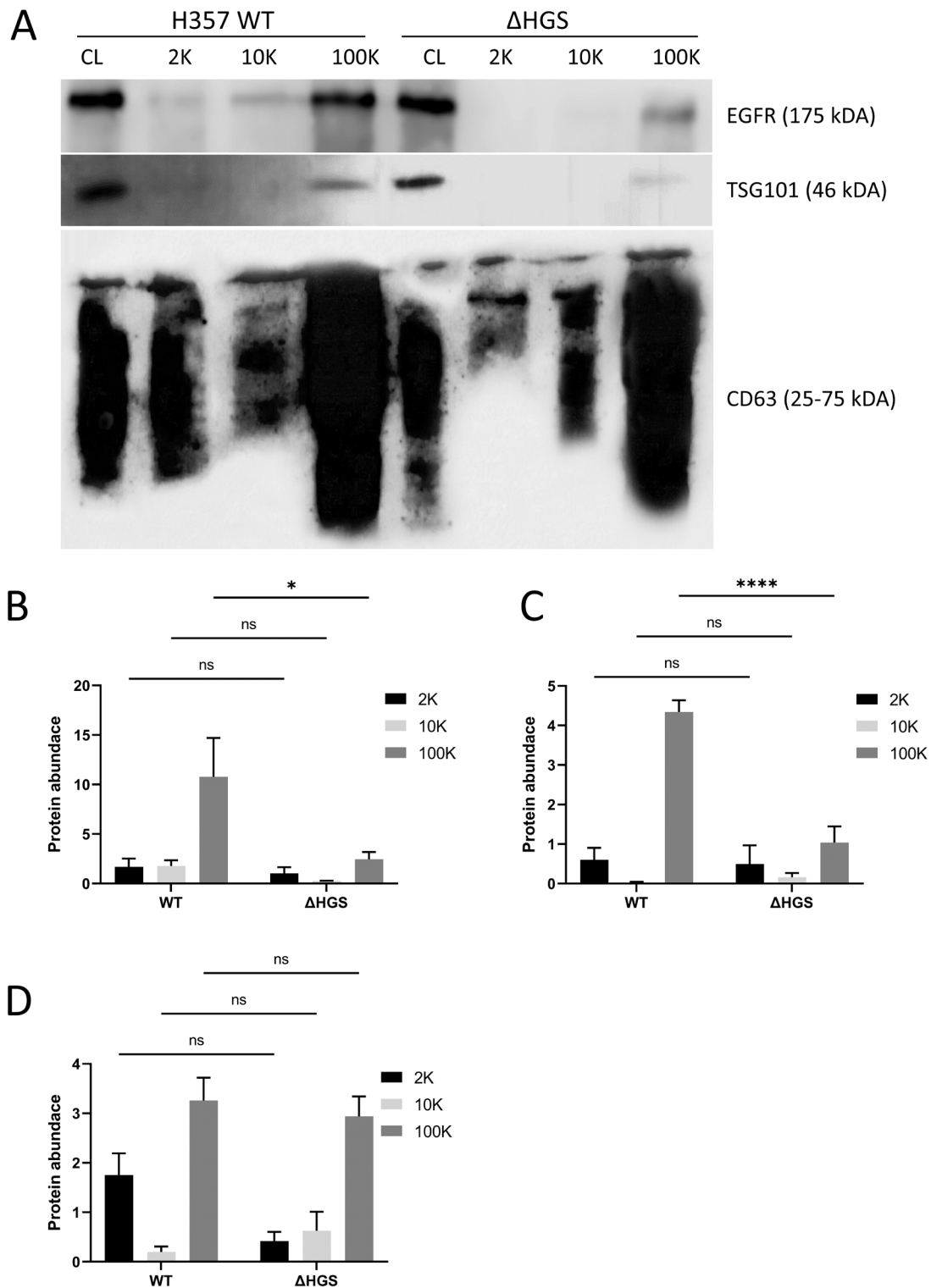


Figure 5.9: Assessment of EVs derived from WT cells and Δ HGS cells by Western blot. (A) Representative western blots of EV cargo (EGFR) and EV marker (TSG101 and CD63) abundance from 2k, 10k, and 100k pellets derived from WT and Δ HGS cells by differential centrifugation. Densitometry analysis of (B) EGFR, (C) TSG101 and (D) CD63. All data were calculated as mean of three biological replicates \pm SEM. * = p <0.05, ****= p <0.0001, ns= not significant by two-way ANOVA.

The reduced EGFR and TSG101 abundance in Δ HGS derived 100k pellets was an interesting finding. We next sought to determine if the observed reduction was reflected in cellular EGFR and TSG101 abundance or if it represented a specific decrease in EV association/export. The protein abundance of EGFR, TSG101 and CD63 was confirmed in WT and Δ HGS cell lysates by western blotting and compared to a loading control (Figure 5.10). EGFR protein abundance was 3.9-fold higher ($P < 0.05$) in Δ HGS cell lysates compared to WT, which suggests that HGS knockout caused EGFR to accumulate in the cells (Figure 5.10 A). There was no significant difference in TSG101 and CD63 protein abundance between WT and Δ HGS cells (Figure 5.10 B/C)

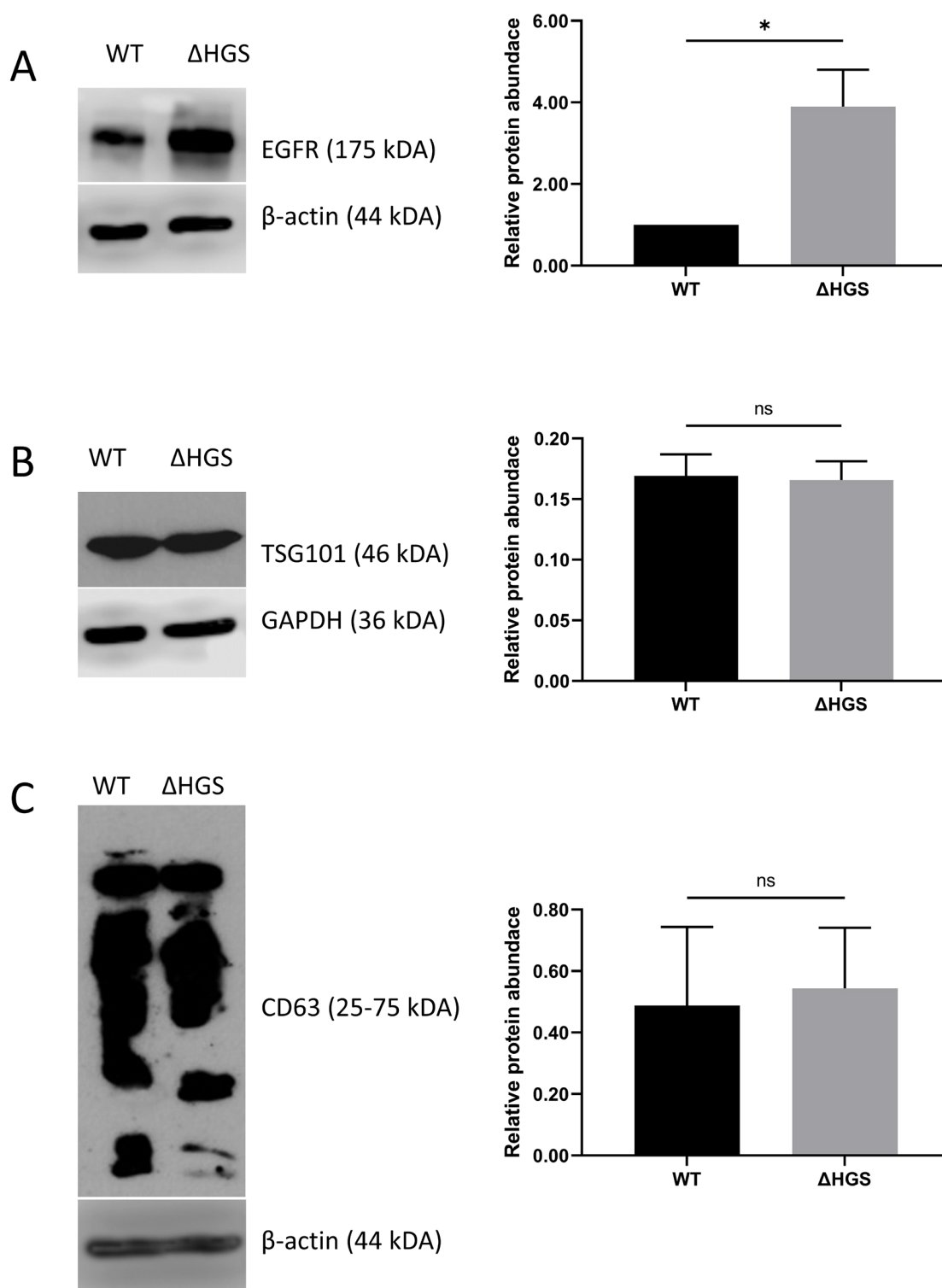


Figure 5.10: Western blot and densitometry of cellular abundance of the EV cargo and EV markers in WT and Δ HGS cells. Representative western blots and densitometry analysis of (A) EGFR protein abundance relative to β -actin; (B) TSG101 protein abundance relative to GAPDH; (C) CD63 protein abundance relative to β -actin. All data were calculated as mean of three biological replicates \pm SEM. * = $p < 0.05$, ns = not significant by Student's t-test.

3.2.4 Determining the role of HGS in EGF/EGFR cellular trafficking

Based on previous data, HGS knockout resulted in the release of less EGFR-positive EVs and caused EGFR accumulation in cells. Therefore, pulse-chase experiments were performed in WT and Δ HGS cells to elucidate the effect of HGS depletion on EGFR trafficking. Alexa-488-labelled EGF (green) was used to track the fate of EGF/EGFR in relation to the early endosomal marker EEA1 (red). Cells were 'pulse'-stimulated with Alexa-488-labelled EGF for 10 minutes and the fluorescent signal was 'chased' for 120 minutes by culturing cells in the absence of EGF and fixing cells for microscopic examination at specific timepoints (0, 10, 20, 60 and 120 minutes). The spatial overlap of EGF signal (green) and EEA1 signal (red) can be seen in the merged images as yellow punctate fluorescent signals (Figure 5.11 A). In WT cells, the EGF-488 signal decreased significantly after 60 and 120 minutes (Figure 5.11 A/B). On the other hand, in Δ HGS cells, the EGF-488 signal progressively accumulated in EEA1-positive early endosomes (Figure 5.11 A/B). The corresponding quantifications of Pearson's coefficient showed a decreased co-localisation of EGF-488 with EEA1 in WT cells and an increased co-localisation of the fluorescent signals in Δ HGS cells with 3.4-fold ($p < 0.0001$) and 7.8-fold ($p < 0.0001$) differences at chase time of 60 and 120 minutes respectively (Figure 5.11 C). Mean gray value was calculated to reveal the intensity of EGF-488 in WT compared to Δ HGS, which indicated HGS depletion altered the trafficking of EGF/EGFR and induces its accumulation in EEA1-positive compartments. The intensity of EGF-488 in WT was 1.4-fold lower at 60 minutes ($p < 0.0001$) and 1.9-fold lower at 120 minutes ($p < 0.0001$) compared to Δ HGS cells, indicating that HGS knockout impaired the degradation mechanism of EGFR (Figure 5.11 D).

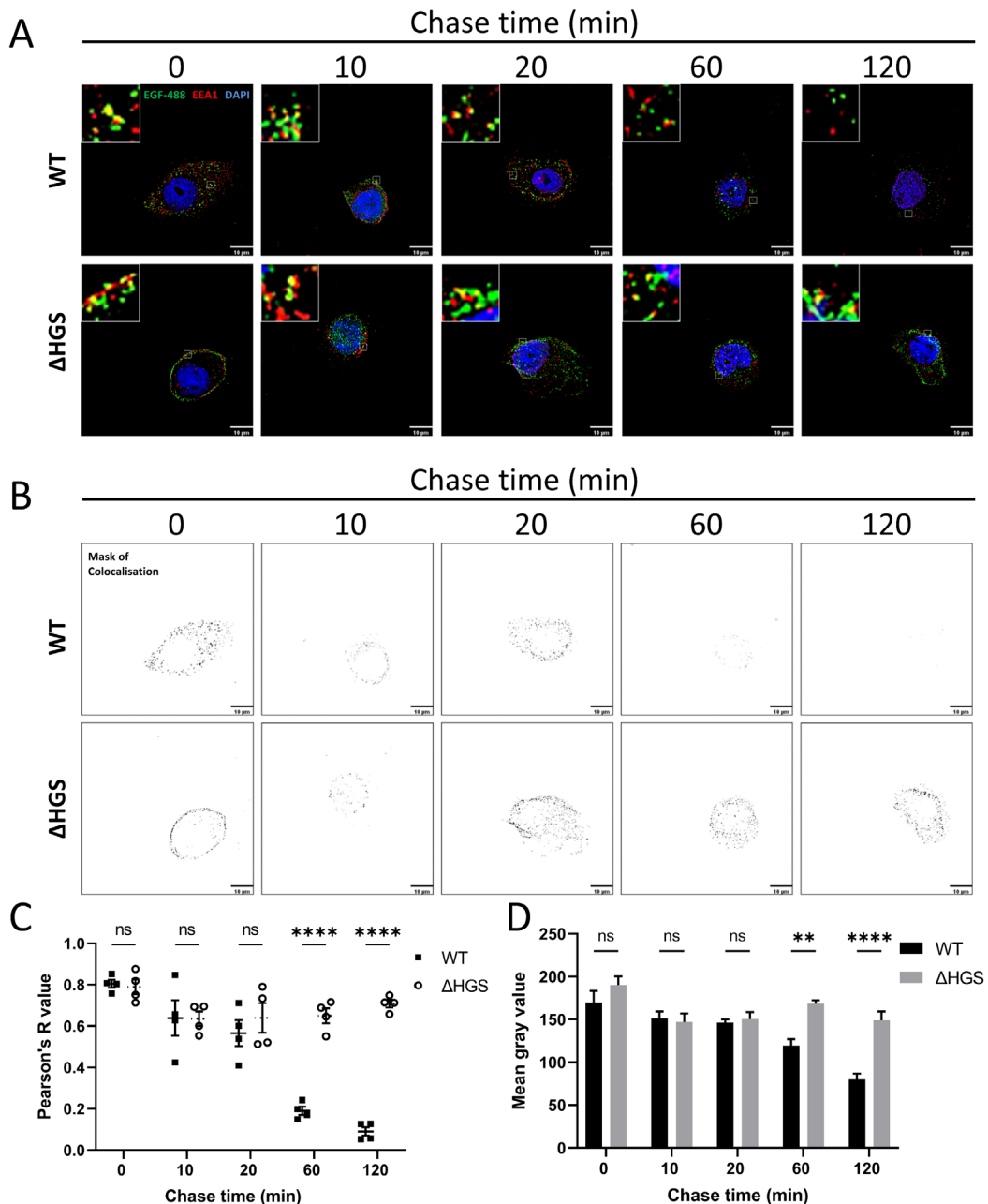


Figure 5.11: Cellular trafficking of EGF/EGFR upon HGS knockout. (A) Representative immunofluorescence images of pulse-chase experiments in WT and Δ HGS cells. All cells were stimulated for 10 min with 50 ng/ml of Alexa 488 labelled EGF (green), followed with ligand-chase at corresponding time-points of 0, 10, 20, 60 and 120 min. Cells were stained with primary anti-EEA1 then incubated with Alexa 568-conjugated secondary antibody. 3D images were acquired by z-stack. The insets represent enlarged views (8 \times) of the corresponding boxed regions. Yellow/orange pixels indicate co-localisation between EGF/EGFR and EEA1. Cell nuclei were stained with DAPI. Images were taken by Leica DMi8 Inverted Microscope. (B) Mask of co-localisation between EGF/EGFR and EEA1. (C) Co-localisation between EGF/EGFR and EEA1 in WT and Δ HGS cells was quantified using Pearson's R value. (D) Fluorescence intensity of EGF-488 in WT and Δ HGS cells at corresponding chase-time. All data were calculated as mean of four biological replicates \pm SEM., **= $p < 0.01$, ****= $p < 0.0001$, ns= not significant by two-way ANOVA. Scale bar: 10 μ m.

3.3 Discussion

3.3.1 The phenotypical and morphological changes of HGS knockout OSCC

In this chapter, we firstly assess the phenotypical changes upon HGS depletion in OSCC cells. HGS knockout cells exhibited a slower growth rate and trypan blue exclusion indicated decreased viability compared to WT cells. However, flow cytometry showed no statistical differences in the proportion of apoptotic and dead cells between WT and Δ HGS cells. Multiple studies showed that loss of ESCRT subunits resulted in cellular apoptosis. For example, transient silencing of HGS impaired cell viability in hepatoblastoma and colorectal cancer cells (Canal *et al.*, 2015) and knockdown of ESCRT-I subunit TSG101 resulted in breast cancer cell apoptosis (Zhu *et al.*, 2004). Suppressed expression of ESCRT-II subunits Vps22, Vps25, Vps36 induced cell death (Herz *et al.*, 2006, Woodfield *et al.*, 2013). The analysis of apoptosis by flow cytometry showed a different result with trypan blue exclusion assay possible due to the different culturing time. In the former experiment, cells were cultured for 48 hours but in the latter experiment, cells were cultured for 96 hours.

We next assessed the impact of HGS knockout on endosomal compartments by using immunofluorescence microscopy and TEM. We previously demonstrated the co-localisation between HGS and early endosome marker EEA1 in WT H357 (section 3.2.5). In this chapter, we further assessed subcellular location of HGS in relation to the late endosome marker RAB7, specifically RAB7a, which is one of two RAB7 isoforms (Pereira-Leal and Seabra, 2001). RAB7a localises to late endosomes, regulating transportation from early endosomes to late endosomes and lysosomes (Bucci *et al.*, 2000). Whereas, RAB7b localises to the Golgi Network, regulating transportation from endosomes to Golgi apparatus (Progida *et al.*, 2012).

Previous studies showed the poor co-localisation between HGS and RAB7 and the alternative late endosome/lysosomal marker lysosomal-associated membrane protein 1 (LAMP1) (Bache *et al.*, 2003, Coudert *et al.*, 2021). The low Pearson's coefficient indicated the weak co-localisation between HGS with RAB7, indicating little interaction of RAB7 with late endocytic compartments. We also observed after HGS depletion that EEA1 accumulated in OSCC cells, which is consistent with a published study that showed the accumulation of another early endosome marker RAB5a in HGS knockdown skeletal myoblast cells (Coudert *et al.*, 2021). Beyond this, RAB5 to RAB7 switch was described as a mechanism of progression from early to late endosomes (Rink *et al.*, 2005). The detection of RAB7 on late endosomes was accompanied with loss of RAB5 (Rink *et al.*, 2005, Poteryaev *et al.*, 2010, Vonderheit and Helenius, 2005). Thus, we hypothesised that accumulated EEA1 in Δ HGS results in less RAB7 intensity. However, we did not see statistical differences of fluorescence intensity of RAB7 between WT and Δ HGS. This may be because of the large biological variation between three independent experiments. After determining the subcellular location of endosomal markers in Δ HGS cells, we used TEM to visualise MVB structure. Our study showed the measurable enlargement of MVBs and reduced ILVs in Δ HGS compared to WT cells, which suggests HGS is vital for development of MVB in OSCC cells. MVB enlargement is possibly due to HGS depletion inhibiting the inward vesiculation (Hanyaloglu *et al.*, 2005, Razi and Futter, 2006). Furthermore, after HGS depletion, the fusion of vacuoles with each other is another possible explanation for MVB enlargement (Razi and Futter, 2006). These enlarged MVBs have potential to induce accumulation of ubiquitylated proteins like EGFR in epidermoid carcinoma and breast cancer cells (Stuffers *et al.*, 2009, Razi and Futter, 2006). Through mediating

ubiquitylated proteins such as P62 and Alfy, enlarged MVBs also function on inhibiting autophagic degradation of neurocytes (Filimonenko *et al.*, 2007). Stuffers *et al.* (2009) found that after depleting ESCRT-0, ESCRT-I, ESCRT-II, and ESCRT-III subunits (HGS, TSG101, Vps22 and Vps24), MVBs were enlarged and ILVs had a greater diameter and less homogenous shape. TEM images from the current study also showed irregular sized ILVs in Δ HGS cells, but they were few in number.

3.3.2 Characterisation of EV pellets derived from HGS deficient cells

After examining the role of HGS in OSCC MVB biogenesis, we moved forward to analyse the EVs released by WT and Δ HGS cells. NTA showed a decreased number of particles were released from Δ HGS compared to parental cells. This is consistent with other reports showing that loss ESCRT-0 subunits reduced exosome release in multiple types of cells (Hoshino *et al.*, 2013, Colombo *et al.*, 2013). The reduction in EV release is most likely due to impaired MVB formation that we and others have observed (Schmidt and Teis, 2012). In addition to causing reduced exosome release, depletion of HGS has been previously shown to reduce the size of exosomes in colorectal cancer cells by TEM (Sun *et al.*, 2016). However, we did not observe a difference in particle size by NTA, but this could be because NTA is unable to detect particles below 70 nm compared to other techniques such TEM and nanoparticle flow cytometry. EV experiments in this chapter were performed with CRISPR-Cas9 edited cells. We also attempted to determine the effect of transient siRNA knockdown of HGS on EV release, but no statistical differences in particle number was observed (Supplementary materials, Figure S1 C). This may be due to poor transfection efficiency, resulting in incomplete knockdown the HGS. Furthermore, it has been reported that transfection reagent complexes may cause artefacts and

be mistaken for EVs by some nanoparticle analysis techniques due to their similar size (McConnell *et al.*, 2022).

Differential centrifugation pellets were abundant in nanoparticles of size consistent with EVs. We therefore used western blotting to measure the abundance of EV markers TSG101 (cytosolic) and CD63 (membrane bound) in accordance with MISEV guidance which states that at least one membrane bound and one cytosolic protein should be used to characterise EVs (Théry *et al.*, 2018, Lötvald *et al.*, 2014). ESCRT-0 was reported to recruit downstream ESCRT-I subunit TSG101 on early endosomes by PtdIns (3) P regulation, to orchestrate many events related to MVB biogenesis including regulating viral budding, ubiquitinated cargo sorting and endocytic trafficking (Strickland *et al.*, 2022, Colombo *et al.*, 2013, Cvjetkovic *et al.*, 2016, Lu *et al.*, 2003, Razi and Futter, 2006). Furthermore, TSG101 was shown to have a notable role in membrane dynamics which function to control endosome fission and fusion (Stuffers *et al.*, 2009). We correctly hypothesised that knockout of HGS would cause a reduction in the biogenesis of TSG101-positive EVs. CD63 is a common EV marker and has been reported to be mainly enriched in small EVs, particularly exosomes (Kowal *et al.*, 2016). Meanwhile, CD63 is a key role of ESCRT-independent pathway (van Niel *et al.*, 2011). In this study, the depletion of HGS did not alter the CD63 abundance in differential centrifugation pellets, which was inconsistent with previous research using breast cancer cells (Colombo *et al.*, 2013). This may be due to cell specific differences in EV biogenesis pathways or because the previous study used transient gene silencing rather than stable genome editing.

3.3.3 Characterisation of EGF/EGFR cellular trafficking upon HGS knockout in OSCC

EGFR is usually overexpressed in HNSCC tumours, which promotes cancer cell proliferation, migration and survival (Ribeiro *et al.*, 2014). EGFR is also ubiquitinated by HGS as part of its normal processing (Stern *et al.*, 2007). But how HGS regulate EGFR transduction on a protein level is still unclear. Thus, we were interested to understand how knockout of HGS altered EGFR trafficking and degradation in OSCC. We firstly measured EGFR protein abundance in WT and Δ HGS differential centrifugation pellets, which showed a reduction in EGFR abundance in 100k pellets derived from Δ HGS cells. This is consistent with previous research that showed HGS knockdown decreased the trafficking of EGFR from the MVB-limiting membrane to ILVs, and hence down-regulated EV-associated EGFR abundance (Razi and Futter, 2006). After determining the extracellular level of EGFR, we further determined whether HGS depletion impacted cellular EGFR abundance. HGS knockout resulted in an increased cellular abundance of EGFR compared to WT cells. This result is consistent with the observed decrease in export of EGFR and the HGS-dependent altered lysosomal degradation of EGFR observed elsewhere (Malerød *et al.*, 2007).

The current study showed that depletion of HGS was associated with an increase of cellular EGFR abundance and decrease of EV-associated EGFR, which suggested altered EGFR trafficking. Our investigation revealed that HGS depletion inhibited endosomal sorting and impaired EGFR degradation. HGS was found to regulate the endosomal trafficking and degradation of different classes of receptors in other models (Jékely and Rørth, 2003). Like EGFR, the activated Toll-like receptor 4 (TLR4) and TGF- β have been reported to promote

HNSCC progression (Szczepanski *et al.*, 2009, Pang *et al.*, 2018). HGS was found to regulate the trafficking of TLR4 which is consequently responsible for the accumulation and its activation (Husebye *et al.*, 2006). Meanwhile, the dynamics of TGF- β signalling was also revealed to be governed by ESCRT-mediated receptor trafficking (Miller *et al.*, 2018).

Many studies have provided evidence to support that ESCRT-0 plays a significant role in ubiquitinated protein sorting (Mosesso *et al.*, 2019, Shields and Piper, 2011). Interestingly, EGFR can still be targeted to early endosomes in an HGS-deficient background, with pulse-chase experiments showing that EGF-488 signals co-localised with EEA1 positive compartments. Stuffers *et al.* (2009) showed that EGFR is usually localised within ILVs. However, upon ESCRT depletion (combined HGS, TSG101, Vps22 and Vps24) by siRNA, EGFR was restricted to the endosomal limiting membrane and not sorted into ILVs (Stuffers *et al.*, 2009). Although the absence of ESCRT subunits strongly inhibited EGFR degradation there was still some partial degradation. Stuffers *et al.* (2009) suggested that this may be due to delayed recruitment of downstream ESCRT complexes. For example, ESCRT-I may compensate for the loss of ESCRT-0 by facilitating the transit of EGFR to EEA1 targeted endosomes, but in a delayed manner (Flores-Rodriguez *et al.*, 2015).

Altogether, this part of the study showed depletion of HGS caused reduced OSCC cell proliferation and reduced EV release. We also observed a dramatic alteration in the morphology of MVBs. Furthermore, EGFR processing was stalled in the HGS mutant leading to cellular accumulation and a significant decrease in EV-associated EGFR.

Chapter 6: Final discussion

To summarise, this study showed HGS protein abundance was significantly higher in two out of three OSCC cell lines tested compared to normal controls. Knockout of HGS by CRISPR-Cas9 genome editing resulted in enlarged endosomes and EEA1-positive early endosome accumulation. NTA and western blotting showed that HGS depletion led to decreased release of extracellular particles including TSG101-positive EVs. Pulse-chase experiments revealed that trafficking of EGFR was stalled in the HGS-deficient cells leading to cellular accumulation and a significant decrease in EV-associated EGFR.

6.1 HGS is a master regulator modulating MVB biogenesis and EGFR trafficking

This study demonstrates the significance of HGS in EGFR trafficking and extracellular export in OSCC cells for the first time. Here we combined the findings from the current study with past findings from the literature to propose a model of how HGS depletion affects EGFR sorting and EV biogenesis (Figure 6.1). In chapter 5, we showed EGF/EGFR trafficking was altered by HGS depletion. However, we do not fully understand the mechanism of how EGFR was blocked from lysosomal degradation. Impaired degradation of EGF/EGFR could be attributed to either failure of delivering ubiquitinated proteins to the MVB lumen or failure of fusing MVBs with lysosomes. The former mechanism seems likely as HGS deficient cells are known to be unable to recognise ubiquitinated cargos, which results in the unsuccessful recruitment of EGFR to ILVs (Wu *et al.*, 2022). Ubiquitinated protein sorting by ESCRT-0 serves two functions during trafficking: directing ubiquitinated cargos to the early endosome and also preventing ubiquitinated activated EGFR from recycling back to the plasma membrane

(Eden *et al.*, 2012). In contrast, knockout of HGS in endothelial cells impaired the recycling of endocytosed VE-cadherin and β 2-adrenergic receptor to the plasma membrane by impairing the motility of recycling endosomes (Yu *et al.*, 2021, Hanyaloglu *et al.*, 2005). These findings indicate the dual role of ESCRT-0 in distinct cargo recycling. Furthermore, ESCRT-0 can be essential for capturing ubiquitylated cargo which controls the balance between the recycling pathway and direction to the endosomal lumen (Flores-Rodriguez *et al.*, 2015). Hence, the loss of HGS inhibits the correct sorting of ubiquitinated receptors (such as EGFR) into microdomains destined to form late endosomes, consequently inhibiting exocytosis of EV-associated EGFR. It is also possible that ubiquitinated EGFR, retained at the limiting membrane of the early endosome, is preferentially recycled to the plasma membrane as is observed for membrane receptors that are not ubiquitinated such as the transferrin receptor (Raiborg *et al.*, 2002). Intriguingly, knockdown of the ESCRT-I subunit TSG101 also showed a similar impact on MVB biogenesis and EGFR trafficking (Razi and Futter, 2006). TSG101 depleted cells contained larger endosomes with fewer ILVs and exhibited reduced EGF/EGFR degradation. The authors stated that HGS knockdown only modestly reduced EGF degradation in comparison to TSG101 knockdown, which almost abolished EGF degradation. However, it is important to note that the above study relied on transient silencing by siRNA transfection, which resulted in more complete knockdown of TSG101 than HGS. Nevertheless, the shared phenotype between HGS and TSG101 silenced cells (enlarged endosomes with fewer ILVs) suggests that recruitment of TSG101 by HGS is required for normal MVB biogenesis. The classic model of the ESCRT-dependent pathway displays the 'conveyor belt' type mechanism, in which cargos are delivered from one complex to the subsequential complexes, with the

ESCRT-0 being the first complex sorting cargos to MVB lumen (Henne *et al.*, 2011). Recently, some studies proposed that multiple routes may exist to transfer cargo to lysosomes upon targeting to MVB, but independently of HGS (Theos *et al.*, 2006, Gullapalli *et al.*, 2006, Hislop *et al.*, 2004). These findings highlight the challenge of determining the mechanism of how distinct ESCRT family members and ESCRT-independent pathways are coordinated to facilitate growth factor receptor trafficking and the impact on the OSCC tumour microenvironment.

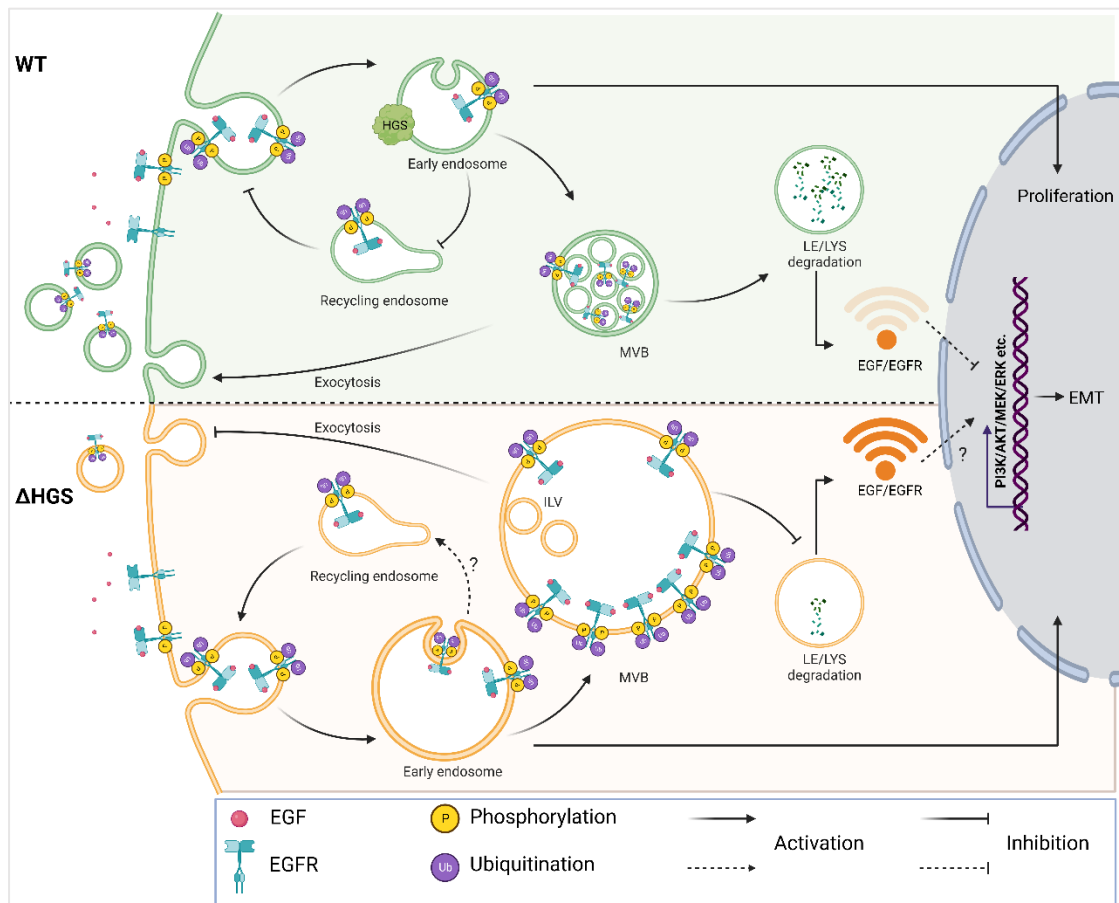


Figure 6.1: Schematic summary of how HGS depletion affects the endosomal pathway. EGFR processing was stalled in the HGS mutant leading to cellular accumulation and a significant decrease in EV-associated EGFR. Mechanistically, HGS depletion inhibits the sorting of ubiquitinated EGFR into MVBs, inhibiting exocytosis of EV-associated EGFR and putatively increasing EGFR recycling to the plasma membrane. HGS depletion had a significant influence on MVB invagination, which blocked EGFR traffic for lysosomal degradation. Accumulated EGFR may up-regulate phosphoinositide-3-kinase (PI3K)/AKT, mitogen-activated protein kinase (MEK)/extracellular signal-regulated kinase (ERK) etc. to activate downstream signalling pathways and further affect the tumour microenvironment. Solid arrows are evidenced mechanisms, dotted arrows are postulated mechanisms, and question marks are unknown mechanisms. The upper panel represents WT cells and the lower panel represents HGS knockout cells. Figure was created with BioRender.

6.2 ESCRT mediated EV release may support OSCC tumourigenesis

There are currently no published studies exploring the relationship between ESCRT-mediated EV release and OSCC tumourigenesis. In our study, we found that HGS was overexpressed in OSCC cell lines and was involved in MVB biogenesis, EV release and EGFR

trafficking. It is possible that increased HGS protein may be associated with OSCC development, but the functional consequences related to receptor-mediated signalling and EV release remain unclear. It is likely that, through altered packaging of protein cargo, EVs derived from OSCC cells will possess distinct cellular activities compared to those from non-cancerous cells. Previous studies revealed that EGFR overexpression is observed in 80% of HNSCC cases, contributing to recurrence and poor prognosis (Kimura *et al.*, 2016, Chung *et al.*, 2006). There is an inverse relationship between Annexin A1 (ANXA1) levels and EGFR, with down-regulation of ANXA1 resulting in increased phosphorylated EGFR and activation of downstream PI3K/AKT pathway in HNSCC (Sento *et al.*, 2016, Raulf *et al.*, 2018). However, a reduction in exosome release and phosphorylated EGFR-positive EV production was observed in HNSCC cell lines with ANXA1 knockdown, which is similar to what was observed upon HGS depletion (Raulf *et al.*, 2018). Clinically, tumour proliferation and progression are associated with increased EV production (Perez-Torres *et al.*, 2008, Matsumoto *et al.*, 2016). OSCC-derived EVs have been shown to modulate multiple tumourigenesis activities including remodelling of matrix and membrane, cellular differentiation, and transcription and translation (Qadir *et al.*, 2018, Yap *et al.*, 2020). In addition, previous studies showed that tumour cells can transfer EGFR to other cancer or non-cancer cells via EVs which affects the tumour microenvironment. Gastric cancer-derived EVs showed the ability to promote liver metastasis by inhibiting miR-26 and up-regulating the expression of hepatocyte growth factor (Zhang *et al.*, 2017a). In chronic myelogenous leukaemia (CML), amphiregulin (a ligand of EGFR) can be transferred by EVs between CML cells and normal stromal cells. This increased CML cell adherence to the stromal monolayer to modulate the bone marrow microenvironment,

which finally supported CML growth and invasion (Corrado *et al.*, 2016). OSCC-derived EGFR-positive EVs were able to increase cellular vimentin protein levels, induce a spindle shape morphology and decrease E-cadherin levels to initiate epithelial-mesenchymal transition (EMT), a key hallmark that promotes cancer cell invasion (Fujiwara *et al.*, 2018a, Hanahan and Weinberg, 2011). Collectively, OSCC-derived EGFR positive EVs have the potential to impact the OSCC tumour microenvironment in a way that favours tumourigenesis.

6.3 Could OSCC-derived EVs play a role in cetuximab therapeutic response?

During preparation of this thesis a study was published showing that HGS is overexpressed in HNSCC *ex vivo* tissues and regulates programmed death ligand-1 (PD-L1) secretion in small EVs, which contribute to tumour immune evasion and anti-PD-1 treatment efficacy (Xiao *et al.*, 2023). It is tempting to speculate that EGFR-positive EVs may play a role in OSCC resistance to the human-mouse chimeric monoclonal antibody (mAb) cetuximab. Cetuximab specifically targets EGFR and showed a 5-fold higher affinity for EGFR than EGF. It blocks EGF and EGFR interaction, inhibiting the downstream MEK/ERK pathways to weaken the EMT progression of OSCC, but often not completely due to drug resistance (Fujiwara *et al.*, 2018a, Fujiwara *et al.*, 2018b, Roberts and Der, 2007). Usually, mAb cetuximab binds to the receptors to form complexes that are internalised via endocytosis. The mAb cetuximab release cytotoxic payloads to induce cell death through cleavage of mAb by lysosomal degradation (Barok *et al.*, 2014, Khongorzul *et al.*, 2020). By accumulating mAb drugs in EVs and disposing of drug-loaded EVs in the extracellular space by exocytosis, budding or blebbing, cancer cells are able to develop drug resistance (Shedden *et al.*, 2003, Maacha *et al.*, 2019). Our data shows that OSCC-

derived EVs contain membrane-embedded EGFR, raising the possibility that they can act as decoys that bind cetuximab and prevent its cellular action (Figure 6.2). Specifically, cetuximab may promote OSCC cells to release EGFR-positive EVs, which sequester cetuximab. This decoy effect could contribute to consuming free cetuximab, which would impair efficiency of cetuximab on the target OSCC cells. Based on this, we hypothesise that HGS depletion (which alters EGFR trafficking and results in less EGFR-positive EVs being released) might reduce EV-mediated resistance to cetuximab and sensitise OSCC cells.

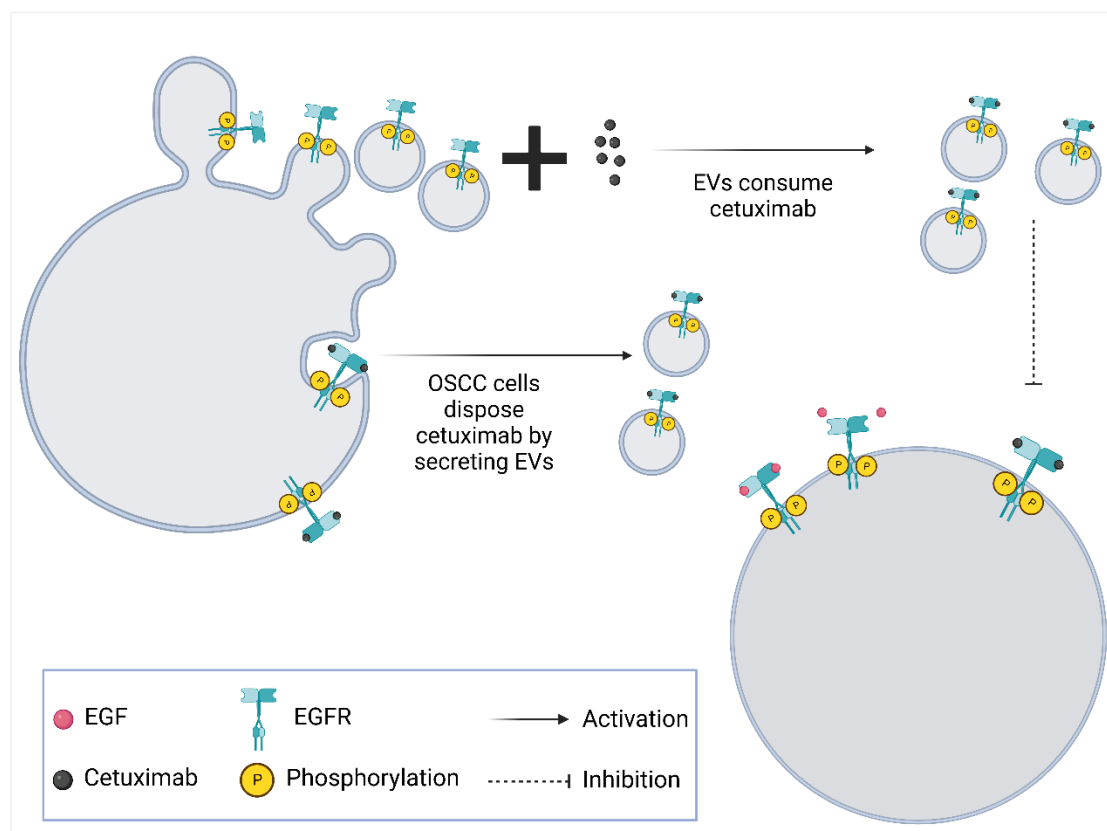


Figure 6.2: Hypothetical mechanisms of EV-mediated cetuximab therapy resistance in OSCC cells. EVs have the potential to cause cetuximab resistance through EV-mediated decoy mechanisms. Secretion of EGFR-positive EVs might contribute to sequestering cetuximab. Alternatively, EGFR-cetuximab complexes may be released from cells via EVs. Figure was created with BioRender.

6.4 Limitations of the study

On reflection, there are several limitations with the current study that could be improved.

We initially used three OSCC cell lines at the start of the study. However, only H357 was chosen for HGS knockout by genome editing and further experiments. Previous work in the Hunt group had shown that H357 were amenable to CRISPR-Cas9 genome editing and expansion from single cell clones, giving the best chance of success for cell line creation.

We chose to use the FNB6 cell line as a substitute for primary NOKs due to their limited replicative potential. Ideally, NOKs would have been used as a normal control in immunofluorescence microscopy experiments. FNB6 is not truly representative of 'normal' keratinocytes because it is immortalised through hTERT overexpression (McGregor *et al.*, 2002), which was evident in FNB6 sharing some traits with the OSCC cell lines used in this study.

EV enrichment was achieved by differential centrifugation of relatively small volumes of conditioned medium from cells cultured in monolayer, which resulted in low yields of particles for downstream experiments. More sophisticated culture methodology such as using hollow fibre bioreactors could have been utilised to generate concentrated conditioned medium to save both time and consumable materials (Storm *et al.*, 2016).

In the pulse-chase experiment, due to equipment limitations, we chose the Leica inverted microscope to observe the co-localisation of different proteins in cells. However, if we were to use the Zeiss confocal microscope, we could obtain higher-resolution images. Additionally, the Zeiss confocal microscope has the capability of fast imaging, allowing the capture of a large number of images in a shorter period of time. This is particularly useful for observing a significant number of samples.

This study was affected by the Covid-19 pandemic as 4 months was lost due to national

lockdown period followed by limited laboratory access for several months due to the social distancing policy. There were also delays in reagent delivery that caused disruption of some experiments. For example, we had hoped to collaborate with NanoFCM to characterise our EVs by nano flow cytometry. However, delays in delivery of fluorescently conjugated antibodies (EpCAM) meant that one preliminary experiment was performed, which revealed that significant experimental optimisation was required to produce meaningful data. Unfortunately, there was insufficient time remaining to address this. If this experiment had been optimised, we could have expanded our analysis to include other antibodies such as EGFR, to confirm that it was truly associated with EVs in our samples.

6.5 Future work

The findings of this study showed promise for future research. Based on these findings, an interesting question has been raised: can targeting extracellular vesicle biogenesis sensitise cetuximab-resistant head and neck cancers? Moving forward to answer this question, future work would need to firstly determine the effect of HGS knockout on EGFR signalling *in vitro*. WT and Δ HGS could be stimulated with EGF, and phosphorylated EGFR and downstream signalling pathways (such as AKT and ERK1/2) assessed by western blotting. The fate of endocytosed EGFR could be tracked by immunofluorescence microscopy and correlated with markers of recycling endosomes (RAB11) and lysosomal degradation (LAMP1). Secondly, the effect of HGS knockout on cetuximab efficacy *in vitro* could be assessed by treating WT and Δ HGS with EGF and cetuximab followed by comparing cell viability, proliferation, and migration. Thirdly, we would determine if OSCC EVs act as decoys to prevent cellular targeting of cetuximab. EVs could be isolated from OSCC cells cultured *in vitro* and *ex vivo* OSCC

patient saliva samples by size exclusion chromatography. The abundance of EGFR on OSCC EVs and binding of fluorescently-labelled cetuximab could be assessed using a NanoAnalyzer flow cytometer.

6.6 Concluding remarks

The data generated in this study elucidates the role of ESCRT-0 subunit HGS in OSCC EV biogenesis. This study has revealed for the first time that HGS protein abundance is increased in oral cancer cells *in vitro*. We have also found that knockout of HGS led to the accumulation of intracellular EGFR and decreased release of EGFR-presenting EVs which indicates the trafficking of EGFR and its release in EVs is governed by HGS. These findings suggest that HGS might be a novel therapeutic target, reducing EV release in the OSCC tumour environment and ablating EV-mediated mechanisms of therapy resistance.

Supplementary materials

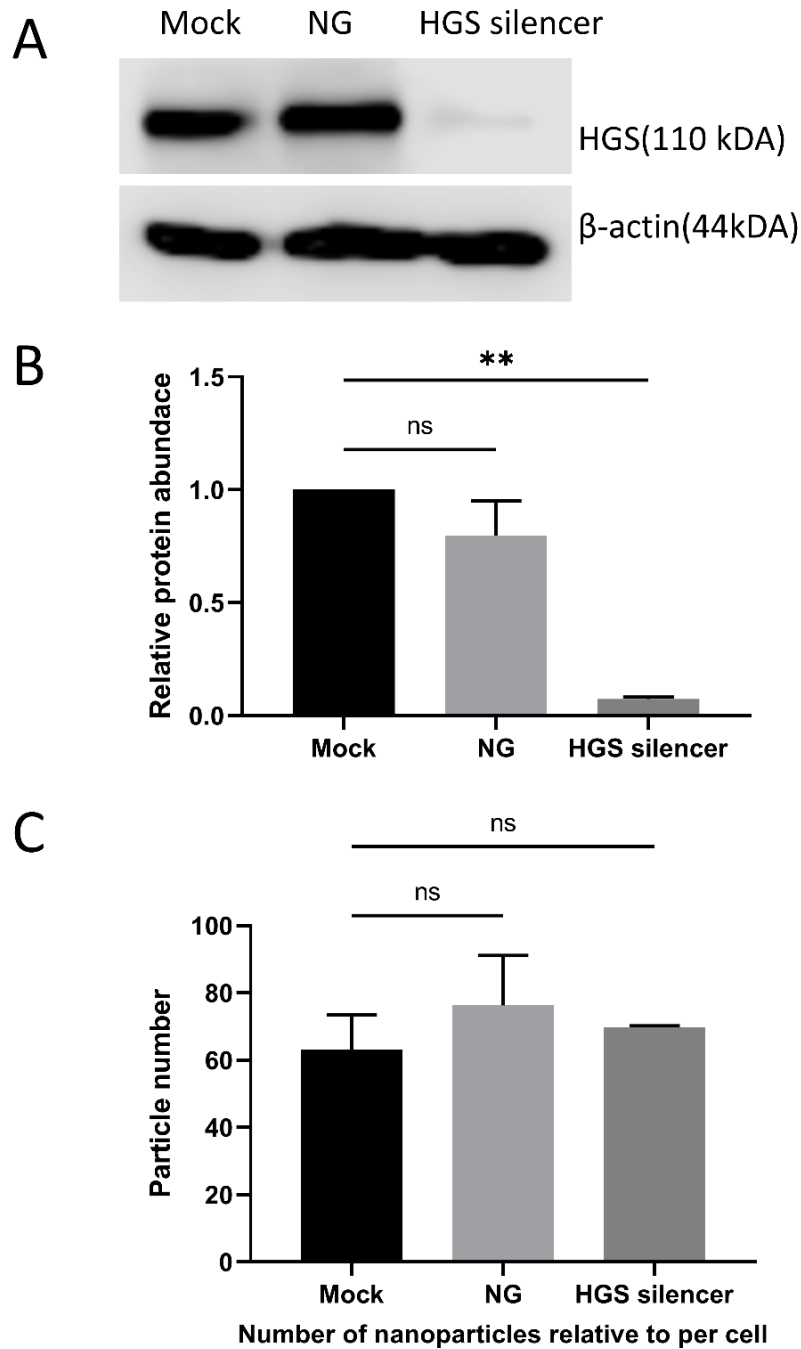


Figure S1: Assessment of particles number in conditioned medium from mock, negative silencer and HGS silencer transfected OSCC cells. (A) Representative western blot of HGS and loading control β -actin abundance in Mock, negative silencer (NG) and HGS silencer transfected cell lines. (B) Densitometry analysis of HGS protein abundance relative to β -actin abundance. (C) The concentration of the particles in the conditioned medium from mock, NG and HGS silencer transfected cell lines were measured by NTA with small particle (~100 nm) settings, normalized by the counted cell number. Data represent the mean of two biological replicates \pm SEM. **= $p < 0.01$, ns= not significant by Dunnett test.

References

- Adell, M. a. Y., Migliano, S. M., Upadhyayula, S., Bykov, Y. S., Sprenger, S., Pakdel, M., Vogel, G. F., Jih, G., Skillern, W., Behrouzi, R., *et al.* 2017. Recruitment dynamics of ESCRT-III and Vps4 to endosomes and implications for reverse membrane budding. *eLife*, 6, e31652.
- Adler, J. & Parmryd, I. 2010. Quantifying colocalization by correlation: The Pearson correlation coefficient is superior to the Mander's overlap coefficient. *Cytometry Part A*, 77A, 733-742.
- Agarwal, V., Bell, G. W., Nam, J. W. & Bartel, D. P. 2015. Predicting effective microRNA target sites in mammalian mRNAs. *Elife*, 4.
- Agromayor, M., Soler, N., Caballe, A., Kueck, T., Freund, S. M., Allen, M. D., Bycroft, M., Perisic, O., Ye, Y., Mcdonald, B., *et al.* 2012. The UBAP1 subunit of ESCRT-I interacts with ubiquitin via a SOUBA domain. *Structure*, 20, 414-28.
- Ajila, V., Shetty, H., Babu, S., Shetty, V. & Hegde, S. 2015. Human Papilloma Virus Associated Squamous Cell Carcinoma of the Head and Neck. *Journal of sexually transmitted diseases*, 2015, 791024-791024.
- Al-Nedawi, K., Meehan, B., Kerbel, R. S., Allison, A. C. & Rak, J. 2009. Endothelial expression of autocrine VEGF upon the uptake of tumor-derived microvesicles containing oncogenic EGFR. *Proc Natl Acad Sci U S A*, 106, 3794-9.
- Al-Nedawi, K., Meehan, B., Micallef, J., Lhotak, V., May, L., Guha, A. & Rak, J. 2008. Intercellular transfer of the oncogenic receptor EGFRvIII by microvesicles derived from tumour cells. *Nat Cell Biol*, 10, 619-24.
- Alam, S. L., Sun, J., Payne, M., Welch, B. D., Blake, B. K., Davis, D. R., Meyer, H. H., Emr, S. D. & Sundquist, W. I. 2004. Ubiquitin interactions of NZF zinc fingers. *Embo j*, 23, 1411-21.
- Alsahafi, E., Begg, K., Amelio, I., Raulf, N., Lucarelli, P., Sauter, T. & Tavassoli, M. 2019. Clinical update on head and neck cancer: molecular biology and ongoing challenges. *Cell Death Dis*, 10, 540.
- Andre, F., Schartz, N. E., Movassagh, M., Flament, C., Pautier, P., Morice, P., Pomel, C., Lhomme, C., Escudier, B., Le Chevalier, T., *et al.* 2002. Malignant effusions and immunogenic tumour-derived exosomes. *Lancet*, 360, 295-305.
- Arber, S., Barbayannis, F. A., Hanser, H., Schneider, C., Stanyon, C. A., Bernard, O. & Caroni, P. 1998. Regulation of actin dynamics through phosphorylation of cofilin by LIM-kinase. *Nature*, 393, 805-9.
- Ariizumi, T., Ogose, A., Kawashima, H., Hotta, T., Umezu, H. & Endo, N. 2009. Multinucleation followed by an acytokinetic cell division in myxofibrosarcoma with giant cell

proliferation. *Journal of Experimental & Clinical Cancer Research*, 28, 44.

Asao, H., Sasaki, Y., Arita, T., Tanaka, N., Endo, K., Kasai, H., Takeshita, T., Endo, Y., Fujita, T. & Sugamura, K. 1997. Hrs Is Associated with STAM, a Signal-transducing Adaptor Molecule: ITS SUPPRESSIVE EFFECT ON CYTOKINE-INDUCED CELL GROWTH*. *Journal of Biological Chemistry*, 272, 32785-32791.

Atkin-Smith, G. K. & Poon, I. K. H. 2017. Disassembly of the Dying: Mechanisms and Functions. *Trends Cell Biol*, 27, 151-162.

Audhya, A., Mcleod, I. X., Yates, J. R., Iii & Oegema, K. 2007. MVB-12, a Fourth Subunit of Metazoan ESCRT-I, Functions in Receptor Downregulation. *PLOS ONE*, 2, e956.

Austin, C. P., Battey, J. F., Bradley, A., Bucan, M., Capecchi, M., Collins, F. S., Dove, W. F., Duyk, G., Dymecki, S., Eppig, J. T., *et al.* 2004. The knockout mouse project. *Nat Genet*, 36, 921-4.

Azmi, I., Davies, B., Dimaano, C., Payne, J., Eckert, D., Babst, M. & Katzmann, D. J. 2006. Recycling of ESCRTs by the AAA-ATPase Vps4 is regulated by a conserved VSL region in Vta1. *J Cell Biol*, 172, 705-17.

Azmi, I. F., Davies, B. A., Xiao, J., Babst, M., Xu, Z. & Katzmann, D. J. 2008. ESCRT-III family members stimulate Vps4 ATPase activity directly or via Vta1. *Dev Cell*, 14, 50-61.

Babst, M. 2005. A protein's final ESCRT. *Traffic*, 6, 2-9.

Babst, M., Katzmann, D. J., Estepa-Sabal, E. J., Meerloo, T. & Emr, S. D. 2002a. Escrt-III: an endosome-associated heterooligomeric protein complex required for mvb sorting. *Dev Cell*, 3, 271-82.

Babst, M., Katzmann, D. J., Snyder, W. B., Wendland, B. & Emr, S. D. 2002b. Endosome-associated complex, ESCRT-II, recruits transport machinery for protein sorting at the multivesicular body. *Dev Cell*, 3, 283-9.

Babst, M., Sato, T. K., Banta, L. M. & Emr, S. D. 1997. Endosomal transport function in yeast requires a novel AAA-type ATPase, Vps4p. *Embo j*, 16, 1820-31.

Babst, M., Wendland, B., Estepa, E. J. & Emr, S. D. 1998. The Vps4p AAA ATPase regulates membrane association of a Vps protein complex required for normal endosome function. *Embo j*, 17, 2982-93.

Bache, K. G., Brech, A., Mehlum, A. & Stenmark, H. 2003. Hrs regulates multivesicular body formation via ESCRT recruitment to endosomes. *J Cell Biol*, 162, 435-42.

Bache, K. G., Slagsvold, T., Cabezas, A., Rosendal, K. R., Raiborg, C. & Stenmark, H. 2004. The growth-regulatory protein HCRP1/hVps37A is a subunit of mammalian ESCRT-I and mediates receptor down-regulation. *Mol Biol Cell*, 15, 4337-46.

- Bache, K. G., Stuffers, S., Malerød, L., Slagsvold, T., Raiborg, C., Lechardeur, D., Wälchli, S., Lukacs, G. L., Brech, A. & Stenmark, H. 2006. The ESCRT-III subunit hVps24 is required for degradation but not silencing of the epidermal growth factor receptor. *Mol Biol Cell*, 17, 2513-23.
- Baglio, S. R., Rooijers, K., Koppers-Lalic, D., Verweij, F. J., Pérez Lanzón, M., Zini, N., Naaijken, B., Perut, F., Niessen, H. W. M., Baldini, N., *et al.* 2015. Human bone marrow- and adipose-mesenchymal stem cells secrete exosomes enriched in distinctive miRNA and tRNA species. *Stem Cell Research & Therapy*, 6, 127.
- Bajorek, M., Schubert, H. L., Mccullough, J., Langelier, C., Eckert, D. M., Stubblefield, W.-M. B., Uter, N. T., Myszka, D. G., Hill, C. P. & Sundquist, W. I. 2009. Structural basis for ESCRT-III protein autoinhibition. *Nature Structural & Molecular Biology*, 16, 754-762.
- Barends, T. R. M., Werbeck, N. D. & Reinstein, J. 2010. Disaggregases in 4 dimensions. *Current Opinion in Structural Biology*, 20, 46-53.
- Barok, M., Joensuu, H. & Isola, J. 2014. Trastuzumab emtansine: mechanisms of action and drug resistance. *Breast cancer research*, 16, 1-12.
- Bashkirov, P. V., Akimov, S. A., Evseev, A. I., Schmid, S. L., Zimmerberg, J. & Frolov, V. A. 2008. GTPase cycle of dynamin is coupled to membrane squeeze and release, leading to spontaneous fission. *Cell*, 135, 1276-86.
- Bebelman, M. P., Smit, M. J., Pegtel, D. M. & Baglio, S. R. 2018. Biogenesis and function of extracellular vesicles in cancer. *Pharmacol Ther*, 188, 1-11.
- Bernstein, E., Caudy, A. A., Hammond, S. M. & Hannon, G. J. 2001. Role for a bidentate ribonuclease in the initiation step of RNA interference. *Nature*, 409, 363-6.
- Bhaya, D., Davison, M. & Barrangou, R. 2011. CRISPR-Cas systems in bacteria and archaea: versatile small RNAs for adaptive defense and regulation. *Annu Rev Genet*, 45, 273-97.
- Bilodeau, P. S., Urbanowski, J. L., Winistorfer, S. C. & Piper, R. C. 2002. The Vps27p Hse1p complex binds ubiquitin and mediates endosomal protein sorting. *Nat Cell Biol*, 4, 534-9.
- Bishop, N. & Woodman, P. 2000. ATPase-defective mammalian VPS4 localizes to aberrant endosomes and impairs cholesterol trafficking. *Mol Biol Cell*, 11, 227-39.
- Boone, M., Mobasher, A., Fenton, R. A., Van Balkom, B. W., Wismans, R., Van Der Zee, C. E. & Deen, P. M. 2010. The lysosomal trafficking regulator interacting protein-5 localizes mainly in epithelial cells. *J Mol Histol*, 41, 61-74.
- Brankatschk, B., Wichert, S. P., Johnson, S. D., Schaad, O., Rossner, M. J. & Gruenberg, J. 2012. Regulation of the EGF transcriptional response by endocytic sorting. *Sci Signal*, 5, ra21.
- Bravi, F., Bosetti, C., Filomeno, M., Levi, F., Garavello, W., Galimberti, S., Negri, E. & La

- Vecchia, C. 2013. Foods, nutrients and the risk of oral and pharyngeal cancer. *British journal of cancer*, 109, 2904-2910.
- Brunetti, L., Gundry, M. C., Kitano, A., Nakada, D. & Goodell, M. A. 2018. Highly Efficient Gene Disruption of Murine and Human Hematopoietic Progenitor Cells by CRISPR/Cas9. *J Vis Exp*.
- Bucci, C., Thomsen, P., Nicoziani, P., McCarthy, J. & Van Deurs, B. 2000. Rab7: a key to lysosome biogenesis. *Mol Biol Cell*, 11, 467-80.
- Bundgaard, T., Bentzen, S. M. & Wildt, J. 1994. The prognostic effect of tobacco and alcohol consumption in intra-oral squamous cell carcinoma. *Eur J Cancer B Oral Oncol*, 5, 323-8.
- Burd, C. G. & Emr, S. D. 1998. Phosphatidylinositol(3)-phosphate signaling mediated by specific binding to RING FYVE domains. *Mol Cell*, 2, 157-62.
- Burma, S., Chen, B. P. & Chen, D. J. 2006. Role of non-homologous end joining (NHEJ) in maintaining genomic integrity. *DNA Repair (Amst)*, 5, 1042-8.
- Caby, M.-P., Lankar, D., Vincendeau-Scherrer, C., Raposo, G. & Bonnerot, C. 2005. Exosomal-like vesicles are present in human blood plasma. *International Immunology*, 17, 879-887.
- Caffrey, D. R., Zhao, J., Song, Z., Schaffer, M. E., Haney, S. A., Subramanian, R. R., Seymour, A. B. & Hughes, J. D. 2011. siRNA off-target effects can be reduced at concentrations that match their individual potency. *PLoS One*, 6, e21503.
- Canal, F., Anthony, E., Lescure, A., Del Nery, E., Camonis, J., Perez, F., Ragazzon, B. & Perret, C. 2015. A kinome siRNA screen identifies HGS as a potential target for liver cancers with oncogenic mutations in CTNNB1. *BMC Cancer*, 15, 1020.
- Canning, M., Guo, G., Yu, M., Myint, C., Groves, M. W., Byrd, J. K. & Cui, Y. 2019. Heterogeneity of the Head and Neck Squamous Cell Carcinoma Immune Landscape and Its Impact on Immunotherapy. *Front Cell Dev Biol*, 7, 52.
- Capalbo, L., Mela, I., Abad, M. A., Jeyaprakash, A. A., Edwardson, J. M. & D'avino, P. P. 2016. Coordinated regulation of the ESCRT-III component CHMP4C by the chromosomal passenger complex and centralspindlin during cytokinesis. *Open Biol*, 6.
- Carlton, J. G., Agromayor, M. & Martin-Serrano, J. 2008. Differential requirements for Alix and ESCRT-III in cytokinesis and HIV-1 release. *Proceedings of the National Academy of Sciences*, 105, 10541-10546.
- Carlton, J. G. & Martin-Serrano, J. 2007. Parallels Between Cytokinesis and Retroviral Budding: A Role for the ESCRT Machinery. *Science*, 316, 1908-1912.
- Chairoungdua, A., Smith, D. L., Pochard, P., Hull, M. & Caplan, M. J. 2010. Exosome release of β -catenin: a novel mechanism that antagonizes Wnt signaling. *J Cell Biol*, 190, 1079-91.

- Chan, G. G., Tai, B. C., Liang, S., Lim, D. T. & Soo, K. C. 2002. Squamous cell carcinoma of the head and neck (HNSCC)--multi-modality treatment and impact on survival. *Asian J Surg*, 25, 35-40.
- Chang, S. M. & Hu, W. W. 2018. Long non-coding RNA MALAT1 promotes oral squamous cell carcinoma development via microRNA-125b/STAT3 axis. *J Cell Physiol*, 233, 3384-3396.
- Chen, C., Liu, Y., Rappaport, A. R., Kitzing, T., Schultz, N., Zhao, Z., Shroff, A. S., Dickins, R. A., Vakoc, C. R., Bradner, J. E., *et al.* 2014. MLL3 is a haploinsufficient 7q tumor suppressor in acute myeloid leukemia. *Cancer Cell*, 25, 652-65.
- Chen, J., Hou, N., Zhang, C., Teng, Y., Cheng, X., Li, Z., Ren, J., Zeng, J., Li, R., Wang, W., *et al.* 2015. Smooth Muscle Hgs Deficiency Leads to Impaired Esophageal Motility. *Int J Biol Sci*, 11, 794-802.
- Chen, Y., Liu, L., Li, J., Du, Y., Wang, J. & Liu, J. 2019. Effects of long noncoding RNA (linc-VLDLR) existing in extracellular vesicles on the occurrence and multidrug resistance of esophageal cancer cells. *Pathol Res Pract*, 215, 470-477.
- Chow, A., Zhou, W., Liu, L., Fong, M. Y., Champer, J., Van Haute, D., Chin, A. R., Ren, X., Gugiu, B. G., Meng, Z., *et al.* 2014. Macrophage immunomodulation by breast cancer-derived exosomes requires Toll-like receptor 2-mediated activation of NF- κ B. *Sci Rep*, 4, 5750.
- Chung, C. H., Ely, K., MCGavran, L., Varella-Garcia, M., Parker, J., Parker, N., Jarrett, C., Carter, J., Murphy, B. A., Netterville, J., *et al.* 2006. Increased epidermal growth factor receptor gene copy number is associated with poor prognosis in head and neck squamous cell carcinomas. *J Clin Oncol*, 24, 4170-6.
- Colley, H. E., Hearnden, V., Jones, A. V., Weinreb, P. H., Violette, S. M., Macneil, S., Thornhill, M. H. & Murdoch, C. 2011. Development of tissue-engineered models of oral dysplasia and early invasive oral squamous cell carcinoma. *British Journal of Cancer*, 105, 1582-1592.
- Colombo, M., Moita, C., Van Niel, G., Kowal, J., Vigneron, J., Benaroch, P., Manel, N., Moita, L. F., Théry, C. & Raposo, G. 2013. Analysis of ESCRT functions in exosome biogenesis, composition and secretion highlights the heterogeneity of extracellular vesicles. *J Cell Sci*, 126, 5553-65.
- Colombo, M., Raposo, G. & Théry, C. 2014. Biogenesis, secretion, and intercellular interactions of exosomes and other extracellular vesicles. *Annu Rev Cell Dev Biol*, 30, 255-89.
- Connell, J. W., Allison, R. J., Rodger, C. E., Pearson, G., Zlamalova, E. & Reid, E. 2020. ESCRT-III-associated proteins and spastin inhibit protrudin-dependent polarised membrane traffic. *Cellular and Molecular Life Sciences*, 77, 2641-2658.
- Corrado, C., Saieva, L., Raimondo, S., Santoro, A., De Leo, G. & Alessandro, R. 2016. Chronic myelogenous leukaemia exosomes modulate bone marrow microenvironment through activation of epidermal growth factor receptor. *J Cell Mol Med*, 20, 1829-39.

- Coudert, L., Osseni, A., Gangloff, Y. G., Schaeffer, L. & Leblanc, P. 2021. The ESCRT-0 subcomplex component Hrs/Hgs is a master regulator of myogenesis via modulation of signaling and degradation pathways. *BMC Biology*, 19, 153.
- Curry, J. M., Sprandio, J., Cognetti, D., Luginbuhl, A., Bar-Ad, V., Pribitkin, E. & Tuluc, M. 2014. Tumor Microenvironment in Head and Neck Squamous Cell Carcinoma. *Seminars in Oncology*, 41, 217-234.
- Cvjetkovic, A., Jang, S. C., Konečná, B., Höög, J. L., Sihlbom, C., Lässer, C. & Lötval, J. 2016. Detailed Analysis of Protein Topology of Extracellular Vesicles-Evidence of Unconventional Membrane Protein Orientation. *Sci Rep*, 6, 36338.
- Da Rocha, A. A., Giorgi, R. R., De Sa, S. V., Correa-Giannella, M. L., Fortes, M. A., Cavaleiro, A. M., Machado, M. C., Cescato, V. A., Bronstein, M. D. & Giannella-Neto, D. 2006. Hepatocyte growth factor-regulated tyrosine kinase substrate (HGS) and guanylate kinase 1 (GUK1) are differentially expressed in GH-secreting adenomas. *Pituitary*, 9, 83-92.
- De Andrade, A., De Oliveira, C. E., Dourado, M. R., Macedo, C., Winck, F. V., Paes Leme, A. F., Salo, T., Coletta, R. D., De Almeida Freitas, R. & Galvão, H. C. 2018. Extracellular vesicles from oral squamous carcinoma cells display pro- and anti-angiogenic properties. *Oral Dis*, 24, 725-731.
- De Souza, R. F. & Aravind, L. 2010. UMA and MABP domains throw light on receptor endocytosis and selection of endosomal cargoes. *Bioinformatics*, 26, 1477-80.
- Deatherage, B. L. & Cookson, B. T. 2012. Membrane vesicle release in bacteria, eukaryotes, and archaea: a conserved yet underappreciated aspect of microbial life. *Infect Immun*, 80, 1948-57.
- Di Vizio, D., Kim, J., Hager, M. H., Morello, M., Yang, W., Lafargue, C. J., True, L. D., Rubin, M. A., Adam, R. M., Beroukhi, R., *et al.* 2009. Oncosome formation in prostate cancer: association with a region of frequent chromosomal deletion in metastatic disease. *Cancer Res*, 69, 5601-9.
- Diepenbruck, M. & Christofori, G. 2016. Epithelial-mesenchymal transition (EMT) and metastasis: yes, no, maybe? *Curr Opin Cell Biol*, 43, 7-13.
- Dimaano, C., Jones, C. B., Hanono, A., Curtiss, M. & Babst, M. 2008. Ist1 regulates Vps4 localization and assembly. *Mol Biol Cell*, 19, 465-74.
- Dobrowolski, R. & De Robertis, E. M. 2011. Endocytic control of growth factor signalling: multivesicular bodies as signalling organelles. *Nature reviews. Molecular cell biology*, 13, 53-60.
- Du, Z. & Lovly, C. M. 2018. Mechanisms of receptor tyrosine kinase activation in cancer. *Molecular Cancer*, 17, 58.

- Dudás, A. & Chovanec, M. 2004. DNA double-strand break repair by homologous recombination. *Mutat Res*, 566, 131-67.
- Dukes, J. D., Fish, L., Richardson, J. D., Blaikley, E., Burns, S., Caunt, C. J., Chalmers, A. D. & Whitley, P. 2011. Functional ESCRT machinery is required for constitutive recycling of claudin-1 and maintenance of polarity in vertebrate epithelial cells. *Mol Biol Cell*, 22, 3192-205.
- Dunn, K. W., Kamocka, M. M. & McDonald, J. H. 2011. A practical guide to evaluating colocalization in biological microscopy. *Am J Physiol Cell Physiol*, 300, C723-42.
- Echeverri, C. J., Beachy, P. A., Baum, B., Boutros, M., Buchholz, F., Chanda, S. K., Downward, J., Ellenberg, J., Fraser, A. G., Hacohen, N., *et al.* 2006. Minimizing the risk of reporting false positives in large-scale RNAi screens. *Nat Methods*, 3, 777-9.
- Eden, E. R., Huang, F., Sorkin, A. & Futter, C. E. 2012. The Role of EGF Receptor Ubiquitination in Regulating Its Intracellular Traffic. *Traffic*, 13, 329-337.
- Effantin, G., Dordor, A., Sandrin, V., Martinelli, N., Sundquist, W. I., Schoehn, G. & Weissenhorn, W. 2013. ESCRT-III CHMP2A and CHMP3 form variable helical polymers in vitro and act synergistically during HIV-1 budding. *Cell Microbiol*, 15, 213-26.
- Ekström, E. J., Bergenfelz, C., Von Bülow, V., Serifler, F., Carlemalm, E., Jönsson, G., Andersson, T. & Leandersson, K. 2014. WNT5A induces release of exosomes containing pro-angiogenic and immunosuppressive factors from malignant melanoma cells. *Mol Cancer*, 13, 88.
- Erzberger, J. P. & Berger, J. M. 2006. Evolutionary relationships and structural mechanisms of AAA+ proteins. *Annu Rev Biophys Biomol Struct*, 35, 93-114.
- Fahey, M. S., Paterson, I. C., Stone, A., Collier, A. J., Heung, Y. L., Davies, M., Patel, V., Parkinson, E. K. & Prime, S. S. 1996. Dysregulation of autocrine TGF-beta isoform production and ligand responses in human tumour-derived and Ha-ras-transfected keratinocytes and fibroblasts. *Br J Cancer*, 74, 1074-80.
- Fedorov, Y., Anderson, E. M., Birmingham, A., Reynolds, A., Karpilow, J., Robinson, K., Leake, D., Marshall, W. S. & Khvorova, A. 2006. Off-target effects by siRNA can induce toxic phenotype. *Rna*, 12, 1188-96.
- Feller, L. & Lemmer, J. 2012. Oral Squamous Cell Carcinoma: Epidemiology, Clinical Presentation and Treatment. *Journal of Cancer Therapy*, Vol.03No.04, 6.
- Feller, L. L., Khammissa, R. R., Kramer, B. B. & Lemmer, J. J. 2013. Oral squamous cell carcinoma in relation to field precancerisation: pathobiology. *Cancer cell international*, 13, 31-31.
- Filimonenko, M., Stuffers, S., Raiborg, C., Yamamoto, A., Malerød, L., Fisher, E. M., Isaacs,

A., Brech, A., Stenmark, H. & Simonsen, A. 2007. Functional multivesicular bodies are required for autophagic clearance of protein aggregates associated with neurodegenerative disease. *J Cell Biol*, 179, 485-500.

Flores-Rodriguez, N., Kenwright, D. A., Chung, P.-H., Harrison, A. W., Stefani, F., Waigh, T. A., Allan, V. J. & Woodman, P. G. 2015. ESCRT-0 marks an APPL1-independent transit route for EGFR between the cell surface and the EEA1-positive early endosome. *Journal of Cell Science*, 128, 755-767.

Fraser, J., Simpson, J., Fontana, R., Kishi-Itakura, C., Ktistakis, N. T. & Gammoh, N. 2019. Targeting of early endosomes by autophagy facilitates EGFR recycling and signalling. *EMBO reports*, 20, e47734-e47734.

Frickey, T. & Lupas, A. N. 2004. Phylogenetic analysis of AAA proteins. *Journal of Structural Biology*, 146, 2-10.

Fu, Y., Sander, J. D., Reyon, D., Cascio, V. M. & Joung, J. K. 2014. Improving CRISPR-Cas nuclease specificity using truncated guide RNAs. *Nature Biotechnology*, 32, 279-284.

Fujita, H., Yamanaka, M., Imamura, K., Tanaka, Y., Nara, A., Yoshimori, T., Yokota, S. & Himeno, M. 2003. A dominant negative form of the AAA ATPase SKD1/VPS4 impairs membrane trafficking out of endosomal/lysosomal compartments: class E vps phenotype in mammalian cells. *Journal of Cell Science*, 116, 401-414.

Fujiwara, T., Eguchi, T., Sogawa, C., Ono, K., Murakami, J., Ibaragi, S., Asaumi, J.-I., Calderwood, S. K., Okamoto, K. & Kozaki, K.-I. 2018a. Carcinogenic epithelial-mesenchymal transition initiated by oral cancer exosomes is inhibited by anti-EGFR antibody cetuximab. *Oral Oncology*, 86, 251-257.

Fujiwara, T., Eguchi, T., Sogawa, C., Ono, K., Murakami, J., Ibaragi, S., Asaumi, J.-I., Okamoto, K., Calderwood, S. K. & Kozaki, K.-I. 2018b. Anti-EGFR antibody cetuximab is secreted by oral squamous cell carcinoma and alters EGF-driven mesenchymal transition. *Biochemical and Biophysical Research Communications*, 503, 1267-1272.

Gahlth, D., Levy, C., Heaven, G., Stefani, F., Wunderley, L., Mould, P., Cliff, M. J., Bella, J., Fielding, A. J., Woodman, P., *et al.* 2016. Structural Basis for Selective Interaction between the ESCRT Regulator HD-PTP and UBAP1. *Structure*, 24, 2115-2126.

Gaj, T., Sirk, S. J., Shui, S. L. & Liu, J. 2016. Genome-Editing Technologies: Principles and Applications. *Cold Spring Harb Perspect Biol*, 8.

Gaullier, J. M., Ronning, E., Gillooly, D. J. & Stenmark, H. 2000. Interaction of the EEA1 FYVE finger with phosphatidylinositol 3-phosphate and early endosomes. Role of conserved residues. *J Biol Chem*, 275, 24595-600.

Gaullier, J. M., Simonsen, A., D'arrigo, A., Bremnes, B., Stenmark, H. & Aasland, R. 1998. FYVE fingers bind PtdIns(3)P. *Nature*, 394, 432-3.

- Géminard, C., De Gassart, A., Blanc, L. & Vidal, M. 2004. Degradation of AP2 during reticulocyte maturation enhances binding of hsc70 and Alix to a common site on TFR for sorting into exosomes. *Traffic*, 5, 181-93.
- Gill, D. J., Teo, H., Sun, J., Perisic, O., Veprintsev, D. B., Emr, S. D. & Williams, R. L. 2007. Structural insight into the ESCRT-I/-II link and its role in MVB trafficking. *Embo j*, 26, 600-12.
- Girard, E., Chmiest, D., Fournier, N., Johannes, L., Paul, J. L., Védie, B. & Lamaze, C. 2014. Rab7 is functionally required for selective cargo sorting at the early endosome. *Traffic*, 15, 309-26.
- Gonciarz, M. D., Whitby, F. G., Eckert, D. M., Kieffer, C., Heroux, A., Sundquist, W. I. & Hill, C. P. 2008. Biochemical and structural studies of yeast Vps4 oligomerization. *J Mol Biol*, 384, 878-95.
- Gopal, S. K., Greening, D. W., Rai, A., Chen, M., Xu, R., Shafiq, A., Mathias, R. A., Zhu, H. J. & Simpson, R. J. 2017. Extracellular vesicles: their role in cancer biology and epithelial-mesenchymal transition. *Biochem J*, 474, 21-45.
- Gotzmann, J., Mikula, M., Eger, A., Schulte-Hermann, R., Foisner, R., Beug, H. & Mikulits, W. 2004. Molecular aspects of epithelial cell plasticity: implications for local tumor invasion and metastasis. *Mutat Res*, 566, 9-20.
- Grant, B. D. & Donaldson, J. G. 2009. Pathways and mechanisms of endocytic recycling. *Nat Rev Mol Cell Biol*, 10, 597-608.
- Grivennikov, S. I., Greten, F. R. & Karin, M. 2010. Immunity, inflammation, and cancer. *Cell*, 140, 883-899.
- Gullapalli, A., Wolfe, B. L., Griffin, C. T., Magnuson, T. & Trejo, J. 2006. An essential role for SNX1 in lysosomal sorting of protease-activated receptor-1: evidence for retromer-, Hrs-, and Tsg101-independent functions of sorting nexins. *Mol Biol Cell*, 17, 1228-38.
- Guo, Y., Tan, J., Miao, Y., Sun, Z. & Zhang, Q. 2019. Effects of Microvesicles on Cell Apoptosis under Hypoxia. *Oxidative medicine and cellular longevity*, 2019, 5972152-5972152.
- Gurung, S., Perocheau, D., Touramanidou, L. & Baruteau, J. 2021. The exosome journey: from biogenesis to uptake and intracellular signalling. *Cell Communication and Signaling*, 19, 47.
- Haglund, K. & Dikic, I. 2012. The role of ubiquitylation in receptor endocytosis and endosomal sorting. *Journal of Cell Science*, 125, 265-275.
- Hall, B., Limaye, A. & Kulkarni, A. B. 2009. Overview: generation of gene knockout mice. *Curr Protoc Cell Biol*, Chapter 19, Unit 19.12 19.12.1-17.
- Hammerman, P. S., Hayes, D. N. & Grandis, J. R. 2015. Therapeutic insights from genomic

- studies of head and neck squamous cell carcinomas. *Cancer Discov*, 5, 239-44.
- Han, H., Monroe, N., Sundquist, W. I., Shen, P. S. & Hill, C. P. 2017. The AAA ATPase Vps4 binds ESCRT-III substrates through a repeating array of dipeptide-binding pockets. *Elife*, 6.
- Hanahan, D. & Weinberg, Robert a. 2011. Hallmarks of Cancer: The Next Generation. *Cell*, 144, 646-674.
- Hanson, P. I. & Whiteheart, S. W. 2005. AAA+ proteins: have engine, will work. *Nat Rev Mol Cell Biol*, 6, 519-29.
- Hanyaloglu, A. C., Mccullagh, E. & Von Zastrow, M. 2005. Essential role of Hrs in a recycling mechanism mediating functional resensitization of cell signaling. *Embo j*, 24, 2265-83.
- Hartmann, C., Chami, M., Zachariae, U., De Groot, B. L., Engel, A. & Grütter, M. G. 2008. Vacuolar protein sorting: two different functional states of the AAA-ATPase Vps4p. *J Mol Biol*, 377, 352-63.
- Headley, M. B., Bins, A., Nip, A., Roberts, E. W., Looney, M. R., Gerard, A. & Krummel, M. F. 2016. Visualization of immediate immune responses to pioneer metastatic cells in the lung. *Nature*, 531, 513-517.
- Hendel, A., Bak, R. O., Clark, J. T., Kennedy, A. B., Ryan, D. E., Roy, S., Steinfeld, I., Lunstad, B. D., Kaiser, R. J., Wilkens, A. B., *et al.* 2015. Chemically modified guide RNAs enhance CRISPR-Cas genome editing in human primary cells. *Nature Biotechnology*, 33, 985-989.
- Hendriks, D., Clevers, H. & Artegiani, B. 2020. CRISPR-Cas Tools and Their Application in Genetic Engineering of Human Stem Cells and Organoids. *Cell Stem Cell*, 27, 705-731.
- Henne, William m., Buchkovich, Nicholas j. & Emr, Scott d. 2011. The ESCRT Pathway. *Developmental Cell*, 21, 77-91.
- Henne, W. M., Stenmark, H. & Emr, S. D. 2013. Molecular mechanisms of the membrane sculpting ESCRT pathway. *Cold Spring Harb Perspect Biol*, 5.
- Herz, H. M., Chen, Z., Scherr, H., Lackey, M., Bolduc, C. & Bergmann, A. 2006. vps25 mosaics display non-autonomous cell survival and overgrowth, and autonomous apoptosis. *Development*, 133, 1871-80.
- Hessvik, N. P. & Llorente, A. 2018. Current knowledge on exosome biogenesis and release. *Cellular and molecular life sciences : CMLS*, 75, 193-208.
- Hierro, A., Sun, J., Rusnak, A. S., Kim, J., Prag, G., Emr, S. D. & Hurley, J. H. 2004. Structure of the ESCRT-II endosomal trafficking complex. *Nature*, 431, 221-5.
- Hingorani, S. R. 2015. Intercepting Cancer Communiques: Exosomes as Heralds of Malignancy. *Cancer Cell*, 28, 151-3.

- Hirano, S., Suzuki, N., Slagsvold, T., Kawasaki, M., Trambaiolo, D., Kato, R., Stenmark, H. & Wakatsuki, S. 2006. Structural basis of ubiquitin recognition by mammalian Eap45 GLUE domain. *Nat Struct Mol Biol*, 13, 1031-2.
- Hislop, J. N., Marley, A. & Von Zastrow, M. 2004. Role of mammalian vacuolar protein-sorting proteins in endocytic trafficking of a non-ubiquitinated G protein-coupled receptor to lysosomes. *J Biol Chem*, 279, 22522-31.
- Hood, J. L. 2016. Melanoma exosome induction of endothelial cell GM-CSF in pre-metastatic lymph nodes may result in different M1 and M2 macrophage mediated angiogenic processes. *Med Hypotheses*, 94, 118-22.
- Hornick, C. A., Hamilton, R. L., Spaziani, E., Enders, G. H. & Havel, R. J. 1985. Isolation and characterization of multivesicular bodies from rat hepatocytes: an organelle distinct from secretory vesicles of the Golgi apparatus. *J Cell Biol*, 100, 1558-69.
- Hoshino, A., Costa-Silva, B., Shen, T.-L., Rodrigues, G., Hashimoto, A., Tesic Mark, M., Molina, H., Kohsaka, S., Di Giannatale, A., Ceder, S., *et al.* 2015. Tumour exosome integrins determine organotropic metastasis. *Nature*, 527, 329-335.
- Hoshino, D., Kirkbride, K. C., Costello, K., Clark, E. S., Sinha, S., Grega-Larson, N., Tyska, M. J. & Weaver, A. M. 2013. Exosome secretion is enhanced by invadopodia and drives invasive behavior. *Cell Rep*, 5, 1159-68.
- Hsu, P. D., Lander, E. S. & Zhang, F. 2014. Development and applications of CRISPR-Cas9 for genome engineering. *Cell*, 157, 1262-1278.
- Hsu, P. D., Scott, D. A., Weinstein, J. A., Ran, F. A., Konermann, S., Agarwala, V., Li, Y., Fine, E. J., Wu, X., Shalem, O., *et al.* 2013. DNA targeting specificity of RNA-guided Cas9 nucleases. *Nature Biotechnology*, 31, 827-832.
- Hunt, S., Jones, A. V., Hinsley, E. E., Whawell, S. A. & Lambert, D. W. 2011. MicroRNA-124 suppresses oral squamous cell carcinoma motility by targeting ITGB1. *FEBS Lett*, 585, 187-92.
- Huotari, J. & Helenius, A. 2011. Endosome maturation. *Embo j*, 30, 3481-500.
- Hurley, J. H. 2008. ESCRT complexes and the biogenesis of multivesicular bodies. *Curr Opin Cell Biol*, 20, 4-11.
- Hurley, J. H. 2015. ESCRTs are everywhere. *The EMBO Journal*, 34, 2398-2407.
- Hurley, J. H. & Yang, D. 2008. MIT Domainia. *Developmental Cell*, 14, 6-8.
- Hurwitz, S. N., Conlon, M. M., Rider, M. A., Brownstein, N. C. & Meckes, D. G., Jr. 2016. Nanoparticle analysis sheds budding insights into genetic drivers of extracellular vesicle biogenesis. *J Extracell Vesicles*, 5, 31295.

Husebye, H., Halaas, Ø., Stenmark, H., Tunheim, G., Sandanger, Ø., Bogen, B., Brech, A., Latz, E. & Espevik, T. 2006. Endocytic pathways regulate Toll-like receptor 4 signaling and link innate and adaptive immunity. *Embo j*, 25, 683-92.

Im, Y. J. & Hurley, J. H. 2008. Integrated structural model and membrane targeting mechanism of the human ESCRT-II complex. *Dev Cell*, 14, 902-13.

Im, Y. J., Wollert, T., Boura, E. & Hurley, J. H. 2009. Structure and function of the ESCRT-II-III interface in multivesicular body biogenesis. *Dev Cell*, 17, 234-43.

Irion, U. & St Johnston, D. 2007. bicoid RNA localization requires specific binding of an endosomal sorting complex. *Nature*, 445, 554-8.

Jackson, C. E., Scruggs, B. S., Schaffer, J. E. & Hanson, P. I. 2017. Effects of Inhibiting VPS4 Support a General Role for ESCRTs in Extracellular Vesicle Biogenesis. *Biophys J*, 113, 1342-1352.

Jékely, G. & Rørth, P. 2003. Hrs mediates downregulation of multiple signalling receptors in Drosophila. *EMBO Rep*, 4, 1163-8.

Jennings, L. R., Colley, H. E., Ong, J., Panagakos, F., Masters, J. G., Trivedi, H. M., Murdoch, C. & Whawell, S. 2016. Development and Characterization of In Vitro Human Oral Mucosal Equivalents Derived from Immortalized Oral Keratinocytes. *Tissue Engineering Part C: Methods*, 22, 1108-1117.

Jiang, L., Paone, S., Caruso, S., Atkin-Smith, G. K., Phan, T. K., Hulett, M. D. & Poon, I. K. H. 2017. Determining the contents and cell origins of apoptotic bodies by flow cytometry. *Scientific Reports*, 7, 14444.

Jiang, Y., Ou, Y. & Cheng, X. 2013. Role of TSG101 in cancer. *FBL*, 18, 279-288.

Jingushi, K., Uemura, M., Nakano, K., Hayashi, Y., Wang, C., Ishizuya, Y., Yamamoto, Y., Hayashi, T., Kinouchi, T., Matsuzaki, K., *et al.* 2019. Leukocyte-associated immunoglobulin-like receptor 1 promotes tumorigenesis in RCC. *Oncol Rep*, 41, 1293-1303.

Johnson, I. R., Parkinson-Lawrence, E. J., Shandala, T., Weigert, R., Butler, L. M. & Brooks, D. A. 2014. Altered endosome biogenesis in prostate cancer has biomarker potential. *Mol Cancer Res*, 12, 1851-62.

Jovic, M., Sharma, M., Rahajeng, J. & Caplan, S. 2010. The early endosome: a busy sorting station for proteins at the crossroads. *Histology and histopathology*, 25, 99-112.

Katoh, M. 2013. Therapeutics targeting angiogenesis: genetics and epigenetics, extracellular miRNAs and signaling networks (Review). *International journal of molecular medicine*, 32, 763-767.

Katsiarimpa, A., Kalinowska, K., Anzenberger, F., Weis, C., Ostertag, M., Tsutsumi, C.,

Schwechheimer, C., Brunner, F., Huckelhoven, R. & Isono, E. 2013. The deubiquitinating enzyme AMSH1 and the ESCRT-III subunit VPS2.1 are required for autophagic degradation in Arabidopsis. *Plant Cell*, 25, 2236-52.

Katz, M., Shtiegman, K., Tal-Or, P., Yakir, L., Mosesson, Y., Harari, D., Machluf, Y., Asao, H., Jovin, T., Sugamura, K., *et al.* 2002. Ligand-independent degradation of epidermal growth factor receptor involves receptor ubiquitylation and Hgs, an adaptor whose ubiquitin-interacting motif targets ubiquitylation by Nedd4. *Traffic*, 3, 740-51.

Katzmann, D. J., Stefan, C. J., Babst, M. & Emr, S. D. 2003. Vps27 recruits ESCRT machinery to endosomes during MVB sorting. *J Cell Biol*, 162, 413-23.

Kaur, G. & Lakkaraju, A. 2018. Early Endosome Morphology in Health and Disease. *Advances in experimental medicine and biology*, 1074, 335-343.

Khongorzul, P., Ling, C. J., Khan, F. U., Ihsan, A. U. & Zhang, J. 2020. Antibody–Drug Conjugates: A Comprehensive Review Antibody–Drug Conjugates in Cancer Immunotherapy. *Molecular Cancer Research*, 18, 3-19.

Kim, Y. H. 2010. Small interfering RNA (siRNA): a hope for the loss-of-function studies in anesthesiology? *Korean J Anesthesiol*, 59, 369-70.

Kimura, I., Kitahara, H., Ooi, K., Kato, K., Noguchi, N., Yoshizawa, K., Nakamura, H. & Kawashiri, S. 2016. Loss of epidermal growth factor receptor expression in oral squamous cell carcinoma is associated with invasiveness and epithelial-mesenchymal transition. *Oncol Lett*, 11, 201-207.

Kleinstiver, B. P., Pattanayak, V., Prew, M. S., Tsai, S. Q., Nguyen, N. T., Zheng, Z. & Joung, J. K. 2016. High-fidelity CRISPR–Cas9 nucleases with no detectable genome-wide off-target effects. *Nature*, 529, 490-495.

Kojima, K., Amano, Y., Yoshino, K., Tanaka, N., Sugamura, K. & Takeshita, T. 2014. ESCRT-0 protein hepatocyte growth factor-regulated tyrosine kinase substrate (Hrs) is targeted to endosomes independently of signal-transducing adaptor molecule (STAM) and the complex formation with STAM promotes its endosomal dissociation. *J Biol Chem*, 289, 33296-310.

Kolmus, K., Erdenebat, P., Szymańska, E., Stewig, B., Goryca, K., Derezińska-Wólek, E., Szumera-Ciećkiewicz, A., Brewińska-Olchowik, M., Piwocka, K., Prochorec-Sobieszek, M., *et al.* 2021. Concurrent depletion of Vps37 proteins evokes ESCRT-I destabilization and profound cellular stress responses. *Journal of Cell Science*, 134, jcs250951.

Komada, M. & Soriano, P. 1999. Hrs, a FYVE finger protein localized to early endosomes, is implicated in vesicular traffic and required for ventral folding morphogenesis. *Genes Dev*, 13, 1475-85.

Kornilov, R., Puhka, M., Mannerström, B., Hiidenmaa, H., Peltoniemi, H., Siljander, P., Seppänen-Kajansinkko, R. & Kaur, S. 2018. Efficient ultrafiltration-based protocol to deplete

extracellular vesicles from fetal bovine serum. *J Extracell Vesicles*, 7, 1422674.

Kostelansky, M. S., Schluter, C., Tam, Y. Y., Lee, S., Ghirlando, R., Beach, B., Conibear, E. & Hurley, J. H. 2007. Molecular architecture and functional model of the complete yeast ESCRT-I heterotetramer. *Cell*, 129, 485-98.

Kostelansky, M. S., Sun, J., Lee, S., Kim, J., Ghirlando, R., Hierro, A., Emr, S. D. & Hurley, J. H. 2006. Structural and functional organization of the ESCRT-I trafficking complex. *Cell*, 125, 113-26.

Kowal, J., Arras, G., Colombo, M., Jouve, M., Morath, J. P., Primdal-Bengtson, B., Dingli, F., Loew, D., Tkach, M. & Théry, C. 2016. Proteomic comparison defines novel markers to characterize heterogeneous populations of extracellular vesicle subtypes. *Proc Natl Acad Sci U S A*, 113, E968-77.

Kugimoto, T., Morita, K. & Omura, K. 2012. Development of oral cancer screening test by detection of squamous cell carcinoma among exfoliated oral mucosal cells. *Oral Oncol*, 48, 794-8.

Landsberg, M. J., Vajjhala, P. R., Rothnagel, R., Munn, A. L. & Hankamer, B. 2009. Three-dimensional structure of AAA ATPase Vps4: advancing structural insights into the mechanisms of endosomal sorting and enveloped virus budding. *Structure*, 17, 427-37.

Lata, S., Roessle, M., Solomons, J., Jamin, M., Gottlinger, H. G., Svergun, D. I. & Weissenhorn, W. 2008a. Structural basis for autoinhibition of ESCRT-III CHMP3. *J Mol Biol*, 378, 818-27.

Lata, S., Schoehn, G., Jain, A., Pires, R., Piehler, J., Gottlinger, H. G. & Weissenhorn, W. 2008b. Helical structures of ESCRT-III are disassembled by VPS4. *Science*, 321, 1354-7.

Lee, J., Oh, K.-J., Lee, D., Kim, B. Y., Choi, J. S., Ku, B. & Kim, S. J. 2016. Structural Study of the HD-PTP Bro1 Domain in a Complex with the Core Region of STAM2, a Subunit of ESCRT-0. *PLOS ONE*, 11, e0149113.

Lee, J. A., Beigneux, A., Ahmad, S. T., Young, S. G. & Gao, F. B. 2007. ESCRT-III dysfunction causes autophagosome accumulation and neurodegeneration. *Curr Biol*, 17, 1561-7.

Lee, K., Conboy, M., Park, H. M., Jiang, F., Kim, H. J., Dewitt, M. A., Mackley, V. A., Chang, K., Rao, A., Skinner, C., *et al.* 2017. Nanoparticle delivery of Cas9 ribonucleoprotein and donor DNA in vivo induces homology-directed DNA repair. *Nature Biomedical Engineering*, 1, 889-901.

Li, J., Belogortseva, N., Porter, D. & Park, M. 2008. Chmp1A functions as a novel tumor suppressor gene in human embryonic kidney and ductal pancreatic tumor cells. *Cell Cycle*, 7, 2886-2893.

Li, L., Lu, S., Liang, X., Cao, B., Wang, S., Jiang, J., Luo, H., He, S., Lang, J. & Zhu, G. 2019. γ DTDEs: An Efficient Delivery System for miR-138 with Anti-tumoral and Immunostimulatory

- Roles on Oral Squamous Cell Carcinoma. *Molecular therapy. Nucleic acids*, 14, 101-113.
- Li, M., Liao, L. & Tian, W. 2020. Extracellular Vesicles Derived From Apoptotic Cells: An Essential Link Between Death and Regeneration. *Front Cell Dev Biol*, 8, 573511.
- Li, Z., Wang, T., Xin, C., Song, Y., Kong, J., Xu, J., Liu, Q., Teng, Y., Hou, N., Cheng, X., *et al.* 2022. Hgs Deficiency Caused Restrictive Cardiomyopathy via Disrupting Proteostasis. *Int J Biol Sci*, 18, 2018-2031.
- Lin, A., Giuliano, C. J., Palladino, A., John, K. M., Abramowicz, C., Yuan, M. L., Sausville, E. L., Lukow, D. A., Liu, L., Chait, A. R., *et al.* 2019. Off-target toxicity is a common mechanism of action of cancer drugs undergoing clinical trials. *Sci Transl Med*, 11.
- Lin, X., Ruan, X., Anderson, M. G., Mcdowell, J. A., Kroeger, P. E., Fesik, S. W. & Shen, Y. 2005. siRNA-mediated off-target gene silencing triggered by a 7 nt complementation. *Nucleic Acids Res*, 33, 4527-35.
- Liu, C. J., Kao, S. Y., Tu, H. F., Tsai, M. M., Chang, K. W. & Lin, S. C. 2010. Increase of microRNA miR-31 level in plasma could be a potential marker of oral cancer. *Oral Dis*, 16, 360-4.
- Liu, F., Chen, F., Huang, J., Yan, L., Liu, F., Wu, J., Qiu, Y., Zheng, X., Zhang, R., Lin, L., *et al.* 2017. Prospective study on factors affecting the prognosis of oral cancer in a Chinese population. *Oncotarget*, 8, 4352-4359.
- Liu, J., Carmell, M. A., Rivas, F. V., Marsden, C. G., Thomson, J. M., Song, J. J., Hammond, S. M., Joshua-Tor, L. & Hannon, G. J. 2004. Argonaute2 is the catalytic engine of mammalian RNAi. *Science*, 305, 1437-41.
- Liu, L. & Fan, X. D. 2014. CRISPR-Cas system: a powerful tool for genome engineering. *Plant Mol Biol*, 85, 209-18.
- Liu, M., Rehman, S., Tang, X., Gu, K., Fan, Q., Chen, D. & Ma, W. 2018. Methodologies for Improving HDR Efficiency. *Front Genet*, 9, 691.
- Liu, R. T., Huang, C. C., You, H. L., Chou, F. F., Hu, C. C., Chao, F. P., Chen, C. M. & Cheng, J. T. 2002. Overexpression of tumor susceptibility gene TSG101 in human papillary thyroid carcinomas. *Oncogene*, 21, 4830-7.
- Liu, Y., Zhao, L., Li, D., Yin, Y., Zhang, C. Y., Li, J. & Zhang, Y. 2013. Microvesicle-delivery miR-150 promotes tumorigenesis by up-regulating VEGF, and the neutralization of miR-150 attenuate tumor development. *Protein Cell*, 4, 932-41.
- Llorente, A., Skotland, T., Sylvänne, T., Kauhanen, D., Róg, T., Orłowski, A., Vattulainen, I., Ekroos, K. & Sandvig, K. 2013. Molecular lipidomics of exosomes released by PC-3 prostate cancer cells. *Biochim Biophys Acta*, 1831, 1302-9.

- Lloyd, T. E., Atkinson, R., Wu, M. N., Zhou, Y., Pennetta, G. & Bellen, H. J. 2002a. Hrs Regulates Endosome Membrane Invagination and Tyrosine Kinase Receptor Signaling in *Drosophila*. *Cell*, 108, 261-269.
- Lloyd, T. E., Atkinson, R., Wu, M. N., Zhou, Y., Pennetta, G. & Bellen, H. J. 2002b. Hrs regulates endosome membrane invagination and tyrosine kinase receptor signaling in *Drosophila*. *Cell*, 108, 261-9.
- Lobert, V. H., Brech, A., Pedersen, N. M., Wesche, J., Oppelt, A., Malerød, L. & Stenmark, H. 2010. Ubiquitination of alpha 5 beta 1 integrin controls fibroblast migration through lysosomal degradation of fibronectin-integrin complexes. *Dev Cell*, 19, 148-59.
- Lottridge, J. M., Flannery, A. R., Vincelli, J. L. & Stevens, T. H. 2006. Vta1p and Vps46p regulate the membrane association and ATPase activity of Vps4p at the yeast multivesicular body. *Proc Natl Acad Sci U S A*, 103, 6202-7.
- Lötvall, J., Hill, A. F., Hochberg, F., Buzás, E. I., Di Vizio, D., Gardiner, C., Gho, Y. S., Kurochkin, I. V., Mathivanan, S., Quesenberry, P., *et al.* 2014. Minimal experimental requirements for definition of extracellular vesicles and their functions: a position statement from the International Society for Extracellular Vesicles. *J Extracell Vesicles*, 3, 26913.
- Lu, Q., Hope, L. W., Brasch, M., Reinhard, C. & Cohen, S. N. 2003. TSG101 interaction with HRS mediates endosomal trafficking and receptor down-regulation. *Proc Natl Acad Sci U S A*, 100, 7626-31.
- Luhtala, N. & Odorizzi, G. 2004. Bro1 coordinates deubiquitination in the multivesicular body pathway by recruiting Doa4 to endosomes. *The Journal of cell biology*, 166, 717-729.
- Ma, X. R., Edmund Sim, U. H., Pauline, B., Patricia, L. & Rahman, J. 2008. Overexpression of WNT2 and TSG101 genes in colorectal carcinoma. *Trop Biomed*, 25, 46-57.
- Maacha, S., Bhat, A. A., Jimenez, L., Raza, A., Haris, M., Uddin, S. & Grivel, J. C. 2019. Extracellular vesicles-mediated intercellular communication: roles in the tumor microenvironment and anti-cancer drug resistance. *Mol Cancer*, 18, 55.
- Maas, S. L. N., Breakefield, X. O. & Weaver, A. M. 2017. Extracellular Vesicles: Unique Intercellular Delivery Vehicles. *Trends Cell Biol*, 27, 172-188.
- Malerød, L., Stuffers, S., Brech, A. & Stenmark, H. 2007. Vps22/EAP30 in ESCRT-II mediates endosomal sorting of growth factor and chemokine receptors destined for lysosomal degradation. *Traffic*, 8, 1617-29.
- Manikandan, M., Deva Magendhra Rao, A. K., Arunkumar, G., Manickavasagam, M., Rajkumar, K. S., Rajaraman, R. & Munirajan, A. K. 2016. Oral squamous cell carcinoma: microRNA expression profiling and integrative analyses for elucidation of tumorigenesis mechanism. *Molecular Cancer*, 15, 28.

Manteghi, S., Gingras, M.-C., Kharitidi, D., Galarneau, L., Marques, M., Yan, M., Cencic, R., Robert, F., Paquet, M., Witcher, M., *et al.* 2016. Haploinsufficiency of the ESCRT Component HD-PTP Predisposes to Cancer. *Cell Reports*, 15, 1893-1900.

Marayati, R., Stafman, L. L., Williams, A. P., Bownes, L. V., Quinn, C. H., Markert, H. R., Easlick, J. L., Stewart, J. E., Crossman, D. K., Mroczek-Musulman, E., *et al.* 2022. CRISPR/Cas9-mediated knockout of PIM3 suppresses tumorigenesis and cancer cell stemness in human hepatoblastoma cells. *Cancer Gene Ther*, 29, 558-572.

Markopoulos, A. K. 2012. Current aspects on oral squamous cell carcinoma. *Open Dent J*, 6, 126-30.

Martin, H. C., Wani, S., Steptoe, A. L., Krishnan, K., Nones, K., Nourbakhsh, E., Vlassov, A., Grimmond, S. M. & Cloonan, N. 2014. Imperfect centered miRNA binding sites are common and can mediate repression of target mRNAs. *Genome Biology*, 15, R51.

Martinez, J., Patkaniowska, A., Urlaub, H., Lührmann, R. & Tuschl, T. 2002. Single-stranded antisense siRNAs guide target RNA cleavage in RNAi. *Cell*, 110, 563-74.

Matsumoto, Y., Kano, M., Akutsu, Y., Hanari, N., Hoshino, I., Murakami, K., Usui, A., Suito, H., Takahashi, M., Otsuka, R., *et al.* 2016. Quantification of plasma exosome is a potential prognostic marker for esophageal squamous cell carcinoma. *Oncol Rep*, 36, 2535-2543.

Mattisek, C. & Teis, D. 2014. The role of the endosomal sorting complexes required for transport (ESCRT) in tumorigenesis. *Mol Membr Biol*, 31, 111-9.

Mayers, J. R., Fyfe, I., Schuh, A. L., Chapman, E. R., Edwardson, J. M. & Audhya, A. 2011. ESCRT-0 assembles as a heterotetrameric complex on membranes and binds multiple ubiquitinated cargoes simultaneously. *J Biol Chem*, 286, 9636-45.

McConnell, R. E., Youniss, M., Gnanasambandam, B., Shah, P., Zhang, W. & Finn, J. D. 2022. Transfection reagent artefact likely accounts for some reports of extracellular vesicle function. *Journal of Extracellular Vesicles*, 11, e12253.

Mccullough, J., Clague, M. J. & Urbé, S. 2004. AMSH is an endosome-associated ubiquitin isopeptidase. *J Cell Biol*, 166, 487-92.

Mcgregor, F., Muntoni, A., Fleming, J., Brown, J., Felix, D. H., Macdonald, D. G., Parkinson, E. K. & Harrison, P. R. 2002. Molecular changes associated with oral dysplasia progression and acquisition of immortality: potential for its reversal by 5-azacytidine. *Cancer Res*, 62, 4757-66.

Melean, J. W., Wilson, J. A., Tian, T., Watson, J. A., Vanhart, M., Bean, A. J., Scherer, S. S., Crossman, D. K., Ubogu, E. & Wilson, S. M. 2022. Disruption of Endosomal Sorting in Schwann Cells Leads to Defective Myelination and Endosomal Abnormalities Observed in Charcot-Marie-Tooth Disease. *The Journal of Neuroscience*, 42, 5085-5101.

Mehrara, E., Forssell-Aronsson, E., Ahlman, H. & Bernhardt, P. 2007. Specific growth rate

versus doubling time for quantitative characterization of tumor growth rate. *Cancer Res*, 67, 3970-5.

Meister, G. & Tuschl, T. 2004. Mechanisms of gene silencing by double-stranded RNA. *Nature*, 431, 343-9.

Merrill, S. A. & Hanson, P. I. 2010. Activation of human VPS4A by ESCRT-III proteins reveals ability of substrates to relieve enzyme autoinhibition. *J Biol Chem*, 285, 35428-38.

Miller, D. S. J., Bloxham, R. D., Jiang, M., Gori, I., Saunders, R. E., Das, D., Chakravarty, P., Howell, M. & Hill, C. S. 2018. The Dynamics of TGF- β Signaling Are Dictated by Receptor Trafficking via the ESCRT Machinery. *Cell Reports*, 25, 1841-1855.e5.

Mizuno, E., Iura, T., Mukai, A., Yoshimori, T., Kitamura, N. & Komada, M. 2005. Regulation of epidermal growth factor receptor down-regulation by UBPY-mediated deubiquitination at endosomes. *Mol Biol Cell*, 16, 5163-74.

Momen-Heravi, F. & Bala, S. 2018. Extracellular vesicles in oral squamous carcinoma carry oncogenic miRNA profile and reprogram monocytes via NF- κ B pathway. *Oncotarget*, 9, 34838-34854.

Monroe, N., Han, H., Gonciarz, M. D., Eckert, D. M., Karren, M. A., Whitby, F. G., Sundquist, W. I. & Hill, C. P. 2014. The oligomeric state of the active Vps4 AAA ATPase. *J Mol Biol*, 426, 510-25.

Morita, E., Sandrin, V., Alam, S. L., Eckert, D. M., Gygi, S. P. & Sundquist, W. I. 2007a. Identification of human MVB12 proteins as ESCRT-I subunits that function in HIV budding. *Cell Host Microbe*, 2, 41-53.

Morita, E., Sandrin, V., Chung, H. Y., Morham, S. G., Gygi, S. P., Rodesch, C. K. & Sundquist, W. I. 2007b. Human ESCRT and ALIX proteins interact with proteins of the midbody and function in cytokinesis. *Embo j*, 26, 4215-27.

Moroishi, T., Hayashi, T., Pan, W.-W., Fujita, Y., Holt, M. V., Qin, J., Carson, D. A. & Guan, K.-L. 2016. The Hippo Pathway Kinases LATS1/2 Suppress Cancer Immunity. *Cell*, 167, 1525-1539.e17.

Moser Von Filseck, J., Barberi, L., Talledge, N., Johnson, I. E., Frost, A., Lenz, M. & Roux, A. 2020. Anisotropic ESCRT-III architecture governs helical membrane tube formation. *Nature Communications*, 11, 1516.

Mosesso, N., Nagel, M.-K. & Isono, E. 2019. Ubiquitin recognition in endocytic trafficking – with or without ESCRT-0. *Journal of Cell Science*, 132, jcs232868.

Moss, D. K., Betin, V. M., Malesinski, S. D. & Lane, J. D. 2006. A novel role for microtubules in apoptotic chromatin dynamics and cellular fragmentation. *J Cell Sci*, 119, 2362-74.

- Mulcahy, L. A., Pink, R. C. & Carter, D. R. 2014. Routes and mechanisms of extracellular vesicle uptake. *J Extracell Vesicles*, 3.
- Muralidharan-Chari, V., Clancy, J., Plou, C., Romao, M., Chavrier, P., Raposo, G. & D'souza-Schorey, C. 2009. ARF6-regulated shedding of tumor cell-derived plasma membrane microvesicles. *Current biology : CB*, 19, 1875-1885.
- Muzioł, T., Pineda-Molina, E., Ravelli, R. B., Zamborlini, A., Usami, Y., Göttlinger, H. & Weissenhorn, W. 2006. Structural basis for budding by the ESCRT-III factor CHMP3. *Dev Cell*, 10, 821-30.
- Nabhan, J. F., Hu, R., Oh, R. S., Cohen, S. N. & Lu, Q. 2012. Formation and release of arrestin domain-containing protein 1-mediated microvesicles (ARMMs) at plasma membrane by recruitment of TSG101 protein. *Proceedings of the National Academy of Sciences of the United States of America*, 109, 4146-4151.
- Nagano, M., Toshima, J. Y., Siekhaus, D. E. & Toshima, J. 2019. Rab5-mediated endosome formation is regulated at the trans-Golgi network. *Commun Biol*, 2, 419.
- Nazarenko, I., Rana, S., Baumann, A., Mclear, J., Hellwig, A., Trendelenburg, M., Lochnit, G., Preissner, K. T. & Zöller, M. 2010. Cell Surface Tetraspanin Tspan8 Contributes to Molecular Pathways of Exosome-Induced Endothelial Cell Activation. *Cancer Research*, 70, 1668.
- Nickerson, D. P., West, M., Henry, R. & Odorizzi, G. 2010. Regulators of Vps4 ATPase activity at endosomes differentially influence the size and rate of formation of intraluminal vesicles. *Mol Biol Cell*, 21, 1023-32.
- Norgan, A. P., Davies, B. A., Azmi, I. F., Schroeder, A. S., Payne, J. A., Lynch, G. M., Xu, Z. & Katzmann, D. J. 2013. Relief of autoinhibition enhances Vta1 activation of Vps4 via the Vps4 stimulatory element. *J Biol Chem*, 288, 26147-26156.
- Odorizzi, G., Katzmann, D. J., Babst, M., Audhya, A. & Emr, S. D. 2003. Bro1 is an endosome-associated protein that functions in the MVB pathway in *Saccharomyces cerevisiae*. *Journal of cell science*, 116, 1893-1903.
- Oh, K. B., Stanton, M. J., West, W. W., Todd, G. L. & Wagner, K. U. 2007. Tsg101 is upregulated in a subset of invasive human breast cancers and its targeted overexpression in transgenic mice reveals weak oncogenic properties for mammary cancer initiation. *Oncogene*, 26, 5950-9.
- Ostrowski, M., Carmo, N. B., Krumeich, S., Fanget, I., Raposo, G., Savina, A., Moita, C. F., Schauer, K., Hume, A. N., Freitas, R. P., *et al.* 2010. Rab27a and Rab27b control different steps of the exosome secretion pathway. *Nat Cell Biol*, 12, 19-30; sup pp 1-13.
- Pang, X., Tang, Y. L. & Liang, X. H. 2018. Transforming growth factor- β signaling in head and neck squamous cell carcinoma: Insights into cellular responses. *Oncol Lett*, 16, 4799-4806.

- Park, J. E., Lenter, M. C., Zimmermann, R. N., Garin-Chesa, P., Old, L. J. & Rettig, W. J. 1999. Fibroblast activation protein, a dual specificity serine protease expressed in reactive human tumor stromal fibroblasts. *J Biol Chem*, 274, 36505-12.
- Park, N. J., Zhou, H., Elashoff, D., Henson, B. S., Kastratovic, D. A., Abemayor, E. & Wong, D. T. 2009. Salivary microRNA: Discovery, Characterization, and Clinical Utility for Oral Cancer Detection. *Clinical Cancer Research*, 15, 5473.
- Pashkova, N., Yu, L., Schnicker, N. J., Tseng, C. C., Gakhar, L., Katzmann, D. J. & Piper, R. C. 2021. Interactions of ubiquitin and CHMP5 with the V domain of HD-PTP reveals role for regulation of Vps4 ATPase. *Mol Biol Cell*, 32, ar42.
- Patki, V., Lawe, D. C., Corvera, S., Virbasius, J. V. & Chawla, A. 1998. A functional PtdIns(3)P-binding motif. *Nature*, 394, 433-4.
- Pereira-Leal, J. B. & Seabra, M. C. 2001. Evolution of the Rab family of small GTP-binding proteins. *J Mol Biol*, 313, 889-901.
- Perez-Hernandez, D., Gutiérrez-Vázquez, C., Jorge, I., López-Martín, S., Ursa, A., Sánchez-Madrid, F., Vázquez, J. & Yáñez-Mó, M. 2013. The intracellular interactome of tetraspanin-enriched microdomains reveals their function as sorting machineries toward exosomes. *J Biol Chem*, 288, 11649-61.
- Perez-Torres, M., Valle, B. L., Maihle, N. J., Negron-Vega, L., Nieves-Alicea, R. & Cora, E. M. 2008. Shedding of epidermal growth factor receptor is a regulated process that occurs with overexpression in malignant cells. *Experimental Cell Research*, 314, 2907-2918.
- Pineda-Molina, E., Belrhali, H., Piefer, A. J., Akula, I., Bates, P. & Weissenhorn, W. 2006. The crystal structure of the C-terminal domain of Vps28 reveals a conserved surface required for Vps20 recruitment. *Traffic*, 7, 1007-16.
- Pisitkun, T., Shen, R. F. & Knepper, M. A. 2004. Identification and proteomic profiling of exosomes in human urine. *Proc Natl Acad Sci U S A*, 101, 13368-73.
- Platt, R. J., Chen, S., Zhou, Y., Yim, M. J., Swiech, L., Kempton, H. R., Dahlman, J. E., Parnas, O., Eisenhaure, T. M., Jovanovic, M., *et al.* 2014. CRISPR-Cas9 knockin mice for genome editing and cancer modeling. *Cell*, 159, 440-55.
- Poon, I. K., Chiu, Y. H., Armstrong, A. J., Kinchen, J. M., Juncadella, I. J., Bayliss, D. A. & Ravichandran, K. S. 2014a. Unexpected link between an antibiotic, pannexin channels and apoptosis. *Nature*, 507, 329-34.
- Poon, I. K. H., Lucas, C. D., Rossi, A. G. & Ravichandran, K. S. 2014b. Apoptotic cell clearance: basic biology and therapeutic potential. *Nature reviews. Immunology*, 14, 166-180.
- Pornillos, O., Higginson, D. S., Stray, K. M., Fisher, R. D., Garrus, J. E., Payne, M., He, G. P., Wang, H. E., Morham, S. G. & Sundquist, W. I. 2003. HIV Gag mimics the Tsg101-recruiting

- activity of the human Hrs protein. *J Cell Biol*, 162, 425-34.
- Poteryaev, D., Datta, S., Ackema, K., Zerial, M. & Spang, A. 2010. Identification of the switch in early-to-late endosome transition. *Cell*, 141, 497-508.
- Probert, C., Dottorini, T., Speakman, A., Hunt, S., Nafee, T., Fazeli, A., Wood, S., Brown, J. E. & James, V. 2019. Communication of prostate cancer cells with bone cells via extracellular vesicle RNA; a potential mechanism of metastasis. *Oncogene*, 38, 1751-1763.
- Progida, C., Nielsen, M. S., Koster, G., Bucci, C. & Bakke, O. 2012. Dynamics of Rab7b-dependent transport of sorting receptors. *Traffic*, 13, 1273-85.
- Purba, E. R., Saita, E. I. & Maruyama, I. N. 2017. Activation of the EGF Receptor by Ligand Binding and Oncogenic Mutations: The "Rotation Model". *Cells*, 6.
- Qadir, F., Aziz, M. A., Sari, C. P., Ma, H., Dai, H., Wang, X., Raithatha, D., Da Silva, L. G. L., Hussain, M., Poorkasreiy, S. P., *et al.* 2018. Transcriptome reprogramming by cancer exosomes: identification of novel molecular targets in matrix and immune modulation. *Mol Cancer*, 17, 97.
- Ragin, C. C., Modugno, F. & Gollin, S. M. 2007. The epidemiology and risk factors of head and neck cancer: a focus on human papillomavirus. *J Dent Res*, 86, 104-14.
- Rahdar, M., McMahon, M. A., Prakash, T. P., Swayze, E. E., Bennett, C. F. & Cleveland, D. W. 2015. Synthetic CRISPR RNA-Cas9-guided genome editing in human cells. *Proceedings of the National Academy of Sciences*, 112, E7110-E7117.
- Raiborg, C., Bache, K. G., Gillooly, D. J., Madshus, I. H., Stang, E. & Stenmark, H. 2002. Hrs sorts ubiquitinated proteins into clathrin-coated microdomains of early endosomes. *Nat Cell Biol*, 4, 394-8.
- Raiborg, C., Bremnes, B., Mehlum, A., Gillooly, D. J., D'arrigo, A., Stang, E. & Stenmark, H. 2001. FYVE and coiled-coil domains determine the specific localisation of Hrs to early endosomes. *J Cell Sci*, 114, 2255-63.
- Raiborg, C., Malerød, L., Pedersen, N. M. & Stenmark, H. 2008. Differential functions of Hrs and ESCRT proteins in endocytic membrane trafficking. *Experimental Cell Research*, 314, 801-813.
- Raiborg, C. & Stenmark, H. 2009. The ESCRT machinery in endosomal sorting of ubiquitylated membrane proteins. *Nature*, 458, 445-52.
- Rajagopal, C. & Harikumar, K. B. 2018. The Origin and Functions of Exosomes in Cancer. *Frontiers in Oncology*, 8.
- Raposo, G. & Stoorvogel, W. 2013. Extracellular vesicles: Exosomes, microvesicles, and friends. *Journal of Cell Biology*, 200, 373-383.

- Raposo, G., Tenza, D., Murphy, D. M., Berson, J. F. & Marks, M. S. 2001. Distinct protein sorting and localization to premelanosomes, melanosomes, and lysosomes in pigmented melanocytic cells. *J Cell Biol*, 152, 809-24.
- Raulf, N., Lucarelli, P., Thavaraj, S., Brown, S., Vicencio, J. M., Sauter, T. & Tavassoli, M. 2018. Annexin A1 regulates EGFR activity and alters EGFR-containing tumour-derived exosomes in head and neck cancers. *Eur J Cancer*; 102, 52-68.
- Rayala, S. K., Hollander, P., Balasenthil, S., Molli, P. R., Bean, A. J., Vadlamudi, R. K., Wang, R. A. & Kumar, R. 2006. Hepatocyte growth factor-regulated tyrosine kinase substrate (HRS) interacts with PELP1 and activates MAPK. *J Biol Chem*, 281, 4395-403.
- Razi, M. & Futter, C. E. 2006. Distinct roles for Tsg101 and Hrs in multivesicular body formation and inward vesiculation. *Mol Biol Cell*, 17, 3469-83.
- Ren, K. 2019. Exosomes in perspective: a potential surrogate for stem cell therapy. *Odontology*, 107, 271-284.
- Ren, X. & Hurley, J. H. 2010. VHS domains of ESCRT-0 cooperate in high-avidity binding to polyubiquitinated cargo. *Embo j*, 29, 1045-54.
- Ren, X., Kloer, D. P., Kim, Y. C., Ghirlando, R., Saidi, L. F., Hummer, G. & Hurley, J. H. 2009. Hybrid Structural Model of the Complete Human ESCRT-0 Complex. *Structure*, 17, 406-416.
- Ren, X., Yang, Z., Xu, J., Sun, J., Mao, D., Hu, Y., Yang, S.-J., Qiao, H.-H., Wang, X., Hu, Q., *et al.* 2014. Enhanced Specificity and Efficiency of the CRISPR/Cas9 System with Optimized sgRNA Parameters in Drosophila. *Cell Reports*, 9, 1151-1162.
- Rheinwald, J. G. & Beckett, M. A. 1981. Tumorigenic keratinocyte lines requiring anchorage and fibroblast support cultured from human squamous cell carcinomas. *Cancer Res*, 41, 1657-63.
- Ribeiro, F. A., Noguti, J., Oshima, C. T. & Ribeiro, D. A. 2014. Effective targeting of the epidermal growth factor receptor (EGFR) for treating oral cancer: a promising approach. *Anticancer Res*, 34, 1547-52.
- Rieger, A. M., Nelson, K. L., Konowalchuk, J. D. & Barreda, D. R. 2011. Modified annexin V/propidium iodide apoptosis assay for accurate assessment of cell death. *J Vis Exp*.
- Rink, J., Ghigo, E., Kalaidzidis, Y. & Zerial, M. 2005. Rab Conversion as a Mechanism of Progression from Early to Late Endosomes. *Cell*, 122, 735-749.
- Roberts, P. J. & Der, C. J. 2007. Targeting the Raf-MEK-ERK mitogen-activated protein kinase cascade for the treatment of cancer. *Oncogene*, 26, 3291-310.
- Row, P. E., Prior, I. A., Mccullough, J., Clague, M. J. & Urbé, S. 2006. The ubiquitin isopeptidase UBPY regulates endosomal ubiquitin dynamics and is essential for receptor down-

- regulation. *J Biol Chem*, 281, 12618-24.
- Rue, S. M., Mattei, S., Saksena, S. & Emr, S. D. 2008. Novel Ist1-Did2 complex functions at a late step in multivesicular body sorting. *Mol Biol Cell*, 19, 475-84.
- Sahu, R., Kaushik, S., Clement, C. C., Cannizzo, E. S., Scharf, B., Follenzi, A., Potolicchio, I., Nieves, E., Cuervo, A. M. & Santambrogio, L. 2011. Microautophagy of cytosolic proteins by late endosomes. *Dev Cell*, 20, 131-9.
- Saksena, S., Wahlman, J., Teis, D., Johnson, A. E. & Emr, S. D. 2009. Functional reconstitution of ESCRT-III assembly and disassembly. *Cell*, 136, 97-109.
- Samson, R. Y., Obita, T., Freund, S. M., Williams, R. L. & Bell, S. D. 2008. A role for the ESCRT system in cell division in archaea. *Science*, 322, 1710-3.
- Sanderson, R. J. & Ironside, J. A. 2002. Squamous cell carcinomas of the head and neck. *BMJ*, 325, 822-7.
- Sanz-Moreno, V., Gadea, G., Ahn, J., Paterson, H., Marra, P., Pinner, S., Sahai, E. & Marshall, C. J. 2008. Rac Activation and Inactivation Control Plasticity of Tumor Cell Movement. *Cell*, 135, 510-523.
- Saraste, A. & Pulkki, K. 2000. Morphologic and biochemical hallmarks of apoptosis. *Cardiovascular Research*, 45, 528-537.
- Scheuring, S., Bodor, O., Röhricht, R. A., Müller, S., Beyer, A. & Köhrer, K. 1999. Cloning, characterisation, and functional expression of the *Mus musculus* SKD1 gene in yeast demonstrates that the mouse SKD1 and the yeast VPS4 genes are orthologues and involved in intracellular protein trafficking. *Gene*, 234, 149-59.
- Scheuring, S., Röhricht, R. A., Schöning-Burkhardt, B., Beyer, A., Müller, S., Abts, H. F. & Köhrer, K. 2001. Mammalian cells express two VPS4 proteins both of which are involved in intracellular protein trafficking. *J Mol Biol*, 312, 469-80.
- Schlienger, S., Campbell, S. & Claing, A. 2014. ARF1 regulates the Rho/MLC pathway to control EGF-dependent breast cancer cell invasion. *Molecular Biology of the Cell*, 25, 17-29.
- Schmidt, O. & Teis, D. 2012. The ESCRT machinery. *Curr Biol*, 22, R116-20.
- Schwickert, A., Weghake, E., Brüggemann, K., Engbers, A., Brinkmann, B. F., Kemper, B., Seggewiß, J., Stock, C., Ebnet, K., Kiesel, L., *et al.* 2015. microRNA miR-142-3p Inhibits Breast Cancer Cell Invasiveness by Synchronous Targeting of WASL, Integrin Alpha V, and Additional Cytoskeletal Elements. *PLOS ONE*, 10, e0143993.
- Sciubba, J. J. 2001. Oral Cancer. *American Journal of Clinical Dermatology*, 2, 239-251.
- Scott, A., Chung, H. Y., Gonciarz-Swiatek, M., Hill, G. C., Whitby, F. G., Gaspar, J., Holton, J.

M., Viswanathan, R., Ghaffarian, S., Hill, C. P., *et al.* 2005. Structural and mechanistic studies of VPS4 proteins. *Embo j*, 24, 3658-69.

Sedgwick, A. E., Clancy, J. W., Olivia Balmert, M. & D'souza-Schorey, C. 2015. Extracellular microvesicles and invadopodia mediate non-overlapping modes of tumor cell invasion. *Scientific Reports*, 5, 14748.

Sento, S., Sasabe, E. & Yamamoto, T. 2016. Application of a Persistent Heparin Treatment Inhibits the Malignant Potential of Oral Squamous Carcinoma Cells Induced by Tumor Cell-Derived Exosomes. *PLoS One*, 11, e0148454.

Shah, J. P. & Gil, Z. 2009. CURRENT CONCEPTS IN MANAGEMENT OF ORAL CANCER – SURGERY. *Oral oncology*, 45, 394-401.

Sharma, S., Gillespie, B. M., Palanisamy, V. & Gimzewski, J. K. 2011. Quantitative nanostructural and single-molecule force spectroscopy biomolecular analysis of human-saliva-derived exosomes. *Langmuir*, 27, 14394-400.

Shedden, K., Xie, X. T., Chandaroy, P., Chang, Y. T. & Rosania, G. R. 2003. Expulsion of Small Molecules in Vesicles Shed by Cancer Cells: Association with Gene Expression and Chemosensitivity Profiles^{1,2}. *Cancer Research*, 63, 4331-4337.

Shen, B., Zhang, W., Zhang, J., Zhou, J., Wang, J., Chen, L., Wang, L., Hodgkins, A., Iyer, V., Huang, X., *et al.* 2014. Efficient genome modification by CRISPR-Cas9 nickase with minimal off-target effects. *Nature Methods*, 11, 399-402.

Shestakova, A., Curtiss, M., Davies, B. A., Katzmann, D. J. & Babst, M. 2013. The Linker Region Plays a Regulatory Role in Assembly and Activity of the Vps4 AAA ATPase *. *Journal of Biological Chemistry*, 288, 26810-26819.

Shestakova, A., Hanono, A., Drosner, S., Curtiss, M., Davies, B. A., Katzmann, D. J. & Babst, M. 2010. Assembly of the AAA ATPase Vps4 on ESCRT-III. *Mol Biol Cell*, 21, 1059-71.

Shields, S. B. & Piper, R. C. 2011. How ubiquitin functions with ESCRTs. *Traffic*, 12, 1306-17.

Shim, S., Kimpler, L. A. & Hanson, P. I. 2007. Structure/function analysis of four core ESCRT-III proteins reveals common regulatory role for extreme C-terminal domain. *Traffic*, 8, 1068-79.

Shim, S., Merrill, S. A. & Hanson, P. I. 2008. Novel interactions of ESCRT-III with LIP5 and VPS4 and their implications for ESCRT-III disassembly. *Mol Biol Cell*, 19, 2661-72.

Singh, K., Evens, H., Nair, N., Rincón, M. Y., Sarcar, S., Samara-Kuko, E., Chuah, M. K. & Vandendriessche, T. 2018. Efficient In Vivo Liver-Directed Gene Editing Using CRISPR/Cas9. *Mol Ther*, 26, 1241-1254.

- Sjoqvist, S., Kasai, Y., Shimura, D., Ishikawa, T., Ali, N., Iwata, T. & Kanai, N. 2019. Oral keratinocyte-derived exosomes regulate proliferation of fibroblasts and epithelial cells. *Biochem Biophys Res Commun*, 514, 706-712.
- Skalicky, J. J., Arii, J., Wenzel, D. M., Stubblefield, W. M., Katsuyama, A., Uter, N. T., Bajorek, M., Myszkowski, D. G. & Sundquist, W. I. 2012. Interactions of the human LIP5 regulatory protein with endosomal sorting complexes required for transport. *J Biol Chem*, 287, 43910-26.
- Slagsvold, T., Aasland, R., Hirano, S., Bache, K. G., Raiborg, C., Trambaiolo, D., Wakatsuki, S. & Stenmark, H. 2005. Eap45 in mammalian ESCRT-II binds ubiquitin via a phosphoinositide-interacting GLUE domain. *J Biol Chem*, 280, 19600-6.
- Song, B., Yang, S., Hwang, G. H., Yu, J. & Bae, S. 2021. Analysis of NHEJ-Based DNA Repair after CRISPR-Mediated DNA Cleavage. *Int J Mol Sci*, 22.
- Sorkina, T., Bild, A., Tebar, F. & Sorkin, A. 1999. Clathrin, adaptors and eps15 in endosomes containing activated epidermal growth factor receptors. *J Cell Sci*, 112 (Pt 3), 317-27.
- Stahelin, R. V., Long, F., Diraviyam, K., Bruzik, K. S., Murray, D. & Cho, W. 2002. Phosphatidylinositol 3-phosphate induces the membrane penetration of the FYVE domains of Vps27p and Hrs. *J Biol Chem*, 277, 26379-88.
- Ståhl, A.-L., Johansson, K., Mossberg, M., Kahn, R. & Karpman, D. 2019. Exosomes and microvesicles in normal physiology, pathophysiology, and renal diseases. *Pediatric nephrology (Berlin, Germany)*, 34, 11-30.
- Stenmark, H. 2009. Rab GTPases as coordinators of vesicle traffic. *Nat Rev Mol Cell Biol*, 10, 513-25.
- Stenmark, H. & Aasland, R. 1999. FYVE-finger proteins--effectors of an inositol lipid. *J Cell Sci*, 112 (Pt 23), 4175-83.
- Stenmark, H., Aasland, R., Toh, B. H. & D'arrigo, A. 1996. Endosomal localization of the autoantigen EEA1 is mediated by a zinc-binding FYVE finger. *J Biol Chem*, 271, 24048-54.
- Stern, K. A., Visser Smit, G. D., Place, T. L., Winistorfer, S., Piper, R. C. & Lill, N. L. 2007. Epidermal growth factor receptor fate is controlled by Hrs tyrosine phosphorylation sites that regulate Hrs degradation. *Mol Cell Biol*, 27, 888-98.
- Stoorvogel, W., Oorschot, V. & Geuze, H. J. 1996. A novel class of clathrin-coated vesicles budding from endosomes. *J Cell Biol*, 132, 21-33.
- Storm, M. P., Sorrell, I., Shipley, R., Regan, S., Luetchford, K. A., Sathish, J., Webb, S. & Ellis, M. J. 2016. Hollow Fiber Bioreactors for In Vivo-like Mammalian Tissue Culture. *J Vis Exp*.
- Strauss, K., Goebel, C., Runz, H., Möbius, W., Weiss, S., Feussner, I., Simons, M. & Schneider, A. 2010. Exosome secretion ameliorates lysosomal storage of cholesterol in Niemann-Pick type

C disease. *J Biol Chem*, 285, 26279-88.

Strickland, M., Watanabe, S., Bonn, S. M., Camara, C. M., Starich, M. R., Fushman, D., Carter, C. A. & Tjandra, N. 2022. Tsg101/ESCRT-I recruitment regulated by the dual binding modes of K63-linked diubiquitin. *Structure*, 30, 289-299.e6.

Striebel, F., Kress, W. & Weber-Ban, E. 2009. Controlled destruction: AAA+ ATPases in protein degradation from bacteria to eukaryotes. *Current opinion in structural biology*, 19, 209-217.

Stuffers, S., Sem Wegner, C., Stenmark, H. & Brech, A. 2009. Multivesicular endosome biogenesis in the absence of ESCRTs. *Traffic*, 10, 925-37.

Sudbery, I., Enright, A. J., Fraser, A. G. & Dunham, I. 2010. Systematic analysis of off-target effects in an RNAi screen reveals microRNAs affecting sensitivity to TRAIL-induced apoptosis. *BMC Genomics*, 11, 175.

Sun, Y., Zheng, W., Guo, Z., Ju, Q., Zhu, L., Gao, J., Zhou, L., Liu, F., Xu, Y., Zhan, Q., *et al.* 2016. A novel TP53 pathway influences the HGS-mediated exosome formation in colorectal cancer. *Sci Rep*, 6, 28083.

Syn, N., Wang, L., Sethi, G., Thiery, J. P. & Goh, B. C. 2016. Exosome-Mediated Metastasis: From Epithelial-Mesenchymal Transition to Escape from Immunosurveillance. *Trends Pharmacol Sci*, 37, 606-617.

Szczepanski, M. J., Czystowska, M., Szajnik, M., Harasymczuk, M., Boyiadzis, M., Kruk-Zagajewska, A., Szyfter, W., Zeromski, J. & Whiteside, T. L. 2009. Triggering of Toll-like Receptor 4 Expressed on Human Head and Neck Squamous Cell Carcinoma Promotes Tumor Development and Protects the Tumor from Immune Attack. *Cancer Research*, 69, 3105-3113.

Tamai, K., Tanaka, N., Nakano, T., Kakazu, E., Kondo, Y., Inoue, J., Shiina, M., Fukushima, K., Hoshino, T., Sano, K., *et al.* 2010. Exosome secretion of dendritic cells is regulated by Hrs, an ESCRT-0 protein. *Biochem Biophys Res Commun*, 399, 384-90.

Tandon, P., Dadhich, A., Saluja, H., Bawane, S. & Sachdeva, S. 2017. The prevalence of squamous cell carcinoma in different sites of oral cavity at our Rural Health Care Centre in Loni, Maharashtra - a retrospective 10-year study. *Contemporary oncology (Poznan, Poland)*, 21, 178-183.

Teis, D., Saksena, S. & Emr, S. D. 2008. Ordered assembly of the ESCRT-III complex on endosomes is required to sequester cargo during MVB formation. *Dev Cell*, 15, 578-89.

Teis, D., Saksena, S., Judson, B. L. & Emr, S. D. 2010. ESCRT-II coordinates the assembly of ESCRT-III filaments for cargo sorting and multivesicular body vesicle formation. *Embo j*, 29, 871-83.

Teo, H., Gill, D. J., Sun, J., Perisic, O., Veprintsev, D. B., Vallis, Y., Emr, S. D. & Williams, R. L. 2006. ESCRT-I core and ESCRT-II GLUE domain structures reveal role for GLUE in linking

to ESCRT-I and membranes. *Cell*, 125, 99-111.

Terns, M. P. & Terns, R. M. 2011. CRISPR-based adaptive immune systems. *Curr Opin Microbiol*, 14, 321-7.

Theos, A. C., Truschel, S. T., Tenza, D., Hurbain, I., Harper, D. C., Berson, J. F., Thomas, P. C., Raposo, G. & Marks, M. S. 2006. A luminal domain-dependent pathway for sorting to intraluminal vesicles of multivesicular endosomes involved in organelle morphogenesis. *Dev Cell*, 10, 343-54.

Théry, C. 2011. Exosomes: secreted vesicles and intercellular communications. *F1000 Biol Rep*, 3, 15.

Théry, C., Amigorena, S., Raposo, G. & Clayton, A. 2006. Isolation and characterization of exosomes from cell culture supernatants and biological fluids. *Curr Protoc Cell Biol*, Chapter 3, Unit 3.22.

Théry, C., Witwer, K. W., Aikawa, E., Alcaraz, M. J., Anderson, J. D., Andriantsitohaina, R., Antoniou, A., Arab, T., Archer, F., Atkin-Smith, G. K., *et al.* 2018. Minimal information for studies of extracellular vesicles 2018 (MISEV2018): a position statement of the International Society for Extracellular Vesicles and update of the MISEV2014 guidelines. *J Extracell Vesicles*, 7, 1535750.

Thomas, G. R. & Jefferson, G. 2013. *Chapter 64 - Head and Neck Cancer*.

Toker, A. & Cantley, L. C. 1997. Signalling through the lipid products of phosphoinositide-3-OH kinase. *Nature*, 387, 673-6.

Tomas, A., Futter, C. E. & Eden, E. R. 2014. EGF receptor trafficking: consequences for signaling and cancer. *Trends Cell Biol*, 24, 26-34.

Toyoshima, M., Tanaka, N., Aoki, J., Tanaka, Y., Murata, K., Kyuuma, M., Kobayashi, H., Ishii, N., Yaegashi, N. & Sugamura, K. 2007. Inhibition of tumor growth and metastasis by depletion of vesicular sorting protein Hrs: its regulatory role on E-cadherin and beta-catenin. *Cancer Res*, 67, 5162-71.

Trajkovic, K., Hsu, C., Chiantia, S., Rajendran, L., Wenzel, D., Wieland, F., Schwille, P., Brügger, B. & Simons, M. 2008. Ceramide Triggers Budding of Exosome Vesicles into Multivesicular Endosomes. *Science*, 319, 1244.

Tricarico, C., Clancy, J. & D'souza-Schorey, C. 2017. Biology and biogenesis of shed microvesicles. *Small GTPases*, 8, 220-232.

Triozi, P. M., Schmidt, H. W., Dervinis, C., Kirst, M. & Conde, D. 2021. Simple, efficient and open-source CRISPR/Cas9 strategy for multi-site genome editing in *Populus tremula* × *alba*. *Tree Physiol*, 41, 2216-2227.

- Tu, C., Ahmad, G., Mohapatra, B., Bhattacharyya, S., Ortega-Cava, C. F., Chung, B. M., Wagner, K. U., Raja, S. M., Naramura, M., Band, V., *et al.* 2011. ESCRT proteins: Double-edged regulators of cellular signaling. *Bioarchitecture*, 1, 45-48.
- Tu, C., Ortega-Cava, C. F., Winograd, P., Stanton, M. J., Reddi, A. L., Dodge, I., Arya, R., Dimri, M., Clubb, R. J., Naramura, M., *et al.* 2010. Endosomal-sorting complexes required for transport (ESCRT) pathway-dependent endosomal traffic regulates the localization of active Src at focal adhesions. *Proc Natl Acad Sci U S A*, 107, 16107-12.
- Vajjhala, P. R., Nguyen, C. H., Landsberg, M. J., Kistler, C., Gan, A. L., King, G. F., Hankamer, B. & Munn, A. L. 2008. The Vps4 C-terminal helix is a critical determinant for assembly and ATPase activity and has elements conserved in other members of the meiotic clade of AAA ATPases. *Febs j*, 275, 1427-1449.
- Van Niel, G., Charrin, S., Simoes, S., Romao, M., Rochin, L., Saftig, P., Marks, M. S., Rubinstein, E. & Raposo, G. 2011. The tetraspanin CD63 regulates ESCRT-independent and -dependent endosomal sorting during melanogenesis. *Dev Cell*, 21, 708-21.
- Van niel, G., Charrin, S., Simoes, S., Romao, M., Rochin, L., Saftig, P., Marks, Michael s., Rubinstein, E. & Raposo, G. 2011. The Tetraspanin CD63 Regulates ESCRT-Independent and -Dependent Endosomal Sorting during Melanogenesis. *Developmental Cell*, 21, 708-721.
- Vanlandingham, P. A. & Ceresa, B. P. 2009. Rab7 regulates late endocytic trafficking downstream of multivesicular body biogenesis and cargo sequestration. *J Biol Chem*, 284, 12110-24.
- Vasconcelos, M. H., Caires, H. R., Ābols, A., Xavier, C. P. R. & Linē, A. 2019. Extracellular vesicles as a novel source of biomarkers in liquid biopsies for monitoring cancer progression and drug resistance. *Drug Resist Updat*, 47, 100647.
- Ventimiglia, L. N. & Alonso, M. A. 2016. Biogenesis and Function of T Cell-Derived Exosomes. *Frontiers in Cell and Developmental Biology*, 4.
- Vickers, T. A., Lima, W. F., Wu, H., Nichols, J. G., Linsley, P. S. & Crooke, S. T. 2009. Off-target and a portion of target-specific siRNA mediated mRNA degradation is Ago2 'Slicer' independent and can be mediated by Ago1. *Nucleic Acids Res*, 37, 6927-41.
- Vieira, A. V., Lamaze, C. & Schmid, S. L. 1996. Control of EGF receptor signaling by clathrin-mediated endocytosis. *Science*, 274, 2086-9.
- Vietri, M., Schink, K. O., Campsteijn, C., Wegner, C. S., Schultz, S. W., Christ, L., Thoresen, S. B., Brech, A., Raiborg, C. & Stenmark, H. 2015. Spastin and ESCRT-III coordinate mitotic spindle disassembly and nuclear envelope sealing. *Nature*, 522, 231-235.
- Vonderheit, A. & Helenius, A. 2005. Rab7 associates with early endosomes to mediate sorting and transport of Semliki forest virus to late endosomes. *PLoS Biol*, 3, e233.

- Wang, T., Gilkes, D. M., Takano, N., Xiang, L., Luo, W., Bishop, C. J., Chaturvedi, P., Green, J. J. & Semenza, G. L. 2014. Hypoxia-inducible factors and RAB22A mediate formation of microvesicles that stimulate breast cancer invasion and metastasis. *Proceedings of the National Academy of Sciences of the United States of America*, 111, E3234-E3242.
- Wang, T. & Hong, W. 2006. RILP interacts with VPS22 and VPS36 of ESCRT-II and regulates their membrane recruitment. *Biochem Biophys Res Commun*, 350, 413-23.
- Weihua, Z., Lin, Q., Ramoth, A. J., Fan, D. & Fidler, I. J. 2011. Formation of solid tumors by a single multinucleated cancer cell. *Cancer*, 117, 4092-9.
- Werner, C. W. & Seymour, R. A. 2009. Are alcohol containing mouthwashes safe? *Br Dent J*, 207, 488-9.
- Wiedenheft, B., Sternberg, S. H. & Doudna, J. A. 2012. RNA-guided genetic silencing systems in bacteria and archaea. *Nature*, 482, 331-8.
- Wollert, T. & Hurley, J. H. 2010. Molecular mechanism of multivesicular body biogenesis by ESCRT complexes. *Nature*, 464, 864-9.
- Wollert, T., Wunder, C., Lippincott-Schwartz, J. & Hurley, J. H. 2009. Membrane scission by the ESCRT-III complex. *Nature*, 458, 172-7.
- Wonganu, B. & Berger, B. W. 2016. A specific, transmembrane interface regulates fibroblast activation protein (FAP) homodimerization, trafficking and exopeptidase activity. *Biochim Biophys Acta*, 1858, 1876-82.
- Woodfield, S. E., Graves, H. K., Hernandez, J. A. & Bergmann, A. 2013. De-regulation of JNK and JAK/STAT signaling in ESCRT-II mutant tissues cooperatively contributes to neoplastic tumorigenesis. *PLoS One*, 8, e56021.
- Wu, L., Cheng, Y., Geng, D., Fan, Z., Lin, B., Zhu, Q., Li, J., Qin, W. & Yi, W. 2022. O-GlcNAcylation regulates epidermal growth factor receptor intracellular trafficking and signaling. *Proceedings of the National Academy of Sciences*, 119, e2107453119.
- Wu, T. & Dai, Y. 2017. Tumor microenvironment and therapeutic response. *Cancer Lett*, 387, 61-68.
- Wu, X., Kriz, A. J. & Sharp, P. A. 2014. Target specificity of the CRISPR-Cas9 system. *Quant Biol*, 2, 59-70.
- Xiao, B., Fan, S., Zeng, Z., Xiong, W., Cao, L., Yang, Y., Li, W., Wang, R., Tang, K., Qian, J., et al. 2006. Purification of novel UBAP1 protein and its decreased expression on nasopharyngeal carcinoma tissue microarray. *Protein Expr Purif*, 47, 60-7.
- Xiao, B. L., Wang, X. L., Xia, H. F., Zhang, L. Z., Wang, K. M., Chen, Z. K., Zhong, Y. H., Jiang, H. G., Zhou, F. X., Wang, W., et al. 2023. HRS Regulates Small Extracellular Vesicle

PD-L1 Secretion and Is Associated with Anti-PD-1 Treatment Efficacy. *Cancer Immunol Res*, 11, 228-240.

Xiao, J., Chen, X. W., Davies, B. A., Saltiel, A. R., Katzmann, D. J. & Xu, Z. 2009. Structural basis of Ist1 function and Ist1-Did2 interaction in the multivesicular body pathway and cytokinesis. *Mol Biol Cell*, 20, 3514-24.

Xiao, J., Xia, H., Yoshino-Koh, K., Zhou, J. & Xu, Z. 2007. Structural characterization of the ATPase reaction cycle of endosomal AAA protein Vps4. *J Mol Biol*, 374, 655-70.

Xiao, J., Xia, H., Zhou, J., Azmi, I. F., Davies, B. A., Katzmann, D. J. & Xu, Z. 2008. Structural basis of Vta1 function in the multivesicular body sorting pathway. *Dev Cell*, 14, 37-49.

Xie, F., Zhou, X., Fang, M., Li, H., Su, P., Tu, Y., Zhang, L. & Zhou, F. 2019. Extracellular Vesicles in Cancer Immune Microenvironment and Cancer Immunotherapy. *Advanced science (Weinheim, Baden-Wuerttemberg, Germany)*, 6, 1901779-1901779.

Xie, N., Meng, Q., Zhang, Y., Luo, Z., Xue, F., Liu, S., Li, Y. & Huang, Y. 2021. MicroRNA-142-3p suppresses cell proliferation, invasion and epithelial-to-mesenchymal transition via RAC1-ERK1/2 signaling in colorectal cancer. *Mol Med Rep*, 24.

Xu, R., Rai, A., Chen, M., Suwakulsiri, W., Greening, D. W. & Simpson, R. J. 2018. Extracellular vesicles in cancer — implications for future improvements in cancer care. *Nature Reviews Clinical Oncology*, 15, 617-638.

Xu, Z., Liang, L., Wang, H., Li, T. & Zhao, M. 2003. HCRP1, a novel gene that is downregulated in hepatocellular carcinoma, encodes a growth-inhibitory protein. *Biochemical and Biophysical Research Communications*, 311, 1057-1066.

Yamakawa, K., Takahashi, T., Horio, Y., Murata, Y., Takahashi, E., Hibi, K., Yokoyama, S., Ueda, R., Takahashi, T. & Nakamura, Y. 1993. Frequent homozygous deletions in lung cancer cell lines detected by a DNA marker located at 3p21.3-p22. *Oncogene*, 8, 327-330.

Yang, D. & Hurley, J. H. 2010. Structural role of the Vps4-Vta1 interface in ESCRT-III recycling. *Structure (London, England : 1993)*, 18, 976-984.

Yang, Z., Vild, C., Ju, J., Zhang, X., Liu, J., Shen, J., Zhao, B., Lan, W., Gong, F., Liu, M., *et al.* 2012. Structural basis of molecular recognition between ESCRT-III-like protein Vps60 and AAA-ATPase regulator Vta1 in the multivesicular body pathway. *J Biol Chem*, 287, 43899-908.

Yap, T., Pruthi, N., Seers, C., Belobrov, S., Mccullough, M. & Celentano, A. 2020. Extracellular Vesicles in Oral Squamous Cell Carcinoma and Oral Potentially Malignant Disorders: A Systematic Review. *Int J Mol Sci*, 21.

Yau, W. L., Lung, H. L., Zabarovsky, E. R., Lerman, M. I., Sham, J. S., Chua, D. T., Tsao, S. W., Stanbridge, E. J. & Lung, M. L. 2006. Functional studies of the chromosome 3p21.3 candidate tumor suppressor gene BLU/ZMYND10 in nasopharyngeal carcinoma. *Int J Cancer*,

119, 2821-6.

Young, T. W., Mei, F. C., Rosen, D. G., Yang, G., Li, N., Liu, J. & Cheng, X. 2007a. Up-regulation of tumor susceptibility gene 101 protein in ovarian carcinomas revealed by proteomics analyses. *Mol Cell Proteomics*, 6, 294-304.

Young, T. W., Rosen, D. G., Mei, F. C., Li, N., Liu, J., Wang, X. F. & Cheng, X. 2007b. Up-regulation of tumor susceptibility gene 101 conveys poor prognosis through suppression of p21 expression in ovarian cancer. *Clin Cancer Res*, 13, 3848-54.

Yu, Z., Zeng, J., Wang, J., Cui, Y., Song, X., Zhang, Y., Cheng, X., Hou, N., Teng, Y., Lan, Y., *et al.* 2020. Hepatocyte growth factor-regulated tyrosine kinase substrate is essential for endothelial cell polarity and cerebrovascular stability. *Cardiovascular Research*, 117, 533-546.

Yu, Z., Zeng, J., Wang, J., Cui, Y., Song, X., Zhang, Y., Cheng, X., Hou, N., Teng, Y., Lan, Y., *et al.* 2021. Hepatocyte growth factor-regulated tyrosine kinase substrate is essential for endothelial cell polarity and cerebrovascular stability. *Cardiovascular Research*, 117, 533-546.

Yu, Z. W., Zhong, L. P., Ji, T., Zhang, P., Chen, W. T. & Zhang, C. P. 2010. MicroRNAs contribute to the chemoresistance of cisplatin in tongue squamous cell carcinoma lines. *Oral Oncol*, 46, 317-22.

Zagalak, J. A., Menzi, M., Schmich, F., Jahns, H., Dogar, A. M., Wullschleger, F., Towbin, H. & Hall, J. 2015. Properties of short double-stranded RNAs carrying randomized base pairs: toward better controls for RNAi experiments. *Rna*, 21, 2132-42.

Zamborlini, A., Usami, Y., Radoshitzky, S. R., Popova, E., Palu, G. & Göttlinger, H. 2006. Release of autoinhibition converts ESCRT-III components into potent inhibitors of HIV-1 budding. *Proc Natl Acad Sci U S A*, 103, 19140-5.

Zha, Q. B., Yao, Y. F., Ren, Z. J., Li, X. J. & Tang, J. H. 2017. Extracellular vesicles: An overview of biogenesis, function, and role in breast cancer. *Tumour Biol*, 39, 1010428317691182.

Zhang, H., Deng, T., Liu, R., Bai, M., Zhou, L., Wang, X., Li, S., Wang, X., Yang, H., Li, J., *et al.* 2017a. Exosome-delivered EGFR regulates liver microenvironment to promote gastric cancer liver metastasis. *Nat Commun*, 8, 15016.

Zhang, H., Deng, T., Liu, R., Bai, M., Zhou, L., Wang, X., Li, S., Wang, X., Yang, H., Li, J., *et al.* 2017b. Exosome-delivered EGFR regulates liver microenvironment to promote gastric cancer liver metastasis. *Nature Communications*, 8, 15016.

Zhang, H., Qin, C., An, C., Zheng, X., Wen, S., Chen, W., Liu, X., Lv, Z., Yang, P., Xu, W., *et al.* 2021. Application of the CRISPR/Cas9-based gene editing technique in basic research, diagnosis, and therapy of cancer. *Molecular Cancer*, 20, 126.

Zhang, Y., Chen, X., Gueydan, C. & Han, J. 2018. Plasma membrane changes during

programmed cell deaths. *Cell Res*, 28, 9-21.

Zhang, Y., Liu, Y., Liu, H. & Tang, W. H. 2019. Exosomes: biogenesis, biologic function and clinical potential. *Cell & Bioscience*, 9, 19.

Zhu, G., Gilchrist, R., Borley, N., Chng, H. W., Morgan, M., Marshall, J. F., Camplejohn, R. S., Muir, G. H. & Hart, I. R. 2004. Reduction of TSG101 protein has a negative impact on tumor cell growth. *International Journal of Cancer*, 109, 541-547.

Zhuang, G., Wu, X., Jiang, Z., Kasman, I., Yao, J., Guan, Y., Oeh, J., Modrusan, Z., Bais, C., Sampath, D., *et al.* 2012. Tumour-secreted miR-9 promotes endothelial cell migration and angiogenesis by activating the JAK-STAT pathway. *Embo j*, 31, 3513-23.

Zirngibl, M., Fürnrohr, B. G., Janko, C., Munoz, L. E., Voll, R. E., Gregory, C. D., Schett, G. & Herrmann, M. 2015. Loading of nuclear autoantigens prototypically recognized by systemic lupus erythematosus sera into late apoptotic vesicles requires intact microtubules and myosin light chain kinase activity. *Clin Exp Immunol*, 179, 39-49.

Zlotogorski-Hurvitz, A., Dayan, D., Chaushu, G., Salo, T. & Vered, M. 2016. Morphological and molecular features of oral fluid-derived exosomes: oral cancer patients versus healthy individuals. *J Cancer Res Clin Oncol*, 142, 101-10.

Zlotogorski-Hurvitz, A., Dekel, B. Z., Malonek, D., Yahalom, R. & Vered, M. 2019. FTIR-based spectrum of salivary exosomes coupled with computational-aided discriminating analysis in the diagnosis of oral cancer. *J Cancer Res Clin Oncol*, 145, 685-694.

Zuris, J. A., Thompson, D. B., Shu, Y., Guilinger, J. P., Bessen, J. L., Hu, J. H., Maeder, M. L., Joung, J. K., Chen, Z.-Y. & Liu, D. R. 2015. Cationic lipid-mediated delivery of proteins enables efficient protein-based genome editing in vitro and in vivo. *Nature Biotechnology*, 33, 73-80.